Pierre Baumann, BSc MSc

Synthesis and Characterization of Nanosized Silicon Particles for Lithium-Ion Batteries

DOCTORAL THESIS

to achieve the university degree of

Doktor der technischen Wissenschaften

submitted to

Graz University of Technology

Supervisor

Assoc.Prof. Dipl.-Ing. Dr.techn. Roland Fischer

Institute for Inorganic Chemistry

in Cooperation with VARTA Micro Innovation GmbH

Graz, January 2016

AFFIDAVIT

I declare that I have authored this thesis independently, that I have not used other than the declared sources/resources, and that I have explicitly indicated all material which has been quoted either literally or by content from the sources used. The text document uploaded to TUGRAZonline is identical to the present doctoral thesis.

Date	Signature

Acknowledgement

Herewith I would like to express my deep gratitude for the supervision of Assoc.Prof. Dipl.-Ing. Dr.techn. Roland Fischer. Thank you for giving me the possibility to write this thesis and for being always at my side when I needed scientific help.

Furthermore, I would like to express my perfect appreciation to my financial supporter, the VARTA Micro Innovation GmbH. In this context, special thanks go to CEO of the company Dipl.-Ing. Dr.techn. Stefan Koller and Dipl.-Ing. Dr.techn. Harald Kren.

I am particularly grateful that I had the opportunity to work with such great colleagues. I would like to thank Dipl.-Ing. Michaela Scharfegger for introducing me in the synthesis of core-shell structured composite materials in the fluidized bed reactor. I am much obliged to Ing. Stephania Toulis and Ing. Christian Baumann for their patience in introducing me to preparing electrodes and assembling half cells, as well as for the great working atmosphere in the office. The same applies for Christian Lenardt during the last months. I also want to thank Dipl.-Ing. Gisela Fauler for the GC/MS measurements and Ing. Katja Kapper for helping me with the software. Special thanks also to Dipl.-Ing. Christoph Stangl for his help in preparing full cells for performing neutron scattering experiments at LLB Saclay. In addition, heartfelt thanks to Andrea Droisner, Dipl.-Ing. Dr.techn. Bernd Fuchsbichler, Dipl.-Ing. Dr.techn. Colin God, Dipl.-Ing. Dr.techn. Martin Schmuck, Dipl.-Ing. Dr.techn. Katharina Gruber, Dipl.-Ing. Dr.techn. Patricia Handel and Dr.techn. Sandra Pötz MSc for the pleasant time during the stay at the company.

I also want to thank the head of the Inorganic Chemistry Institute Univ.-Prof. Dipl.-Chem. Dr.rer.nat. Frank Uhlig, as well as thanks to the scientific and non scientific staff of the institute. In this context, special thanks go to Cathrin Zeppek MSc, Ph.D. Ana Torvisco Gomez, Dipl.-Ing. Dr.techn. Johann Pichler , Dipl.-Ing. Michael Haas. and Dipl.-Ing. Thomas Hafner.

At this point I also want to thank Dipl.-Ing. Dr.techn. Brigitte Bitschnau and Ao.Univ.-Prof. Dipl.-Ing. Dr.techn. Franz Mautner for the XRD measurements and evaluation. I would also like to thank Dipl.-Ing. Theresa Kainz for performing the TGA/DSC/MS measurements at the Institute for Chemistry and Technology of Materials.

Special thanks also go to Ao.Univ.-Prof. Dipl.-Ing. Dr.techn. Ferdinand Hofer and Prof. Dr. Rudolf Pietschnig for peer reviewing this thesis.

I want to acknowledge the Austrian Centre for Electron Microscopy and Nanoanalysis FELMI-ZFE for the FIB cut and BIB slope cut images.

Very special thanks to my girlfriend Julia for the wonderful, unforgettable time we had. Furthermore, thanks to Lukas for the funny time and the BBQ nosh-up's we had.

However, most thanks deserves my dear mother Michaela, without her all this would not have been possible. Special thanks also to Andreas for being a good friend.

Abstract

Lithium-ion batteries represent the state-of-the-art technology in rechargeable energy storage devices and have become not only omnipresent power sources for mobile electronics, but their usage has also expanded into power sources for electric vehicles. They are also becoming an attractive option for stationary energy storage units for renewable energies. The fast development of these applications leads to increasing demands concerning higher energy and power densities, as well as longer life cycles.

To achieve these requirements, much research is performed on new negative electrode materials with high specific capacities, such as alloy-type materials. In this context, silicon attracts significant attention as potential replacement of so far used carbonaceous materials due to its nearly 10 times higher specific capacity, higher safety and stability. However, silicon negative electrode materials suffer from drastic volume changes of more than 300 % during lithiation/delithiation and low intrinsic electrical conductivity. Hence, nanosizing of the silicon is required to reduce the mechanical stress caused by the volume changes and to shorten the diffusion pathways of lithium ions. Unfortunately, the synthesis of nanosized silicon materials is a cost-intensive procedure.

Therefore, high energy planetary ball milling is applied in this thesis as a new and cheap method producing nanosized silicon for lithium-ion batteries. It outlines the influence of various milling parameters on the particle size distribution and the mechanochemical surface functionalization caused by the solvent during milling. Furthermore, the electrochemical performance and characteristics are studied on the basis of simple electrode mixtures and core-shell structured composite materials produced in a fluidized bed reactor.

Kurzfassung

Lithium-Ionen-Batterien repräsentieren die modernste Technologie im Bereich der wiederaufladbaren Energiespeichermedien und sind heutzutage nicht nur omnipräsente Stromquellen für mobile Elektronik, sondern deren Anwendung expandierte auch in den Bereich elektrisch betriebener Fahrzeuge. Desweiteren stellen sie eine attraktive Möglichkeit zur Speicherung erneuerbarer Energien in stationär betriebenen Energiespeichereinheiten dar. Die schnelle Entwicklung dieser Anwendungsmöglichkeiten führt zu einem steigenden Bedarf betreffend höherer Energie- und Leistungsdichten, sowie längerer Lebenszyklen.

Um diese Anforderungen zu erfüllen wird viel Forschungsarbeit bezüglich neuer negativer Elektrodenmaterialien mit hohen spezifischen Kapazitäten, wie zum Beispiel legierungsartige Materialien, durchgeführt. In diesem Zusammenhang erregt Silicium besondere Aufmerksamkeit als potentieller Ersatz für bisher verwendete kohlenstoffhaltige Materialien, aufgrund seiner beinahe 10-fach höheren spezifischen Kapazität, Sicherheit und Stabilität. Jedoch leiden siliciumhaltige Elektrodenmaterialien unter drastischen Volumensänderungen von mehr als 300 % während der Lithiierung/Delithiierung und einer niedrigen intrinsischen elektrischen Leitfähigkeit. Daher wird nanoskaliges Silicium benötigt um den durch die Volumensänderungen verursachten mechanischen Stress zu reduzieren, sowie die Diffusionswege für Lithium-Ionen zu verkürzen. Leider ist die Synthese von Siliciummaterialien im Nanometerbereich ein kostenintensives Verfahren.

Demzufolge wird in dieser Doktorarbeit Hochenergieplanetenkugelmahlen als neue und günstige Methode zur Produktion von Nano-Silicium für Lithium-Ionen-Batterien angewendet. Die Arbeit behandelt hierbei den Einfluss diverser Mahlparameter auf die Partikelgrößenverteilung, sowie die durch das Lösungsmittel während des Mahlens verursachte mechanochemische Oberflächenfunktionalisierung. Desweiteren werden das elektrochemische Verhalten sowie Charakteristika anhand von einfachen Elektrodenmixturen sowie Kern-Schale strukturierten Kompositmaterialien, welche in einem Wirbelschichtreaktor hergestellt werden, untersucht.

Abbreviations

1-M-2-p	1-Methoxy-2-propanol
AA	Acrylic acid
ATR	Attenuated total reflectance
BADGE	Bisphenol A diglycidyl ether
BIB	Broad ion beam
BMW	Bayerische Motoren Werke
BPR	Ball-to-powder weight ratio
CCC	Constant current charging
CE	Coulomb efficiency
CNT	Carbon nanotube
CR	Charge ratio
CV	Cyclic voltammetry
DCP	Differential capacity plot
DEC	Diethyl carbonate
DMC	Dimethyl carbonate
DSC	Differential scanning calorimetry
EC	Ethylene carbonate
EDX	Energy-dispersive X-ray spectroscopy
EMC	Ethyl methyl carbonate
FEC	Fluoroethylene carbonate
FIB	Focused ion beam
FTIR	Fourier transform infrared spectroscopy
GC	Gas chromatography
GPC	Gel permeation chromatography
HEA	Hydroxyethyl acrylate
HEBM	High energy ball milling
HPA	2-Hydroxypropyl acrylate
HSQ	Hydrogen silsesquioxane
LIB	Lithium-ion battery
LLO	Lithium-rich layered oxide
LTO	Lithium titan oxide
MACE	Metal-assisted chemical etching
MBE	Molecular beam epitaxy
MS	Mass spectrometry
NaAlg	Sodium alginate

NaCMC	Sodium carboxymethyl cellulose
NAM	Nanostructured & Amorphous Materials
NCA	Lithium nickel cobalt aluminum oxide
NMC	Lithium nickel manganese cobalt oxide
NMP	*N*-Methyl-2-pyrrolidone
OCV	Open-circuit voltage
PAA	Polyacrylic acid
PC	Propylene carbonate
PE	Polyethylene
PET	Polyethylene terephthalate
POM	Polyoxometalate
PP	Polypropylene
PVDF	Polyvinylidene fluoride
SEI	Solid electrolyte interface
SEM	Scanning electron microscope
SHE	Standard hydrogen electrode
SiNP	Silicon nanoparticle
SiNT	Silicon nanotube
SiNW	Silicon nanowire
SiQD	Silicon quantum dot
SRO	Silicon-rich oxide
TGA	Thermogravimetric analysis
THF	Tetrahydrofuran
VC	Vinylene carbonate
XRD	X-ray diffraction
YAG	Yttrium aluminum garnet

Table of Contents

1 Introduction

Since its commercialization in 1991 by Sony, the lithium-ion battery was able to develop an outstanding position within electronic industries (*1*). Due to their high gravimetric and volumetric energy density (compared to lead-acid, nickel-cadmium (Ni-Cd) and nickel-metal hydride (Ni-MH) batteries) lithium-ion batteries (LIBs) have become the state-of-the-art rechargeable compact energy storage systems for portable consumer electronics (mobile phones, notebooks, tablet computers etc.) and industrial electronic devices.

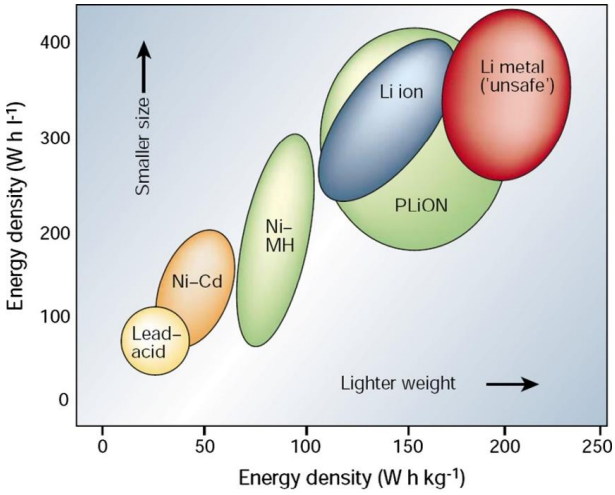

Figure 1. Comparison of the different batteries in terms of volumetric and gravimetric energy density (*2*)

In this century, the era of fossil fuels such as coal, natural gas and mineral oil will continuously expire and an upcoming era of green renewable energy is expected. Lithium-ion batteries play a crucial role in fulfilling this change by e.g. replacing combustion engines with electric motors for sustainable vehicles, such as hybrid vehicles or even full electric vehicles. Furthermore a very important field of application will be the storage of green, sustainable energy (solar, wind, geothermal). The fluctuations in the production of electricity from these renewable resources results in severe problems to stabilize the power supply system. Accordingly, an energy storage device is needed to store the produced energy in times of high power generation and to release it in times of shortage. In this field home storage systems are of particular importance as they give the possibility to store one's own energy in times of excess instead of (over-)supplying the grid with current. For this reason the market for lithium-ion batteries gets broader and will increase further, indicated as trend in Figure 2.

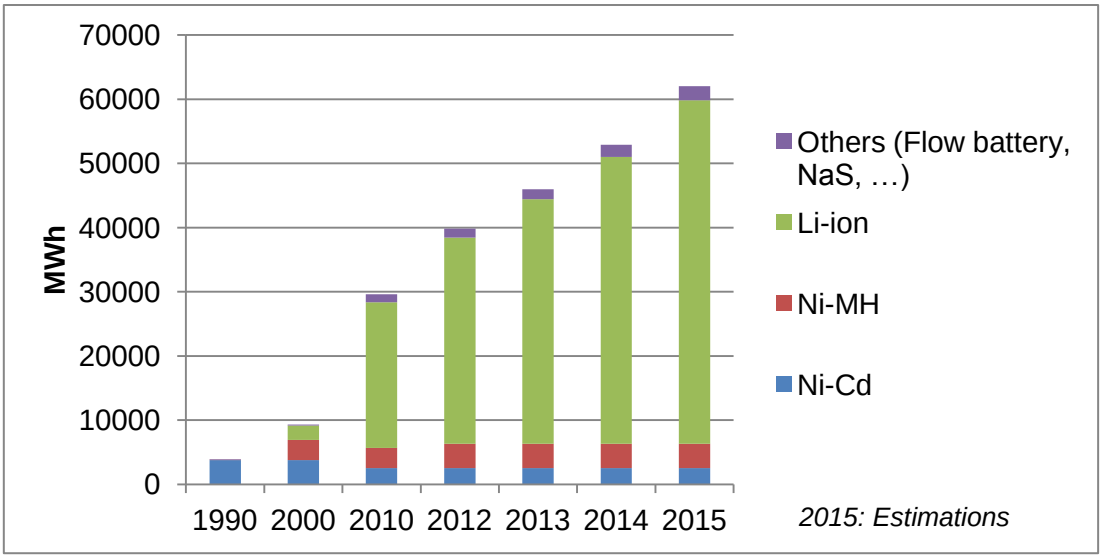

Figure 2. Worldwide rechargeable battery market – redrawn from (*3*)

However, the development of lithium-ion batteries not only drags behind the improvement of consumer electronics and their energy requirements, but also this battery system is not at the technological level to provide driving ranges for full electric vehicles comparable to gasoline-driven one's (*4*,*5*).

Hence a noticeable improvement in energy density is required to satisfy the demands for high capacity and power. To attain this goal new electrode materials with higher specific capacities have to be developed and/or the potential difference between the positive and negative electrode has to be enlarged. A promising approach to increase the capacity is based on the substitution of the commonly used carbonaceous negative electrode materials with a high capacity alloy-type material such as silicon. Unfortunately, these high capacity negative electrode materials suffer from poor cycle stability due to large volume changes during the lithiation and delithiation. By using nanoparticles the cycle stability can be improved, but with disadvantages in regard to the price.

In the context of this doctoral thesis silicon nanoparticles are produced via high energy planetary ball milling, which offers a cheap and up-scalable route for industrial production. The milled silicon nanoparticles are furthermore used to produce composite materials, such as core-shell particles, and their electrochemical performance is investigated and compared to commercial nano-silicon, obtained via an expensive pyrolysis route.

Furthermore the influence of different particle sizes, binders, electrolytes and cycling conditions on the electrochemical performance of these composites will be discussed.

2 Nanosized Silicon

2.1 General Background on Nanomaterials

The term *nano*, derived from the Greek word *nanos* (as well *nannos*) (*6*) which means dwarf, designates a billionth fraction of a unit (10^{-9}), for example of a meter (*7*). Thus the science of nanomaterials is often defined as dealing with objects on a size scale of 1-100 nm, sometimes up to 1000 nm (*8*,*9*). Infrequently nanomaterials are also named *mesoscopic materials* due to an IUPAC norm of 1985 which deals with the classification of porous materials. Therein the materials are classified according to their pore diameters (*10*):

- Pores with widths exceeding about 50 nm are called *macropores*
- Pores with widths between 2 nm and 50 nm are called *mesopores*
- Pores with widths not exceeding 2 nm are called *micropores*

In this context *meso* indicates that the properties of such materials are in between those of bulk materials and molecules, which is also appropriate for materials in the nanometer scale. Due to the small sizes they exhibit large surfaces (several 10 m^2/g) and surface properties become dominant over those of the bulk, as wells as size dependent quantum effects can be observed (*11*). This leads to different physical and chemical properties such as electrical conductivity, magnetism, fluorescence, melting point, reactivity and mechanical stiffness (*12*).

Figure 3. CdSe quantum dots with different particle sizes (*13*)

The use of the prefix *nano* started in the 1990's and results quite often in the wrong conclusion that nanoparticles are something fairly new. However, they have always been attended in nature due to volcanic eruptions, forest fires and natural composite materials such as bones, theeth or seashells in which nanocrystalline inorganic substances are imbedded in a protein matrix (*14*).

From a historical viewpoint the first man-made nanoparticles (apart from those probably made by early ancestors via grinding pigments or carbon black from their fires) were already produced in antiquity. Here they used colloidal gold to make ruby glass or for coloring ceramics, and these applications are still continuing now (*15*). In medieval times gold colloids were known to alchemists as *aurum potabile*, which means drinkable gold, and they were used as treatment for all kinds of then known diseases (*16*).

Figure 4. Colloidal gold suspension (*17*)

Scientific research on nanoparticles began with Michael Faraday in 1857 (*18*). He was the first one to have the notion that gold sols indeed contain small metal particles and studied their optical properties. Significant progress in this area was then provided by Wilhelm Ostwald with his observation that small crystals or particles dissolve in a sol (colloid) and redeposit onto larger ones (*19*). This effect is known as *Ostwald ripening* nowadays and enables the synthesis of monodisperse particles. Further contribution to the comprehension of nanosized materials was performed by Gustav Mie by the calculation of size dependent optical properties starting from the Maxwell equations (*20*). Finally, the discovery of colloidal semi-conductor nanocrystals (*quantum dots*) by Louis Brus in 1982 led to a boost in nanoscience which continues to this day (*21*). A Scifinder request (June 18, 2015) for the research topic *Nano* leads to almost 1.7 million references dealing with it, showing that

immense progress has been made over the last decades. The result is a wide range of available, commercial products containing nanomaterials (*22*,*23*):

- Encapsulation of glue in nanospheres, which burst under pressure and lead to a self-healing effect of the host material
- TiO_2 nanoparticles are used as UV filter in suncream or photocatalytic self-cleaning surfaces
- Water and dirt repellent surface coatings (*Lotus effect*)
- Scratch-resistant surfaces
- Antibacterial surfaces
- Anti-reflective coatings (especially for solar panels)
- Reinforcing fillers
- Energy storage materials
- Catalysts etc.

In the future nanomaterials will also play an extraordinary important role in medical applications such as diagnosis, therapy and drug delivery (*9*).

Basically the synthesic routes to nanomaterials are divided between two opposed major categories (*24*):

- *Bottom-up*: The buildup of particles starts with molecules or even atoms. Accordingly, larger particles are created from smaller building blocks, mainly through self-organization processes.
- *Top-down*: This approach starts from macroscopic materials which are continuously size-reduced to the nanometer region via milling, etching or laser ablation.

These approaches are now being discussed by the author with reference to silicon nanoparticles (SiNPs), providing an overview of this topic and helping the reader to understand why milled nanosized silicon is used in this thesis.

2.2 Bottom-Up Techniques for Nanosized Silicon

2.2.1 Solution Based Precursor Reduction

This class of *bottom-up* procedures uses reducing agents in the presence of silane precursors in solution. They represent attractive and intensive studied methods in the preparation of semiconducting nanomaterials and are based on the initial attempts by Heath in 1992 (*25*). The synthesis was based on the reduction of $SiCl_4$ and $RSiCl_3$ (R = H or octyl group) by sodium metal in a non-polar organic solvent under high temperature and pressure. Due to the relative straightforwardness of this approach, numerous variants have been established. Those include the use of sodium naphthalenide (*26*), lithium aluminum hydride (*27*) or alkali metal borohydrides (*28*) as reducing agents, different halosilanes (*29*,*30*) and silicon alkoxides (*31*) as precursor and the usage of polar non-protic organic solvents such as THF or glyme (*32*,*33*).

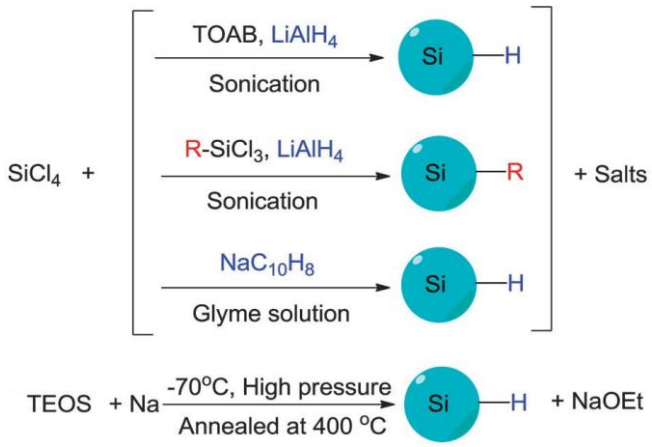

Figure 5. Preparation of colloidal silicon nanocrystals via solution based precursor reduction (*34*)

The hereby synthesized particles usually have a size of several nanometers (< 10 nm), are spherical and show blue or green luminescence (*35*,*36*). However, the drawback is that silicon tends to form a native oxide layer of roughly 1-2 nm thickness and these particles would completely oxidize by contact with air (*37*). Therefore the surface moieties have to be further functionalized. Fortunately for each kind of accessible moiety chemical routes are available for passivation, as shown in Figure 6.

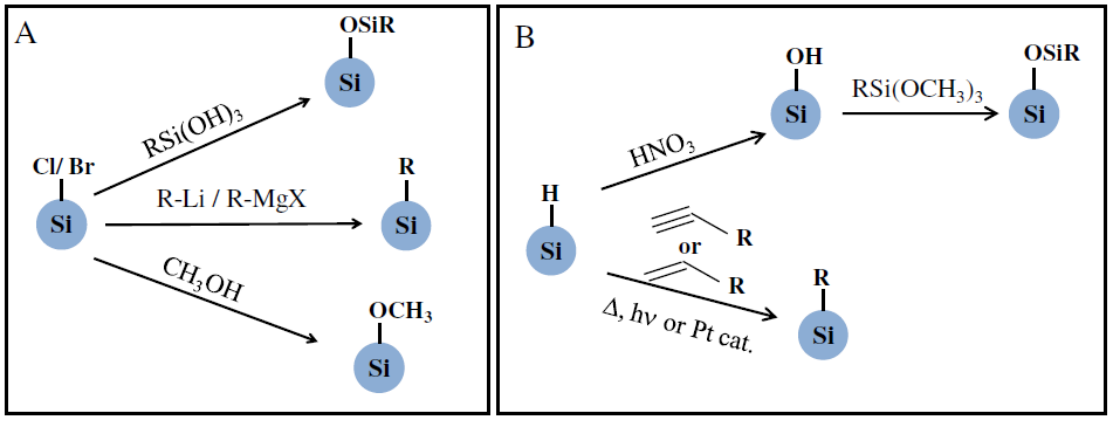

Figure 6. Surface passivation of (A) halide-terminated and (B) hydrogen-terminated SiNPs (*38*)

2.2.2 Oxidation of Zintl Phases

A *Zintl phase* is compound obtained by the reaction between an alkali or alkaline earth metal and post-transition metal or metalloid from group 13-16. These phases are understood to be intermetallic compounds with a strong heteropolar bond character between the alloying elements whereas the group 13-16 element can be considered as polyatomic anion (*39*).

The synthesis of the required compound is not complex, silicon and the desired group I or II metal are loaded in a tantalum or niobium tube and sealed in a quartz jacket under argon or vacuum. Then the reaction mixture is heated e. g. to 650 °C and dwell at this temperature for 4-5 days (*40*). The typical utilized *Zintl phases* for the preparation of silicon nanocrystals are MSi (M = Na, K), Mg_2Si, CaSi and $CaSi_2$ (*41*,*42*). They are dispersed in an organic solvent (usually glyme) and reacted with silicon halides, bromine or ammonium bromide (*43*). Due to the heterogeneous nature of the reaction the used silicide has to be milled before starting the oxidation. The resulting particles exhibit similar shape, size and surface moieties as those prepared by solution based precursor reduction and can therefore be further functionalized (*44*).

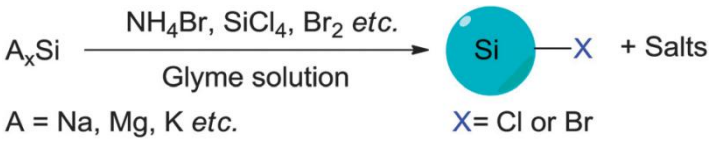

Figure 7. Zintl phase based synthetic method of preparing SiNPs (*34*)

2.2.3 Thermal Decomposition of Silanes

This type of procedure is the most frequently used for commercial SiNPs. It involves the decomposition of molecules bearing silicon such as silane (SiH_4) or higher oligomers followed by re-assembly processes (nucleation) to form nanosized silicon particles, films or wires (*45*).

$$SiH_4 \overset{\Delta}{\rightarrow} Si + 2\,H_2$$

Eq. 1

These methods are usually distinguished by the source used for dissociation, which can be hot wall reactors (tube-furnace reactors, parallel plate reactors → Chemical vapor deposition), laser irradiation (CO_2 laser) or plasma (usually nonthermal) (*46*). The synthesized Si possesses a hydrogen-terminated surface and one can functionalize it according to Figure 6 (*47*). The benefit of the thermal decomposition is that the particle size can be easily changed by the operating parameters of the reactor. The primary particle size, ranging from several nanometers to tens of nanometers, essentially depends on the silane partial pressure (concentration in the gas stream) and the reaction residence time (*48*). Lower concentrations as well as shorter reaction times lead to smaller particles and a narrow particle size distribution. The reaction time can be influenced by the gas flow velocity (stronger gas flow = shorter residence time) and the size of the reactive volume (very small for laser irradiation). However, coalescence is not completely avoidable, leading to some chain aggregates or branched agglomerates (*49*). To keep this effect as low as possible, nonthermal plasma has to be used, since it produces particles carrying negative charge on the surface triggering electrostatic repulsion between these nanoparticles (*50*).

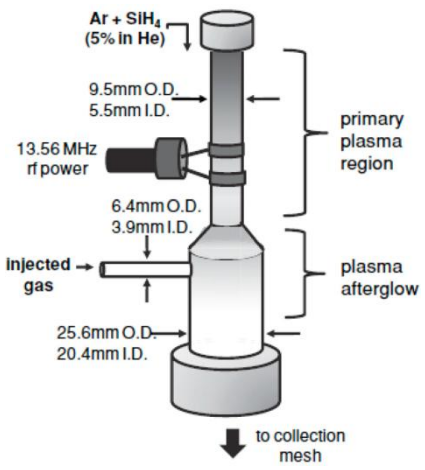

Figure 8. Schematic of a nonthermal plasma reactor for the continuous synthesis of SiNPs (*51*)

In contrast, for the production of films coalescence is required and therefore films are produced by hot wall reactors (especially parallel plate reactors). Nanowires, on the other side, require metal catalysts such as gold or indium, where silane decomposes on the surface of the catalyst forming a liquid metal/Si alloy. Upon reaching supersaturation, a silicon nanowire then precipitates from the melt, the liquid alloy droplet remaining at the tip of the wire as it grows in length (*45*).

The disadvantages of these methods are the use of specialized equipment and the usually low production rates (except microwave plasma reactors → 0.1-10 g h^{-1}), which lead to cost-intensive products (*38*).

A very special decomposition technique is the preparation in supercritical fluids. Korgel *et al.* were the first to show successful synthesis of SiNPs in this media (*52*). In this reference alkoxy-coated crystalline silicon was prepared by the degradation of diphenylsilane in a mixture containing octanol and hexane, which was heated to 500 °C and applied with pressure of 345 bar.

2.2.4 Thermal Decomposition of Silicon Suboxides

Thermal decomposition of silicon suboxides is a very popular method for the synthesis of silicon nanocrystals. Here the suboxide is annealed under inert atmosphere at temperatures higher than 1000 °C (*53*). During annealing a disproportionation reaction occurs and results in silicon nanocrystals embedded in a silicon oxide matrix. In this context one also speaks of silicon rich oxides (SROs) (*54*).

$$SiO_x \xrightarrow{\Delta} \frac{x}{2} SiO_2 + \left(1 - \frac{x}{2}\right) Si$$

Eq. 2

However, to obtain freestanding silicon nanocrystals etching with HF is necessary, and yields particles with sizes in the range from 2 nm to 16 nm and hydrogen-terminated surfaces (*55*).

$$SiO_2 + 4\,HF \rightarrow SiF_4 + 2\,H_2O$$

Eq. 3

So this method displays a transition between *bottom-up* and *top-down* techniques as the particles need to be released from a bulk silicon oxide matrix. Newer approaches utilize thermolysis of hydrogen silsesquioxane (HSQ) to produce bulk amounts of silicon rich oxides (*56*). This method offers a cost-effective approach for the formation of nanocrystalline

silicon, as the HSQ can be prepared via a sol-gel process from trichlorosilane or triethoxysilane without much effort (*57*,*58*).

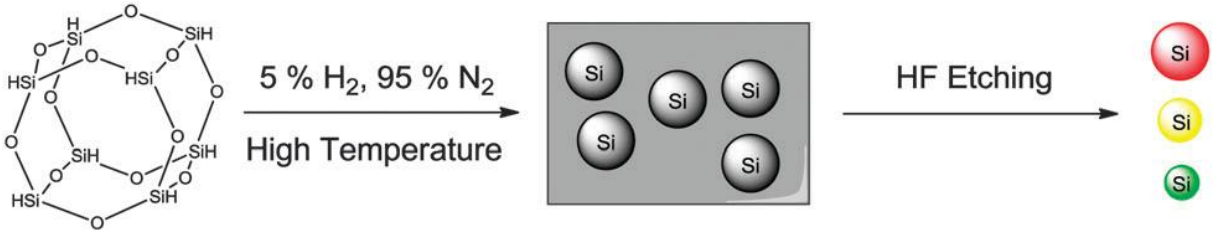

Figure 9. Preparation of SiNPs by breaking down SROs (*34*)

2.3 Top-Down Techniques for Nanosized Silicon

2.3.1 Etching Techniques

In principle, these techniques are further differentiated in chemical etching as well as electrochemical etching. They all have the use of hydrogen fluoride or hydrofluoric acid in common, but differ with regard to the oxidizing agent used.

2.3.1.1 Chemical Etching

The major oxidizing agents in chemical etching are nitric acid and hydrogen peroxide, in contrast to electrochemical oxidation (*59*,*60*). In classical synthesis silicon wafers (or pieces) are cleaned by ultrasonicating them in an organic solvent. The wafers are then put in an etching solution containing hydrofluoric acid and an oxidizing agent, followed by removing solution residues by immersing them in deionized water and subsequent washing with isopropanol. The nanoparticles are now loosely attached to the surface of the silicon and can be suspended by immersing and ultrasonicating them in a solvent of choice, unfortunately with low yields (*61*).

Therefore chemical etching is more often applied to reduce the size of particles already in the nanometer region, at which the size reduction is depending on the dwell time in the etching solution (*60*).

Figure 10. Size reduction of SiNPs via chemical etching (*37*)

In addition there is another chemical etching technique called metal-assisted chemical etching (MACE). It offers the possibility for a convenient synthesis of various silicon nanostructures, such as SiNWs, porous SiNWs or silicon nanopores. In this process metal nanoparticles, wires or stripes (usually Ag or Au) are deposited on the silicon surface followed by etching in H_2O_2/HF (*62*). The oxidant is preferred to be reduced at the surface of the metal catalyst and electrons are transferred from the silicon to the metal. For this reason, silicon underneath the metal catalyst has the highest concentration in electron holes and therefore the oxidation and dissolution of silicon occurs preferentially underneath the metal catalyst (*63*). The morphologies of the obtained surface nanostructures are strongly affected by the parameters such as shape and species of the catalyst, etching temperature and time, solution concentration as well as the space between catalyst particles (*64*,*65*).

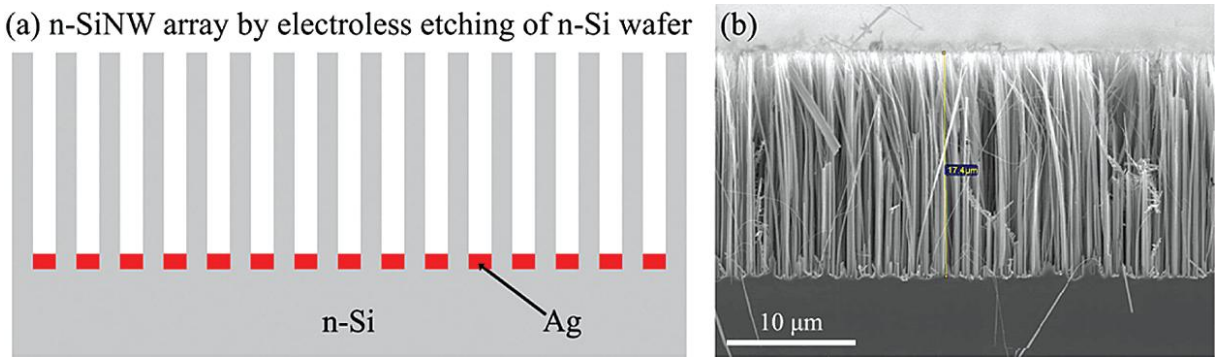

Figure 11. (a) Schematic of a MACE produced SiNW array (b) Cross-sectional SEM of as-prepared array (*66*)

The disadvantage of this method is that the SiNWs are still attached to the bulk silicon and need to be detached in most cases for further use. This can be done either by mechanical peeling or via delamination of the metal catalyst in water and re-etching with H_2O_2/HF (*67*).

2.3.1.2 Electrochemical Etching

This method is one of the oldest ones for producing nanostructured silicon. It was first performed some 60 years ago at Bell Labs, USA (*68*). During electropolishing of silicon wafers in hydrogen fluoride based solutions it was observed that the surfaces developed a matte black, brown or red deposit. The deposits were preliminary supposed to be silicon suboxides and it took nearly 20 years to realize its nanoporous nature (*69*). However, this field of research has been neglected until the visible light emission of the highly porous silicon was discovered in the 1990's (*70*), leading to an impulse in research.

In common syntheses silicon nanostructures or particles are formed by anodizing p- or n-type wafers in aqueous HF or ethanoic HF (*71*). The form and size of the etched silicon mainly depends on the current densities (1-50 mA/cm^2), as well as the concentration of HF. The higher these parameters are, the smaller the particles or pores get. If a separation of the nanoporous silicon layer is wanted, another etching step is performed in diluted HF solutions with a very high current density (up to 160 mA/cm^2) and short dwell time (*72*). But normally these structures show irregular shapes and broad size distribution (*38*).

This issue can be reduced by using a variant of the etching method developed by Kang *et al.* (*73*). The key feature of this method is the usage of polyoxometalates (POMs), with their unique ability to act as an electron donor and acceptor simultaneously. This method produces not only SiNPs with a narrow size distribution but also SiNWs or ordered silicon micro- and nanostructures by the use of $H_3PMo_{12}O_{14}{\cdot}nH_2O$ (POM) or HPOM (H_2O_2 + POM) (*73*,*74*).

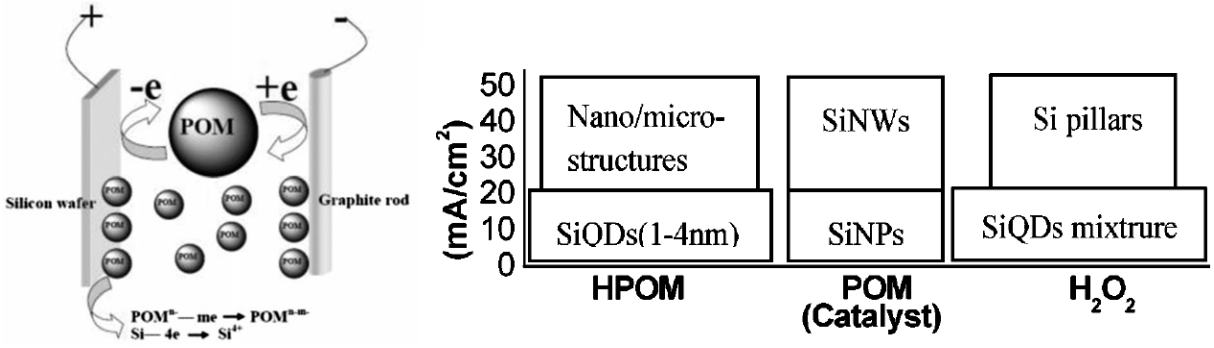

Figure 12. Scheme of POM assisted electrochemical etching (left) and relationship between current density, catalyst and structure of the products (right) (*73*)

2.3.2 Laser Ablation

Laser ablation displays a popular method for the production of a variety of SiNPs (*75*), SiNWs (metal catalyst needed) (*76*) or films (*77*). The first studies on the laser ablation of silicon were carried out in the early 1990's by Okada and Iijima (*78*). The ablation was performed using a YAG laser and a silicon wafer as target under an argon atmosphere.

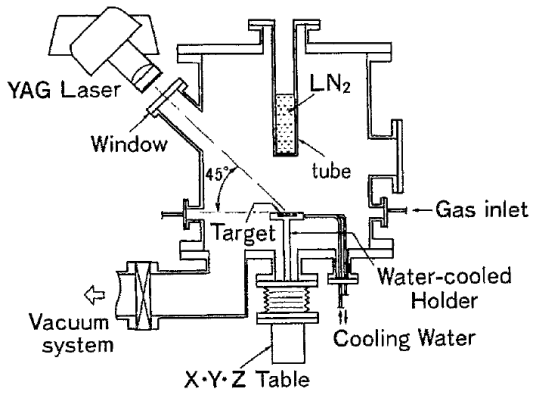

laser pulse energy	40–90 J/p
pulse width	12 ms
irradiation rate	1 pps
area of laser beam on target	~0.7 mm^2
laser power density	0.48×10^6–1.1×10^6 W/cm^2
atmosphere	Ar (99.999%), 0.75–3.0 Pa

Figure 13. Experimental arrangement and preparing conditions of the first laser ablation of Si (*78*)

In this method short laser pulses evaporate small parts of the silicon surface, the silicon atoms then condense into small clusters, their size depending on the pressure and sort of inert carrier gas (Ar, He or N_2), as well as the laser fluences, used (*79*,*80*). The as-produced particles have sizes from several nm up to 500 nm (*78*,*81*) and usually suffer from broad particle size distribution and low yield as well as low scalability (*79*). Some more recent approaches perform the laser ablation in a sealed quartz tube in aqueous solution or a reactive organic solvent, which leads to in situ surface passivation and smaller particles with a more narrow size distribution (*82*,*83*).

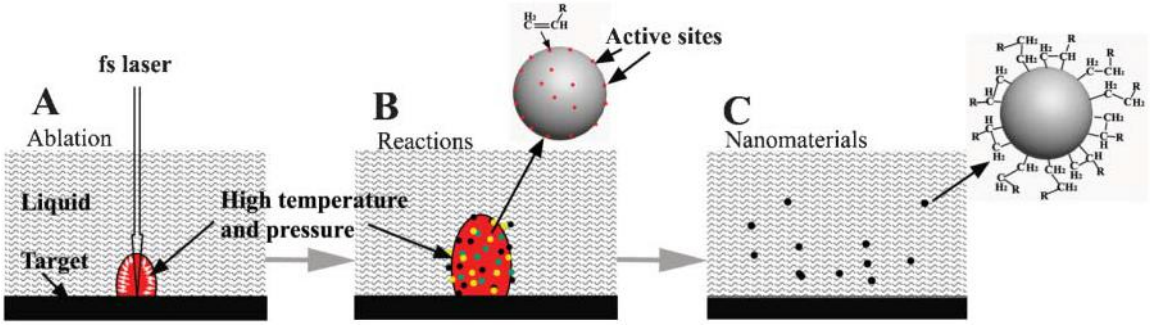

Figure 14. Schematic illustration of laser ablation in solution (*84*)

2.3.3 High-Energy Ball Milling

High-energy ball milling (HEBM) has become a quite popular method in recent years for the production of nano-scaled materials due its simplicity, low cost, high productivity, scalability and environmental friendliness (*85*,*86*). The milling can be performed in a various types of high energy mills such as attrition, planetary or vibratory mills (*87*). Balls and vials are usually made of hardened steel, tungsten carbide, silicon nitride or zirconia (*88*). The energy transfer to the powder particles is based on shearing action and impact of the high velocity balls with the powder (*85*). This process is governed by many parameters (*89*) such as:

- type of mill
- milling speed
- milling time
- type, size, and size distribution of the grinding medium
- ball-to-powder weight ratio (BPR)
- extent of filling the vial
- process control agent

HEBM is a very dynamic process, as plastic formation, cold-welding and fracture occur simultaneous and therefore accurate control of these milling parameters is necessary (*90*). *Dry-milling* leads to the formation of aggregates (van der Waals forces) as the particles reach the submicron region. Further ball impacts lead to disassembly/reassembly processes and larger particles and broader particle size distributions are obtained (*91*). For nanosized silicon, milling is usually performed in a solvent (*wet-milling*). Typical solvents are alkenes, alkynes or alcohols as they lead to in situ functionalization of the surface due to the reaction with reactive silicon radicals or double bonds exposed by the fracture of larger particles (*92*).

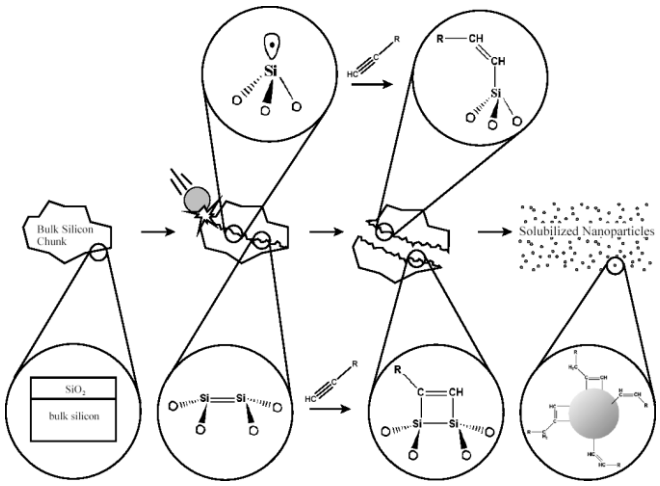

Figure 15. Mechanochemical synthesis of functionalized silicon nanoparticles (*93*)

Therefore, the wet-milling of silicon is also referred to as *reactive-milling*. The advantages of wet-milling are that particle agglomeration can be prevented and the size of the as-prepared particles can be tuned over the entire µm and nm region, depending on the milling parameters (*94*). However HEBM always leads to a particle size distribution, if monodisperse particles are needed the suspensions have to be further treated by size-selecting techniques such as gel permeation chromatography (GPC), ultracentrifugation etc. (*95*).

Beyond this conventional milling technique there are some other rarely used reactive-milling methods which are based on the reduction of silicon dioxide with aluminum or magnesium (*96*,*97*), as well as the reduction of silicon tetrachloride with lithium metal (*98*).

$$3\,SiO_2 + 4\,Al \rightarrow 3\,Si + 2\,Al_2O_3$$

Eq. 4

$$SiO_2 + 2\,Mg \rightarrow Si + 2\,MgO$$

Eq. 5

$$SiCl_4 + 4\,Li \rightarrow Si + 4\,LiCl$$

Eq. 6

In these cases the SiNPs are embedded in the corresponding metal oxide or salt matrix and need to be released by washing with acid or deionized water.

For completion one has to mention that there are more, very specialized techniques for the synthesis of nanostructured silicon, than those mentioned in the previous chapters. They are based on molecular beam epitaxy (MBE) or nanolithography and will not be discussed further (for reviews see e.g., (*99*,*100*)).

2.4 Comparison of the Techniques in Consideration of LIBs

For LIBs nanosized silicon needs to be produced in an inexpensive and easy way, due to large amounts needed for this application. Moreover the used silicon should have particle sizes above 30 nm, otherwise the ratio of native surface silicon oxide (electrochemically dead weight, caused by handling in air) to core silicon is too high due to the large surfaces, as shown in the author's master thesis (*101*).

As solution based precursor reduction methods or the oxidation of *Zintl phases* usually yield particle sizes below 10 nm, these methods cannot be used for the production of silicon suitable in LIBs. In this context even the particles obtained via thermal decomposition of silicon suboxides are too small. This method also has the disadvantage of high temperature demand, which leads to a cost-intensive production process. Furthermore the particles need to be released from the oxide matrix, making it even more expensive due to special devices necessary and safety issues associated with HF etching.

Chemical and electrochemical etching techniques are very simple to perform and can be done at room temperature, but they also suffer from the disadvantage of HF usage. However the main problem concerning these techniques is the low quantity of nanosized silicon produced per batch, which leads to low throughput and high prices, making them unfavorable methods. The same applies to Laser ablation methods.

Thermal decompositions of silanes are already performed and popular techniques for the commercial production of SiNPs. Their magnificent features are the production of monodisperse particles and the size tunability. The disadvantages, however, are the specialized equipment needed, as well as a not excessively high throughput, which in turns leads to cost-intensive production.

In contrast to these techniques large quantities of nanosized silicon can be achieved by HEBM, with the benefit of not too specialized equipment required. Therefore this approach was chosen within this doctoral thesis, as it offers the cheapest and easiest way to produce SiNPs, which is very important for future large scale production. Furthermore, doped silicon and alloys can be produced via mechanical alloying.

For a better overview of the advantages and disadvantages of the techniques see Table 1.

Table 1. Comparison of the preparation methods for nanosized Si

Preparation method	Size tunability	Size distribution	Throughput	Up-scaling	Simple equipment	Costs	Environmental benign	Atom economy
Solution based precursor reduction	-	+	-	-	+	-	~	-
Oxidation of Zintl phases	-	+	-	-	+	-	~	-
Thermal decomposition of silanes	+	+	~	+	-	-	+	+
Thermal decomposition of SiO_x	-	+	-	~	+	-	-	-
Chemical etching	~	+	-	-	+	-	-	-
Electrochemical etching	~	~	-	-	+	-	-	-
Laser ablation	-	-	-	-	-	-	+	+
High-energy ball milling	+	~	+	+	~	+	+	+

3 Lithium-Ion Batteries

3.1 Introduction to Lithium-Ion Batteries

Batteries are closed systems in which one or more electrically connected electrochemical cells convert the chemical energy stored in its active materials directly into electric energy via an electrochemical reduction-oxidation (redox) reaction. An electrochemical cell consists of a cathode where reduction takes place during discharge, an anode (oxidation), a separator and an electrolyte which conducts the current via ions within the cell. As during discharge the reactions at the cathode usually take place at higher potentials than at the anode, the terms positive (cathode) and negative electrode (anode) may also be used (*102*).

In principle batteries are divided into *primary* and *secondary batteries.* Primary batteries display non-rechargeable batteries. They are assembled in the charged state and are intended to be used until exhausted and then discarded. Secondary batteries (accumulators), on the other hand, are intended to be used several times. After being discharged, the battery is restored to its original charged condition by an electric current flowing in the opposite direction to flow when the battery was discharged. This type of battery is usually assembled in the discharged state and needs to be charged first before it can undergo discharge in a secondary process (*103*). In addition to this classification batteries may also be classified by the type of electrolyte employed, either aqueous or nonaqueous (*104*).

	Aqueos electrolyte battery	Nonaqueos electrolyte battery (high voltage, capacity)
Primary battery (disposable)	Mn dry cell, Alkaline dry cell	Metallic lithium battery
Secondary battery (rechargeable)	Lead-acid battery, Nickel-cadmium battery, Nickel-metal hydride battery	**Lithium-ion battery**

Figure 16. Types of batteries (*105*)

Batteries are usually compared by the amount of electrical energy they contain and/or their rate capability. The terms *specific energy* (W h kg^{-1}) and *energy density* (W h L^{-1}) are used to

compare the energy content that a battery is able to deliver [function of the cell potential (V) and capacity (A h kg^{-1})], whereas the rate capability is expressed as *specific power* (W kg^{-1}) and *power density* (W L^{-1}) (*103*). Alternatively, the attributes *gravimetric* (kg^{-1}) and *volumetric* (L^{-1}) can be used (*106*).

The first lithium containing batteries were of the primary type and were developed in 1960's. These devices contained lithium metal as negative and iodine as positive electrode material and provided a practical specific energy of about 250 W h kg^{-1}, almost five times higher than the former state of the art zinc-mercury oxide battery (*107*). The motivation behind using lithium metal as negative electrode material relied on the fact that Li is the most electropositive (-3.04 V vs. SHE) as well as the lightest (M = 6.94 g mol^{-1}, ρ = 0.53 g cm^{-3}) metal with a specific capacity (charge per mass) of 3,860 A h kg^{-1} (= mA h g^{-1}), thus enabling the design of battery systems with high voltage and high energy density (*2*). Therefore it was only a matter of time till research on secondary lithium batteries began. The attention was initially focused on the cathode side, as it was believed that metallic lithium dissolution and deposition at the negative electrode can be performed without major problems, with the aim of identifying materials with long cycle stability.

In 1978 tremendous progress was achieved by Whittingham with the development of the so-called *insertion electrodes* (*108*). The term *insertion* refers to a host/guest solid-state redox reaction at which electrochemical charge transfer is coupled with the insertion of mobile guest ions from an electrolyte into the structure of a solid host (*109*). To obtain this, these materials must assure the reversibly change of the oxidation state as well as keep their major structural features. Therefore the first electrode materials of this type were transition metal compounds, such as TiS_2 (*110*). However, it was soon realized that the lithium metal needs to be replaced due to lithium corrosion and dendrite formation, which lead to poor cycle performance and severe, undesirable safety characteristics of these batteries (cell shorting, fire incidents). To overcome this weakness Li alloys with aluminum or Wood's alloy appeared as the first solution, nevertheless these materials suffered from strong morphological changes upon cycling due to large volume changes, leading to poor cycling behavior (*111*). The key concept for solving this problem involved the substitution of the metallic lithium with a second insertion material. It was first demonstrated by Murphy *et al.* (*112*) and led to the so-called *rocking-chair batteries*, where lithium ions are shuttled between the positive and the negative insertion electrode during operation (*113*).

The breakthrough was achieved by Yoshino *et al.* in 1985 (*114*) with a new battery system comprising a $LiCoO_2$ positive electrode [disclosed by Goodenough in 1981 (*115*)], which acts as lithium ion source and carbonaceous material as negative electrode, where the lithium ions are embedded between the graphene layers during charging. This invention led to the

successful commercialization by Sony in 1991 and the term *lithium-ion battery* was coined (*116*). The success of this type of lithium-ion cell was, and is still, outstanding due to having a potential exceeding 3.6 V (three times that of alkaline systems) and gravimetric energy densities as high as 120-150 W h kg^{-1} (three times those of usual Ni-Cd systems) (*2*), and it nearly remained unchanged even after almost 25 years since its commercialization (*117*). Today lithium-ion batteries are the power sources of choice for portable electronic devices, such as mobile phones (especially “smart phones”), notebooks, tablet computers etc. and they are also used for electric vehicles, as well as for stationary energy storage systems (*118*).

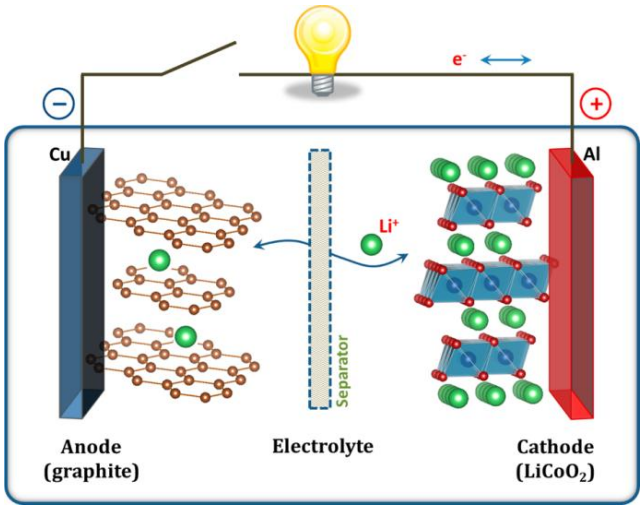

Figure 17. Schematic drawing of a lithium-ion battery (*119*)

During charging, lithium ions are extracted from the positive electrode host, solvate into and move through the non-aqueous electrolyte, and intercalate into the negative electrode host. Meanwhile, electrons are moved from the positive to the negative electrode through the outside current collectors forming an electric circuit. The process is reversed when the battery is being discharged and the stored electrochemical energy is released in the form of electric energy. The electrode materials are electrically separated by a microporous membrane that prevents short circuits but still allows Li ions to penetrate (*120*).

The materials used or intended to be used in lithium-ion batteries will now be discussed in the further chapters based on the major components (positive and negative electrode, electrolyte and separator), involving recent research. The terms positive and negative electrode are subsequently used instead of anode and cathode, since the use of the latter ones is only correct for discharging and oppose during charging.

3.2 Positive Electrode Materials

Positive electrode materials are typically transition metal compounds (basically oxides or phosphates) that are able to undergo reversible extraction and insertion of lithium ions by changing the oxidation state of the transition metal, maintaining charge neutrality (*121*). The materials need to be structural very stable, as structural changes would lead to poor cycle performance, and should allow good ionic and electric conductivity (*122*). Commercial relevant examples for these materials can be distinguished by their crystallographic structure.

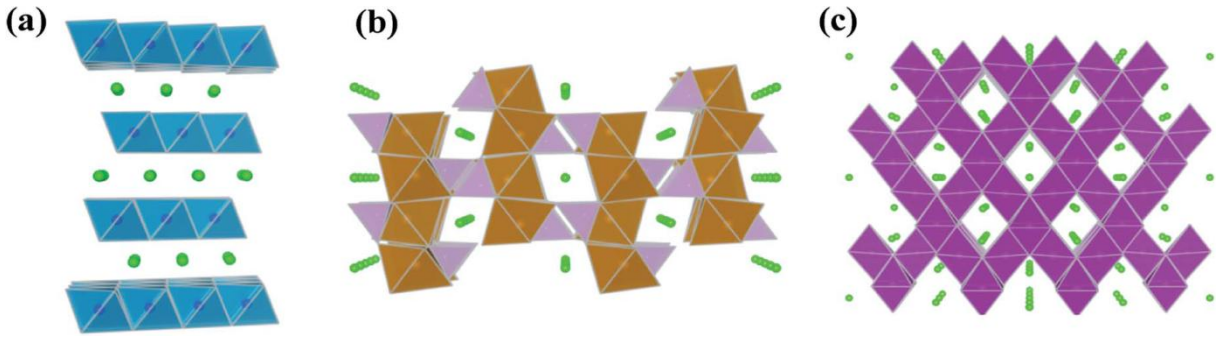

Figure 18. Main structures of used positive electrode materials: layered (a), olivine (b) and spinel (c) (*123*)

Furthermore they can be classified according to their operational voltage (average insertion/deinsertion potential against Li/Li^+) and are therefore sometimes named “3 V”, “4 V” or “5 V” positive electrode (or cathode) materials (*109*,*124*). Current research focuses, as well as for negative electrode materials, on the optimization of the energy density (specific capacity and/or voltage), rate capability, cycling performance, safety, cost and environment-friendliness.

3.2.1 Layered Compounds

The most common layered compounds are transition metal oxides with the general formula $LiMO_2$ (M = Co, Ni, Mn) (*125*). Among all positive electrode materials $LiCoO_2$ has been the predominant material for more than two decades since the commercialization of lithium-ion batteries (*126*). Although complete delithiation to CoO_2 is possible (specific capacity of ~ 280 mAh g^{-1}), only the half of the lithium-ions can be reversible extracted/inserted during

operation, yielding a specific capacity of 140 mAh g^{-1} and an open-circuit voltage (OCV) of 4 V vs. Li/Li^+ (*120*,*127*). This limitation can be attributed to lattice shrinkage, oxygen evolution and cobalt dissolution which evolves during further delithiation, resulting in capacity fade and safety problems (*124*). As cobalt is expensive and toxic, research focuses on derivatives where cobalt is partially or fully substituted by cheaper or less toxic transition metals, like nickel or manganese (*128*). Fully substituted compounds containing one sort of transition metal, like $LiNiO_2$ or $LiMnO_2$, represented one of the first layered materials thought to replace $LiCoO_2$ (*129*,*130*). However, $LiNiO_2$ shows a stronger tendency for oxygen evolution (*131*) and $LiMnO_2$ suffers from irreversible structural changes during delithiation (formation of spinel structure) (*132*), which limit their practical application. In recent years mixed metal oxides, such as $LiNi_xCo_yAl_{1-x-y}O_2$ (NCA) or $LiNi_xCo_yMn_{1-x-y}O_2$ (NMC), have become more prevalent. As these materials have an inherently higher specific capacity, a high rate capability and lower cost compared to $LiCoO_2$, they are already used in cells to power electric vehicles produced by Tesla ($LiNi_{0.80}Co_{0.15}Al_{0.05}O_2$) or BMW ($LiNi_{1/3}Co_{1/3}Mn_{1/3}O_2$) (*133*). In these solid solution materials the predomimant redox couple is Ni^{2+}/Ni^{4+} (contributes to the high capacity of Ni containing materials), while the cobalt helps to reduce the Li-Ni interlayer mixing and contributes to the capacity at high voltages (Co^{3+}/Co^{4+}) (*120*). In NMC the Mn^{4+} ions remain unchanged and help to stabilize the structure and reduce costs (*134*). The aluminum in NCA materials prevents the complete oxidation of the nickel and, thus, reduces the oxygen evolution potential and increases the safety (*133*).

Among the mentioned materials the available rechargeable specific capacity is in the range of 140-200 mAh g^{-1}, but new cathode materials are needed to meet the future energy density requirements. Therefore *lithium-rich layered oxide materials* (LLOs) have attracted much attention in recent times (*135*). These materials can be described as solid solutions with the general formula $xLi_2MnO_3 \cdot (1-x)LiMO_2$ and their specific capacities can be higher than 300 mAh g^{-1} and show a high voltage plateau at 4.8 V. The Li_2MnO_3 units contribute to structural stability as it is electrochemically inactive over a wide potential window of 2.0-4.4 V and get electrochemically actived at 4.5 V in the first charge (*136*). At this potential Li^+ is extracted from Li_2MnO_3 and leads to the formation of the MnO_2 host structure, which can than reversible intercalate Li-ions (*137*). This process leads to a large irreversible capacity in the first cycle and origins from a transformation of the original layered structure to a mixed spinel-like and layered structure (*138*). Although loosing capacity in the first cycle, the material still shows considerably high capacity (> 200 mAh g^{-1}) and good capacity retention during further cycling. However, efforts have to be made as these LLOs unfortunately suffer from oxygen evolution and voltage fade upon cycling, furthermore electrolytes are needed, which are stable at a voltage close to 5 V (*133*).

3.2.2 Olivine-Type Compounds

Olivine-type compounds which contain polyanionic groups and can be described with the general formula $LiMPO_4$ (M = Fe, Co, Mn, Ni) (*139*). It would be advantageous to use this type of materials in cells powering electric vehicles, as these materials show no oxygen release during over charge (oxygen is tightly bond to phosphorus). In particular $LiFePO_4$ displays a very promising candidate as it is inexpensive, non-toxic, environmentally benign and shows good electrochemical, structural and thermal stability (*140*). Compared with $LiCoO_2$, it has a reasonable specific capacity of 170 mAh g^{-1} and excellent cycle stability, but the low operational potential of 3.5 V results in lower energy density. Other disadvantages are the low intrinsic electric and ionic conductivity which cause small rate capacity (*141*). Numerous efforts have been devoted to circumvent these disadvantages, including carbon-coating, size-reduction, doping etc., and lead to an outstanding rate capability (*142*,*143*) Therefore $LiFePO_4$ can now be found in cells produced by A123 Inc. and Sony (*140*). In future, materials with higher energy densities are needed, therefore research is being performed in the area of "5 V" olivine-type materials, such as $LiCoPO_4$ or $LiNiPO_4$ (*144*).

3.2.3 Spinel-Type Compounds

This type of positive electrode materials represent promising materials for high power applications and can be described with the general formula LiM_2O_4 (M = mainly Mn) (*120*). The MnO_2 framework in $LiMn_2O_4$ provides 3D Li^+ diffusion pathways, which are responsible for high rate capability, and structural stability (*145*). Another advantage is that manganese is non-toxic and abundant, which ensures low costs for this material. Nevertheless $LiMn_2O_4$ is a problematic positive electrode material as it exhibits low operational specific capacity (~ 120 mAh g^{-1}) and large capacity fading during cycling for several reasons: (I) the material has to be cycled above 3 V (limiting the capacity) otherwise a phase transition from the cubic to the tetragonal phase occurs, (II) micro-crack formation on the surface, (III) *solid electrolyte interface* (SEI) formation due to incompatibility with current electrolytes and (IV) dissolution of Mn^{2+} ions into the electrolyte generated by a disproportional reaction (Eq. 7), which leads to

$$2\,Mn^{3+} \rightarrow Mn^{2+} + Mn^{4+}$$

Eq. 7

degradation of the SEI on the negative electrode (*146*). Substituting Mn with other metal ions (Al, Co, Cr, Cu, Fe, Ni, Mg etc.) has been used as an important approach for improving

cycling performance and $LiNi_{0.5}Mn_{1.5}O_4$ has been identified as attractive positive electrode material for next generation lithium-ion batteries (*147*). It offers a high operating voltage of ~ 4.7 V and a capacity of ~135 mAh g^{-1}, but its commercialization is plagued by intense capacity fade in full cells employing graphite as negative electrode, particularly at elevated temperatures, hence further research is needed (*148*). In the field of high voltage spinel-type oxides compounds like $Li_2M_xMn_{4-x}O_8$ and $LiM_xMn_{2-x}O_4$ (M = Cr, Co, Fe) display possible future candidates for application (*124*).

3.2.4 Other Positive Electrode Materials

In addition to the already mentioned compounds also silicates Li_2MSiO_4 (M = Co, Fe, Mn, Ni), tavorites $LiMPO_4F$ (M = Co, Fe, Ni, V) or borates $LiMBO_3$ (M = Co, Fe, Mn) are investigated as possible positive electrode materials (*120*,*144*,*149*). Besides conventional insertion-type materials, major efforts are done in developing lithium batteries using sulfur or oxygen as positive electrode materials, as they exhibit theoretical specific capacities an order of magnitude higher than the conventional compounds (*150*). Considerable attention is paid to oxygen, as it exhibits with 3350 mAh g^{-1} twice the theoretical capacity of sulfur and does not need to be incorporated in the cells due to its ubiquitous presence (air) facilitating higher energy densities (*151*). More detailed information can be found in the references (*152*,*153*).

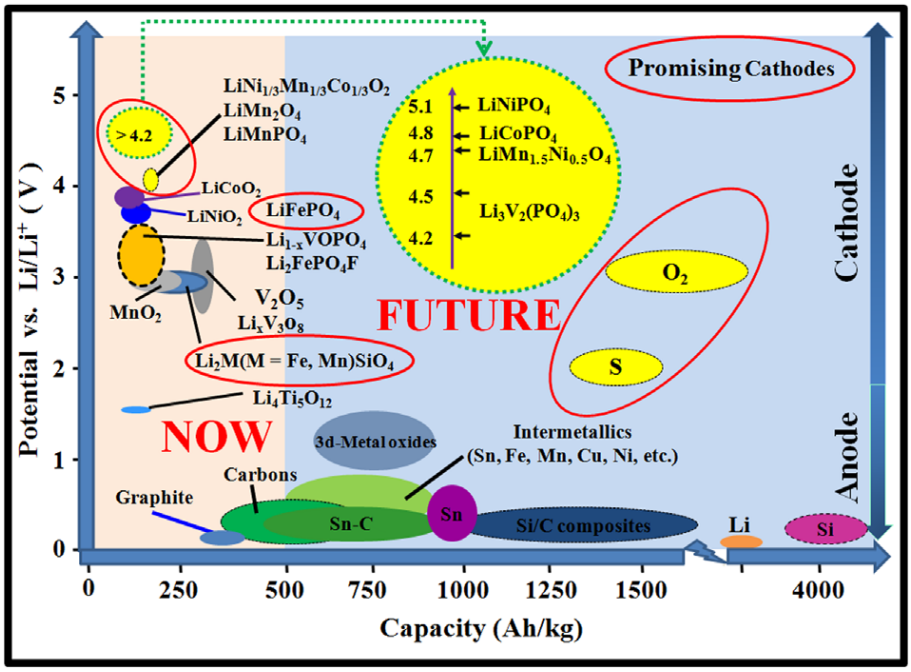

Figure 19. Current and future electrode materials for LIB technologies (*154*)

3.3 Negative Electrode Materials

The sector of negative electrode materials comprises a large number of different compounds, such as carbonaceous materials, metals, semiconductors, intermetallics or metal oxides and can be classified according to the lithium storage mechanisms (intercalation, alloying or conversion reaction) (*155*). For more than 20 years graphite has been the predominant material, however it will not fulfill the demands for future high energy applications due to its low specific capacity of 372 mAh g^{-1} (*156*). Hence, alloy-type and conversion reaction-type materials gained a lot of interest for some time, but also the use of lithium metal has attracted significant interest in recent times, due to the urgent need for "next generation" rechargeable batteries, such as Li-S and Li-air batteries (*152*,*153*). Various approaches, such as mechanical barriers or artificial SEIs, are investigated to overcome the problems related to the use of lithium metal, but they are quite far away from resolute application (*157*,*158*).

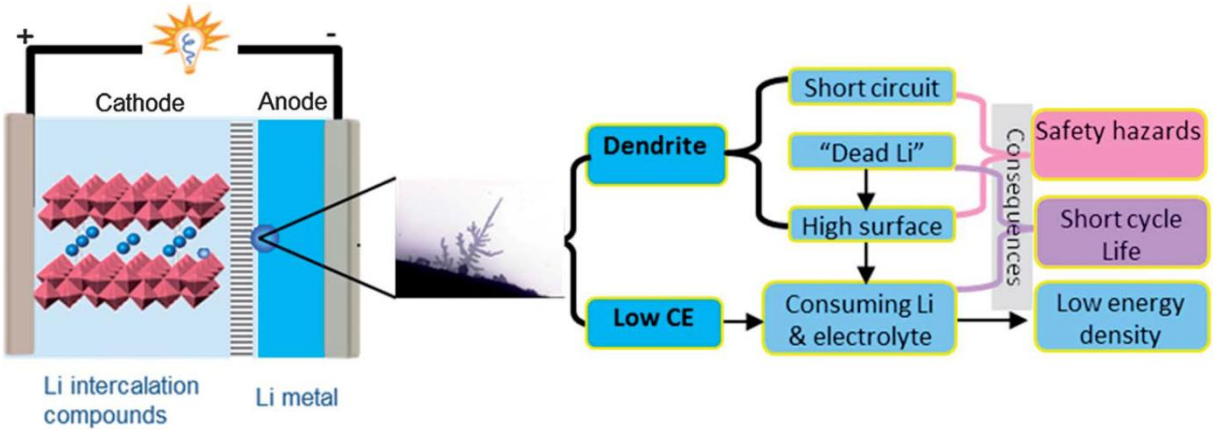

Figure 20. Main problems related to lithium metal negative electrode (*159*)

3.3.1 Intercalation-Type Materials

3.3.1.1 Carbonaceous Materials

At present carbonaceous materials (especially graphite) are the most common used negative electrode materials for commercial rechargeable lithium batteries due to their ease of availability, structural and chemical stability, low cost and good lithium intercalation/deintercalation reversibility (*160*). They can roughly be classified as *graphitic* and *non-graphitic* (disordered) *carbons* (*161*). *Graphitic carbons* have a layered structure

consisting of graphene sheets with the prevalent stacking order AB (less common ABC) and a low number of structural defects (*162*). On the contrary *non-graphitic carbons* show a larger amount of structural defects, which prevent a far-reaching crystallographic order, and can further be subclassified as *soft* or *hard carbons* (*163*). They differ in the ability of developing a graphite-like structure upon heat treatment (graphitizing), which is possible for *soft* but not for *hard carbons* (*164*).

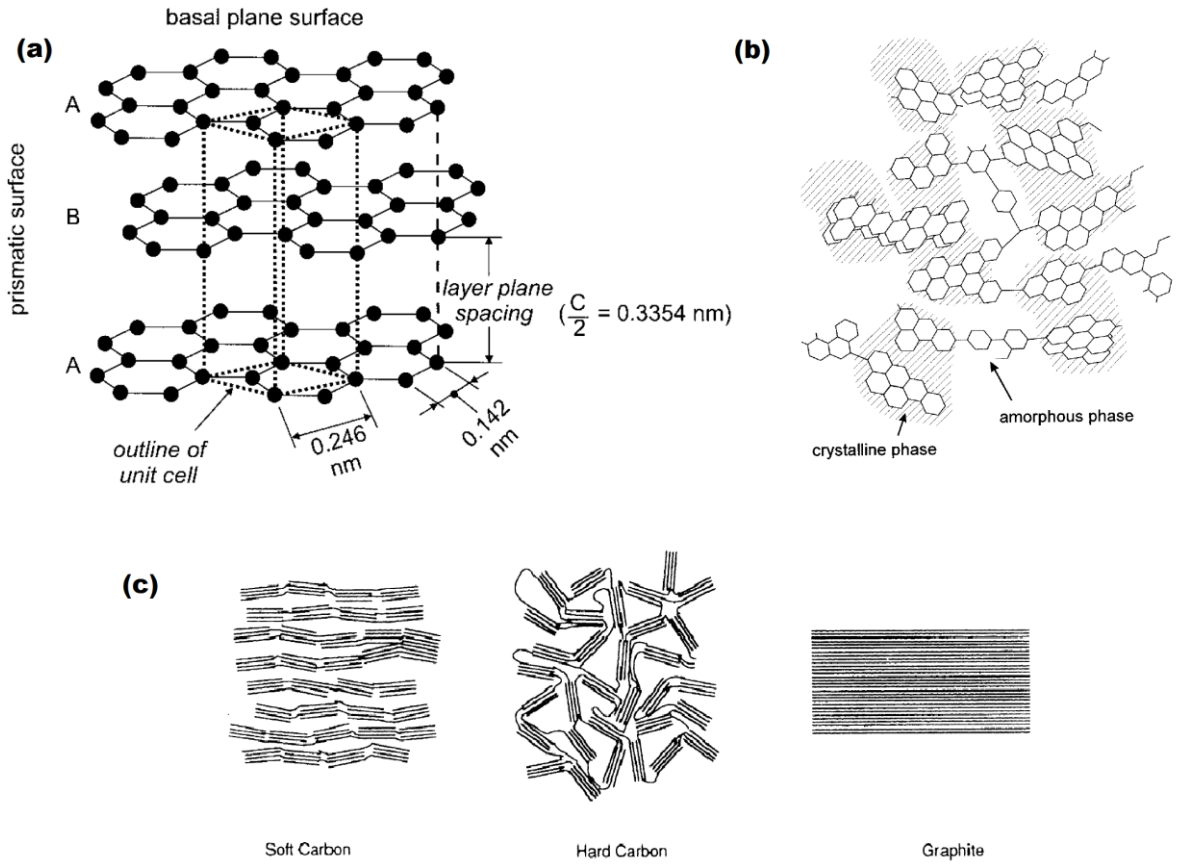

Figure 21. Structural differences of carbonaceous materials: graphitic carbon (a), non-graphtic carbon (b) (*109*) and comparison of the “macroscopic” structures (c) (*164*)

During intercalation the carbon host gets reduced and Li^+ ions penetrate into it along the prismatic surface between the graphene layers and a lithium/carbon intercalation compound according to equation 8 is formed (*109*).

$$x\,Li^+ + x\,e^- + C_n \leftrightarrow Li_xC_n$$

Eq. 8

The lithiation proceeds via the formation of a periodic array of occupied and unoccupied layers, the so-called stage mechanism (*165*). In graphite the stages LiC_{36}, LiC_{27}, LiC_{18} and

LiC_{12} are passed. The intercalation ends with the highest lithiated compound LiC_6 and a shift of the stacking order to AA, yielding the theoretical capacity of 372 mAh g^{-1} (*166*). Some hard carbons exhibit yet higher capacities up to 600 mAh g^{-1}, however they suffer from a large irrerversible capacity in the first cycle and low coulombic efficiency (CE) (*160*). The mechanisms behind the higher capacity are not yet fully understood. It is assumed that it arises from lithium species at the edge of the graphene layers, oxidized moieties or in nanoscopic cavities (*109*,*167*).

Latest research focuses on the use of carbon nanotubes (CNTs), graphene or porous carbons with pores ranging from nanometer to micrometer scale (*160*), as their capacity can reach up to 1116 mAh g^{-1} (corresponding to LiC_2) (*168*). However, they suffer from the same problems related to high capacity hard carbons (*169*).

3.3.1.2 Titanium-Based Compounds

Titanium based compounds have drawn significant attention during the last decade, because they allow the designing of high power operational devices with minor safety concerns due to working potentials around 1.5 V vs. Li/Li^+ (*170*). Moreover, they show other interesting features such as low toxicity, inexpensiveness, excellent cycle stability and low volume change (2-3 %) during operation (*160*). However, they have low theoretical capacity and low conductivity.

The most common material is the spinel $Li_4Ti_5O_{12}$ (LTO) and it can accommodate up to 3 Li^+ ions per unit, resulting in a specific capacity of 175 mAh g^{-1} (*171*). It has an excellent rate capability, if nanoparticles are used, and due to the high voltage vs. Li/Li^+ no SEI or dendrite formation can be observed. However, the low specific capacity and the high working potential vs. Li/Li^+ lead to systems low in energy (*162*).

Very promising future candidates for negative electrodes in the field of high power applications are the various polymorphs of TiO_2 (especially anatase), as they can take up to one Li^+ ion per unit which leads to a theoretical specific capacity of 335 mAh g^{-1} (almost twice of LTO) (*172*). However, the exploitation of the entire capacity is a major problem, as intercalation is strongly dependend on the method of preparation, particle size, shape and morphology (*150*). From the practical viewpoint, reversible intercalation is limited to 0.6-0.7 Li^+ per unit (~ 200 mAh g^{-1}) anatase at 1.75 V (*173*). To obtain higher reversible capacities research focuses on preparation methods for nanoscale, high surface TiO_2 of various morphologies, such as nanorods or nanotubes (*174*).

3.3.2 Alloy-Type Materials

Research on lithium alloy forming elements began in 1971 as Dey demonstrated the feasibility of electrochemical formation of lithium alloys in aprotic organic electrolytes (*175*). The reaction usually proceeds reversibly according to the general equation 9.

$$x\,Li^+ + x\,e^- + M \leftrightarrow Li_xM$$

Eq. 9

It can be performed with a large number of metallic and semi-metallic elements in group 12 (Zn, Cd, Hg), group 14 (Si, Ge, Sn, Pb) and group 15 (P, As, Sb, Bi), as well as other metals such as Mg, Al, Ga, In, Ag or Au (*176*,*177*). Among them Si and Sn have attracted considerable attention, as they are abundant, non-toxic, rather inexpensive and offer high theoretic specific capacities of 3,579 mAh g^{-1} ($Li_{15}Si_4$) and 960 mAh g^{-1} ($Li_{17}Sn_4$) during room temperature lithiation (*178*).

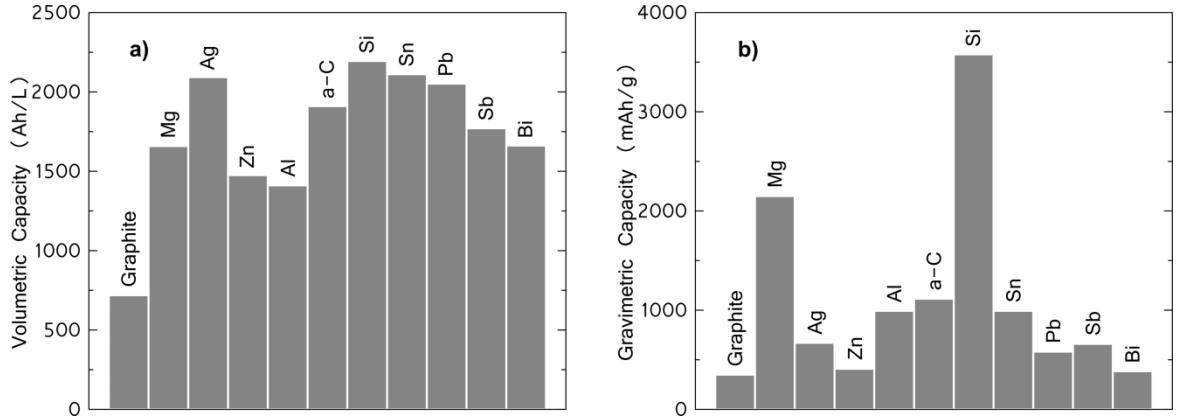

Figure 22. Volumetric (a) and gravimetric (b) capacities at the state of full lithiation of various elements (*178*)

Despite the high capacities and good safety implementation of these negative electrodes remains a challenge due to the severe volume changes up to 300 % during alloying/dealloying processes (*179*). The volume changes lead to a large irreversible capacity in the first cycle, followed by poor cycling performance, due to fracture and subsequent loss of electrical contact between the particles, as well as to a continuous SEI formation (*180*). The most promising approaches to overcome these issues are based on the downsizing to nanoscale particles and the fabrication of composites with both lithium active and inactive materials, which act as conductive buffer matrix for the alloy-type materials (*181*). These approaches will be further discussed in chapter 3.6 based on Si.

3.3.3 Conversion Reaction-Type Materials

With the beginning of this millennium interest was aroused onto a new reactivity concept conventionally referred to as *conversion reaction* (*182*). It is based on the reversible reaction of lithium with 3d transition metal compounds (mostly oxides) according to the equation 10,

$$M_aZ_b + (b \cdot n)\, Li \leftrightarrow a\, M + b\, Li_nZ$$

Eq. 10

where M = Co, Cu, Fe, Mn, Ni; Z = N, O, P, S; and n = formal oxidation state of Z (*160*,*183*). They can have specific capacities of as high as 600-1,000 mAh g^{-1} with good cycling reversibility (*184*), but suffer from high voltage polarization between the charging and discharging (potential hysteresis) and low initial coulombic efficiency (*185*). The most common materials are oxides, such as Fe_2O_3, Fe_3O_4, Co_3O_4, CoO or CuO, which are converted to metal nanoparticles embedded in a Li_2O matrix during lithiation (*186*).

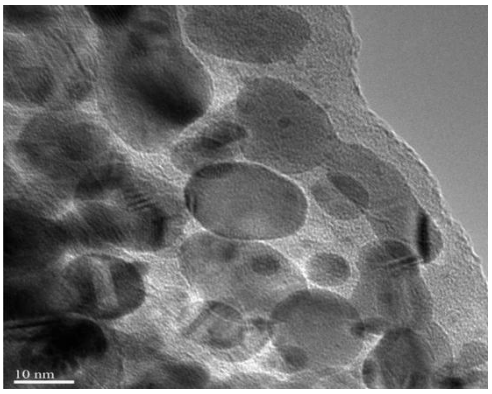

Figure 23. HR-TEM micrograph of nanosized Cu particles embedded in a Li_2O matrix after lithiation (*187*)

As Li_2O is electrochemically inert it can only participate during electrochemical cycling due to the formed metal nanoparticles, which catalyze the backward reaction (*162*). A special type of conversion materials are compounds, such as ZnM_2O_4 (M = Co, Fe), $CdFe_2O_4$ or M_2SnO_4 (M = Co, Mn, Mg, Zn), as at least one metal formed can further react with Li according an alloying mechanism (*188*). Similar behavior show the negative electrode materials SiO_x, SnO or SnO_2, however they are not conversion materials, as the backward reaction to the oxide cannot be performed electrochemically (*176*).

3.4 Separators

A separator is placed between the positive electrode and the negative electrode to prevent physical contact of the electrodes and to isolate electronic flow while enabling free ionic transport (*189*). The separator must be chemically and electrochemically stable towards the electrolyte and electrode materials, as well as mechanically and thermally stable. As it raises cell impedance and takes up limited space in the battery further requirements are imposed. The thickness should be uniform to ensure long cycle life and ≤ 25 µm for high energy and power densities in LIBs. Furthermore a high porosity of 40-60 % and pore sizes below 1 µm are required to assure satisfying permeability and wettability to the electrolyte, as most separators do not posses intrinsic ionic conductivity (*190*).

Most commercially available separators are single- or multilayer polymer sheets typically made of polyolefins, such as polyethylene (PE) or polypropylene (PP). They are manufactured by either an extrusion process (wet or dry) followed by a mechanical stretching process to induce porosity (*microporous membranes*) or by manufacturing *nonwoven mats* based on wet-laid fibers (*191*). Microporous membranes are used primarily, as nonwoven mats are thicker and suffer from a higher tendency of particle penetration and dendrite penetration during over-charging. This is caused by stochastic arrangement of the fibers, resulting in larger and irregular pore sizes (*192*). Membranes consisting of PE/PP bilayers or PP/PE/PP trilayers have been designed as *thermal shutdown separators* and offer safety advantages. In the case of an internal short circuit the temperature of the cell increases, the lower melting PE fills the pores of the PP layer(s) and stops ion transport and current flow in the cell, while the PP retains its structure and mechanical strength (*190*).

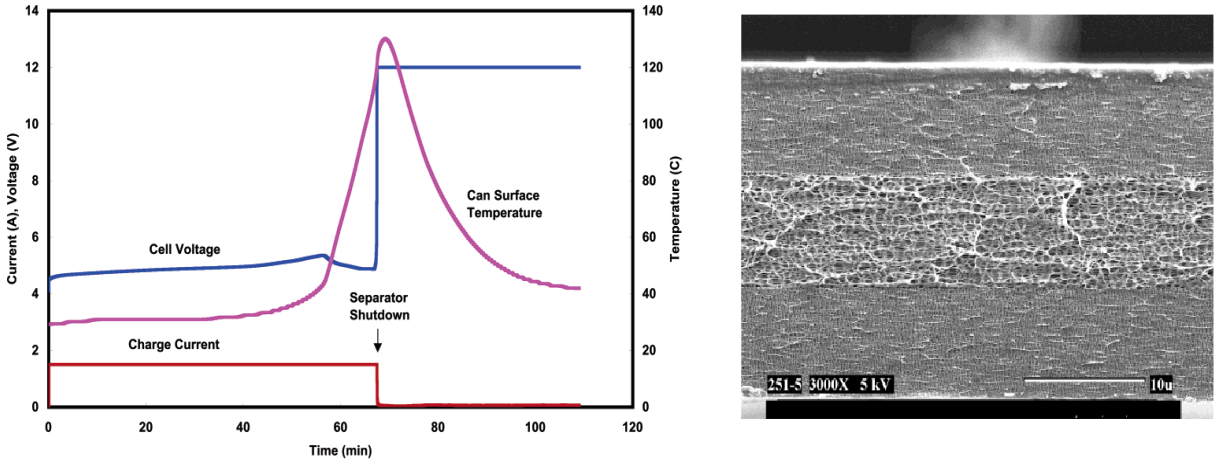

Figure 24. Typical overcharge behavior of a cell with thermal shutdown separator (left), SEM micrograph of a PP/PE/PP trilayer membrane (right) (*193*)

3.5 Electrolytes

Electrolytes are ubiquitous and indispensable in all electrochemical devices and their basic function is to act as medium for charge transfer between the electrodes. The charge transfer is carried out by the migration of ions in the electric field. The vast majority of electrolytes in LIBs are of the electrolytic solution-type, which consist of a lithium salt dissolved in an aprotic organic solvent (*194*). Other electrolytes are based on ionic liquids, polymers, gels or ceramics (*195*). The key property of the electrolyte is the ion conductivity, as it quantifies the ion mobility and availability for the ongoing electrochemical reactions, which in part determines the power output of the cell. Apart from being a good ionic conductor, the electrolyte has to fulfill further demands: (I) the electrolyte must be an electronic insulator to keep self discharge at minimum levels, (II) it should be stable over a wide potential range (electrochemical window) to prevent degradation, (III) it should be inert to all the cell components, (IV) it should be thermally stable and (V) non-toxic (*196*). For liquid electrolytes comprising Li ions and aprotic solvents, salts with complex anions such as $LiBF_4$, $LiPF_6$, $LiAsF_6$ or $LiClO_4$ can be used. Nevertheless $LiPF_6$ displays the best compromise in fulfilling all demands and hence it is the compound of choice for LIB electrolytes (*194*). The solvents should have a high dielectric constant to dissolve the salt and promote ion pair dissociation. Initially, ethers and esters seemed to be suitable candidates. However, it was soon realized that ethers are decomposed oxidatively at the positive electrode during cycling (*197*). On this account, the focus was put on the esters of carbonic acid, as they possess a better electrochemical stability (*198*). Contemporary electrolytes are usually based on a mixture of the cyclic ethylene carbonate (EC) with linear carbonates, such as diethyl carbonate (DEC), dimethyl carbonate (DMC) or ethyl methyl carbonate (EMC) (*199*).

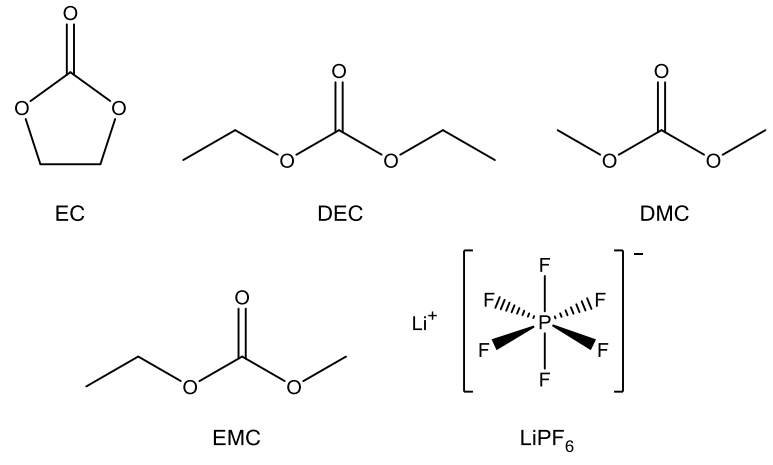

Figure 25. Main components of contemporary solution-type electrolytes

EC is favored, as it possesses a very high dielectric constant, but it is a solid at room temperature. Therefore mixing EC with linear carbonates (low dielectric constants) is necessary to decrease the viscosity of the electrolyte for faster Li^+ diffusion (*156*). The primordial used carbonate, however, was propylene carbonate (PC). It exhibits also a high dielectric capacity and is liquid over a broad temperature range with low viscosity. With these attributes it seems to be the ideal solvent, as mixtures are redundant. However, the utilization of PC leads to exfoliation of graphitic carbons below 0.7 V due to solvent co-intercalation and prevents its application (*200*). Organic carbonates are thermodynamically unstable at voltages below ~ 1.0 V (Li/Li^+) and decompose on the negative electrodes surface by forming a SEI (*201*). The structure of the SEI is strongly dependent on the compounds used. In the case of EC, the decomposition products are able to protect the layered structure from solvent co-intercalation and kinetically protect the electrolyte from further degradation, as the formed SEI is ionically conductive but electronically insulating (*202*). In the case of PC, no stable SEI is formed. The most common decomposition products are Li_2O, LiF, Li_2CO_3, ROLi, $ROCO_2Li$ and polycarbonates, whereat the inorganic compounds are found closer to the electrode materials surface than the organic ones (*203*).

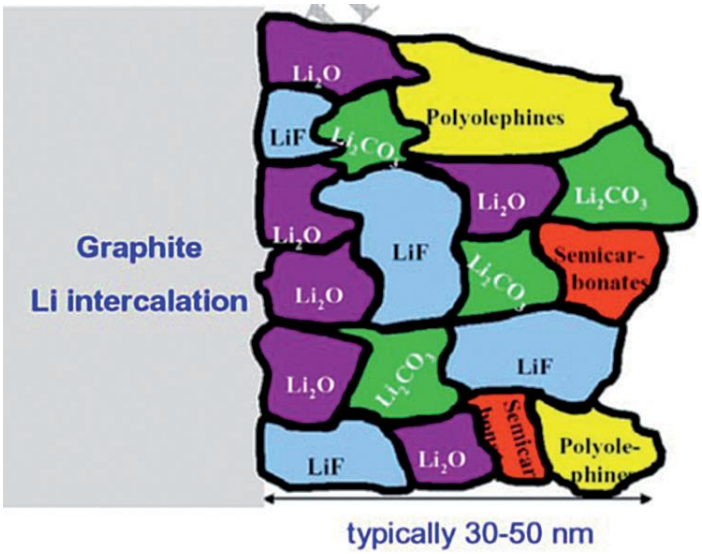

Figure 26. Schematic representation of the chemical composition of the SEI on the surface of graphite (*156*)

3.6 Silicon as Negative Electrode Material

3.6.1 Mechanism of Electrochemical Lithiation/Delithiation

The Li-Si phase diagram shows 5 explicit crystalline phases, namely LiSi, $Li_{12}Si_7$, Li_7Si_3, $Li_{13}Si_4$, $Li_{22}Si_5$ (*204*). Except for the formation of LiSi, the electrochemical alloying of Si with Li follows the phase diagram at a high temperature of 415 °C (*205*), as shown in Figure 28.

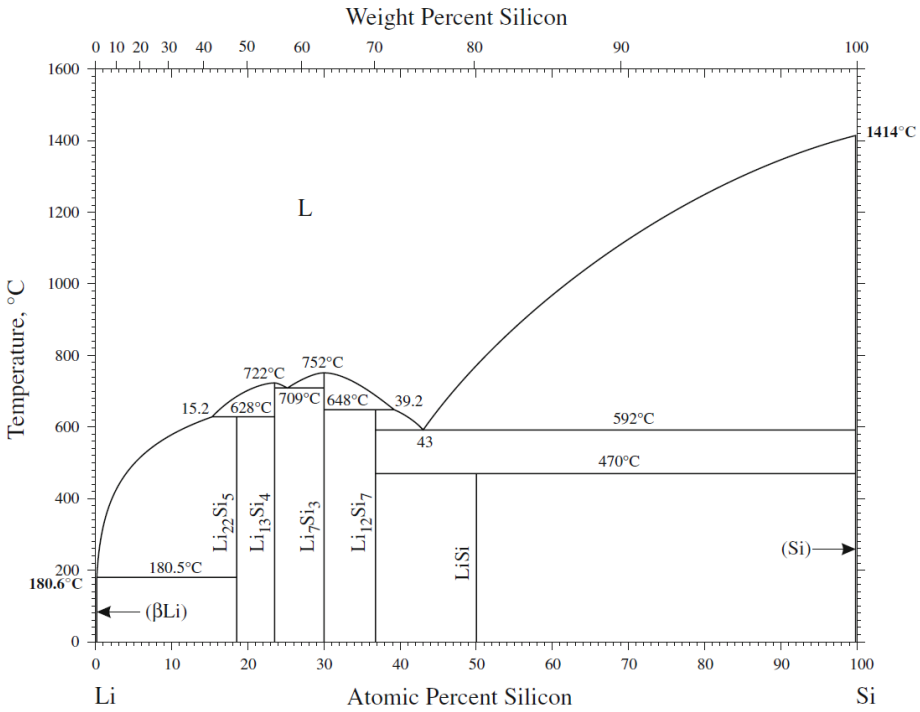

Figure 27. Li-Si phase diagram (*204*)

The $Li_{22}Si_5$ phase represents the maximum possible lithiation of Si (4.4 Li per Si) corresponding to a specific capacity of 4212 mAh g^{-1} (*206*). Some authors refer to $Li_{21}Si_5$ as the highest lithiated phase instead of $Li_{22}Si_5$ (*207*,*208*). However, a definite decision is almost impossible due to the very small differences in the Li content as well as the structural parameters (*209*) and therefore $Li_{22}Si_5$ is the widely accepted composition (*210*). The corresponding capacity of $Li_{22}Si_5$ is often quoted as the theoretical specific capacity of Si negative electrodes, but it can only be reached at high temperature (*211*). At room temperature crystalline Si (c-Si) is electrochemically lithiated via a two-phase mechanism in which the Si is transferred to a lithiated amorphous Si (a-Li_xSi) with a sharp reaction front of nm scale thickness (*212*). This transformation from the crystalline to the amorphous phase

(with a fixed Li concentration) proceeds anisotropically and shows a gentle sloping voltage plateau around 0.1 V vs. Li/Li$^+$ during first lithiation (*213*). It is referred to an electrochemically-driven *solid-state amorphization*, a phenomenon in which disordered materials are formed by a solid-state reaction rather than upon quenching from a melt (*214*). The plateau is not strictly horizontal due to stress effects at the interface of a-Li$_x$Si and c-Si (*211*). The composition of the lithiated amorphous phase is still under debate as x values ranging from 2.17 (*213*) to 3.5 (*215*) have been reported.

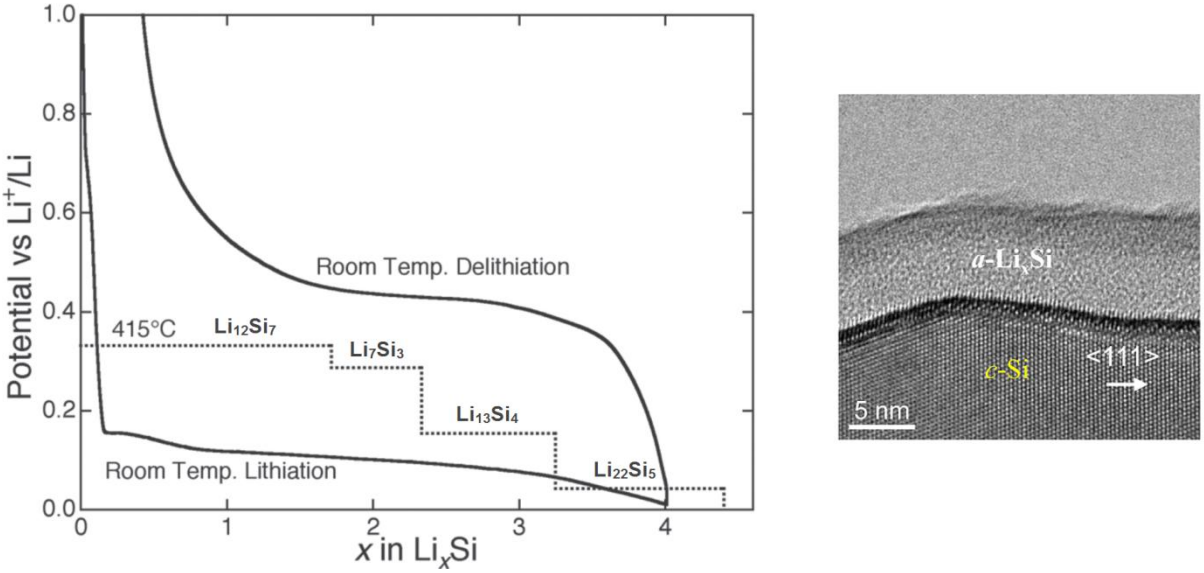

Figure 28. High temperature (dotted line) and room temperature lithiation (solid line) of c-Si (left) (*216*), TEM micrograph of solid-state amorphization of c-Si (right) (*217*)

At the end of the plateau-like lithiation step c-Si has been totally converted to a-Li$_x$Si. Upon further lithiation, the a-Li$_x$Si satures with Li (formation of a-Li$_y$Si, 3.5 < y < 3.75) and crystallizes into the metastable $Li_{15}Si_4$ phase if the voltage reaches ~ 60 mV vs. Li/Li$^+$ (*218*). During the delithiation the crystalline phase converts to an amorphous phase a-Li$_z$Si (z ~ 2) in a two-phase mechanism, showing a plateau at 430 mV vs. Li/Li$^+$ (*215*,*219*). Further Li extraction from a-Li$_z$Si ends in delithiated amorphous Si (a-Si$_{delith}$) and c-Si cannot be detected again (*211*,*216*). The second lithiation behaves differently, as the starting material is now amorphous, and shows 2 major sloping regions at ~ 250 mV and ~ 100 mV vs. Li/Li$^+$ (*220*). The structures and compositions of the Li-Si alloys in these two regions are still not clear and some authors label them as a-Li$_{x'}$Si (250 mV) and a-Li$_{(x'+x'')}$Si (100 mV) (*221*,*222*). Studies on the electrochemical lithiation of a-Si suggest a two-phase reaction for the first sloping region with a sharp interface between the amorphous phases a-Si$_{delith}$ and a-Li$_{x'}$Si, with x' ~ 2.3-2.5 (*217*,*223*). In the second sloping region fast lithiation of

a-$Li_{x'}Si$ takes place to form a-$Li_{(x'+x'')}Si$ in a single-phase reaction (no distinct phases can be observed). Upon further lithiation the formation of c-$Li_{15}Si_4$ can be observed again as the voltage reaches ~ 60 mV vs. Li/Li^+ (*216*). The delithation of this phase in the second cycle proceeds the same way as previously mentioned. A different delithiation behavior appears if the cutoff voltage of the lithiation is set to values above 60 mV vs. Li/Li^+ to prevent formation of c-$Li_{15}Si_4$. As the final lithiated phase is then amorphous, two sloping regions corresponding to the delithiation of a-$Li_{(x'+x'')}Si$ (~ 300 mV) and a-$Li_{x'}Si$ (~500 mV) can be observed (*221*).

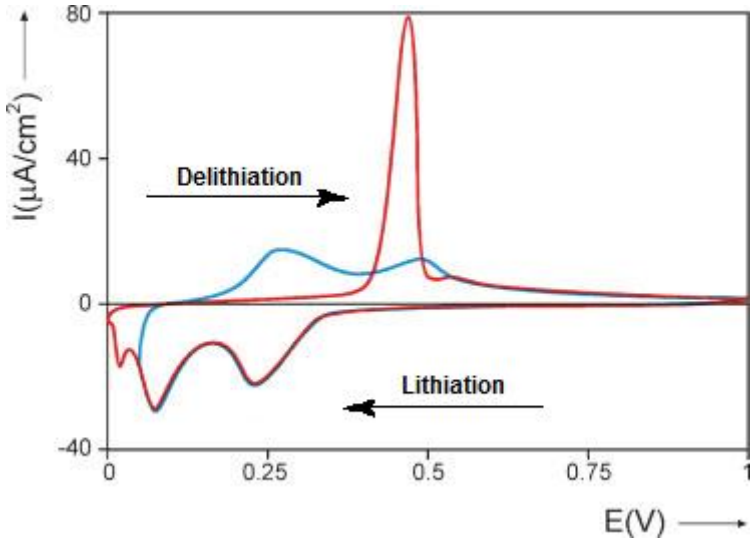

Figure 29. Cyclovoltammograms (CVs) of Si with different reversal points showing the dependency of the delithiation behavior from the final lithiated phase (*224*)

3.6.2 Issues Related to Volume Changes During Lithiation/Delithiation

Besides a relative low electronic conductivity of ~ 10^{-3} S cm^{-1} (increases to ~ 10^2 S cm^{-1} after lithiation) (*225*) and a slow Li diffusion (diffusion coefficient ~ 10^{-13} cm^2 s^{-1}) (*226*), Si suffers from volume expansion/contraction of ~ 300 % upon complete lithiation/delithiation (*227*). These volume changes induce large stresses, which cause cracking or pulverization of the Si (*228*). Most of the fracture events take place in the initial cycle compared to further cycling and this mechanism probably accounts for most of the capacity fade observed in early studies based on Si of µm size (*229*). Capacity fading can also be observed for particles which do not fracture, as the large volume changes can result in detachment of their surrounding electrical connections. In addition, the total volume of the whole electrode increases and decreases during cycling and can lead to electrode peel-off and failure (*230*). Another issue is that the Si particle shrinkage during delithiation leads to cracks or exfoliation

of the SEI layer and exposes fresh surface to the electrolyte (*231*). In the proximate lithiation new SEI is formed on the exposed Si surface and the process continues upon cycling, triggering a gradually growth of the SEI thickness. The thick SEI layer is harmful for cycle life as it consumes electrolyte and Li, raises the cell impedance and decreases the electrochemical activity (*218*).

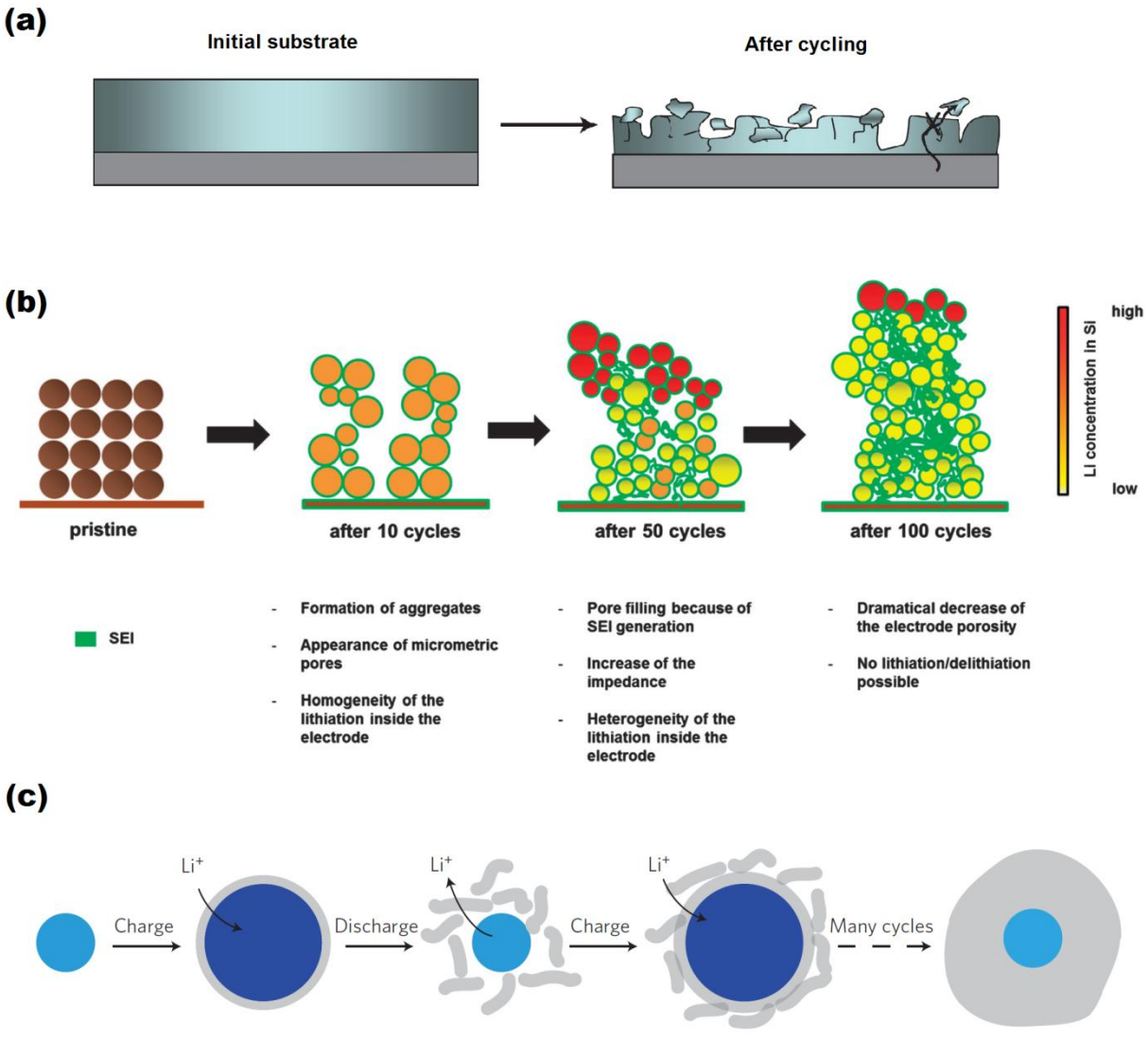

Figure 30. Failure mechanisms of Si electrodes: film (a) (*232*), particles (b) (*233*) and SEI growth (c) (*234*)

The approaches to overcome or diminish the issues related to the large volume changes upon cycling are discussed in the following subchapters.

3.6.3 Reducing Size to the Nanoscale

Moving from bulk or microscale to nanoscale morphologies, such as thin films, nanoparticles, nanotubes or nanowires, has the potential to solve the limitations caused by the expansion and contraction of Si negative electrodes upon cycling. These morphologies improve cycling performance by minimizing the total volumetric expansion and their high surface-to-volume ratios facilitate the relaxation of stress associated to the volume changes, making them more resistant to fracture than bulk materials (*235*). Fracturing is dependent on the morphology and starts at the surface, as the surface is first prone to lithiation and expands more than the less lithiated core (*178*). Therefore different morphologies have different critical sizes below which fracture can be prevented. Critical sizes of ~ 150 nm for SiNPs (*236*), ~ 300 nm for SiNWs (*237*) and ~ 100 nm for Si thin films (*238*) have been reported. Nanosized materials also offer other advantages, including short diffusion pathways, enhanced diffusion along surfaces and grain boundaries, high rate capability and reduced polarization (*227*,*235*).

However, nanostructured Si negative electrodes face some important challenges as well. The production of nanoscale materials is very expensive and the electrodes typically suffer from lower tap densities compared to microscale Si. Furthermore, the high surface area increases side reactions with the electrolyte and leads to a high irreversible capacity in the first cycle and low coulombic efficiency upon further cycling, which results in strong capacity fading in full cells (*239*). To attenuate these problems Si is often used in composite materials and film forming additives are added to the electrolyte to obtain a more stable SEI (*240*).

3.6.4 Electrolyte Additives

The use of electrolyte additives is one of the easiest and most economic ways for the improvement of the cycling performance. Generally, the amount of an additive in the electrolyte is no more than 5 % either by weight or by volume (*201*). Their role is to facilitate the formation of a more stable SEI to prevent its pulverization and to reduce the irreversible capacity as well as gas formation upon long-term cycling. The most common polymerizable additives for Si electrodes are vinylene carbonate (VC) (*241*) and fluoroethylene carbonate (FEC) (*242*), as they are proven to significantly reduce capacity fading. In addition, it has been reported that they also enhance the thermal stability of the lithiated Si (*243*). VC and FEC have higher reductive potentials than the electrolyte solvents and thus are reduced first (*244*,*245*). The formed polymeric layer is thinner, denser and shows higher stability than

the conventional SEI formed without an additive (*246*). However, the decomposition products and mechanisms are still not completely understood (*245*,*246*).

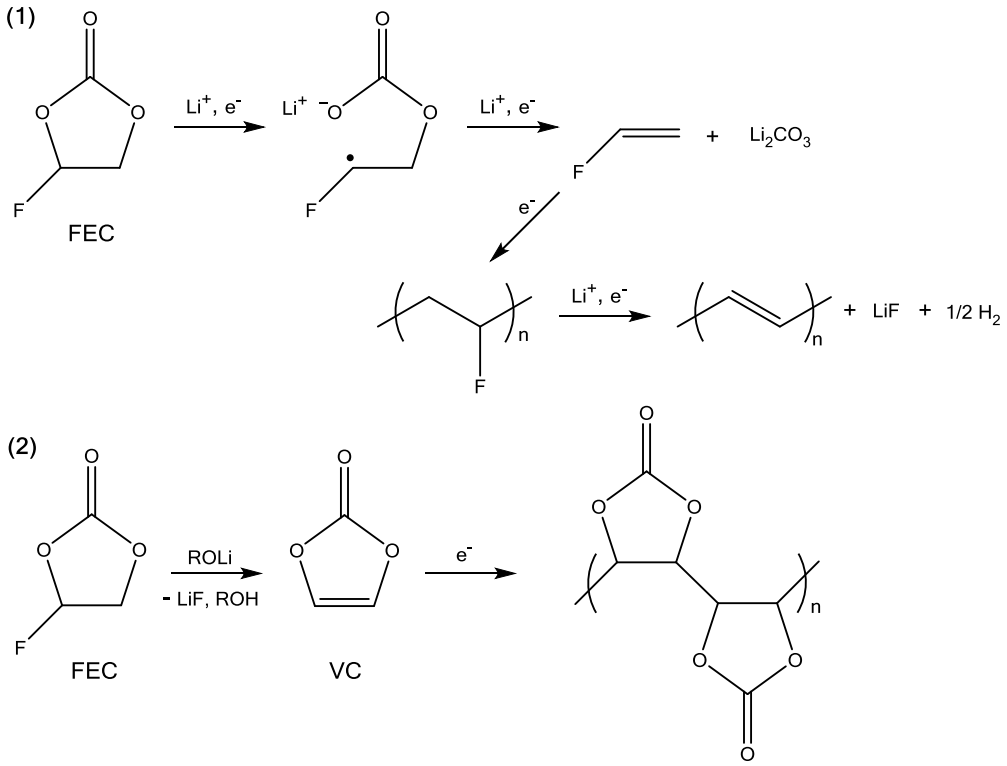

Figure 31. Proposed reaction mechanism for the decomposition of FEC and VC (*247*,*248*)

3.6.5 Composite Materials

As pristine nanosized Si still suffers from loss of electrical contact, low electrical conductivity and electrolyte additives cannot prevent SEI growth on it completely, it is usually used in composite materials for further improvement (*249*).

In an ideal composite material the Si is embedded in a host matrix buffering the large volume changes, so that electrode integrity and electrical contact of the active Si and the conductive phase maintains. To this end, the host matrix must have efficient pathways for electron and Li^+ transport and must maintain the microstructural stability of the electrode. Furthermore the host matrix must also have a dimensional stable surface to prevent continuous SEI growth and must act as a spacer to reduce the aggregation of Si particles upon cycling (*180*).

Nowadays, a vast number of different composite materials exist, with more or less electrochemical improvement. The approaches are usually divided into composites of Si with an active or inactive matrix (*176*).

In *active matrix composites*, both the Si and the host matrix are reactive towards electrochemical lithiation. The idea of this kind of composite is to have one compound lithiated while the other acts as a buffer phase to alleviate the volume change as they react with Li at different onset potential (*180*). The most common materials are graphite or reactive metals like Ag, Ca and Mg. In the case of alkaline earth metals, the intermetallic compounds $CaSi_2$ (*250*) and Mg_2Si (*251*,*252*) are used. The reaction mechanism of the Li insertion into Mg_2Si is proposed as follows (*252*):

$$Mg_2Si + x\ Li^+ + x\ e^- \rightarrow Li_xMg_2Si$$

Eq. 11

$$Li_xMg_2Si + x\ Li^+ + x\ e^- \rightarrow Li_{critical}Mg_2Si \rightarrow Li_{satured}Mg_2Si + Mg + Li - Si\ alloy$$

Eq. 12

$$Mg + x\ Li^+ + x\ e^- \rightarrow Li - Mg\ alloy$$

Eq. 13

As Ag is immiscible with Si and does not form intermetallic compounds (*253*), mechanical alloyed Ag-Si powders (*254*) or Ag-coated Si (*255*) are used. However, active matrix composites still suffer from capacity fading due to the volume changes of the two reactive phases. A better cycle stability can be achieved by limiting the second-component lithiation (*180*).

Inactive matrix composites usually show better cycle stabilities compared to active ones, as the host matrix is nonreactive (or less reactive) towards lithiation and hence it acts as a more efficient buffer, with the drawback of less specific capacity. The matrix can be a metal such as Cu, Fe or Ni (*256*,*257*,*258*), an alloy like $FeSi_2$ or $Si_7Ti_4Ni_4$ (*259*,*260*), a mix of Li_2O and Li_4SiO_4 (obtained by electrochemical reduction of SiO_x) (*261*), or a carbonaceous material (*262*). Among them carbonaceous composites (Si/C) are the most popular ones (*231*), as metals or alloys reduce the specific capacity to a greater extent due to their high molecular weight (*178*) and the reduction of SiO_x leads to unreasonable high irreversible capacity in the first cycle (*263*). A huge variety of Si/C composites exist and they differ generally in their morphology (wires, tubes, spheres, films or 3D networks), in the position of Si (surface or encapsulated) and their structure (core-shell or not, presence or absence of hollow moieties). The most common Si/C composites are summed up in Table 2. including the corresponding references for further detail.

Table 2. Common Si/C composite types and examples

Class of composite material	Highest delithiation capacity [mAh g^{-1}]	Cycling performance [mAh g^{-1}] after # cycles	Ref.
C-coated Si	1525	1354 / 100	(*264*)
Surface grafted C bond to Si	1100	540 / 50	(*265*)
Plum pudding like Si/C	1507	885 / 100	(*266*)
Si embedded in porous 3D C network	2000	1500 / 100	(*267*)
Si-coated CNT	2755	2510 / 80	(*268*)
SiNPs in C fiber	1490	600 / 70	(*269*)
SiNPs in CNT	969	850 / 200	(*270*)
SiNT in CNT	1250	750 / 250	(*271*)
Si/C multilayer films	2200	2000 / 60	(*272*)
Crumbled graphene encapsulated SiNPs	1125	940 / 250	(*273*)
SiNPs/graphene sandwich	2080	1410 / 100	(*274*)
Si-coated graphene	1350	1300 / 30	(*275*)
Si/C nanoporous microspheres	1614	1000 / 50	(*276*)
Yolk-shell Si/C	2833	1500 / 1000	(*277*)

It should be noted that a direct comparison of the electrochemical performance of the different composite types is inadmissable by the illustrated values. This is because the performance is also depend on factors like the lithiation/delithiation times (C-rates), electrolyte, binder, mass loading of the electrodes, cell geometry etc. and they usually differ keenly among the available literature. However, one can say that composites that contain encapsulated silicon and hollow moieties such as SiNPs in CNTs, SiNTs in CNTs or yolk-shell Si/C composites generally exhibit the most stable cycling performance, as they are dimensionally stable and do not show continuous SEI growth (*228*).

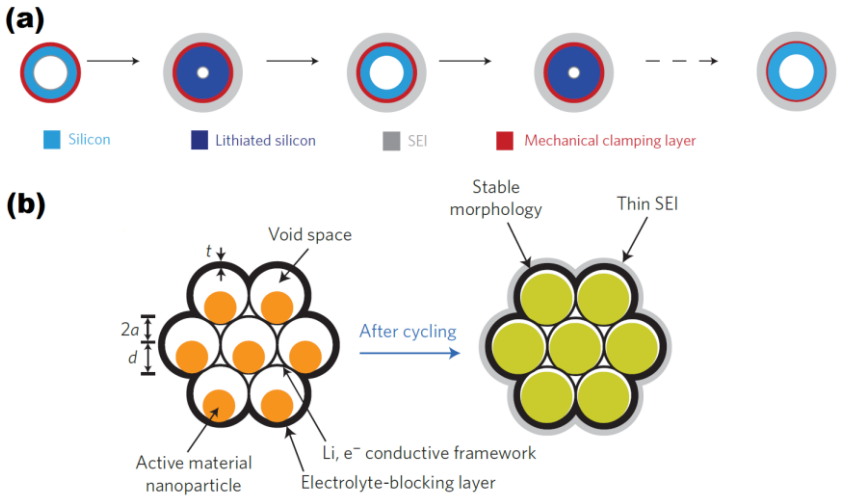

Figure 32. Mechanism of cycling stability for SiNT in CNT (a) (*234*) and yolk-shell Si/C composite (b) (*239*)

4 Experimental Part

4.1 Introduction

The application of Si as negative electrode materials is a promising approach to satisfy the demands for future high capacity power devices. However, cost-effective, scalable routes for the production of nanosized Si and composites thereof are necessary for the implementation in commercial LIBs. Within chapter 2.4 it was shown that HEBM offers an easy and cheap way to achieve this.

Research on ball milled Si for LIBs began in the first half of the last decade and was based on dry-milling (*278*). However, the majority of the obtained particles are larger than 150 nm and the milling times are in the range of 20-200 h (*279*,*280*), which is insufficient for industrial production. On the other hand, wet-milling keenly diminishes the milling times and enables the fabrication of smaller particles. It is therefore the method of choice for this thesis and the motivation behind the utilization of wet-milled, nanosized Si is not only its ease of production, but also that it has not yet been extensively studied in LIBs.

In the following chapters the wet-milling of Si is investigated in detail, including surface functionalization and the influence of the milling parameters. For electrochemical investigations the as obtained nanosized Si is used for the production of simple Si/C composites and more complex core-shell structured ones.

4.2 Analytical Characterization

This chapter gives a brief overview over several analytical techniques applied in this work for the characterization of the prepared SiNPs, composites and corresponding electrodes. If not otherwise stated, for the characterization of SiNPs the solvent of the milling suspension is removed and the obtained powder is further dried at elevated temperatures and reduced pressure to remove residual solvent.

- ***Particle size distribution*** measurements are carried out with static light scattering using a FRITSCH Analysette 22 Nanotec plus. A drop of the surfactant FRITSCH Dusazin 901 is added to the powder or suspension to be measured and mixed with a spatula to obtain a paste-like suspension. 20-30 mL of deionized water is added and ultrasonic is applied,

if further dispersing is necessary. The ultrasonic bath Fisher Scientific FB15063 is used for mild dispersing conditions and a disintegrator is used if harsh conditions are required (SiNPs). The disintegrator consists of the high frequency generator GM2200, the ultrasonic transducer UW2200 and the sonotrode TT13 of the SONOPULS series from BANDELIN.

- ***FT-IR*** measurements are carried out with a PerkinElmer Frontier IR Single-Range System using the Universal ATR Sampling Accessory.
- ***SEM*** pictures are taken with an ESEM TESCAN 500 PA (VEGA 3 control software) with a heated tungsten filament and an OXFORD INSTRUMENTS INCAx-act detector is used for ***EDX*** measurements. If the sample needs to be sputtered with Au, a CRESSINGTON 108auto Sputter Coater is used.
- ***XRD*** measurements are carried out with a BRUKER D8 Advance.
- ***BET*** measurements are performed by the Research Center Pharmaceutical Engineering GmbH using a Micromeritics ASAP 2000.
- ***GC/MS*** measurements are carried out with an Agilent Technologies 7890A gas chromatograph, a HP5-ms column and a 5975C VLMSD mass spectrometer (same company). For ***Py-GC/MS*** a FRONTIER LAB Double Shot Pyrolyzer PY-2020iD is used in addition.
- ***TGA/DSC/MS*** measurements are performed by the Institute for Chemistry and Technology of Materials (ICTM) of Graz University of Technology.

4.3 Electrode Preparation and Electrochemical Characterization

The electrode preparations are carried out by slurry technique using an automated doctor blade. If not otherwise stated, the electrode preparation proceeds as follows. The binder (NaCMC) gets dissolved in deionized water to form a viscous solution. NaCMC is chosen as standard binder as it shows superior cycling performance for Si containing electrodes (*281*). After dissolving the binder, a drop of surfactant (SOPROPHOR® FLK), conductive additive (CNERGY™ Super C65) and the active material(s) are added. The solids content is generally ~ 25 %. The composition varies according to the composite used and is therefore listed in the corresponding chapter. The resulting slurry is then mixed over night via magnetic stirring.

The next day, the slurry is coated on surface roughened copper foil (SCHLENK) by an automated film applicator (ERICHSEN COATMASTER 509; TQC VF2174). The coated copper foil is pre-dried in a compartment dryer (Memmert UF110) for 3-4 hours at 60 °C.

After that, electrodes and 3 blanks with a diameter of 12 mm are punched out from the electrode foil using a hollow punch and a rubber mallet. The electrodes and blanks are dried over night in a BÜCHI Glass Oven B-585 at 120 °C and ~10^{-3} mbar.

The electrodes and the blanks are weighed with a METTLER TOLEDO XS205 Dual Range balance. The mass loading of an electrode is determined by subtracting the average blank weight from the electrodes weight. After weighing the electrodes are dried again over night (under the previous mentioned conditions) and placed in an Ar filled glove box (MBRAUN LABMASTER SP MB20-G; < 0.1 ppm H_2O, < 0.1 ppm O_2).

Electrochemical measurements are performed in a Swagelok® three-electrode half cell setup. In this cell setup Li metal is used as counter electrode as well as reference electrode. The cells are assembled in the above mentioned glovebox using electrodes with a mass loading of ~ 1 mAh cm^{-2} as working electrode. At higher mass loadings the performance would be limited by the Li counter electrode and lower loadings may hide important material limitations, such as high electrical and ionic resistance or low structural stability (*5*).

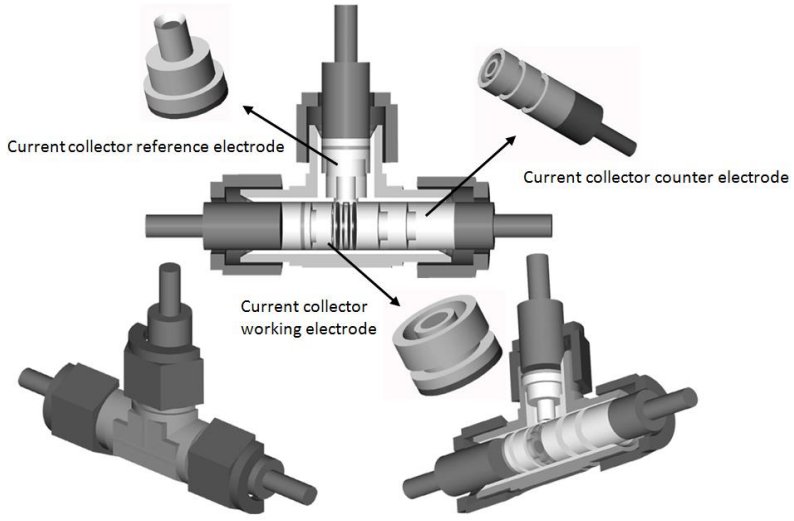

Figure 33. Scheme of a Swagelok® three-electrode setup (*282*)

The current collectors are made from stainless steel (specification 1.4301) jacketed with PP to prevent electrolyte contact, which would lead to a mixed potential. A Mylar® foil (PET, 75 µm) is used to prevent contact of the Swagelok® casing with the current collectors, which would cause a short circuit. The separator is a stack of three-layered Freudenberg FS2190 (PP, 230 µm layer thickness) fleeces with a diameter of 12 mm (between working- and counter electrode) and 6 mm (reference electrode). Prior to cell assembly the separators are

completely soaked with electrolyte (Ø 12 mm: ~ 100 µL; Ø 6 mm: ~ 25 µL). The used electrolyte is an EC/DEC (3:7 w/w) mixture with 1 M $LiPF_6$ and 2 wt% VC additive, as the composition and the additive have shown good cycling and SEI forming properties (*243*,*283*). If another electrolyte composition or additive is used, it will be denoted at the accompanying part of the thesis.

After cell assembly, the electrochemical characterizations are carried out by *cyclic voltammetry* (CV) and *constant current charging* (CCC) measurements.

4.3.1 Cyclic Voltammetry

CV is a potentiodynamic electrochemical measurement technique at which the working electrode's potential is ramped linearly versus time and the current flow is recorded. By reaching a defined potential (*reversal potential*), the working electrode's potential is ramped in the opposite direction to return to the initial potential or a second reversal potential. Depending on the ramping direction these points are named cathodic- or anodic reversal potential. These cycles may be repeated as many times as desired.

The measured current is then plotted versus the applied voltage to obtain the cyclic voltammogram. The peaks observed provide in combination with the scan rate ($\Delta U/t$) both qualitative and quantitative information on electrode processes, such as lithiation/delithiation mechanisms, kinetics and capacities.

The CV measurements are performed on a BioLogic MPG-2 potentiostat and the standard measurement parameters are displayed in Table 3.

Table 3. Standard program used for CV measurements

Standard CV measurement parameters	
Starting point	OCV
Voltage limits of the cycle	0-1.5 V
Scan rate	30 µV s^{-1}

4.3.2 Constant Current Charging

CCC measurements are performed to test the long-term cycling behavior of electrodes under galvanostatic conditions. Here, a constant current is applied to the cell while the working electrodes potential (vs. reference electrode) is measured currentless versus time. The constant current value is usually expressed as *C-rate* and represents the time needed to charge/discharge a cell. If a cell has a nominal capacity of 30 mAh, a C-rate with the value 2 means that 60 mA are applied to cell and it is therefore charged/discharged within half an hour. Contrariwise, 0.5 C (or C/2) is related to a current of 15 mA and charging/discharging is performed within 2 hours. Depending on the active material, the cells are charged/discharged till a certain potential, the so-called *cutoff potential*, is reached. At this point a constant voltage can be applied to the cell to reduce overpotential and other kinetic effects and it is charged/discharged for a certain time or as long as the current drops below a defined value (typically C/20 or C/50). After the constant voltage step the current flow is reversed. The procedure starts again from the beginning as the potential reaches the initial value or another determined one. CCC measurements not only allow the observation of the cycling behavior in terms of capacity but also provide information on the ongoing electrochemical reactions in the form of potential profiles (charge/discharge curves) and differential capacity plots. The measurements are performed on a MACCOR Series 4000 Battery Tester and the standard program is shown in Table 4 (potentials vs. Li/Li^+).

Table 4. Standard CCC measurement program

Rest step of 6 h			
Formation steps			
Cycle 1	Constant current	Lithiation	0.1 C → 5 mV
	Constant voltage	Additional lithiation	4 h @ 5 mV
	Constant current	Delithiation	0.1 C → 1500 mV
Cycle 2	Constant current	Lithiation	0.2 C → 5 mV
	Constant voltage	Additional lithiation	3 h @ 5 mV
	Constant current	Delithiation	0.2 C → 1500 mV
Cycle 3	Constant current	Lithiation	0.3 C → 5 mV
	Constant voltage	Additional lithiation	2 h @ 5 mV
	Constant current	Delithiation	0.3 C → 1500 mV
Cyclization			
Further cycles	Constant current	Lithiation	0.5 C → 5 mV
	Constant voltage	Additional lithiation	1 h @ 5 mV
	Constant current	Delithiation	0.5 C → 1500 mV

4.4 Planetary Ball Milling of Silicon

In planetary ball mills, the comminution of the material to be ground takes place primarily through the high-energy impact of grinding balls in rotating grinding bowls. This special type of high-energy ball mill is so named due to the planetary motion-like movement of the grinding bowls shown in Figure 34.

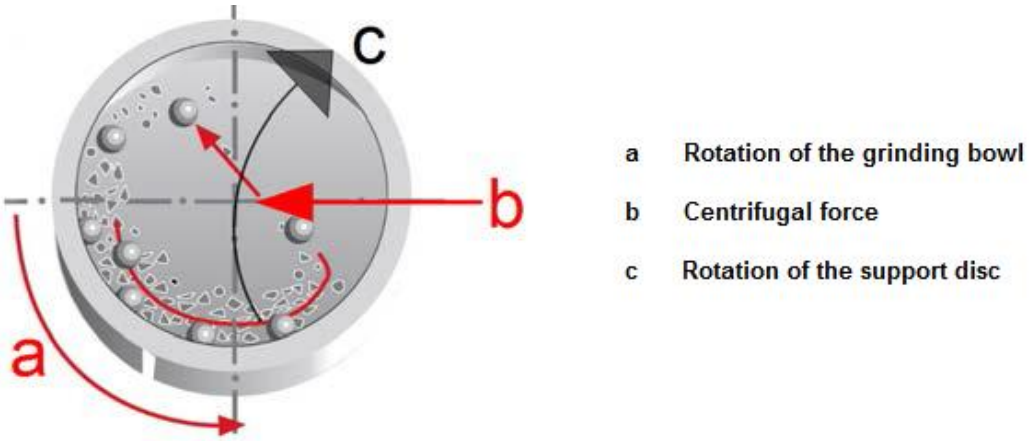

Figure 34. Movement of the grinding bowls in planetary mills (*284*)

The grinding bowl and the support disc have opposite rotation directions; hence the centrifugal forces alternately act in like and opposite directions. The result is that the grinding balls will run down the inside of the bowl's wall with a *friction effect* and at a certain point the grinding balls lift off the wall and collide against the opposing inside wall inducing an *impact effect*. The contrary movement allows much higher rotation speeds, compared to conventional ball milling, leading to higher impact energies. High impact energies in turn reduce milling times and smaller particle sizes can be obtained. In conventional ball mills the rotation speed is limited as at a critical speed the grinding balls and the milling media stick to the wall caused by the centrifugal force, thus no further milling occurs.

It should be noted that in the English language two words exist for the German word "*Mahlen*", namely *grinding* and *milling*. In this regard, milling is used when referring to deagglomeration of particles and dispersing them in a liquid medium. Grinding is used to reference the process of taking particles and shear them down to actually reduce the size (*285*). As both processes occur during wet-milling of Si and as the words are quite often used as synonyms the word milling is used throughout this doctoral thesis.

A FRITSCH PULVERISETTE 7 premium line planetary ball mill is used for the following milling experiments. The feature of this mill is that the grinding bowls are sunk in the main disc (support disc), which allows even higher rotation speeds compared to other planetary ball mills. The most important mill specifications are shown in Table 5.

Table 5. PULVERISETTE 7 premium line specifications (*286*)

PULVERISETTE 7 premium line	
Number of working stations	2
Grinding bowl sizes	20, 45, 80 mL
Sample quantity (depending on bowl size)	0.5 – 70 mL
Final fineness (depending on the material)	< 0.1 µm
Grinding process	Dry/wet
Speed of main disk	100 – 1100 rpm
Transmission ratio	$I_{relative}$ = 1 : -2
Effective diameter of main disk	140 mm
Centrifugal acceleration (g = 9.81 m s^{-2})	95 g

Another advantage is that for this mill a reasonable range of materials is available for the grinding bowls and the grinding balls, shown in Table 6.

Table 6. Available grinding materials and their properties (*284*)

Material (bowl and balls)	Main components of the material	Density [g cm^{-3}]	Abrasion resistance	Use for grinding stock
Agate	99.9 % SiO_2	2.65	Good	Soft to medium-hard samples
Silicon nitride	90 % Si_3N_4	3.25	Extremely good	Abrasive samples, metal-free grinding
Sintered corundum	99.7 % Al_2O_3	3.9	Fairly good	Medium-hard, fibrous samples
Zirconium oxide	96.2 % ZrO_2	5.7	Very good	Fibrous, abrasive samples
Stainless steel	Bowl: 17-19 % Cr + 8-10 % Ni Balls: 12.5-14.5 % Cr + 1 % Ni	7.8	Fairly good	Medium-hard, brittle samples
Tempered steel	Bowl: 11-12 % Cr Balls: 1.0-1.65 % Cr	7.9	Good	Hard, brittle samples
Tungsten carbide	93 % WC + 6 % Co	14.9	Very good	Hard, abrasive samples

Normally grinding bowls and grinding balls are chosen that are made of the same material, otherwise abrasion occurs to a greater extent and in the worst case one of the materials may be pulverized. Furthermore, the hardness and the density of the grinding materials must be greater than that of the material to be ground, to prevent excessive wear by abrasion.

As Si has a density of 2.33 g cm^{-3} (*287*) and a mohs hardness of 7 (*288*), WC-Co is the grinding material of choice as its very high density (14.9 g cm^{-3}) (*284*) and a mohs hardness of 8 (*289*) are ideal for the milling experiments. With a value of 9 on the mohs hardness scale (*288*,*290*), Si_3N_4 and Al_2O_3 are the only at FRITSCH available materials which are harder than WC-Co, however, their low densities make them inappropriate for Si.

80 mL WC-Co grinding bowls are used for all experiments as they are the largest ones available and allow the production of sufficient amounts of nanosized Si.

The size of the grinding balls depends on the initial particle size of the material to be ground and should be substantially larger as shown in Table 7.

Table 7. Size of the grinding balls in dependence of initial particle size (*284*)

Type of feed material	Suitable ball diameter
Hard samples with a maximum feed size of 5 mm	20 mm / 15 mm
Average feed size of 0.5 – 1 mm	15 mm / 10 mm
Fine material 0.1 – 0.5 mm	10 mm / 5 mm
Very fine material < 0.1 mm	3 mm / 1.6 mm / 0.6 mm
Homogenization of dry or liquid samples	10 mm / 5mm

On the contrary, the grinding balls should not be too large as a smaller ball size leads to smaller particles, a narrower particle size distribution and shorter milling times. The primary used Si (-325 mesh, 99 % trace metals basis, SIGMA ALDRICH®) consists of particles ≤ 44 µm (*291*), hence the smallest available WC-Co grinding balls with a size of 0.6 mm can already be used, as the ball size is more than a magnitude larger than the largest Si particles. If the Si particles would be much larger (> 100 µm), pregrinding with larger grinding balls would be necessary.

In addition to the grinding materials and ball size, the ball to powder mass ratio (BPR), sometimes referred to charge ratio (CR), should be rather high. A higher BPR reduces the grinding duration and the grinding result will be within a smaller grain size range (*89*). In technical application the ratio is typically of the order 1:5 to 1:50 (*87*). In the case of the PULVERISETTE 7 pl the BPR is changed by varying the mass of the material to be ground,

as the mass of the balls is specified by FRITSCH according to ball and bowl size. The values for the corresponding WC-Co grinding balls can be found in Table 8 and should be complied with to avoid unnecessary wear.

Table 8. Number or weight of WC-Co grinding balls in dependence of their size (*284*)

Ball diameter [mm]	WC-Co grinding bowl 80 mL
20	5 balls
15	10 balls
10	25-30 balls
5	240 g
≤ 3	300 g

General milling procedure for nanosized Si:

Two 80 mL grinding bowls (WC-Co inlay) and the 0.6 mm WC-Co grinding balls are taken out of a compartment dryer (60 °C). The grinding bowls are weight and marked, as their weights differ slightly (< 0.4 %). The mass difference is calculated (~ 6 g) and divided by 2. The obtained value x is used to calculate the exact weight of grinding balls needed for the respective grinding bowl (300±x g). This is necessary as the grinding bowls are filled with the same quantities of Si and solvent, and each filled bowl must have the same weight to prevent fatal imbalance at high rotation speeds.

The empty grinding bowls are filled with their corresponding quantities of grinding balls and the Si is placed above the grinding balls. Then a certain amount of solvent is added and the filled bowls are placed in a plastic box. The box is filled with Ar (5.0, LINDE GAS) for at least 2 min and the grinding bowls are sealed under gas flow. The bowls are then fixed in the main disc of the mill, the milling parameters (rotation speed, milling duration, cooling time, number of cycles) are entered and the milling process is started.

After milling, the bowls are allowed to cool down below 30 °C and a possibly existing overpressure is released slowly by a valve. The contents of the bowls are poured in a large beaker or crystallizing dish and 100-150 mL solvent (usually the milling solvent) are added. The beaker or dish is placed in an ultrasonic bath for approximately 5 min and the obtained milling suspension is filled in a lidded container for storage until use. A 280 µm sieve (RETSCH) is used to retain the grinding balls. Ultrasonication is used for cleaning.

4.4.1 Milling Parameters

It should be noted that grinding balls with diameters of 5 mm or less cause high thermal stress due to friction. The stress increases with smaller ball size (= larger surface) and higher rotation speeds. Furthermore, occurring chemical reactions can increase the stress and cause overpressure. Thermal stress is particularly hazardous if wet-milling is performed as the inside temperature may reach the boiling point of the solvent easily. In this context serious explosions have been reported (*284*). To reduce the risk of hazardous incidents, the silicon flat seal of the grinding bowl is designed to open above a static internal pressure of 18 bar. However, the overpressure relief does not work in the case of sudden pressure surges and the locking hooks of the bowl's lid could be torn off as they are designed to withstand an internal pressure up to 40 bar. Hence, a for any milling system the maximum milling durations and minimum cooling times have to be determined as function of the rotation speed to ensure safe milling.

These values are determined as follows: After milling for 2 min at a certain rotation speed the surface temperature is measured at the lid and at the bottom with a surface probe (type K). If the higher temperature is below 80 °C further milling can be carried out. The milling duration can be expanded or reduced depending on how far away the measured value is from 80 °C. Milling is carried out as long until the temperature exceeds 80 °C. A cooling step of 1 h follows and the sample is milled again in one step. The milling duration of this step is the sum of those needed to exceed 80 °C. If the temperature does not increase, the cooling times can be reduced in 5 min intervals (but not shorter than 30 min), always followed by the same milling duration. This sequence is exerted as long as an increase of the temperature can be observed. To be economical the milling parameters are then the milling time needed to reach 80 °C and the shortest cooling time in which no increase of temperature could be observed. In general, 5 minutes are added to the cooling time in order to have a safety margin. The measured values for Si milled in 1-methoxy-2-propanol (1-M-2-p) are shown in Table 9.

Table 9. Measured milling parameters for Si milled in 1-M-2-p

7.5 g Si, 20 mL 1-Methoxy-2-propanol, 300 g WC-Co grinding balls Ø 0.6 mm		
Rotation speed [rpm]	Milling duration [min]	Cooling time [min]
500	60*	30
700	10	45
900	4	45

* The temperature does not reach 80 °C, but milling without a break should be restricted to 60 min

Milling with rotation speeds > 900 rpm is not possible with 80 mL WC-Co grinding bowls and the corresponding grinding balls as the overall weight of the filled bowls is too large for the mill. If higher rotation speeds are entered the mill automatically adjusts it to 900 rpm.

In addition to 1-methoxy-2-propanol, milling is also carried out in the following solvents: 1-octene, *n*-heptane, benzene, ethanol and 2-propanol. The physical properties of the used solvents are shown in Table 10 (data is obtained from SciFinder® Substance Identifier).

Table 10. Key physical properties of used milling solvents

Milling solvent	Boiling point [°C]	Density [g cm^{-3}]
1-Methoxy-2-propanol	120	0.962
1-Octene	121	0.715
n-Heptane	98	0.680
Benzene	80	0.879
Ethanol	78	0.789
2-Propanol	82	0.785

The milling parameters for 1-octene and *n*-heptane are ascertained to be equal to 1-methoxy-2-propanol (see Table 9). In the case of the other solvents, rotation speeds above 500 rpm lead to serious overpressure and milling suspension emerges within less than 2 minutes due to the low boiling points. The milling parameters 500 rpm rotation speed, 60 min milling duration and 30 min cooling time are tested for ethanol (lowest boiling point), however, after 2-3 cycles milling suspension emerges too. With a reduction of the milling duration to 30 min, the milling cycles can be performed for all solvents without emerge of suspension. If not otherwise stated, the milling parameters shown in Table 11 are therefore used for all milling operations to have comparable milling parameters.

Table 11. Standard milling parameters for Si milled in various solvents

Rotation speed [rpm]	Milling duration [min]	Cooling time [min]
500	30	30

4.4.2 Influence of the Milling Conditions on the Particle Size Distribution

In this chapter, the influence of various milling conditions on the particle size distribution is discussed for the milling of Si -325 mesh. The particle size distribution and a SEM micrograph of the starting material are shown in Figure 35.

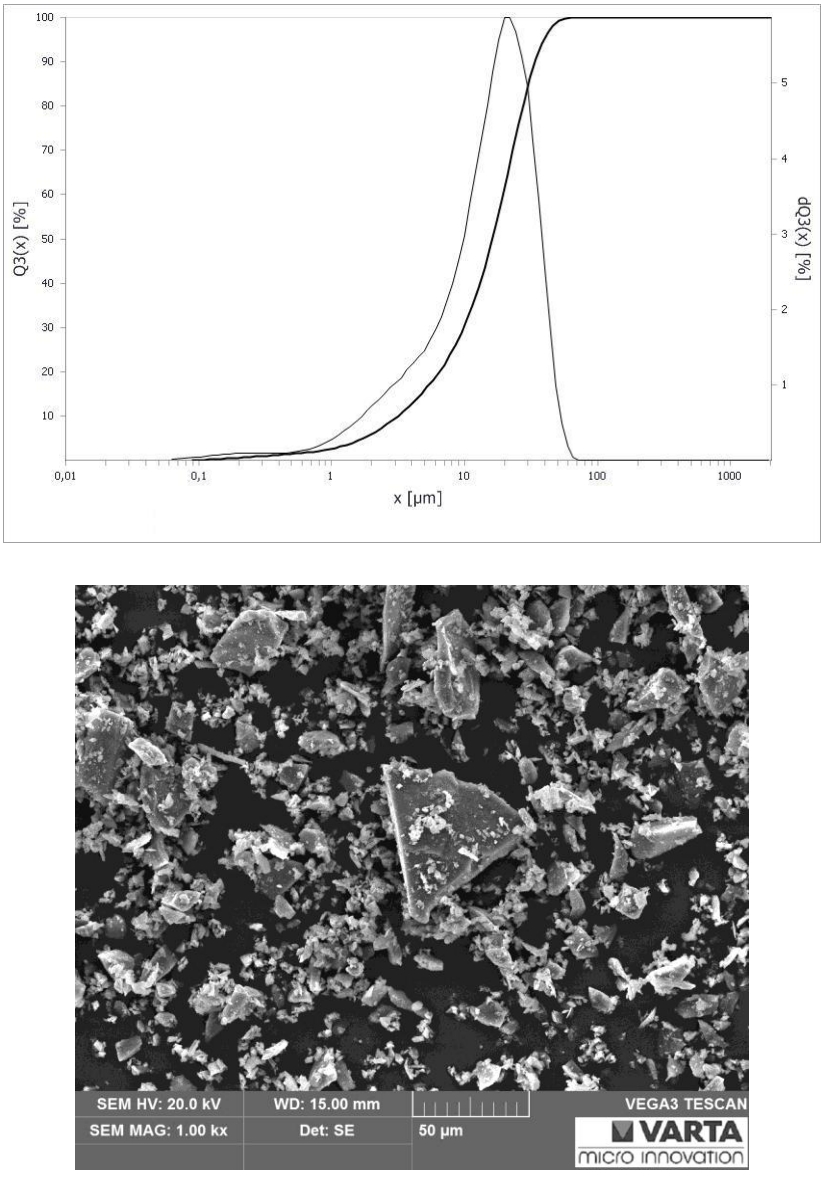

Figure 35. Particle size distribution of Si -325 mesh (top) and SEM micrograph (bottom) of Si -325mesh

Table 12. Particle size distribution values of Si -325 mesh

Ø Particle size [µm]	D10 [µm]	D50 [µm]	D90 [µm]	(D90 - D10) / D50
17.6	3.2	16.2	33.9	1.90

A D10 value of 3.2 µm means that 10 % of the measured particles are smaller than 3.2 µm. Equally, D50 and D90 mean that 50 % and 90 % of the particles are smaller than the denoted value. The dimensionless measure (D90 – D10)/D50 represents the relative span (width) of the particle size distribution.

In the particle size distribution and the SEM micrograph it can be seen that there is a small amount of particles larger than 44 µm (325 mesh = 44 µm). This can be explained by the irregular shape of the Si, which allows slightly larger particles to pass the mesh during sieving.

In general, Fraunhofer diffraction is used for measurements of particles larger than the wavelength of the light used for static light scattering and Mie scattering is used for smaller ones. In the case of the ANALYSETTE 22 NanoTec plus two green semiconductor laser (λ = 532 nm, one laser for backscattering) and an IR semiconductor laser (λ = 940 nm) are used for the measurements (*292*). The particle size distribution is calculated from the scattering pattern with the required theory. According to the laser wavelengths, Fraunhofer diffraction is used for particles in the µm region and Mie scattering is used for the nm region. The used Mie parameters for Si are shown in Table 13.

Table 13. Mie parameters of Si

Refraction index green laser	Refraction index IR laser	Absorption coefficient green laser	Absorption coefficient IR laser
4.242	4.200	0.100	0.100

For the measurements of the milling suspension, the samples are treated with the disintegrator (ultrasonic) as long as no further decrease in the particle size can be observed. The measurements are then repeated at least 3 times in order to ensure reproducibility. In addition, SEM micrographs are taken to verify the particle size distribution measurements.

4.4.2.1 Influence of the Rotation Speed

It is investigated how the rotation speed influences the particle size distribution for milling experiments with the same overall milling duration. Furthermore, the overall milling duration needed to obtain a specific average particle size is investigated for different rotation speeds.

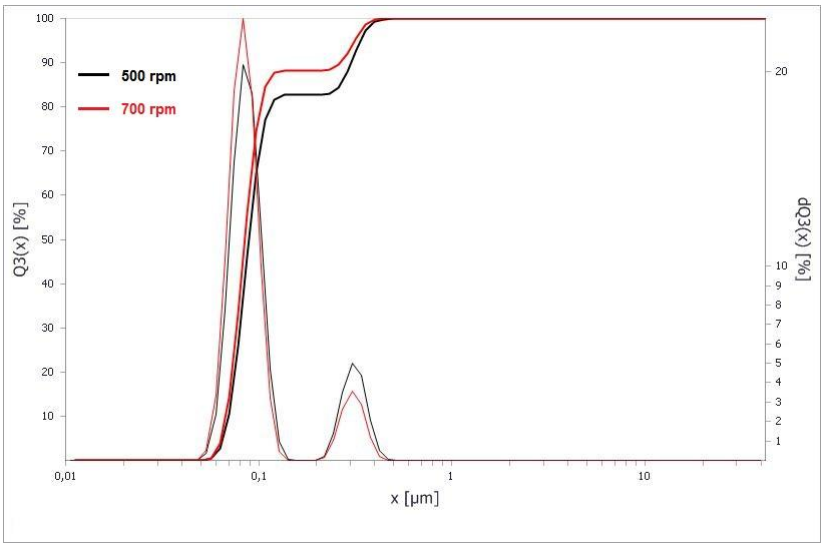

Figure 36. Particle size distribution measurements of Si milled for 2 h with 500 rpm and 700 rpm

Table 14. Particle size distribution and milling values of Si milled for 2 h with 500 rpm and 700 rpm

7.5 g Si, 20 mL 1-Methoxy-2-propanol, 300 g WC-Co grinding balls Ø 0.6 mm						
Rotation speed [rpm]	Overall operation time [h]	Ø Particle size [nm]	D10 [nm]	D50 [nm]	D90 [nm]	(D90 - D10) / D50
500	3	130	70	89	302	2.61
700	11	110	67	85	264	2.32

From Figure 36 and Table 14, it can be seen that for the same milling duration, a higher rotation speed leads to a smaller particles. This can be explained by the higher impact energies of the grinding balls at higher rotation speeds. Noteworthy is that although the difference in the average particle size is < 20 %, the overall operation time (sum of milling duration and necessary cooling times) differs nearly by a factor of 4. This behavior can be particularly seen if one compares the milling duration needed to obtain the same particle size distribution for different rotation speeds.

Table 15. Milling duration and overall operation time needed to obtain the same particle size distribution

7.5 g Si, 20 mL 1-Methoxy-2-propanol, 300 g WC-Co grinding balls Ø 0.6 mm							
Rotation speed [rpm]	Milling duration [min]	Overall operation time [min]	Ø Particle size [nm]	D10 [nm]	D50 [nm]	D90 [nm]	(D90 - D10) / D50
500	90	120	150	71	92	331	2.83
900	40	490	150	71	92	331	2.83

In Table 15 it can be seen the milling duration needed to obtain a certain particle size is significantly lower for higher rotation speeds. However, high rotation speeds require longer cooling times and lead to much longer overall operation times. Hence, high rotation speeds are unfavorable concerning the throughput and are another reason for choosing 500 rpm as standard rotation speed. All further milling experiments are carried out using the standard milling parameters from Table 11.

4.4.2.2 Influence of the Ball-to-Powder Weight Ratio

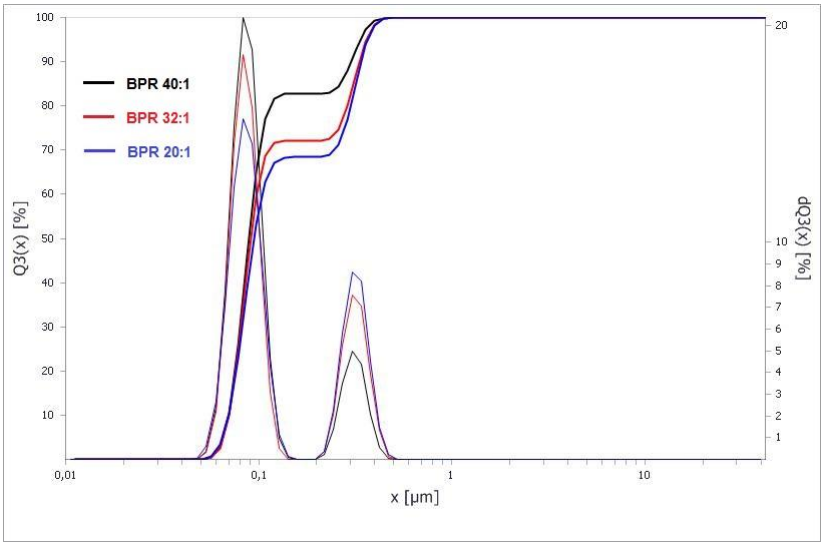

Figure 37. Influence of the BPR on the particle size distribution of 2 h milled Si

Table 16. Particle size distribution and milling values of Si milled for 2 h with different BPR's

500 rpm, 20 mL 1-Methoxy-2-propanol, 300 g WC-Co grinding balls Ø 0.6 mm						
Si [g]	BPR	Ø Particle size [nm]	D10 [nm]	D50 [nm]	D90 [nm]	(D90 - D10) / D50
7.5	40:1	130	70	89	303	2.62
9.5	32:1	150	70	92	334	2.87
15	20:1	165	70	94	341	2.88

From the particle size distributions of Si milled with different BPR's it can be seen that a higher BPR leads to smaller particle sizes and hence reduces the milling duration to obtain a certain particle size distribution.

4.4.2.3 Influence of the Milling Duration

In general, longer milling durations lead to smaller particles. In this context it is investigated how strong the decrease of the particle size depends on the milling duration.

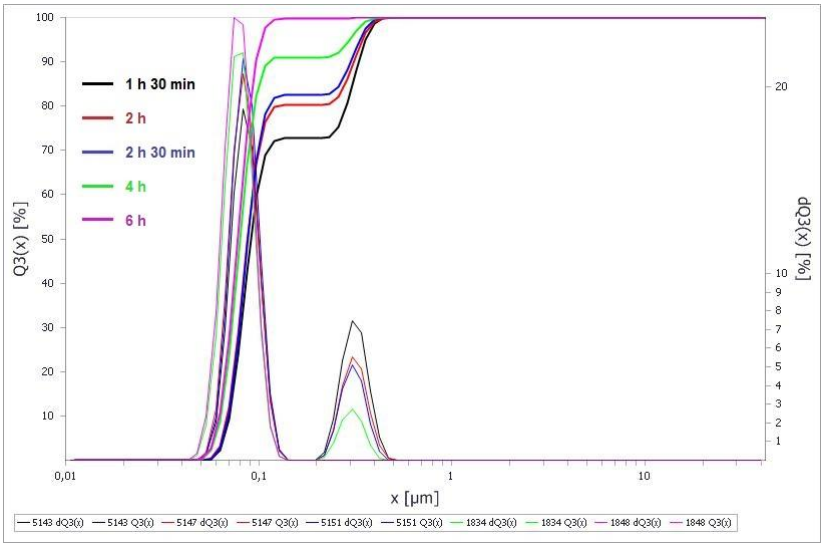

Figure 38. Dependency of particle size distribution and milling duration for Si milled in 1-M-2-p

Table 17. Particle size distributions of Si with different milling durations in 1-M-2-p

7 g Si, 27 mL 1-Methoxy-2-propanol, 300 g WC-Co grinding balls Ø 0.6 mm						
Milling duration [h]	Ø Particle size [nm]	D10 [nm]	D50 [nm]	D90 [nm]	(D90 - D10) / D50	ΔØ/Δt [nm h^{-1}]
1.5	150	71	92	331	2.83	11.6 x 10^{3}
2	135	70	88	311	2.74	30
2.5	125	69	88	300	2.63	20
4	100	64	80	115	0.64	16.7
6	85	63	78	97	0.44	7.5

The particle size distributions shown in Figure 38 and Table 17 show that with increasing milling duration the average particle size and the relative span decrease. After 6 h milling no particles larger than ~ 150 nm can be observed in this milling system. The value ΔØ/Δt displays the decrease of the average particle size within time. It is calculated by dividing the difference of the average particle size of two following milling durations by their corresponding milling duration difference. The value for 1 h 30 min milling is calculated with the difference to the starting material (-325 mesh). These values should show that the

smaller the particles get, the more time it takes to further decrease the size. The influence of the milling duration on the particle size distribution is also determined for a system using EtOH as milling solvent and is shown in Figure 39.

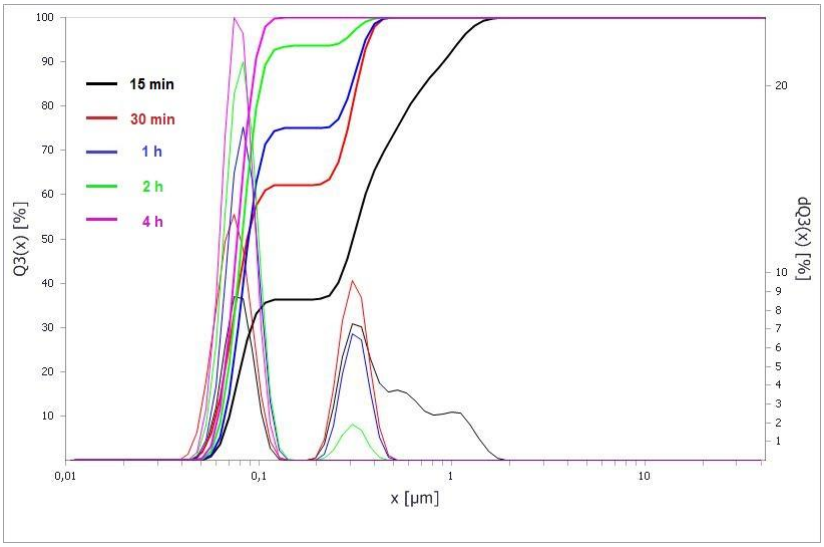

Figure 39. Dependency of particle size distribution and milling duration for Si milled in EtOH

Table 18. Particle size distributions of Si with different milling durations in EtOH

5 g Si, 29 mL EtOH, 300 g WC-Co grinding balls Ø 0.6mm						
Milling duration [h]	Ø Particle size [nm]	D10 [nm]	D50 [nm]	D90 [nm]	(D90 - D10) / D50	ΔØ/Δt [nm h^{-1}]
0.25	380	71	308	902	2.70	68.9 x 10^3
0.5	165	68	91	345	3.04	860
1	140	67	89	329	2.94	50
2	100	64	82	111	0.57	40
4	80	62	78	97	0.45	10

It is remarkably that already after 15 min more than 90 % of the particles are in the nm region and emphasizes that SiNPs can be obtained easily by planetary ball milling. The trend that further particle size reduction requires unproportional longer milling durations can be seen again in Table 18. The higher values for the size reduction rate can be explained by the higher BPR of 60:1 compared to 43:1 for the system shown in Table 17. In Figure 40 the average particle size is plotted vs. the corresponding milling duration for the above shown values.

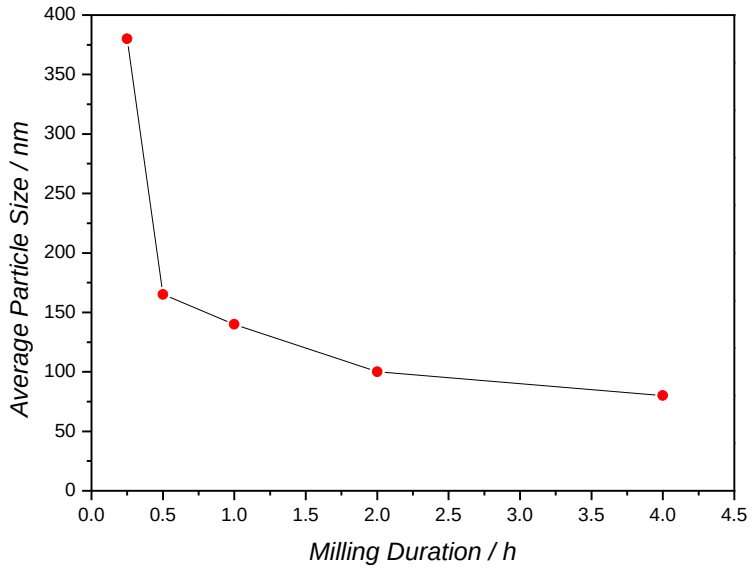

Figure 40. Dependency of average particle size and milling duration of Si in EtOH

4.4.2.4 Influence of the Milling Solvent and Surface Functionalization

During milling Si-Si bonds are homolytically cleaved, the originating Si radicals and dangling bonds are highly reactive towards the milling solvent or oxygen. The mechanochemical reaction leads to surface functionalization and/or oxidation. The influence of the milling solvents on the particle size distribution and the surface of the Si is discussed in this chapter.

A comparison of ATR-FTIR spectra of the starting material, a SiO_2 nanopowder (5-15 nm, Sigma Aldrich) and SiNPs obtained by the pyrolysis of SiH_4 (30-50 nm, Nanostructured & Amorphous Materials, Inc.) is shown in Figure 41. This figure gives a short overview of the peaks that might occur in the spectra of milled Si and are assigned according to available literature and comparisons. It is immediately noticeable that in the spectrum of the starting material not a single peak is visible. This does not imply the absence of oxide moieties, as it is know that Si forms a native oxide layer of 1-2 nm thickness (*37*). However, the low surface to bulk ratio of µm sized particles compared to NPs leads to a significantly lower amount of overall surface oxide and hence the signal might be too weak to be detected by ATR-FTIR. It should be further noted that this measurement technique is mainly used for qualitative characterization. Quantitative characterizations are difficult, as the amount of sample exposed to the IR radiation is impossible to be determined and differs for each measurement. The reason for this is that the IR radiation does not pass through the sample.

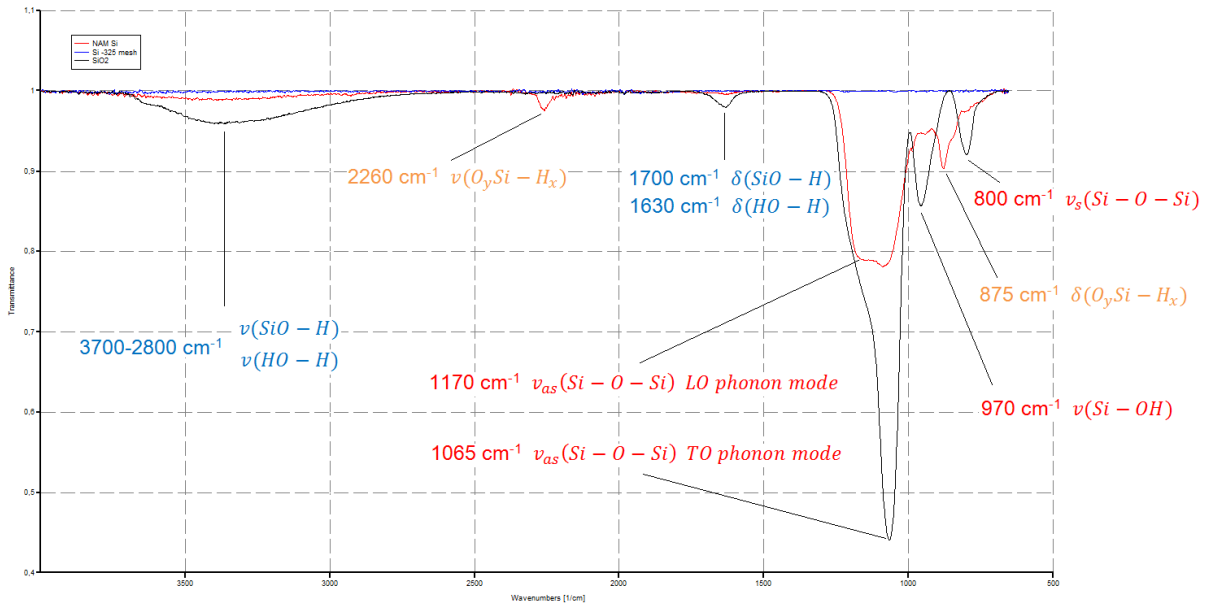

Figure 41. Comparison of ATR-FTIR spectra of Si -325 mesh (blue), NAM Si (red) and SiO_2 (black)

Instead ATR (attenuated total reflection) uses the property of total internal reflection resulting in an evanescent wave. The penetration depth of this wave into the sample is only a few µm. Therefore the amount of sample exposed to the IR radiation depends on the particle size, packing density and the compacting pressure of the stamp used to bring the sample in contact with the ATR crystal. However, changes of a sample can be determined semi-quantitatively, if there are peaks available which do not change upon oxidation or another occurring reaction by the relative transmission of the corresponding peaks.

The spectra of SiO_2 and NAM Si show various peaks for O-H and Si-O stretching (ν) and bending (δ) vibrations. The broad peak in the region above 3000 cm^{-1} can be assigned to O-H stretching vibrations for silanol groups and surface water, whereas the bending vibrations can be found in the region 1700-1600 cm^{-1} (*293*,*294*). The peaks are usually very broad due to hydrogen bonding. The asymmetric Si-O-Si stretching vibration is located in the region 1200-1000 cm^{-1} (*295*). This vibration contains a mode in which adjacent O atoms execute the asymmetric stretching motion in phase with each other (TO phonon mode) and an asymmetrical stretching mode in which the adjacent O atoms execute it out of phase with each other (LO phonon mode) (*296*,*297*). Both modes are visible for each SiO_2 and NAM Si in different ratios at 1170 cm^{-1} and 1065 cm^{-1}. The peak at 970 cm^{-1} is attributed to the Si-O stretching vibration of the silanol group (*298*). A Si-O-Si vibration occurs at 800 cm^{-1}, however there is a discrepancy in the literature whether it is the symmetric stretching vibration (*295*,*298*) or a bending vibration (*297*,*299*). The peaks at 2260 cm^{-1} and 875 cm^{-1}

correspond to the stretching (*300*,*301*) and bending (*296*,*302*) vibration of Si-H bonds of an oxidized Si surface and can only be found in the spectrum of NAM Si. This can be explained by residual Si-H bonds present at the surface after the thermal decomposition of SiH_4. The presence of these peaks is noteworthy as it implies that Si-Si bonds oxidize easier than the Si-H bonds.

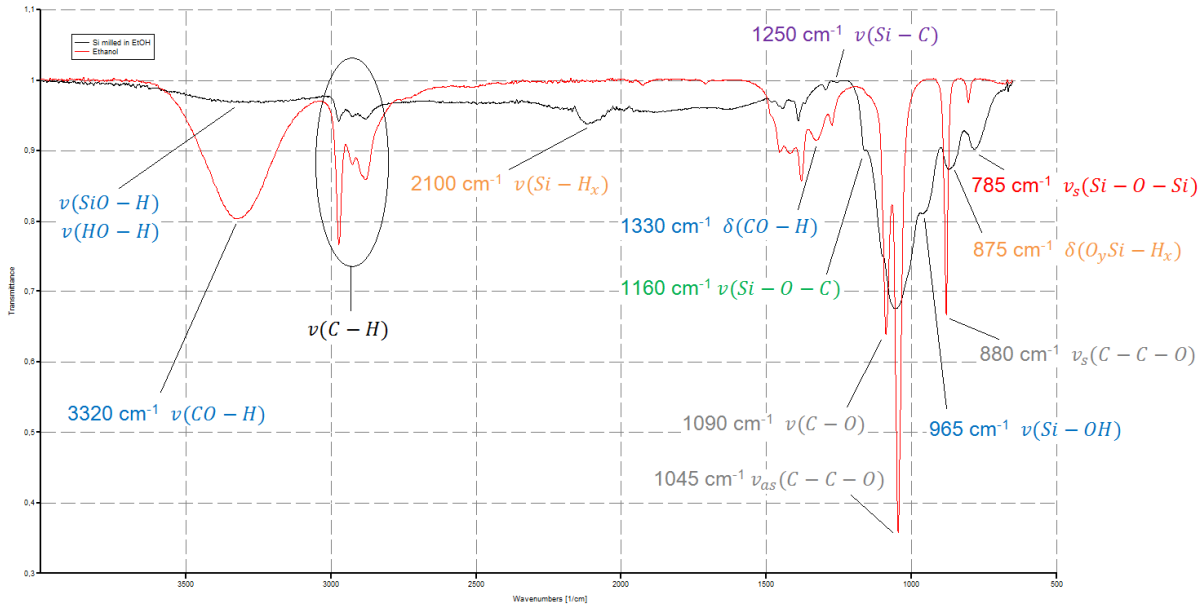

Figure 42. Comparison of the ATR-FTIR spectra of EtOH (red) and Si milled in EtOH (black)

Figure 42 shows the functionalization of Si by milling in ethanol. The peaks in the spectrum of ethanol are assigned according to reference (*303*). It is remarkable that the broad band of the O-H stretching vibration in the region 3700-3000 cm^{-1} has a significantly lower intensity than the adjacent C-H stretching vibration for the milled Si compared to ethanol. This can be explained by the reaction of the ethanol with the Si radicals and dangling bonds upon milling, which leads to the formation of Si-H bonds with the acidic proton and the formation of Si-O-C bonds with the ethoxy-moiety. Further evidence for this reaction is the appearance of the peak at 2100 cm^{-1}, which is attributed to Si-H stretching vibrations (*304*,*305*), as ethanol is the only H source available in the milling system. The reaction of the acidic proton is further confirmed by lack of the O-H bending vibration at 1330 cm^{-1} for the milled Si and the appearance of a peak at 1160 cm^{-1}, which is characteristic for SiOEt groups (*306*). In addition the stretching vibrations of the silanol group (965 cm^{-1}) and the Si-O bond (785 cm^{-1}) indicate that a different reaction occurs too, which includes the cleavage of the C-O bond of the alcohol and the oxidation of the silicon surface. There is also an indication of the ethyl radical

reacting with the Si surface, as a small peak appears at 1250 cm^{-1}, which has been reported to be a Si-C stretching vibration (*94*,*307*). This peak has been reported to be very small, but for Si-Et peaks in the region the regions 1020-1000 cm^{-1}, 975-965 cm^{-1} and around 770 cm^{-1} should be visible too (*306*,*307*). However, these peaks are overlapped not only by Si-O vibrations (1200-1000 cm^{-1}, 965 cm^{-1} and 785 cm^{-1}) but also by various Si-O-C (1200-1000 cm^{-1}) (*308*,*309*) and C-O vibrations (1200-1000 cm^{-1}) (*310*,*311*). Hence, a distinction of these different vibrations is impossible. The $O_ySi\text{-}H_x$ vibration at 875 cm^{-1} is probably overlapped with a C-C-O vibration of the ethoxy-moiety. The stretching vibration of $O_ySi\text{-}H_x$ around 2260 cm^{-1} is difficult to distinguish from the background as the signal is very weak and broad. The same applies for the SiO-H and HO-H bending vibrations in the region 1700-1630 cm^{-1}.

The functionalization of the Si surface is further proven by EDX measurements, especially if one takes a look at the values for different milling times as shown in Table 19.

Table 19. EDX measurements of Si with different milling durations in EtOH

5 g Si, 29 mL EtOH, 300 g WC-Co grinding balls Ø 0.6 mm				
Milling duration [h]	C [wt%]	O [wt%]	Si [wt%]	W [wt%]
0.25	12	5	82	<1
0.5	13	6	79	2
1	14	7	77	2
2	15	9	72	4
4	18	15	61	6

It is apparent that with longer milling durations the C and O contents increase and the Si content decreases due to the surface functionalization. The stronger increase for O might be caused by oxidation of the surface, as the samples are not handled under inert atmosphere during EDX sample preparation. The increase of W content upon longer milling durations is caused by abrasion of the grinding balls and bowls during milling.

The functionalization of Si by milling in 1-methoxy-2-propanol is shown in Figure 43. The lack of the stretching and bending vibrations of the CO-H bond at 3410 cm^{-1} and 1330 cm^{-1} can also be clearly seen for this milled Si. In this case, also the Si-H stretching vibration of the oxidized surface is visible at 2250 cm^{-1} and its bending vibration at 875 cm^{-1} is not overlapped by a C-O vibration. Further the peak maximum in the region 1200-1000 cm^{-1} is not directly overlapped by a C-O vibration, as it is the case for ethanol. The stretching vibration of Si-OH cannot be seen as it is overlapped by C-O vibrations.

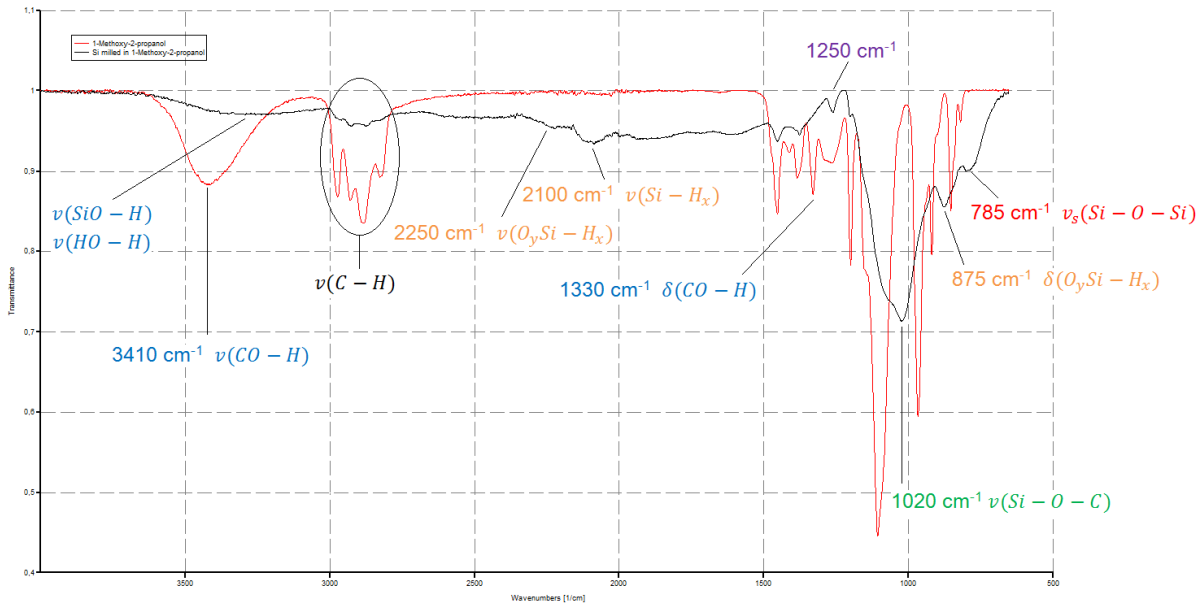

Figure 43. Comparison of the ATR-FTIR spectra of 1-M-2-p (red) and Si milled in 1-M-2-p (black)

A peak at 1250 cm^{-1} can also be seen for the Si milled in 1-methoxy-2-propanol, however, it might not be a Si-C vibration, as a peak at this position is also visible for the alcohol.

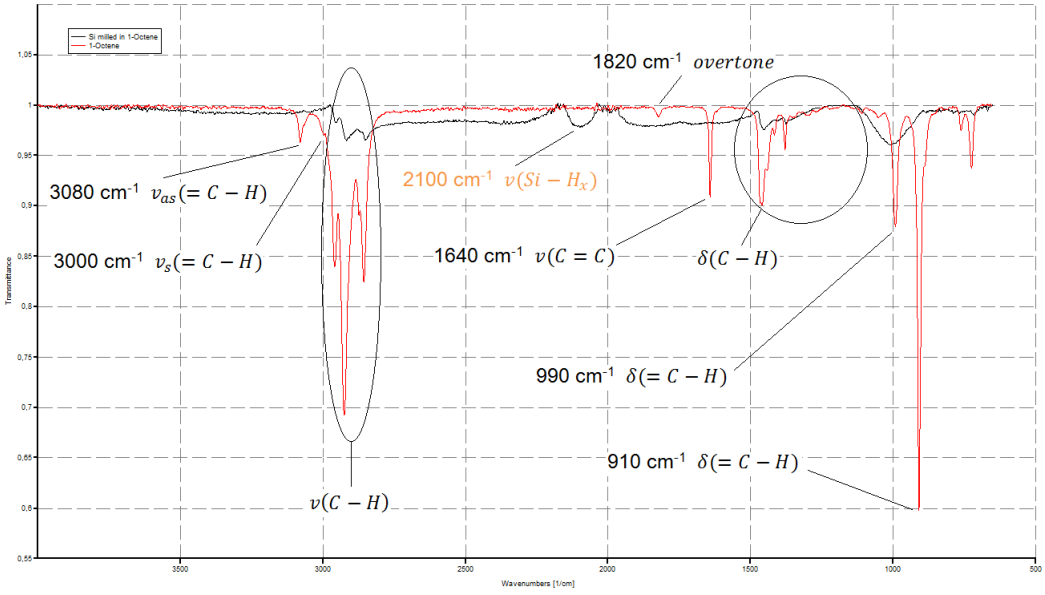

Figure 44. Comparison of the ATR-FTIR spectra of 1-octene (red) and Si milled in 1-octene (black)

Figure 44 shows the functionalization of Si by milling in 1-octene. The peaks in the spectrum of 1-octene are assigned according to reference (*312*). It is striking that for the Si milled in 1-octene stretching vibrations of C-H bonds are visible in the region 2950-2800 cm^{-1} and the bending vibration of double bond C-H at 990 cm^{-1} and 910 cm^{-1} are not, which proves functionalization. Further the C=C stretching vibration is not visible in the spectra of the functionalized Si. Interestingly, the Si-H stretching vibration at 2100 cm^{-1} is also visible. This leads to the conclusion that the fresh Si surface produced during ball milling is not only reactive enough to break O-H and C-O bonds but also C-H bonds. The peak around 1000 cm^{-1} is attributed to Si-O-Si vibrations. The signal is very small compared to Si milled in alcohols as 1-octene does not contain O-atoms and it is not overlapped by C-O or Si-O-C vibrations. The presence of the signal can be explained by the presence of a native oxide layer on the starting material and possible oxidation during sample preparation.

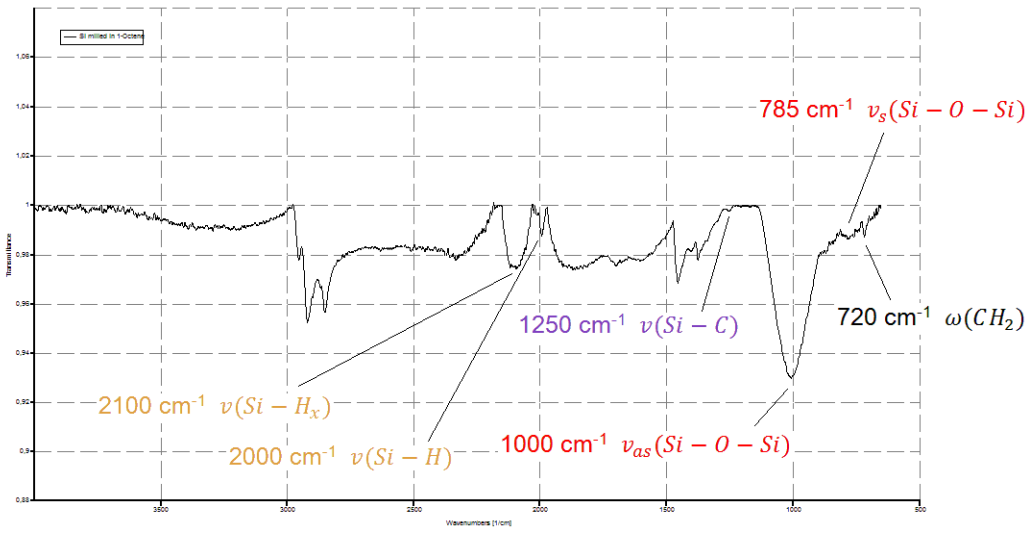

Figure 45. ATR-FTIR spectrum of Si milled in 1-octene (zoomed in)

In this case, the small peak at 1250 cm^{-1} can just correspond to the Si-C stretching vibration. This is confirmed by the presence of the CH_2 wagging vibration at 720 cm^{-1}, which is typical for Si surfaces functionalized with alkyl groups (*93*,*94*). There is a very interesting vibration present at 2000 cm^{-1}, as it is assigned to monohydrogenated *a*-Si-H bond (*313*). This peak is also present in spectra of Si milled in alcohols, however, the signal is usually smaller and it is difficult to distinguish from the background. The amorphous Si originates from the ball impacts during milling which produce nm crystallites with amorphous boundaries (*314*).

A comparison of the particle size distribution measurements for Si milled in 1-methoxy-2-propanol and Si milled in 1-octene is shown in Figure 46. By this figure it is clearly shown that the used milling solvent has a prodigious influence not only on the surface functionalization but also on the particle size distribution.

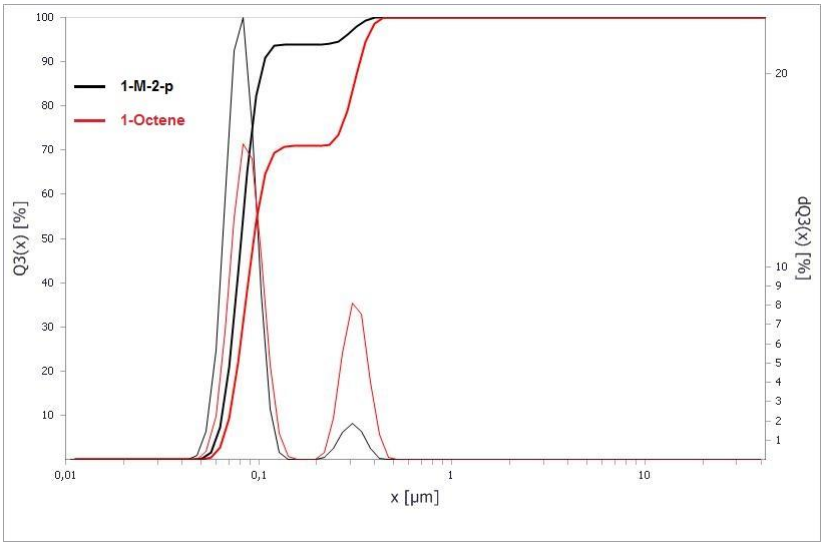

Figure 46. Particle size distribution measurements of Si milled for 3 h in 1-M-2-p and 1-octene

Table 20. Particle size distribution and EDX values of Si milled for 3 h in 1-M-2-p and 1-octene

5 g Si, 27 mL milling solvent, 300 g WC-Co grinding balls Ø 0.6 mm									
Milling solvent	Ø Particle size [nm]	D10 [nm]	D50 [nm]	D90 [nm]	(D90 - D10) / D50	C [wt%]	O [wt%]	Si [wt%]	W [wt%]
1-M-2-p	95	65	82	107	0.51	27	15	53	5
1-Octene	155	71	95	335	2.78	18	4	77	<1

It is remarkable how much larger the particles are for Si milled in 1-octene compared to 1-methoxy-2-propanol. A possible explanation for this behavior might be the stronger oxidation of the Si surface by milling in 1-methoxy-2-propanol, which could facilitate crack formation induced by grinding ball impacts, especially at the crystallite boundaries. In addition, also the larger wear of the grinding balls and bowls for the 1-methoxy-2-propanol system might contribute to this behavior too, as the abraded WC particles are much smaller than the grinding balls. However, this effect would be possibly low as the amount of wear is infinitesimal compared to the grinding balls. The corresponding SEM micrographs of Si milled in the two different solvents are shown in Figure 47. The figure shows clearly that the particles are smaller for Si milled in 1-methoxy-2-propanol than those milled in 1-octene.

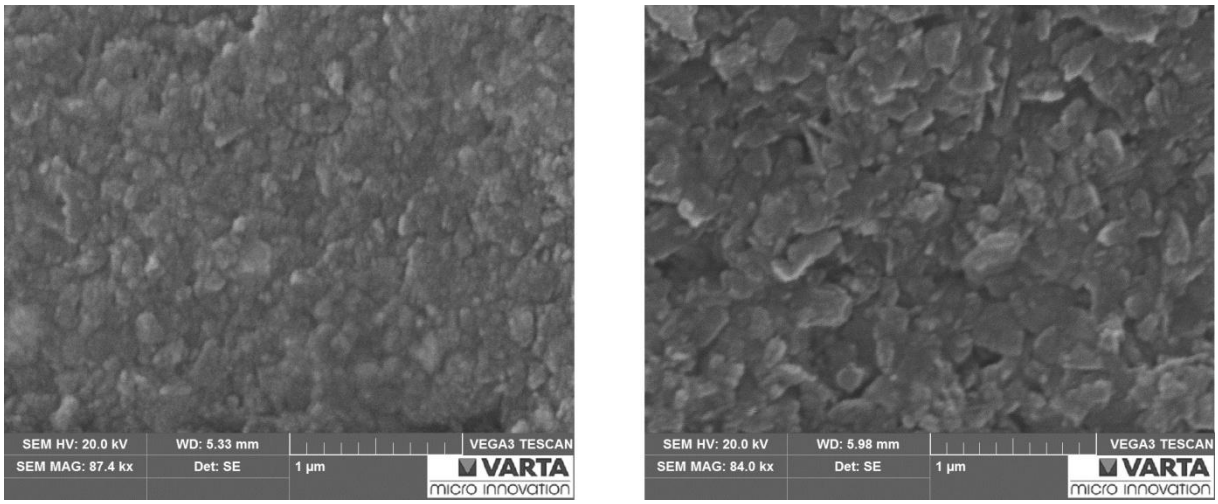

Figure 47. SEM micrographs of Si milled for 3 h in 1-M-2-p (left) and 1-octene (right)

SEM micrographs are of particular importance for Si milled in 1-octene, *n*-heptane and benzene, as particle size measurements are performed in deionized water. The hydrophobic surface of the SiNPs obtained with these solvents hinders dispersing immensely, even if large amounts of surfactant are used. Hence, particle size measurements are not possible for most of these samples.

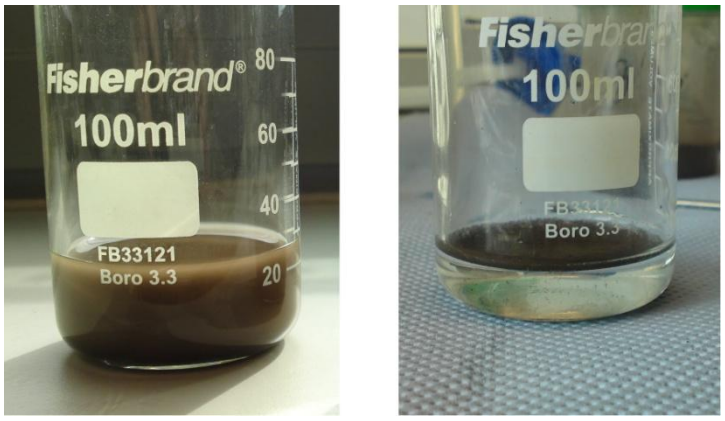

Figure 48. Dispersing behavior of Si milled in 1-M-2-p (left) and 1-octene (right) in deionized water

Figure 48 shows the different dispersing behavior depending on the surface functionalization. Si milled in an alcohol is much easier to disperse due to the partially oxidized surface including silanol groups. Further, the alkoxy-moieties are polar too and the Si-OC bonds tend to hydrolyse within time, resulting in even more Si-OH groups.

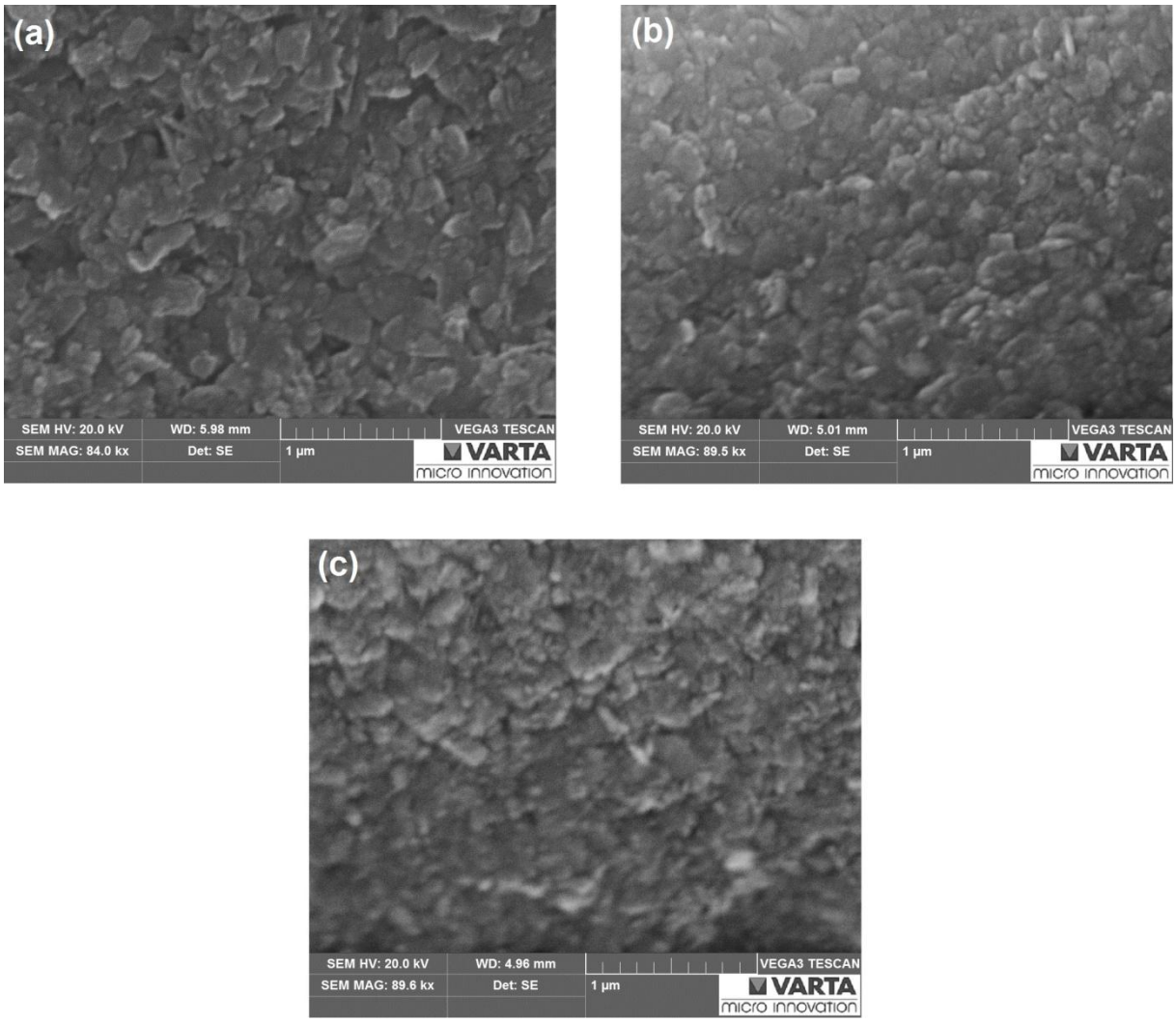

Figure 49. SEM micrographs of Si milled in 1-octene for 3 h (a), 6 h (b) and 12 h (c)

Figure 49 shows that with longer milling durations the particles can be further reduced for 1-octene and results after 12 h in a comparable SEM micrograph as the one for 1-methoxy-2-propanol shown in Figure 48. Table 21 shows that with longer milling durations in 1-octene the C content of the SiNPs increases due to the larger surface functionalized.

Table 21. EDX measurements of Si with different milling durations in 1-octene

5 g Si, 27 mL 1-Octene, 300 g WC-Co grinding balls Ø 0.6 mm				
Milling duration [h]	C [wt%]	O [wt%]	Si [wt%]	W [wt%]
3	18	4	77	<1
6	20	5	73	2
12	23	5	70	2

The O content remains stable upon prolonged milling, which indicates that the grinding bowls are sealed airtight. This fits very well to the circumstance of a slightly overpressure present in the bowls after milling in 1-octene. A low overpressure is also observed for milling in benzene and *n*-heptane and is contrary to the high overpressure for Si milled in alcohols.

Table 22. EDX measurements of Si milled for 4 h in EtOH, 1-M-2-p, *n*-heptane and benzene

5 g Si, 27 mL milling solvent, 300 g WC-Co grinding balls Ø 0.6 mm				
Milling solvent	C [wt%]	O [wt%]	Si [wt%]	W [wt%]
EtOH	18	15	61	6
1-M-2-p	25	17	53	5
n-Heptane	15	5	79	<1
Benzene	36	7	56	<1

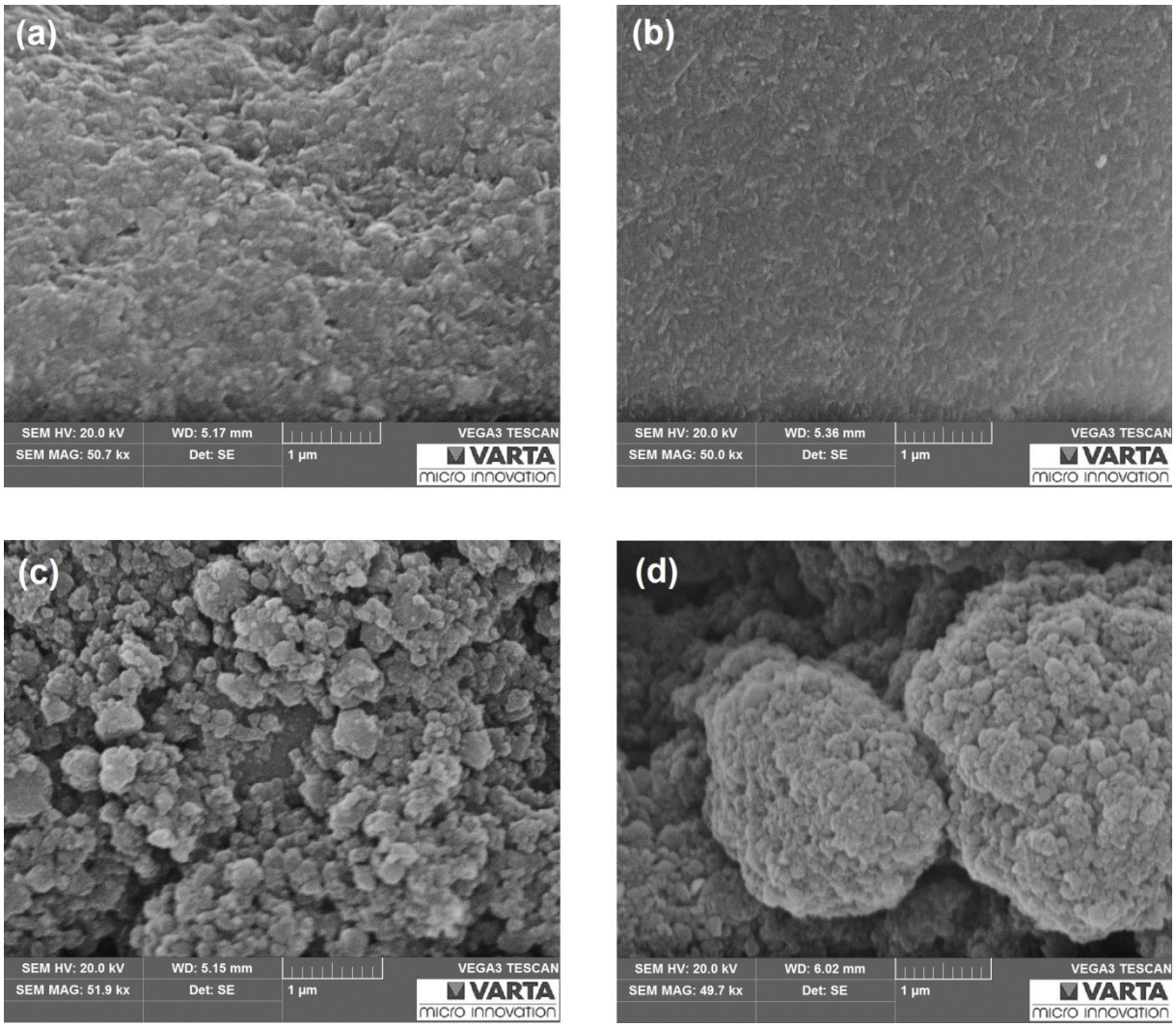

Figure 50. SEM micrographs of Si milled for 4 h in EtOH (a), 1-M-2-p (b), *n*-heptane (c) and benzene (d)

O and W values of Si milled in 1-octene are comparable to Si milled in *n*-heptane and benzene. The slightly higher O content for benzene shown in Table 22 might be caused by water traces present. Interestingly, the Si milled in benzene shows high C values, which leads to the conclusion that it is highly reactive towards the Si radicals. The particle sizes obtained by milling in these solvents are again significantly larger than those obtained from ethanol or 1-methoxy-2-propanol, as shown in Figure 50.

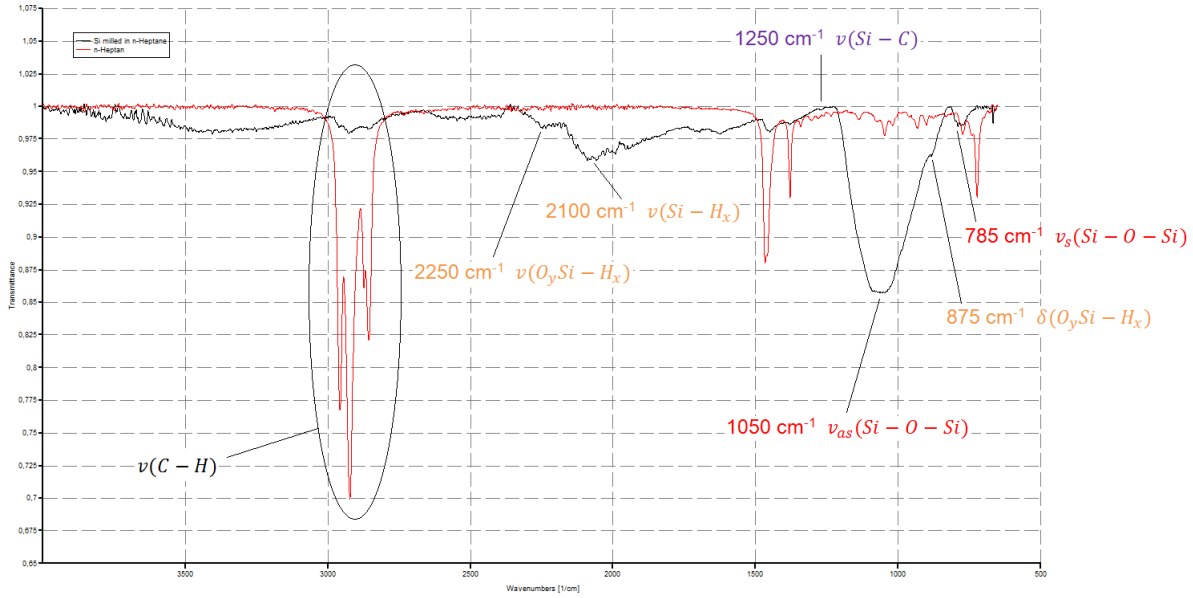

Figure 51. Comparison of the ATR-FTIR spectra of *n*-heptane (red) and Si milled in *n*-heptane (black)

As seen in Figure 51, Si milled in *n*-heptane gets significantly less functionalized than in 1-octene, which is attributed to the weak C-H stretching vibrations compared to the Si-H and Si-O-Si vibrations. This can be explained by the lack of functional groups which preferentially react with the Si radicals and dangling bonds, such as alcohol groups or double bonds, and the high dissociation energies of C-H bonds in linear alkanes due to low radical stability.

This is in contrast to Si milled in benzene (Figure 52), as the conjugated double bonds in the ring are able to stabilize radicals and hence lead to much higher reactivity towards the radicals present at the freshly produced Si surface during milling. The vibrations in the spectra of benzene and the milled Si are assigned according to references (*315*,*316*). The functionalization of Si by milling in benzene can be seen by the disappearance of the aromatic C-H vibration at 665 cm^{-1} and the appearance of vibrations at 735 cm^{-1} and 700 cm^{-1}. These two peaks are characteristic for a monosubstituted benzene derivative and can be attributed to phenyl-groups attached to the Si surface.

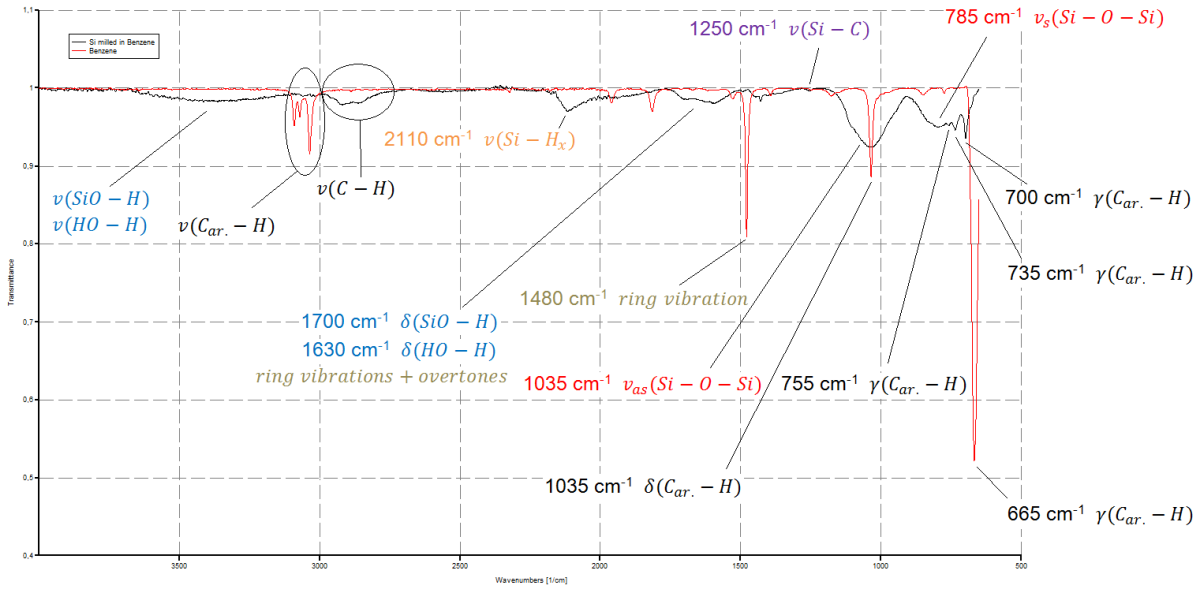

Figure 52. Comparison of the ATR-FTIR spectra of benzene (red) and Si milled in benzene (black)

The vibration at 755 cm^{-1} is attributed to an *ortho*-disubstituted benzene derivative, which leads to the conclusion that a further reaction occurs, where two directly adjacent Si radicals (dangling bond) react with benzene during milling. The Si-C vibration is visible again at 1250 cm^{-1} and shifts to 1265 cm^{-1}, if the Si surface oxidizes (Figure 53).

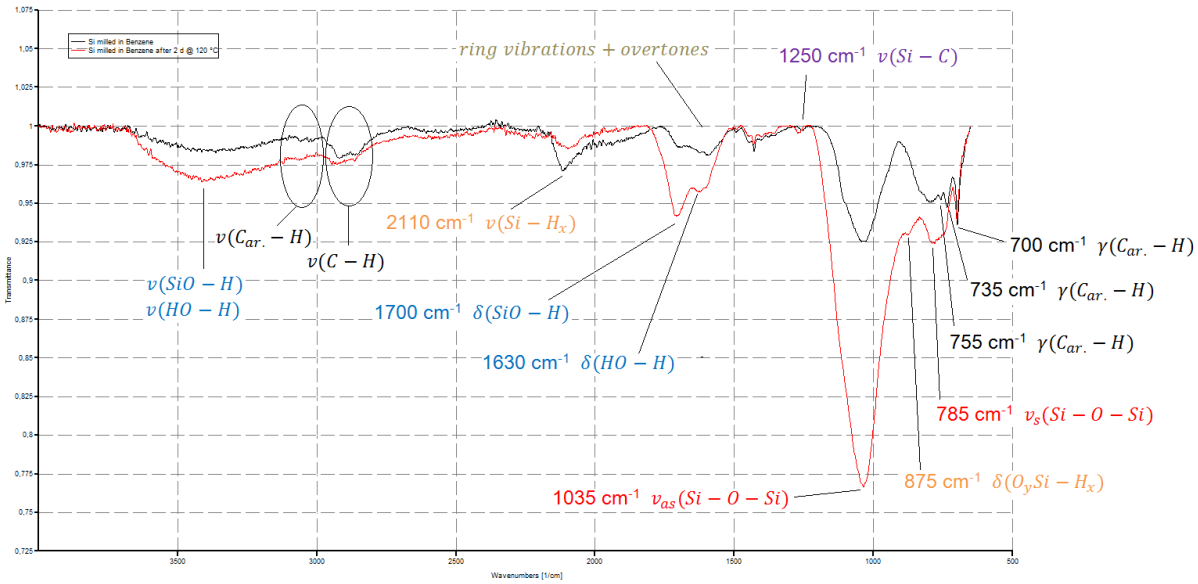

Figure 53. Comparison of the ATR-FTIR spectra of Si milled in benzene and after 2 d at 120 °C (air)

Further, the Si-H stretching vibration decrease and silanol as well as surface water vibrations increase after storage of the sample in a compartment dryer for 2 days at 120 °C. In addition, the Si-O-Si vibrations increase and the Si-H vibration of the oxidized surface is visible at 875 cm^{-1}. The presence of aliphatic C-H vibrations in the region 2970-2850 cm^{-1}, however, is unclear. Their origin might be impurities of the milling solvent or grinding materials or due to a radical induced reaction of benzene with present water traces.

4.4.3 Influence of the Milling Conditions on the Electrochemical Performance

Si/C composites consisting of a mixture of SiNPs, graphite, binder and conductive additive are used for the electrochemical measurements. The solvent of the milling suspension is removed under reduced pressure and elevated temperature. The solid residue is grounded with a mortar to obtain a fine powder consisting of SiNPs. After dissolving the binder and the addition of the surfactant, the SiNP powder is added and ultrasonic is applied to deagglomerate and finely disperse the SiNPs. Then, conductive additive and graphite are added and the electrode preparation procedure continues as described in chapter 4.3. The general electrode composition is shown in Table 23.

Table 23. General electrode composition for Si/C composites

	Components	Composition [wt%]
Binder	Sodium carboxymethyl cellulose (NaCMC)	8
1. Active material	Milled Si	20
2. Active material	Qingdao graphite	62
Conductive additive	CNERGY™ Super C65	10
Deionized water as solvent and 1 drop of SOPROPHOR® FLK		

The active materials of the composite have an overall theoretical specific capacity of ~ 1154 mAh g^{-1} according to Eq. 14:

$$\frac{20}{82} \cdot 3579\ mAh\ g^{-1} + \frac{62}{82} \cdot 372\ mAh\ g^{-1} = 1154\ mAh\ g^{-1}$$

Eq. 14

Higher specific capacities are not useful, as they do not increase the overall cell capacity in full cell applications due to the low specific capacities of currently available positive electrode materials, as shown in Figure 54. Furthermore, a higher Si content would lead to more rapid capacity decay due to the lower cycle stability compared to graphite.

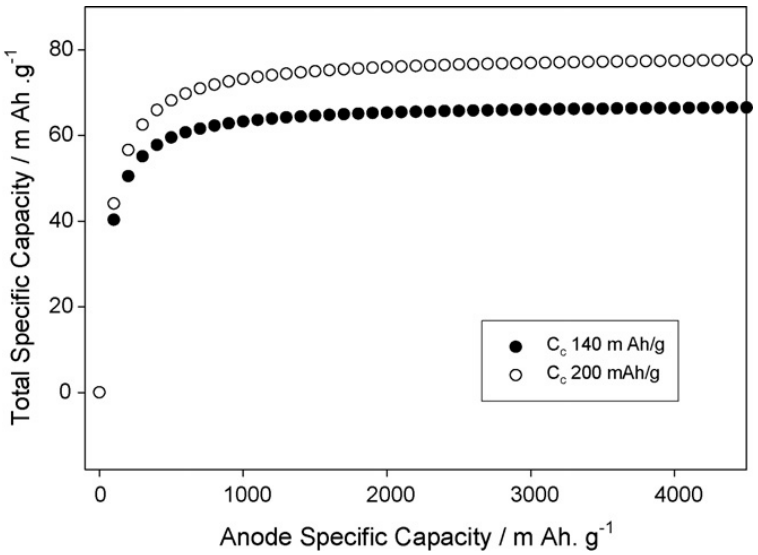

Figure 54. Total cell capacity as a function of the anode capacity. Capacities of the cathodes considered are 140 mAh g^{-1} and 200 mAh g^{-1} (*249*)

The influence of the average particle size and the milling solvent on the electrochemical performance is now discussed on the following pages.

Comparisons of the lithiation and delithiation capacities obtained by the CCC measurements from Si/C composites are shown in Figure 55 and Figure 56 and comprise the starting material and the composites with Si milled in 1-methoxy-2-propanol to different average particle sizes. If one compares the lithiation capacities of the first cycle, it is obvious that they are higher for the milled Si approaches than the capacity of the starting material and even higher than the theoretical capacity. This can be explained by the larger surface of the milled Si, which leads to more SEI formation and reduction of Si oxides (see also Table 24). On the other hand, smaller particles have shorter diffusion pathways and hence increased lithiation/delithiation rates, which in turn increases the feasibility of complete lithiation/delithiation within a certain time. The poor cycling behavior of the starting material can be explained by the µm sized Si particles, which crack and loose electrical contact easily due to the large volume changes.

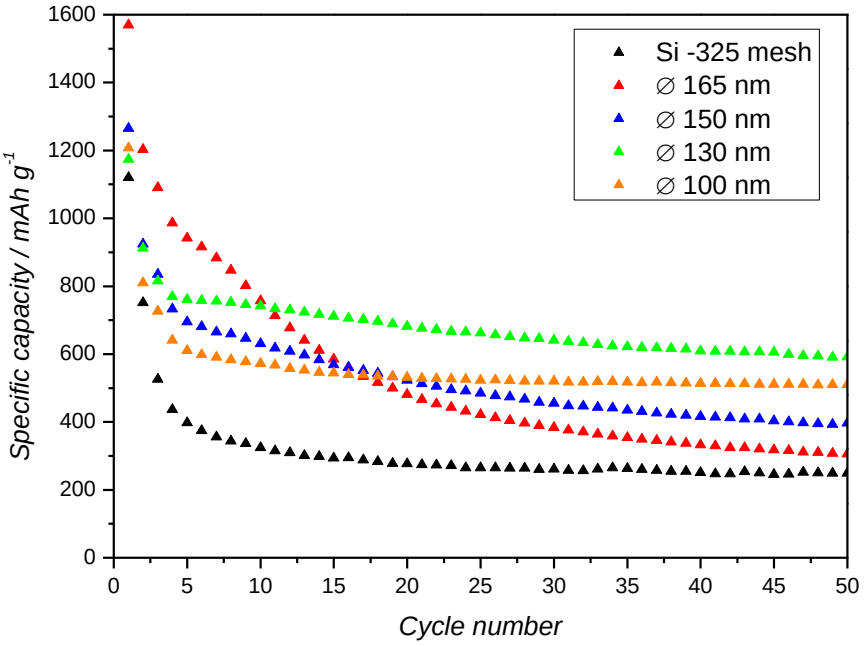

Figure 55. Lithiation capacities of Si/C composites with the starting material and Si milled to different average particle sizes in 1-M-2-p

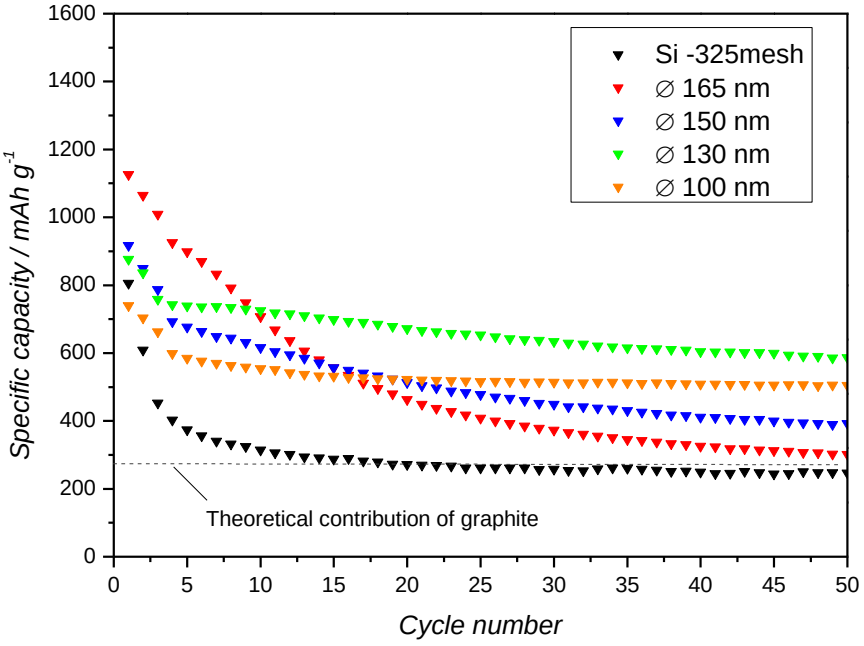

Figure 56. Delithiation capacities of Si/C composites with the starting material and Si milled to different average particle sizes in 1-M-2-p

Table 24. First cycle coulomb efficiencies corresponding to Figure 55 and Figure 56

Cycle	Si -325 mesh [%]	Ø 165 nm [%]	Ø 150 nm [%]	Ø 130 nm [%]	Ø 100 nm [%]
1.	71.94	80.62	74.69	72.55	61.32

The cycling behavior gets significantly better at smaller particle sizes, however, associated with it the capacity decreases due to the larger quantities of surface functionalization and oxide present. Further, the coulomb efficiencies decrease too, which implies more Li immobilization due to SEI formation and will be critical in full cells. The low coulomb efficiency for the starting material cannot only be explained by SEI formation, as the surface is very small, but also with the loss of electrical contact of active material parts in the very first cycle. Particle size experiments of SiNP powders revealed that it is difficult to deagglomerate them completely with ultrasonic and hence, agglomerates are present. The same applies for the electrode preparation and can be seen in elemental distribution maps of EDX measurements.

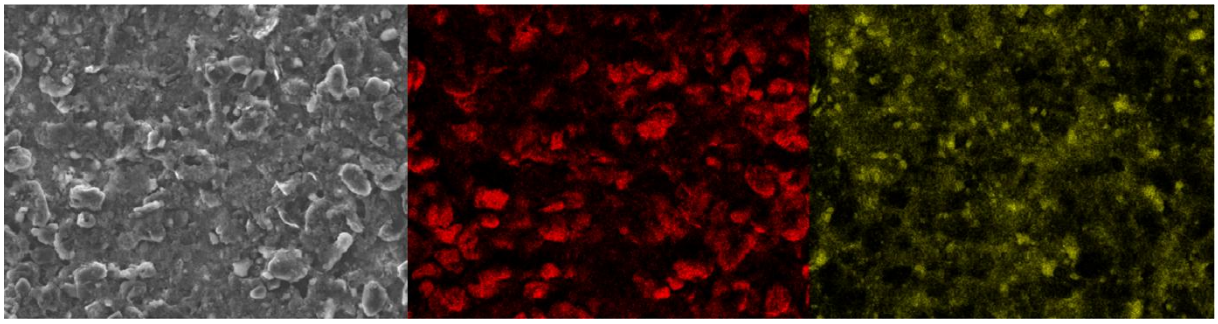

Figure 57. SEM micrograph (left), elemental distribution of C (middle) and Si (right) of a Si/C composite electrode produced with Ø 130 nm Si

The Si distribution in Figure 57 clearly shows the presence of some agglomerates among the finely dispersed particles. These agglomerates behave likewise larger Si particles and are responsible for the rapid capacity decay in the first 3-4 cycles. The agglomerates are a result of the close packing density of milled SiNPs if the solvent is removed, which enhances Si-O-Si bond formation between the particles, and can be larger than the starting material particles. Therefore, the milled material needs to be processed as soon as possible. The bond formation is caused by the condensation tendency of present silanol groups and those produced by the hydrolysis of silyl ether groups. The Si-O-Si bonds then prevent deagglomeration as they are stable enough to withstand the applied ultrasonic disintegration during slurry preparation.

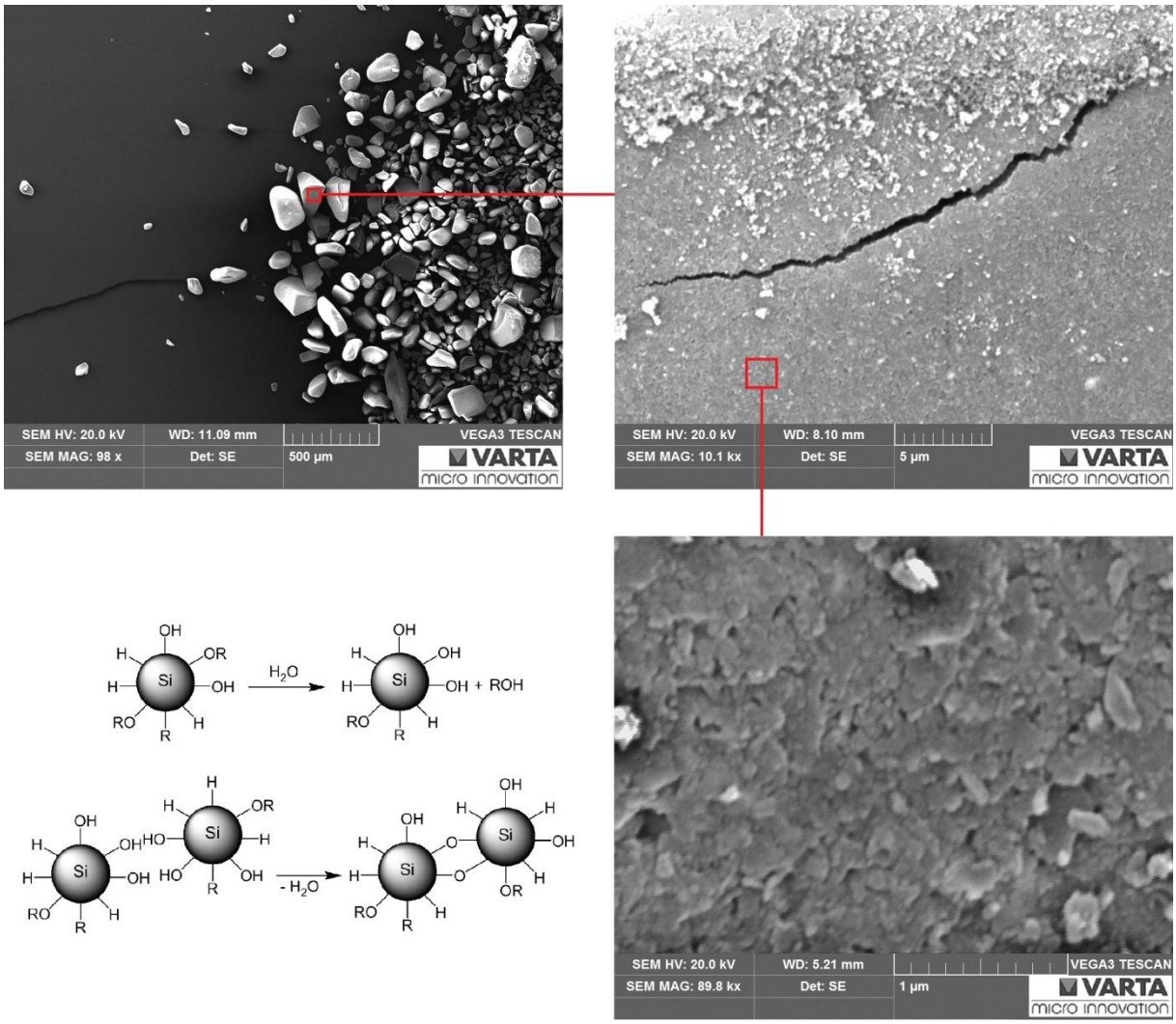

Figure 58. SEM micrograph of a SiNP agglomerate at different magnifications and scheme of the silyl ether hydrolysis as well as Si-O-Si bond formation

Figure 58 shows the residue after deagglomeration of a SiNP powder. The close packing density of the SiNPs can be clearly seen and their proximity simplifies Si-O-Si bond formation according to the scheme shown in the Figure. The problem of agglomerate formation coupled with Si-O-Si inter-particle-bonding is even worse for Si samples milled in EtOH, as shown in Figure 59 and Figure 60. The reason for this behavior is probably the easier hydrolysis of the ethoxy groups compared to 1-methoxy-2-propoxy moieties, which results in faster condensation reactions between the particles. The agglomerates cause not only rapid capacity decay in the first cycles, but also reduce the initial capacity. The lower capacity is attributed to core SiNPs of the agglomerates, which are not or only insufficient electrochemically connected. Hence, these particles are electrochemical dead weight. The CV demonstrates that capacity decrease is caused by Si, as the two broad peaks between 0.25-0.6 V decrease and the delithiation of the graphite remains unaffected (0.08-0.25 V).

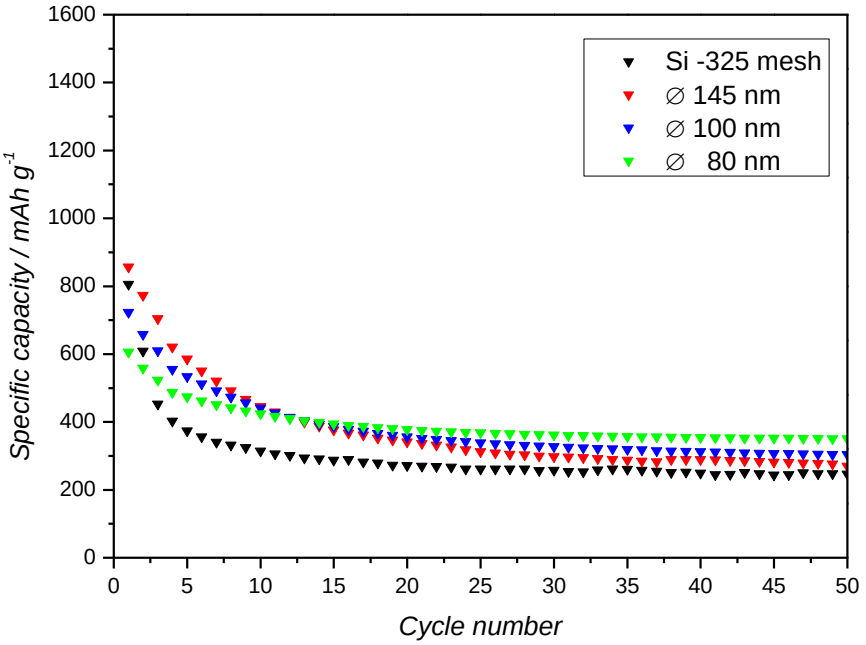

Figure 59. Delithiation capacities of Si/C composites with the starting material and Si milled to different average particle sizes in EtOH

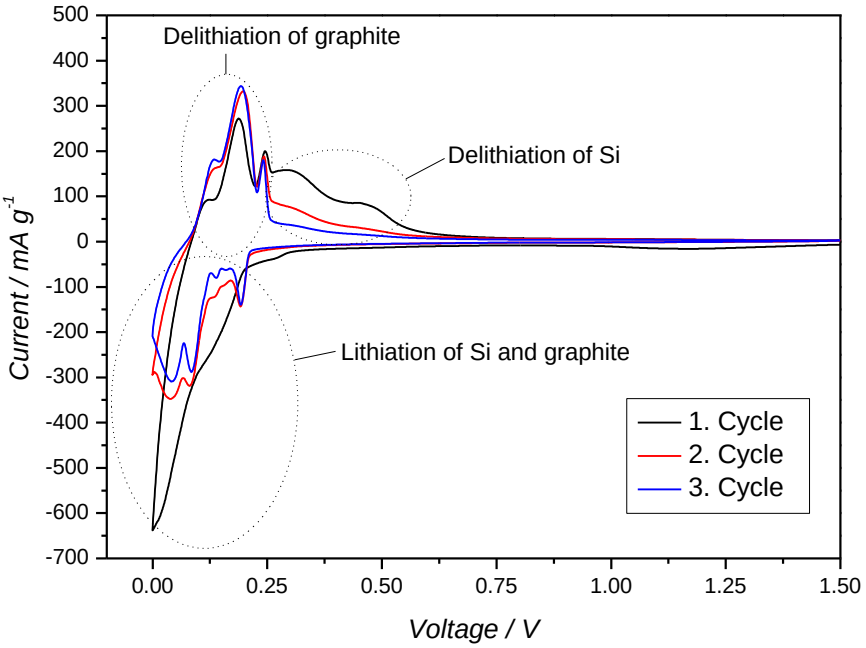

Figure 60. CV of a Si/C composite with Si milled in EtOH to an average particle size of 100 nm

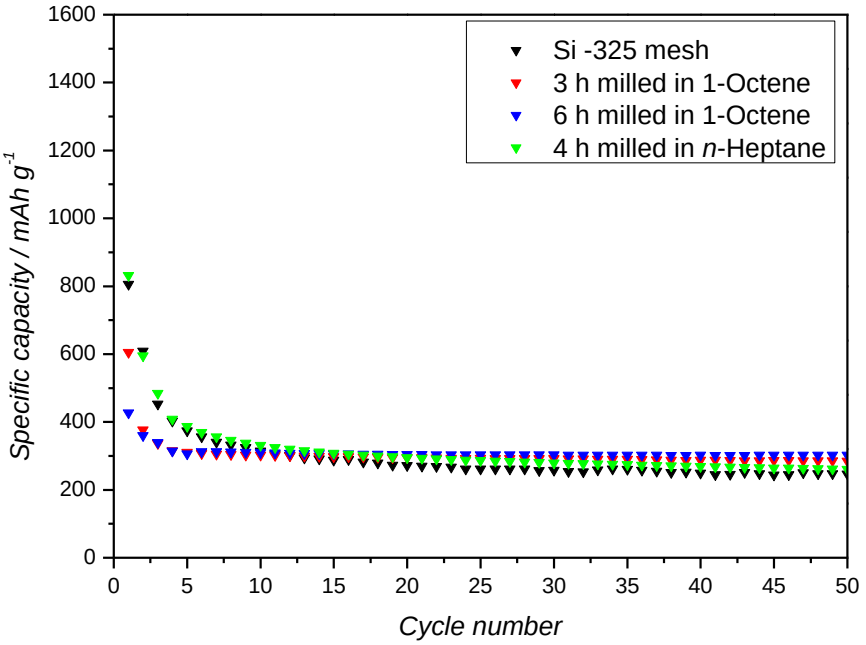

Figure 61. Delithiation capacities of Si/C composites with the starting material and Si milled in different solvents

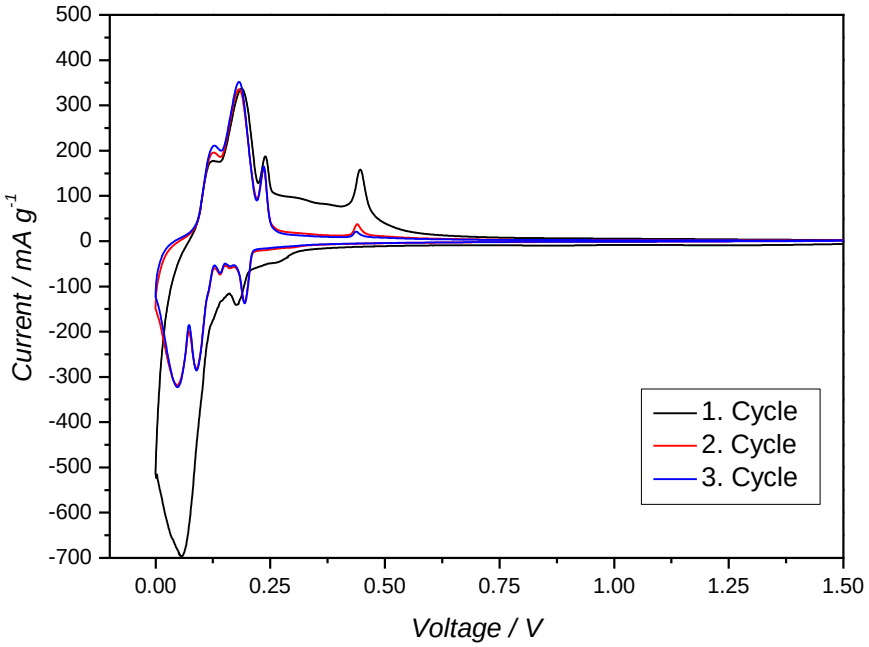

Figure 62. CV of a Si/C composite with Si milled for 3 h in 1-octene

The first cycles in Figure 61 show that Si milled in 1-octene and *n*-heptane is electrochemically active too. However, the performance is equal to the µm sized starting material or even worse. This behavior can be attributed to the hydrophobic surface functionalization which leads to a strong formation of agglomerates during slurry preparation and it might also impede the lithiation/delithiation process. The slightly better cycling performance of Si milled in *n*-heptane, might be a result of its lower reactivity accompanied by less surface functionalization. Figure 62 shows that most of the capacity contributed by the Si milled in 1-octene is lost after the first cycle. In comparison with the CCC measurement it can be said that after 4-5 cycles only graphite contributes to the residual capacity. It has also been tried to prepare Si/C composite electrodes with Si milled in benzene. However, it is impossible as the sample is too hydrophobic and produces foam during slurry preparation. Even the addition of more surfactant and a reduction of the stirring rate cannot prevent foam formation. In order to avoid this, Si milled in benzene is heated up to 900 °C under inert atmosphere to pyrolyze the surface functionalization and to obtain C-coated SiNPs and avoid SiC formation. These particles should then be dispersable in the aqueous electrode slurry. The result is that the sample turned into hard chunks through the heat treatment, which could not be disintegrated anymore. Hence, a deagglomeration is impossible after the pyrolysis and so the electrode preparation.

To conclude, it is necessary to produce more complex Si/C composites, where the milling suspension can be used directly for synthesis to provide a better understanding of the electrochemical performance of milled Si. This step is inevitable, as once the solvent is removed SiNP agglomerates are formed which cannot be redispersed. These agglomerates then impair the electrochemical performance of the residual dispersed SiNPs. The use of the milling suspension offers the advantage that the solvent stabilizes the dispersion and prevents massive agglomeration, as well as oxidation.

A recently developed core-shell Si/C composite allows the use of the milling suspension as Si source during synthesis. The core-shell composite was developed by Scharfegger M., Kren H. and Koller S. at the VARTA Micro Innovation GmbH and uses commercial SiNPs synthesized by SiH_4 pyrolysis (*317*). The following chapters deal with the applicability of milled Si in this composite and its optimization in consideration of the Si particle size, preparation, electrode composition and cycling conditions.

4.5 Core-Shell Structured Si/C Composite

4.5.1 Introduction

The production of the core-shell structured Si/C composite is based on a batch coating process of graphite particles with a slurry containing milling suspension, conductive additive, epoxy resin and an amine based curing agent. The coating process is carried out in a fluidized bed reactor (Mini Glatt, Glatt®) via bottom-spray-coating using a Wurster insert (*Wurster process*). A scheme of this process and the used reactor are shown in Figure 63.

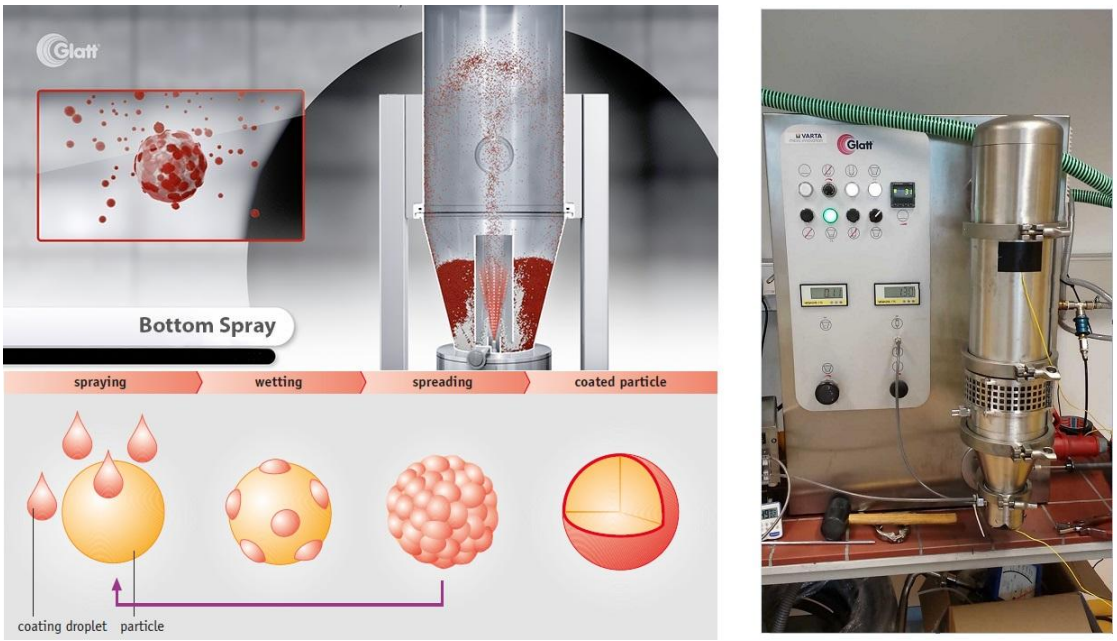

Figure 63. Scheme of the Wurster process (left) (*318*,*319*) and a photograph of the used reactor (right)

The graphite particles are fluidized in the reactor by a preheated compressed air stream inflowing from the bottom of the reactor. A filter plate at the gas inlet and filter rods at the gas outlet guarantee a constant process air flow without loss of particles. During operation the graphite particles in the fluid bed pass the bottom spraying nozzle in an ordered flow pattern. While quickly moving upwards within the Wurster compartment (tube) they can be wetted with the slurry without agglomeration. While moving downwards outside the Wurster compartment, the solvent evaporates, the epoxy resin cures and another layer of coating can be supplied. The short residence time in the coating zone and the multiple coating cycles ensure a very uniform coating of the particles (*319*).

4.5.2 Synthesis

The general procedure for the synthesis of the core-shell structured Si/C composite is described in detail in the following subchapters. The material usually consists of 20 wt% cured epoxy resin and 80 wt% graphite, Si and conductive additive. If not otherwise stated, the composition and raw material quantities shown in Table 25 are used for the synthesis.

Table 25. General composition and raw material quantities of the core-shell structured Si/C composite

	Components	Composition [wt%]	Quantities [g]
Epoxy resin	Araldite® 506	16	9.6
Curing agent	3-(Dimethylamino)-1-propylamine	4	2.4
Si	Milled Si	16	9.6
Conductive additive	CNERGY™ Super C65	8	4.8
Graphite	Qingdao	56	33.6

4.5.2.1 Slurry Preparation

Initially the Si concentration of the milling suspension has to be determined. Therefore, 3 weighted crystallizing dishes are filled with ~ 3 g of the milling suspension and the exact weight of the suspension is noted. The solvent is removed and the averaged concentration is calculated. The concentration is necessary to calculate the quantity of milling suspension necessary for the subsequent process. Then the epoxy resin is dissolved in 100 g 1-methoxy-2-propanol via magnetic stirring. The milling suspension is treated with ultrasonic for 5 min and cooled in the meanwhile to prevent overheating. After disintegrating, the suspension is added to the dissolved epoxy resin and stirred further for 5 minutes. In the meanwhile the required amounts of conductive additive are weight and added to the slurry. The slurry stirs for about 2 h and then small amounts of 1-methoxy-2-propanol are added till the ideal viscosity is reached (about 200 g solvent for 60 g composite material). The beaker is covered with aluminum foil and the slurry stirs over night. The next day, the curing agent is added to the slurry and stiring is continued for about 3 h until the coating process is started.

4.5.2.2 Bottom-Spray-Coating of the Graphite

Before the curing agent is added to the slurry the fluidized bed reactor is assembled and the graphite is added. After addition of curing agent to the slurry the reactor is started and the graphite is fluidized for 3 h. This time is necessary for heating-up and to reach a stable fluidized bed, further the time is needed to pre-cure the epoxy resin. After 3 h the slurry is pumped in the reactor for the coating process and is stirred meanwhile until complete addition. The process parameters are displayed in Table 26.

Table 26. Wurster process parameters for the synthesis of the core-shell structured Si/C composite

Process compressed air [bar]	Spray compressed air [bar]	Pump speed [mL/min]	Setting temperature [°C]
0.11	1.30	10	100

For process control the temperature is measured and recorded with an EXTECH SDL 200 4-Channel Datalogging Thermometer at the following positions: after the heating element, outside the entrance of the gas stream into the coating zone, inside the reactor next to the Wurster compartment and outside the filter housing of the filter rods.

Table 27. Typical temperatures measured at the different reactor parts

	After heating element	Outside process air entrance	Wurster compartment	Outside filter housing
Temperature [°C]	95	60	50	40

The temperature drop along the reactor is caused by heat dissipation, as the reactor is not thermally insulated. During the coating process the temperature inside the reactor drops about 10 °C due to the evaporation of the solvent, but recovers quickly after complete addition of the slurry as the curing is an exothermic reaction. After the completion of the coating process the composite material is fluidized for 1 h to remove residual solvent and to cure the epoxy resin further. Then the reactor is switched off and allowed to cool to room temperature. The reactor is disassembled and the coated graphite particles can be withdrawn.

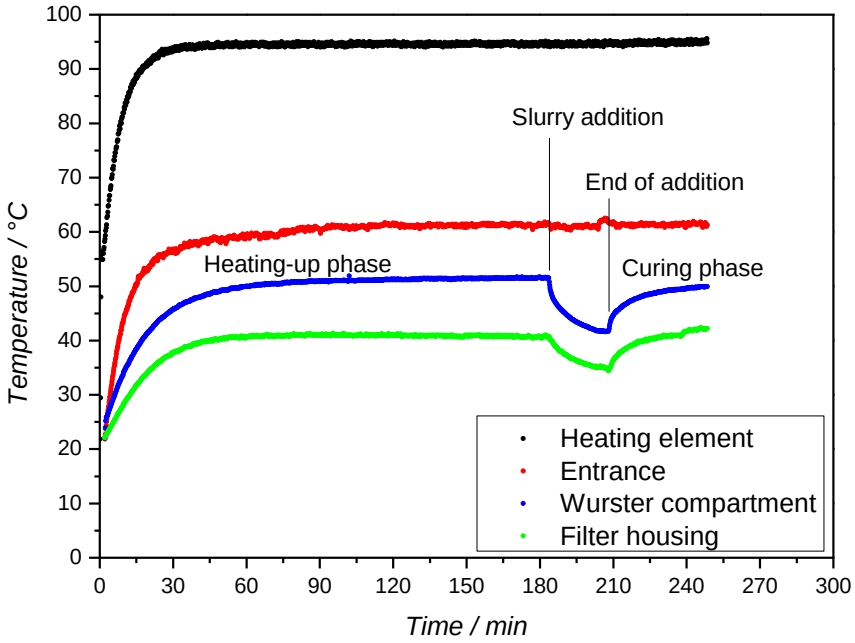

Figure 64. Conventional temperature curves of the process control

4.5.2.3 Pyrolysis of the Epoxy Matrix

After the Wurster process the weighted sample is put in an Al_2O_3 boat and placed in the oven (RHTC 80-230/15, NABERTHERM). The oven is then sealed and evacuated. If a pressure of 8 mbar is reached the oven is carefully vented with Ar 5.0 and the procedure is repeated altogether 3 times. An Ar flow of ~ 0.25 L/h is adjusted and the pyrolysis started.

Table 28. Standard oven parameters of pyrolysis

Heating rate	Target temperature	Dwell time
10 °C/min	900 °C	2 h

The pyrolysis of the core-shell structured Si/C composite material is necessary to obtain a conductive matrix as the epoxy matrix is electrochemically insulating (*320*). After the pyrolysis the sample is weight again to determine the weight loss caused by the pyrolysis of the epoxy matrix and the resulting composite composition is calculated. The composition is

used to calculate the theoretical specific capacity and the C-rate of the composite. The weight loss is typically around 13 % and is associated to the decomposition of the epoxy matrix. The resulting composite composition is shown in Table 29.

Table 29. Composition of the composite material after pyrolysis

Components	Composition [wt%]
Cured epoxy resin residue	8
Si	18.4
Conductive additive	9.2
Graphite	64.4

The corresponding specific capacity for the composite material after pyrolysis is ~ 898 mAh g^{-1} (Eq. 15); or ~ 1085 mAh g^{-1} (Eq. 16) if one considers only Si and graphite as the active material.

$$0.184 \cdot 3579\ mAh\ g^{-1} + 0.644 \cdot 372\ mAh\ g^{-1} = 898\ mAh\ g^{-1}$$

Eq. 15

$$\frac{18.4}{82.8} \cdot 3579\ mAh\ g^{-1} + \frac{64.4}{82.8} \cdot 372\ mAh\ g^{-1} = 1085\ mAh\ g^{-1}$$

Eq. 16

4.5.2.4 Electrode Preparation and Composition of the Composite

The electrode preparation is conducted as described in Chapter 4.3. The electrode composition differs from the composites used in Chapter 4.4.3 and is displayed in Table 30.

Table 30. Electrode composition for core-shell structured Si/C composite materials

	Components	Composition [wt%]
Binder	Sodium carboxymethyl cellulose (NaCMC)	8
Active material	Core-shell Si/C composite	80
Conductive additive	CNERGY™ Super C65	12
Deionized water as solvent and 1 drop of SOPROPHOR® FLK		

4.5.3 Applicability of Milled Si in Core-Shell Structured Si/C Composites

The applicability of milled Si is examined with respect to the synthesis of the core-shell structured Si/C composite and its electrochemistry.

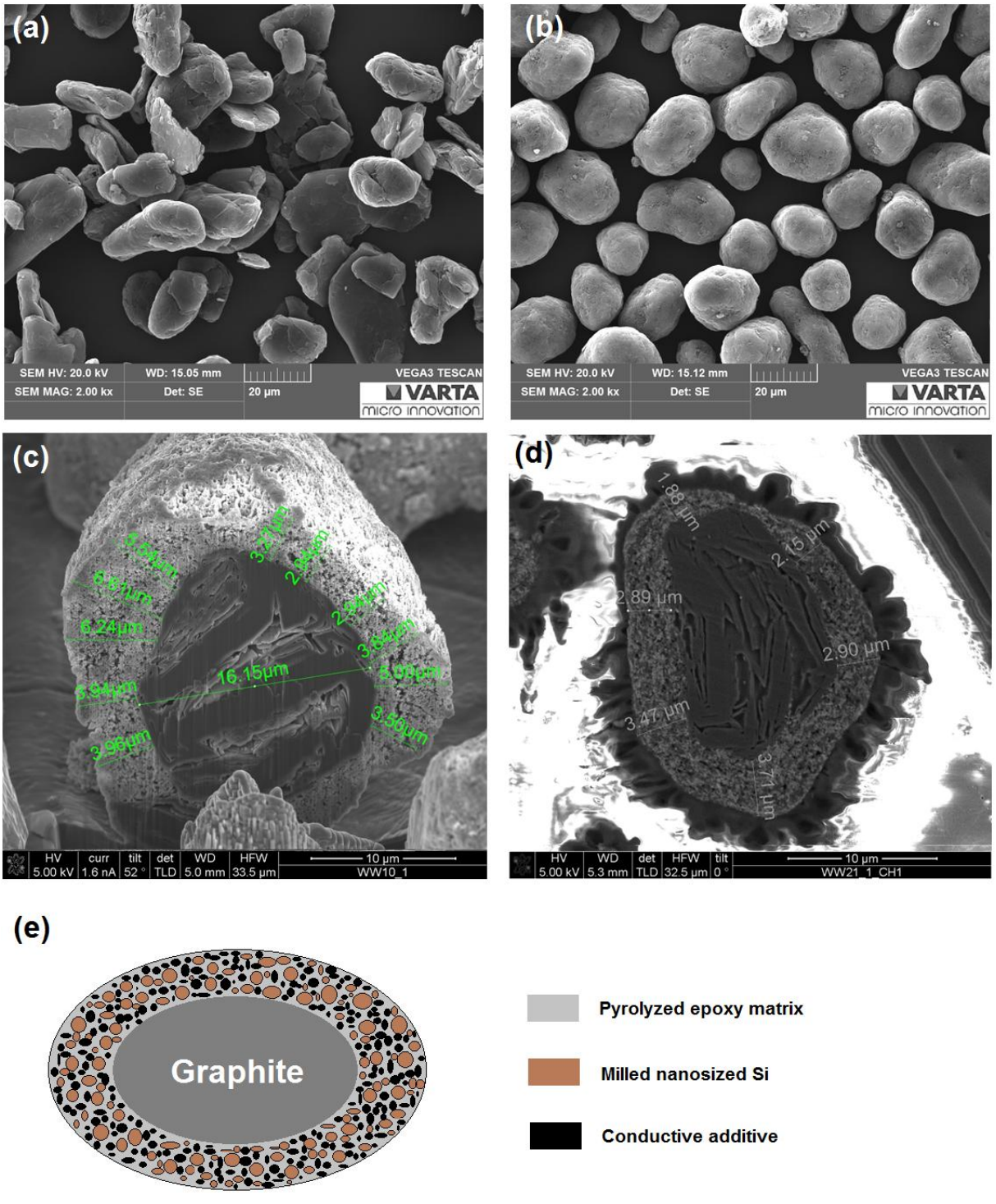

Figure 65. SEM micrograph of Qingdao graphite before (a) and after coating with a slurry containing milled Si (b); FIB cut (c) and BIB slope cut (d) of a composite with commercial Si; scheme of the composite with milled Si (e)

The resulting core-shell particles in Figure 65 indicate that the milling suspension can be used as Si source for the Wurster process without any problems. The graphite particles are well coated without or minimal agglomerate formation. The coating process even works better for milled Si as the particles are already well dispersed in comparison to the Si powder used from commercial sources, which sometimes lead to plugging of the spraying nozzle due to powder aggregates. Furthermore, the cuts shown in the figure confirm the feasibility of a uniform coating by the Wurster process.

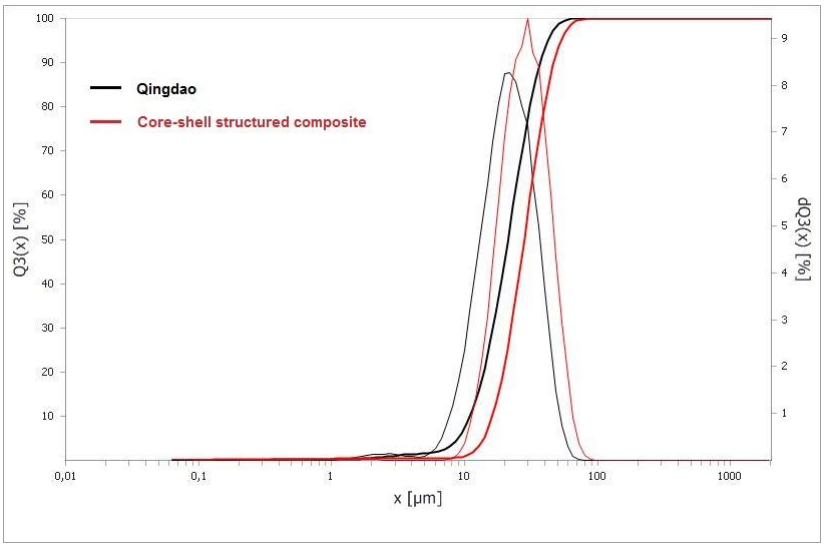

Figure 66. Particle size distribution measurements of Qingdao graphite before and after bottom-spray-coating

Table 31. Particle size distribution values of Qingdao graphite before and after bottom-spray-coating

Material	Ø Particle size [µm]	D10 [µm]	D50 [µm]	D90 [µm]	(D90 - D10) / D50
Qingdao	23	11	21	37	1.24
Composite	30	16	28	47	1.11

The average particle size of the standard core-shell structured composite is typically in the region between 28-32 µm. The size increase caused by the coating fits perfectly with the coating thickness determined from the cuts of a composite produced with commercial SiNPs, shown in Figure 65. Another effect of the coating process is that the relative span of the particle size distribution is slightly smaller after the coating. This effect is caused by the aggregate formation of the smallest graphite particles during coating.

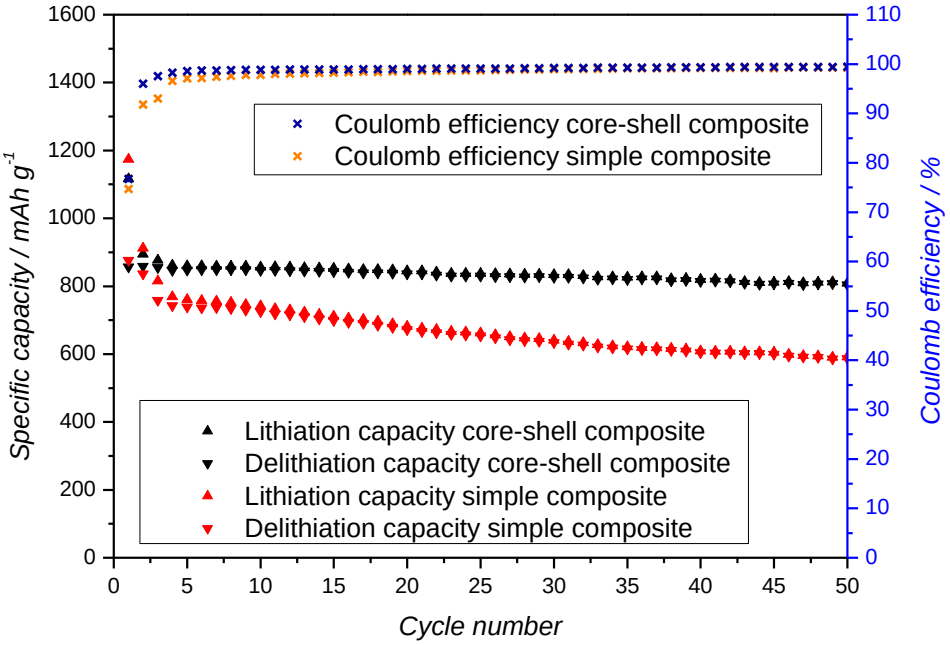

Figure 67. Comparison of the cyclizations of a simple composite and the core-shell structured composite produced with milled Si Ø 130 nm (1-M-2-p)

Table 32. CE comparison of different cycles for the simple composite and the core-shell structure one

Cycle	CE for simple composite [%]	CE for core-shell structured composite [%]	ΔCE [%]
1.	74.69	76.75	2.06
2.	91.80	96.02	4.22
3.	93.00	97.55	4.55
4.	96.60	98.27	1.67
5.	97.12	98.58	1.46
25.	98.72	99.09	0.37
50.	99.29	99.46	0.17

Figure 67 shows the applicability and the superior electrochemical performance of the core-shell structured composite compared to a simple physical mixture produced with the same milled Si (Ø 130 nm). For a better comparison the specific capacity is calculated considering only Si and graphite as the active materials. The features of this composite are the use of the milling suspension during preparation, which prevents SiNP agglomerate formation, and the embedding of the Si in a carbonaceous matrix, which minimizes the loss of electrical contact of the SiNPs. This behavior cannot only be seen in the stable capacity

retention upon cycling but also in the coulomb efficiency (CE), which is significantly better for the core-shell composite.

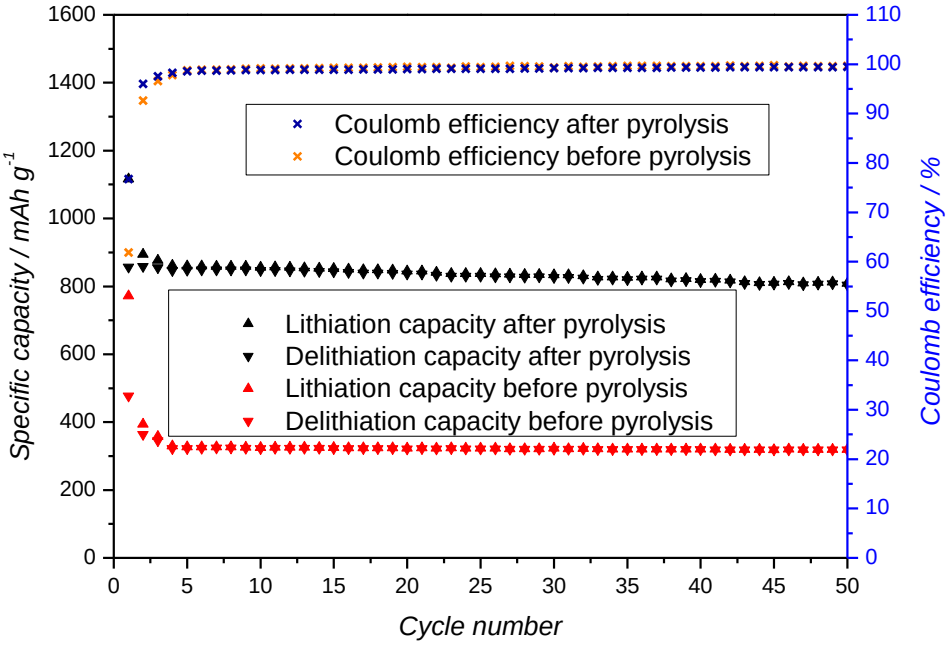

Figure 68. Comparison of the cyclizations of a core-shell structured composite produced with milled Si Ø 130 nm (1-M-2-p) before and after pyrolysis

The comparison of the cyclizations for the composite before and after pyrolysis clearly shows the insulating character of the epoxy matrix. However, not all Si particles in the non-pyrolyzed material are electrochemically insulated, discernible by the delithiation capacity of the first cycle. These particles are possibly located at the surface of the coating or in pores which can soak up electrolyte and are electrically connected by the conductive additive. The loss of electrochemical activity in the first cycles for these particles is presumably caused by the volume expansions and contractions, which facilitate the loss of connectivity to the conductive additive in the insulating epoxy matrix. The residual capacity arises from the graphite core, which can be seen in the CV shown in Figure 69. Its activity is caused by pores or cracks in the coating of the non-pyrolyzed composite.

Another advantage of this composite material is that it can be also produced with Si milled in solvents other than alcohols as shown in Figure 70. The stronger capacity decay of the Si milled in 1-octene is attributed to the larger particle sizes generally obtained by milling in this solvent (see chapter 4.4.2.4).

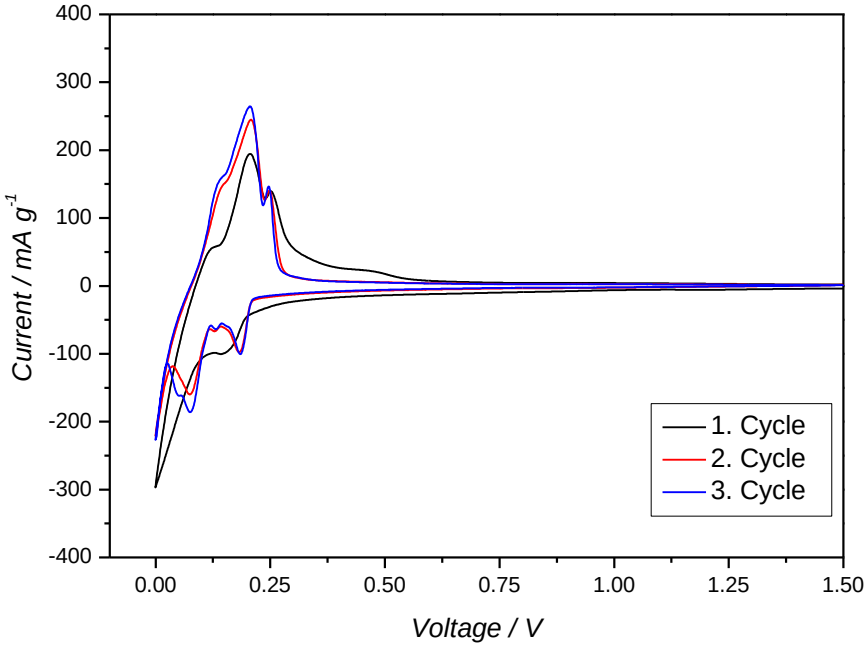

Figure 69. CV of a core-shell structured composite produced with milled Si Ø 130 nm (1-M-2-p) before pyrolysis

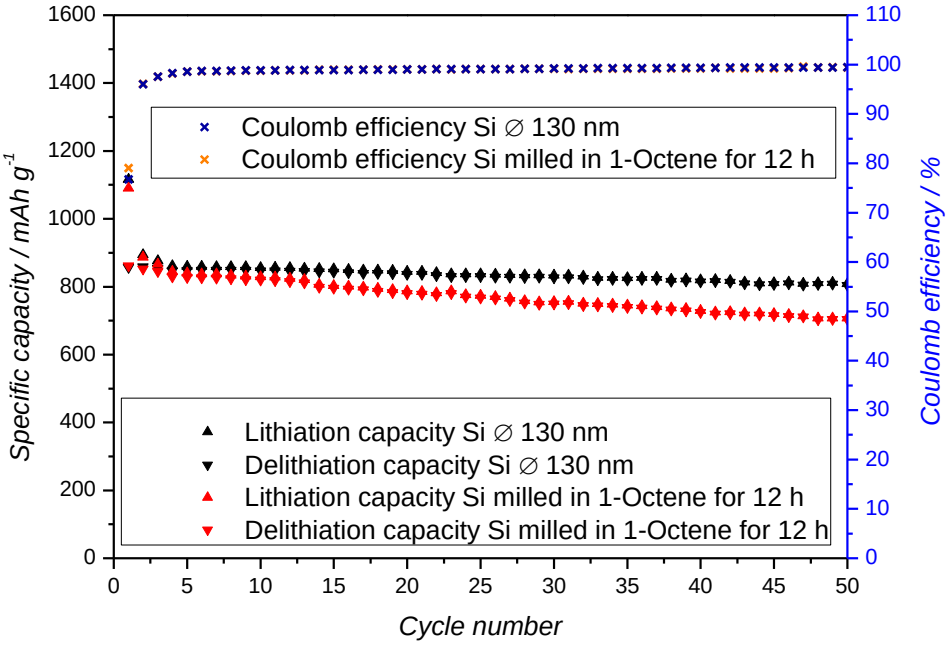

Figure 70. Comparison of the cyclizations of core-shell structured composites produced with milled Si Ø 130 nm (1-M-2-p) and Si milled in 1-octene for 12 h

4.5.4 Influence of the Si Particle Size on the Electrochemical Performance

The influence of the Si particle size on the electrochemical performance is discussed for the prepared core-shell structured composite materials. It should be noted that the specific capacity is now related to the composite material itself and not only to the Si and graphite content. Hence, slightly lower specific capacities are displayed in the figures due to the included weight of the conductive additive and the pyrolysis residues of the epoxy matrix.

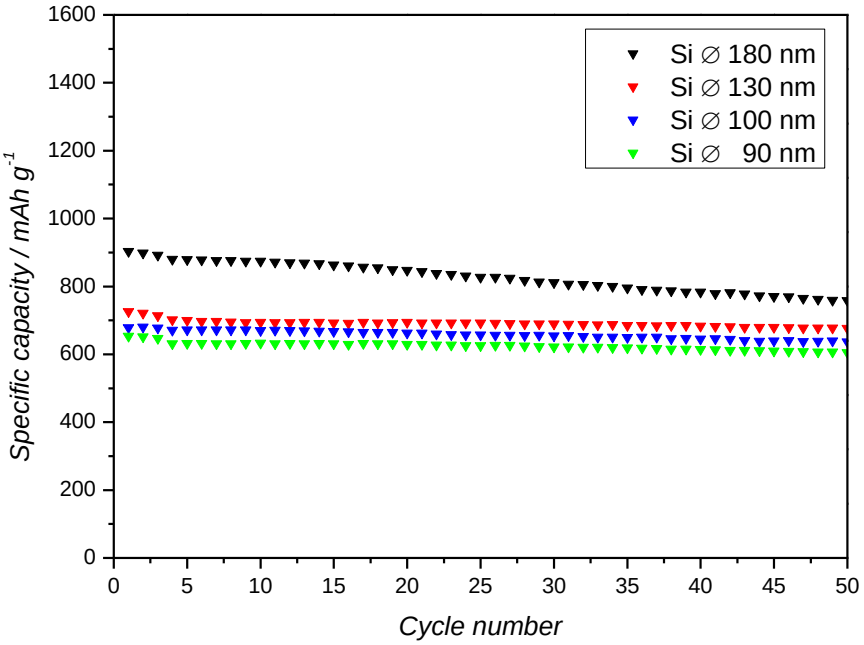

Figure 71. Delithiation capacities of core-shell structured composites produced with milled Si of different average particle sizes

Figure 71 again clearly displays the correlation between the particle size and the starting capacity. The smaller the particles are the more surface functionalization and WC-Co wear are present, which reduce the net weight of electrochemically active Si and hence reduce the specific capacity. Furthermore, smaller Si particle sizes lead to lower CE in the composite material due to SEI formation, as shown in Table 33.

Table 33. CE comparison of different cycles for core-shell structured composites produced with milled Si of different average particle sizes

Cycle	CE Si Ø 180 nm [%]	CE Si Ø 130 nm [%]	CE Si Ø 100 nm [%]	CE Si Ø 90 nm [%]
1.	80.46	76.75	74.82	71.47
2.	96.47	96.02	95.76	94.66
3.	97.72	97.55	97.41	96.80
4.	98.28	98.27	98.17	97.71
5.	98.44	98.58	98.52	98.21
25.	98.50	99.09	99.03	98.88
50.	99.25	99.46	99.23	99.23

Except of the lower starting capacity it is remarkable that reducing the particle size from 130 nm to 90 nm has no significant influence on the cycle stability. This can be especially seen if one looks at the normalized capacities of these measurements shown in Figure 72. The normalized capacities are calculated from the delithiation capacity of the first cycle.

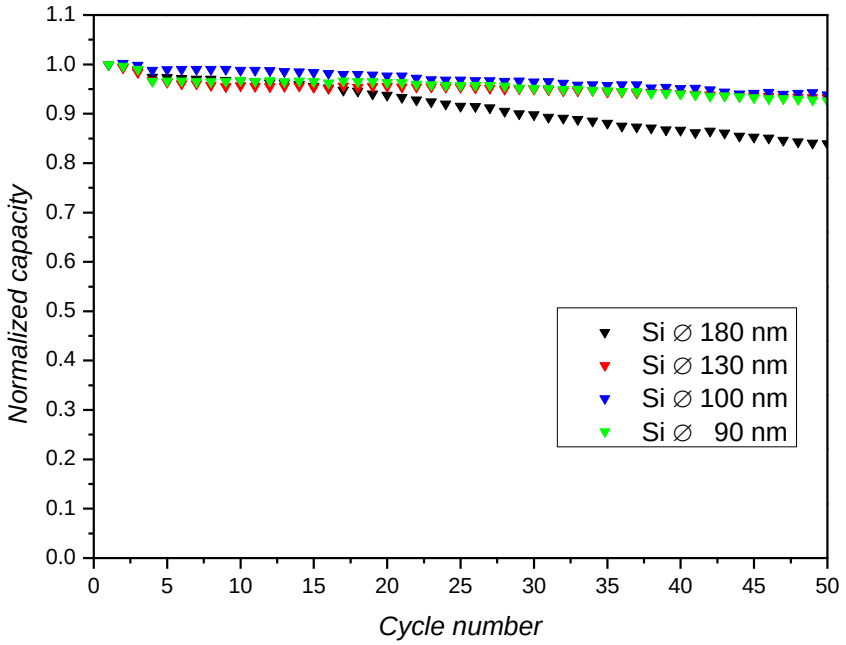

Figure 72. Normalized delithiation capacities of core-shell structured composites produced with milled Si of different average particle sizes

Hence, there is a certain particle size at which the pores are large enough and/or the stability of the carbonaceous matrix is strong enough to withstand the volume changes of the SiNPs

upon cycling. The ideal particle size for milled Si must therefore be between 130 nm and 180 nm, since the latter exhibits appreciable capacity fade. Rather unlikely is that the fade is caused by the cracking of SiNPs which occurs at sizes above ~ 150 nm, as the cracking occurs mainly in the first cycles (*216*,*235*). If the cracking would have an obvious influence, the capacity fade for this material would be much stronger in the first cycles compared to the later ones. However, a partial participation of the particle cracking on the capacity fade cannot be ruled out completely. Another exciting trend is visible if one compares the differential capacity plots (DCPs) of the first cycle for these composites shown in Figure 73.

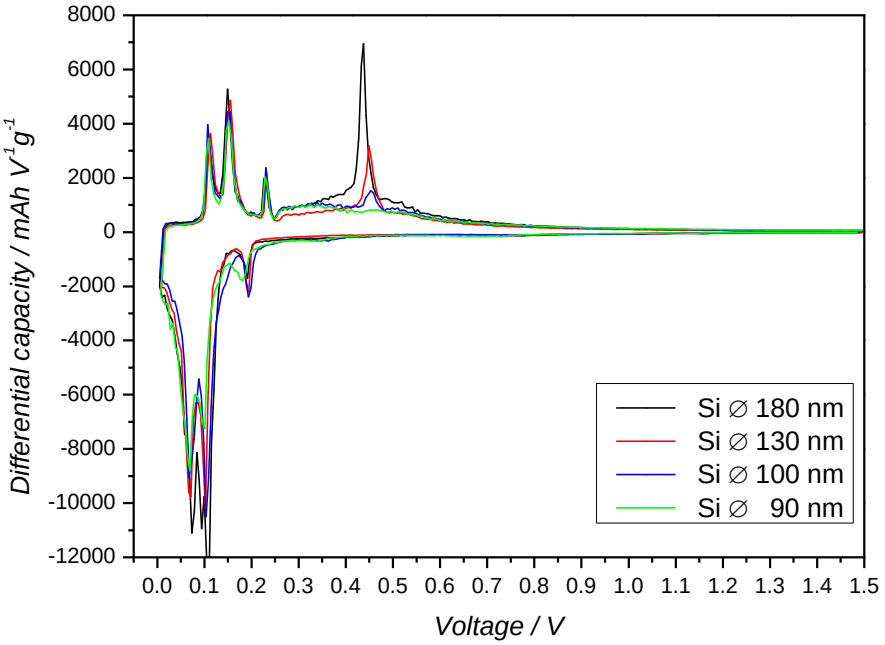

Figure 73. DCP comparison of the first cycle for core-shell structured composites produced with milled Si of different average size

The smaller the Si particles get the more unlikely is the formation of the c-$Li_{15}Si_4$ phase, visible at ~ 450 mV vs. Li/Li^+ due to its delithiation. For the Si with an average particle size of 90 nm the formation cannot be observed. Impurities from WC wear might additionally contribute to this behavior although it is considered to be electrochemically inert. Interesting is also the observation, that this peak is always stronger in the second cycle, as shown in Figure 74. This behavior is possible a kinetic phenomenon as the crystalline parts of the milled Si are exposed to electrochemical solid-state amorphization in the first cycle and hence lithiation of the amorphous phase proceeds faster in the second cycle.

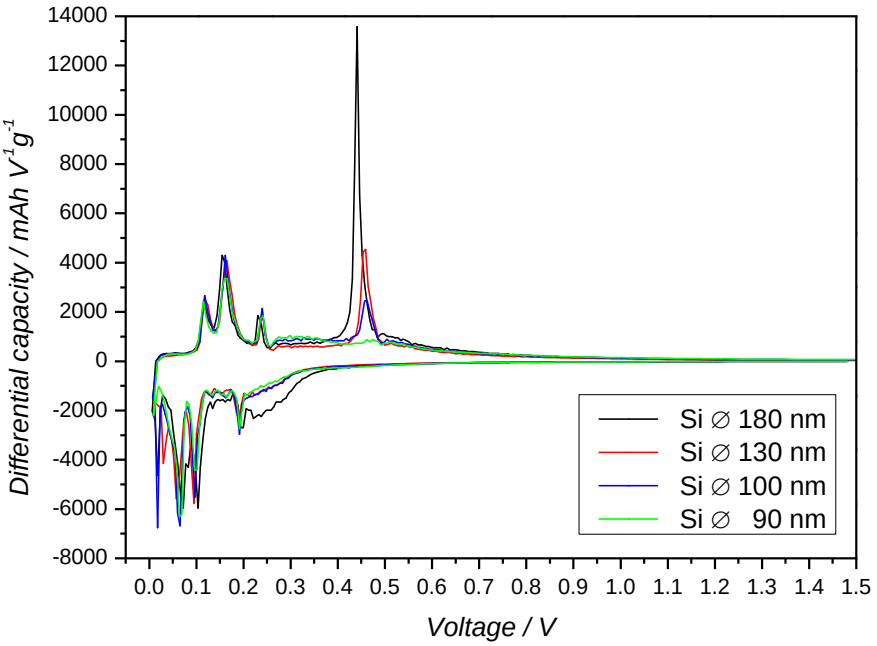

Figure 74. DCP comparison of the second cycle for core-shell structured composites produced with milled Si of different average size

Furthermore, the signal would be even stronger if a C-rate of 0.1 would be used in the second cycle instead of 0.2 C, as there is less time for the phase formation during lithiation. The peak for the formation of the c-$Li_{15}Si_4$ during lithiation is visible in the region between 0-50 mV vs. Li/Li^+. Due to the absence of this peak in the first cycle one can assume that the formation occurs during the constant voltage step and is therefore not visible in the DCP. Again this peak is not observable for Si with an average particle size of 90 nm, hence smaller particle sizes seem to suppress the formation.

However, DCP comparisons of the first and second cycle for core-shell structured Si/C composites produced with milled Si Ø 180 nm and one produced with commercial Si (Nanostructured & Amorphous Materials, Inc.) obtained by the pyrolysis of silane and particle sizes of 30-50 nm revealed something different (see Figure 75 and Figure 76). The peak for the delithiation of the c-$Li_{15}Si_4$ phase is clearly visible in the first cycle for the composite produced with commercial Si, which contradicts the observations made with milled Si of different size. It is remarkable that the peak is even much stronger in the second cycle for the commercial Si than for the larger milled Si, and hence the reason for this behavior must not be the particle size. If one thinks about the synthetic route for the commercial Si it is noticeable that the high temperatures required are ideal to produce crystalline particles.

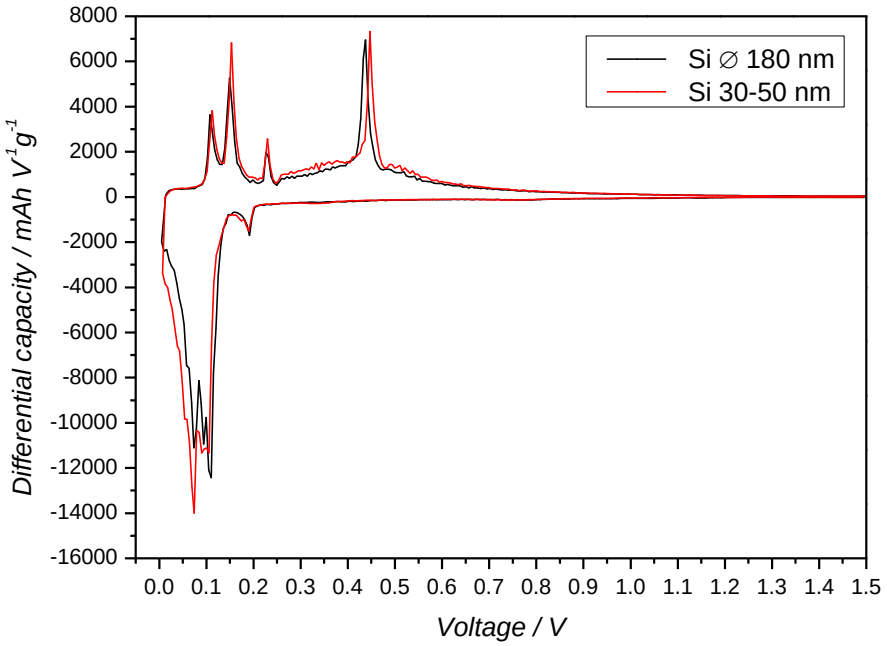

Figure 75. DCP comparison of the first cycle for core-shell structured composites produced with milled Si Ø 180 nm and commercial SiNPs 30-50 nm

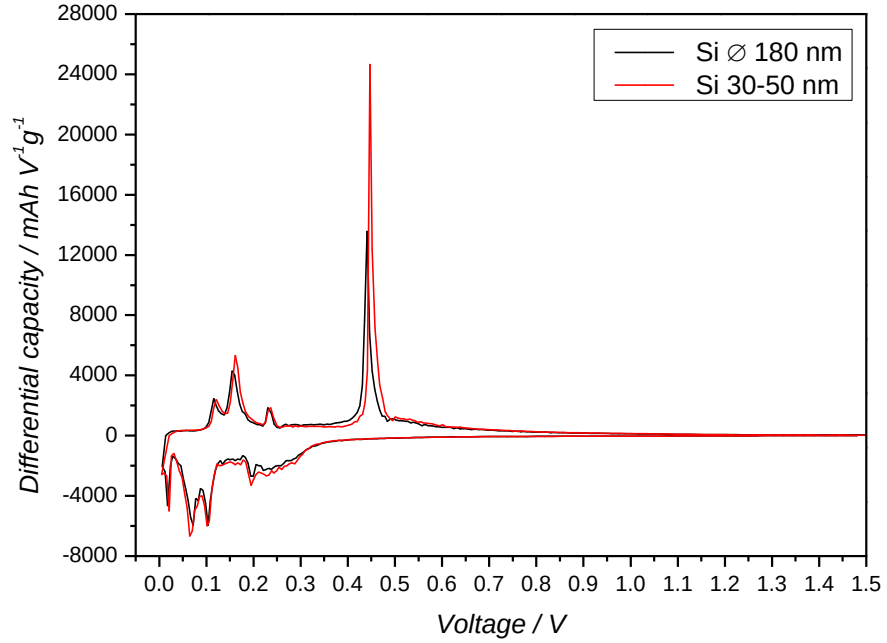

Figure 76. DCP comparison of the second cycle for core-shell structured composites produced with milled Si Ø 180 nm and commercial SiNPs 30-50 nm

On the other hand, the milling of the Si reduces the crystallinity due to the formation nanoscale crystallite sizes and amorphous crystallite boundaries caused by the high energy ball impacts. It is therefore evident that the formation of the c-$Li_{15}Si_4$ is linked to the crystalline Si parts. This assumption is confirmed by XRD measurements, using the *Scherrer equation* to calculate the average particle size with the approximation of spherical crystallites.

Table 34. Average crystallite sizes for milled Si and commercial SiNPs of different size

Si particle size [nm]	Ø Crystallite size [nm]
Ø 180	12
Ø 130	10
Ø 100	8
Ø 90	7
30-50	29

The previous figures and Table 34 clearly reveal the correlation between c-$Li_{15}Si_4$ and the crystallite size. However, it remains unclear if the suppression of the c-$Li_{15}Si_4$ phase is just caused by smaller crystallite sizes or if the amorphous areas in milled Si also contribute to it. Furthermore, it remains unclear why generally the formation of this crystalline lithiated phase is suppressed as the c-Si is converted to a-Si anyway due to the solid-state amorphization upon first lithiation. The only possible explanation is that the mechanically induced amorphous areas differ from electrochemically produced a-Si.

The influence of the c-$Li_{15}Si_4$ formation on the cycling behavior is difficult to determine as Si particles of the same particle size and different crystallites size would be necessary to do so. Furthermore, these particles should be produced with the same method to exclude influences caused by method itself such as surface functionalization etc. However, the influence of the phase transition is possibly low compared to particle size itself, as shown in Figure 77. The composite produced with the commercial Si with particle sizes 30-50 nm has a much better cycle stability compared to the Si with an average particle size of 180 nm, although the phase transition is much stronger in the commercial Si (see Figure 76). In general it is, however, beneficial to avoid the crystalline phase transformation not only to reduce the mechanical stress but also to lower the voltage hysteresis (see Figure 29). This makes milled Si, besides its ease of production, a particular desirable candidate for commercial application.

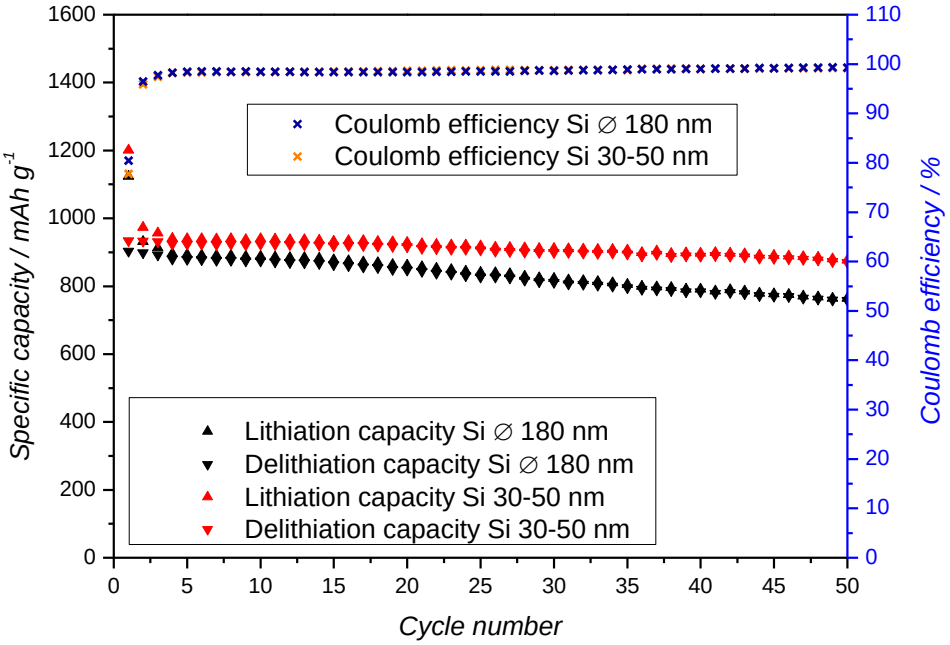

Figure 77. Comparison of the cyclizations of core-shell structured composites produced with milled Si Ø 180 nm and commercial Si 30-50 nm

4.5.5 Influence of the Curing Agent

In this chapter different curing agents are tested for the fabrication of the core-shell structured composite and the results are compared with the standard curing agent 3-(dimethylamino)-1-propylamine. This is necessary as for industrial large scale production large amounts of low-cost curing agents are required without detriment of the cycle stability. The standard curing agent is monofunctional (one amine group), cures slowly and leads to linear polymer chains. Hence, di- or trifunctional curing agents are tested, as they cure much faster and lead to branched polymer chains with higher stability. The used curing agents are shown in Figure 78. The curing speed is dependent on the nucleophilicity, type and the number of the amine groups. Aliphatic amines cure faster than aromatic ones and primary amines cure faster than secondary ones (steric hindrance). In addition, a higher number of amine groups increases the curing rate due to the exothermic type of reaction which rises the temperature and hence increases the reaction rate. The fastest curing agent is diethylenetriamine and *m*-phenylenediamine is the slowest one. The high reaction rate of diethylenetriamine can also be seen in the temperature curves of the process control shown in Figure 79. The exothermic curing reaction leads to a rapid temperature rise and exceeds the temperature before addition of the coating slurry in the Wurster compartment.

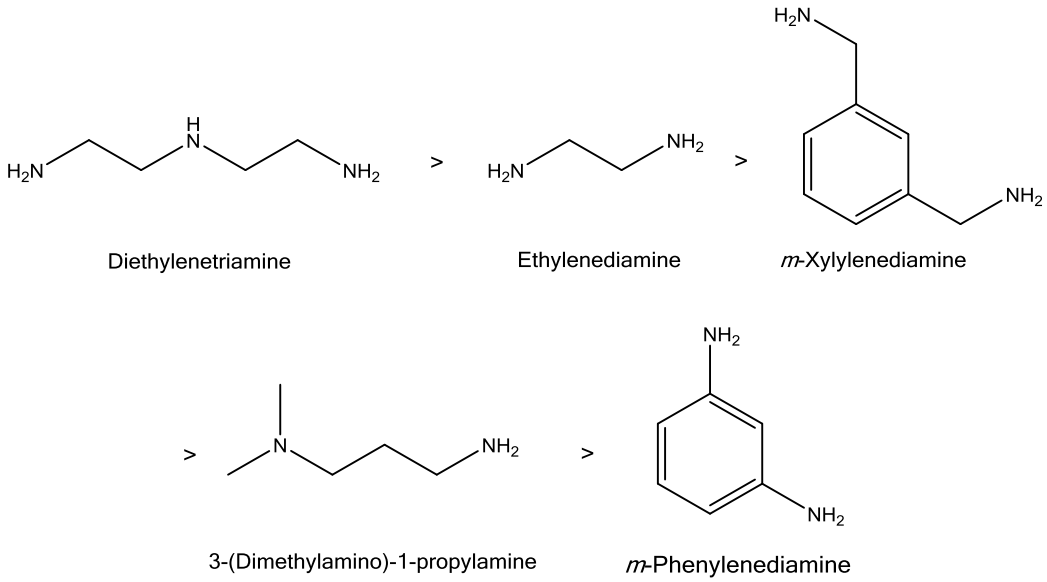

Figure 78. List of the used curing agents and their relative curing rate

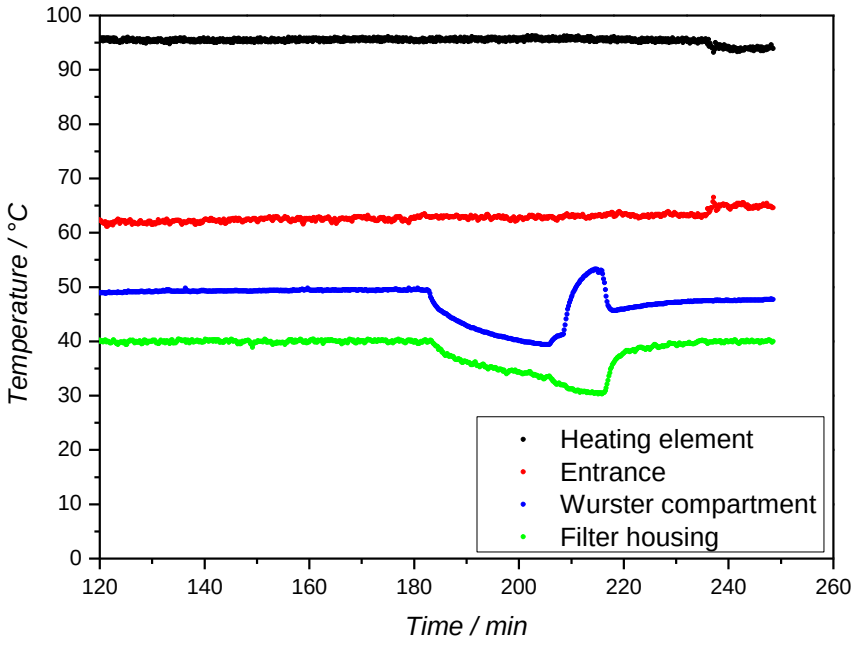

Figure 79. Process control of a core-shell structured composite cured with diethylenetriamine

After approximate completion of the curing reaction a temperature drop can be observed. This behavior is only visible if diethylenetriamine is used as curing agent, all other curing agents exhibit a temperature curve like the one shown in Figure 64.

As the curing reaction is a stoichiometric ring opening reaction the composition varies slightly while using different curing agents. The amount of epoxy resin is kept constant and the amount of curing agent needed is calculated according to an epoxide equivalent weight of 185 Da (*321*). The corresponding compositions are shown in Table 35.

Table 35. Composite composition in dependency of the used curing agent

Curing agent	Weight ratio Epoxy resin : curing agent	Share of the epoxy matrix in the composite [wt%]
3-(Dimethylamino)-1-propylamine	80 : 20	20
Diethylenetriamine	90 : 10	18.2
Ethylenediamine	92.5 : 7.5	17.8
m-Xylylenediamine	84.5 : 15.5	19.2
m-Phenylenediamine	87.2 : 12.8	18.6

The composition of the epoxy resin itself is not revealed by Huntsman Advanced Materials Inc. However, GC-MS measurements demonstrated that it consists mainly of bisphenol A diglycidyl ether (BADGE) and small quantities of butyl glycidyl ether (monoreactive diluent). A more accurate determination of the quantities is not possible due to column carryover of the BADGE caused by its boiling point/decomposition point above 400 °C (SciFinder®).

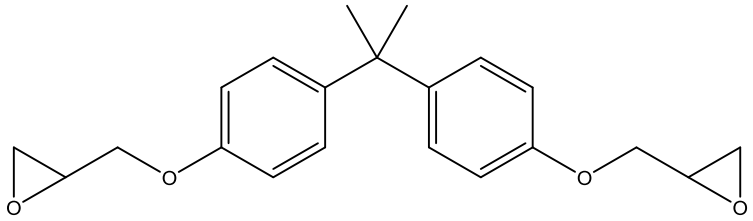

Bisphenol A diglycidyl ether (BADGE)

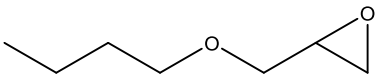

Butyl glycidyl ether

Figure 80. Chemical structures of BADGE and butyl glycidyl ether

The core-shell structured composites for the characterization of the different curing agents are produced with Si of an average particle size of 180 nm. With exception of the slightly different composition, the synthesis proceeds as described in chapter 4.5.2.

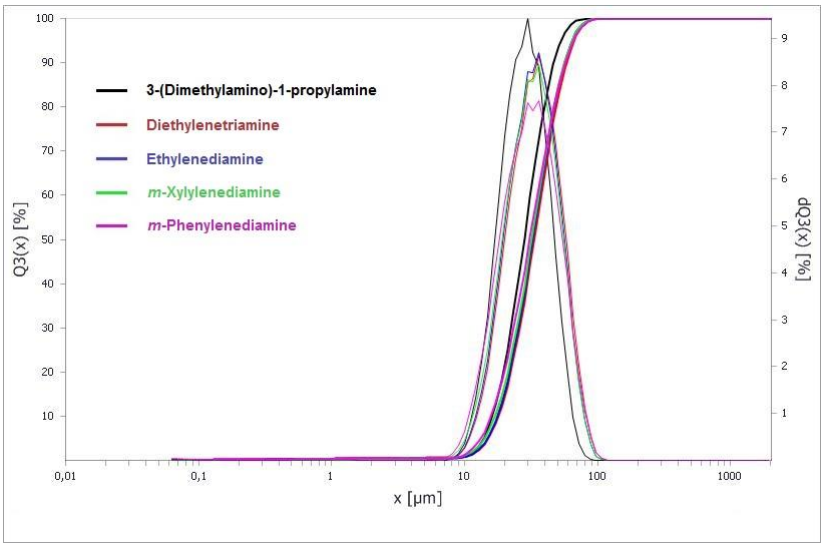

Figure 81. Particle size distribution measurements of core-shell structured composites produced with different curing agents

Table 36. Particle size distribution values of core-shell structured composites produced with different curing agents

Curing agent	Ø Particle size [µm]	D10 [µm]	D50 [µm]	D90 [µm]	(D90 - D10) / D50
3-(Dimethylamino)-1-propylamine	30	16	28	47	1.11
Diethylenetriamine	36	18	34	58	1.18
Ethylenediamine	35	18	33	56	1.15
m-Xylylenediamine	35	17	32	56	1.22
m-Phenylenediamine	34	16	32	56	1.25

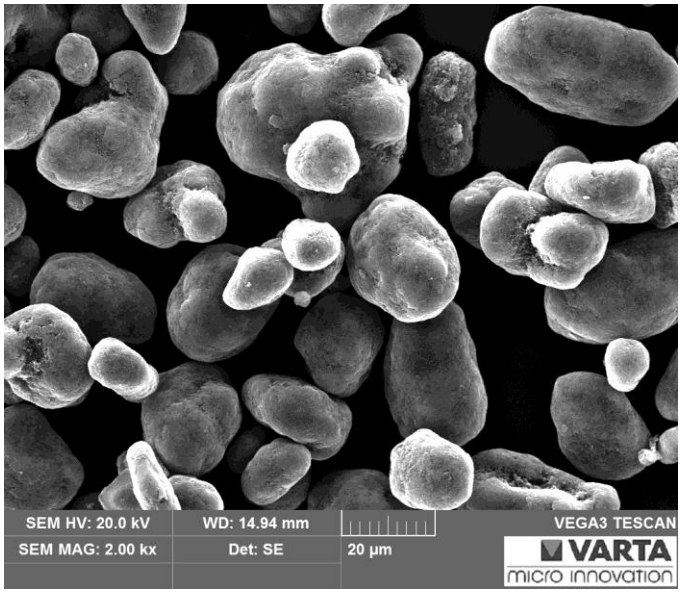

Figure 82. SEM micrograph of a core-shell structured composite with ethylenediamine as curing agent

The table and the figures on the previous page show that the use of di- or trifunctional curing agents leads to significantly larger composite particles. This behavior is attributed to the faster curing and the formation of crosslinked epoxy polymers with these curing agents, which leads to coalescence of some composite particles during synthesis. However, they lead to a higher mechanical stability of the epoxy matrix too. The better mechanical stability, for example, allows particle size measurements directly after synthesis, which is important for process control. This is not self-evident as the dispersing unit of the particle sizer applies strong ultrasonic for the measurements, and this leads to disintegration of the coating layer if the standard curing agent is used for production, as shown in Figure 83.

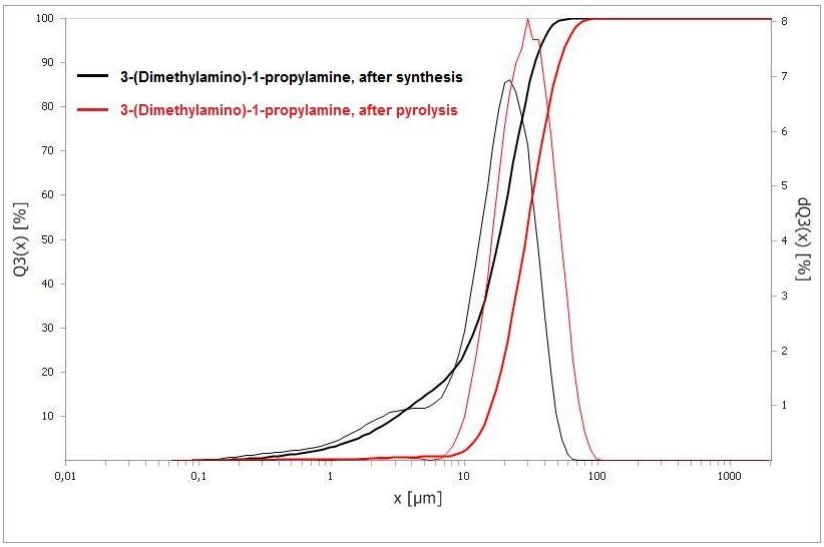

Figure 83. Core-shell structured composite produced with the standard curing agent measured after synthesis and after pyrolysis

The composite produced with the standard curing agent needs to be post cured for ~ 5 d at room temperature or pyrolyzed for particle size measurements. During pyrolysis, the standard composite cures further in the heating phase and the decomposition of the epoxy matrix leads to a mechanical stable carbon network.

A difference in the weight loss of the composite during pyrolysis cannot be observed if different curing agents are used (~ 13 %). However, the pyrolysis itself proceeds slightly different as seen in Figure 84. The composites produced with aliphatic curing agents typically have signals of low weight fragments in the region 200-300 °C. These signals are not visible for diethylenetriamine if the temperature ramping is 20 °C/min, but are visible at 10 °C/min. For aromatic curing agents these signals are not visible at all. Hence, they must be a result of the decomposition of the curing agents itself.

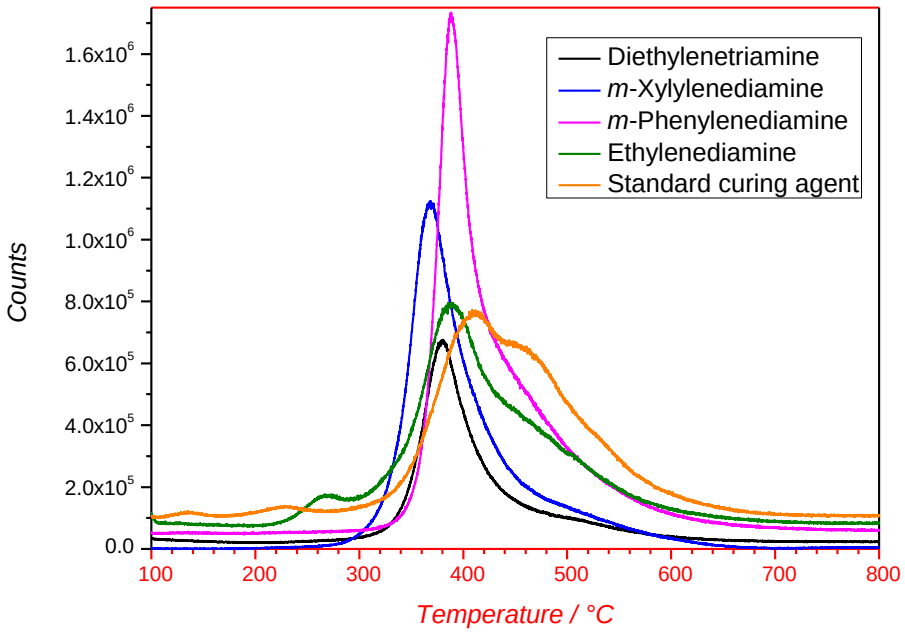

Figure 84. Py-GC/MS measurements of core-shell structured composites produced with different curing agents, temperature ramping: 20 °C/min

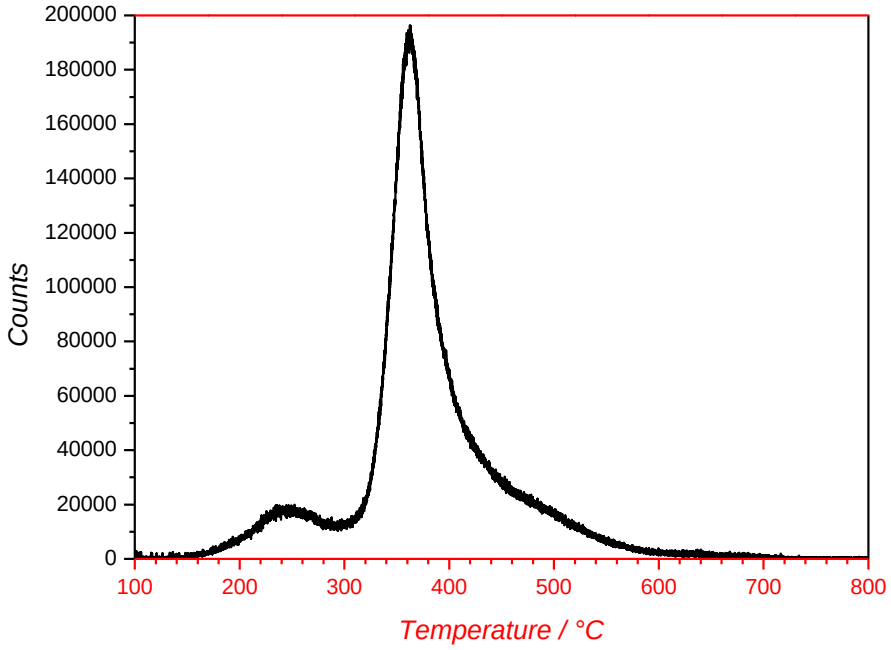

Figure 85. Py-GC/MS measurement of a core-shell structured composite produced with diethylenetriamine, temperature ramping: 10 °C/min

If one takes a look at the bond-dissociation energies shown in Table 37 it seems reasonable that the polymer parts contributed by the curing agent decompose first as the C-N bond is the weakest one in the epoxy.

Table 37. Bond-dissociation energies of various carbon-element bonds (*322*,*323*)

Bond	Bond-dissociation energy [kJ/mol]
Aromatic C-C	~ 560
C-C	345
C-H	416
C-N	305
C-O	358

The signals for the decomposition products of the aromatic curing agent parts are overlapped by those of the epoxy resin due to their higher boiling points and are not visible as a separated “peak”. Unfortunately, it is impossible to determine certain decomposition products with this pyrolysis mode as the gas flow from the pyrolyzer is initiated directly in the mass spectrometer.

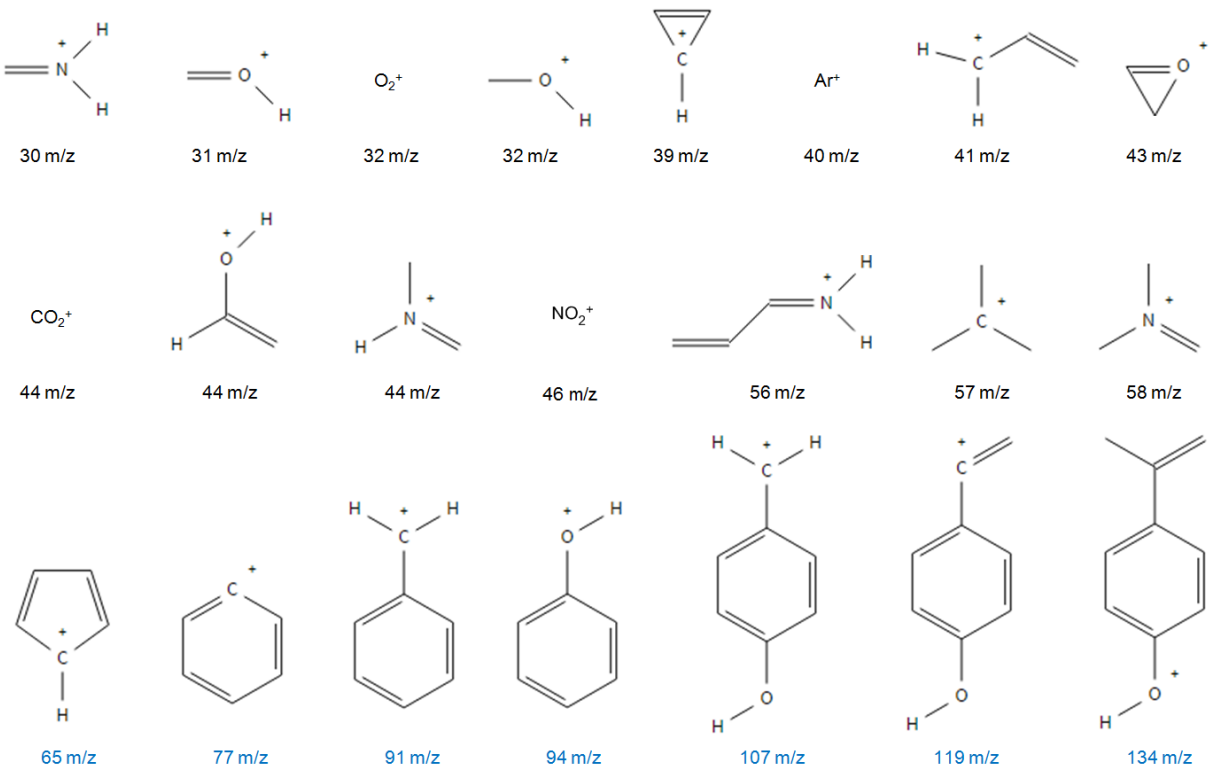

Figure 86. Typical MS fragments of the pyrolysis of a composite produced with the standard curing agent

MS fragments help to distinguish whether the signal comes from the curing agent, the glycidyl moiety or the bisphenol A backbone. TGA/DSC/MS measurements are conducted for further examination.

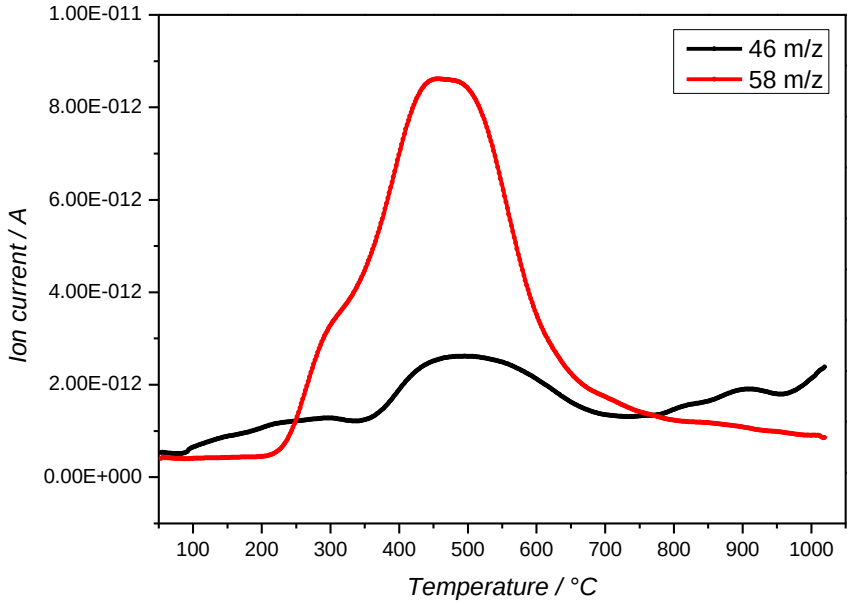

Figure 87. Ion current profiles of characteristic curing agent fragments

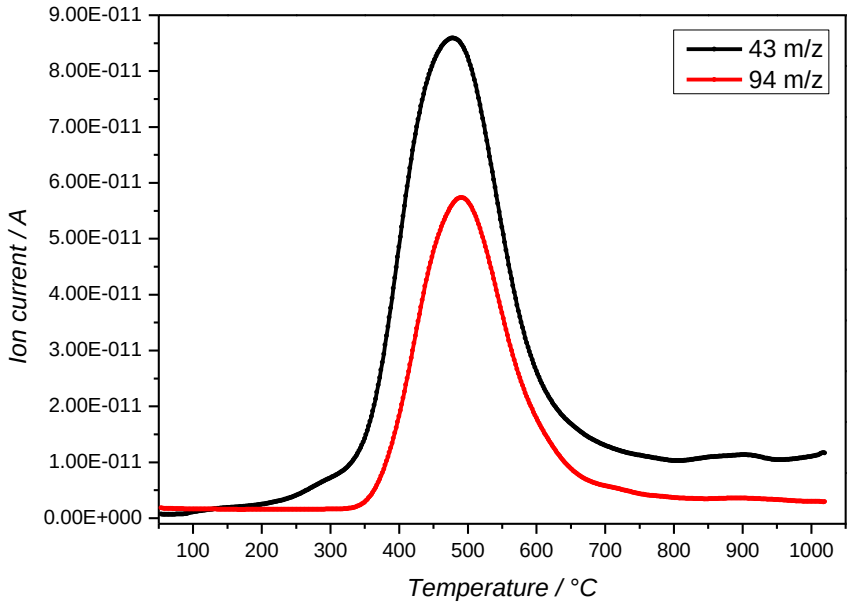

Figure 88. Ion current profiles of characteristic epoxy resin fragments

Figure 87 clearly reveals that the decomposition of the curing agents starts in the region 200-300 °C. However, the major part of its decomposition occurs between 400 °C and 600 °C. This is also the range where the decomposition of the epoxy resin parts takes place. If one takes a closer look at Figure 88 one can see that the decomposition of the former glycidyl moiety (43 m/z) starts in the same range as the curing agent, which is a subsequent reaction caused by the first C-N bond cleavages.

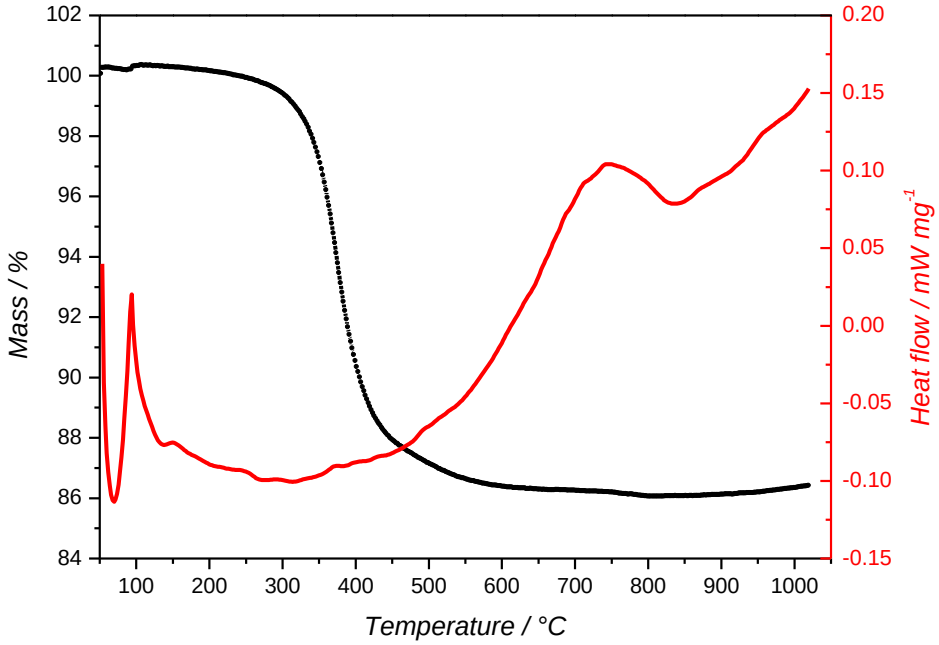

Figure 89. TGA and DSC measurements of the decomposition of composite produced with standard curing agent

Figure 84 and Figure 89 show that the decomposition is almost completed around 600 °C for all curing agents. However, the DSC profile reveals that another reaction or phase transition occurs in the region between 700 °C and 800 °C. This explains why Scharfegger observed poor electrochemical performance of composites pyrolyzed at 700 °C (*324*), as the transformation is not completed.

From the electrochemical point of view only the composite produced with diethylenetriamine differs from the other curing agents, as shown in Figure 90. The worse performance is unexpected and must be caused by structural differences due to the strong crosslinking of this curing agent and/or an elsewise proceeding pyrolysis, which leads to differences in the carbonaceous matrix.

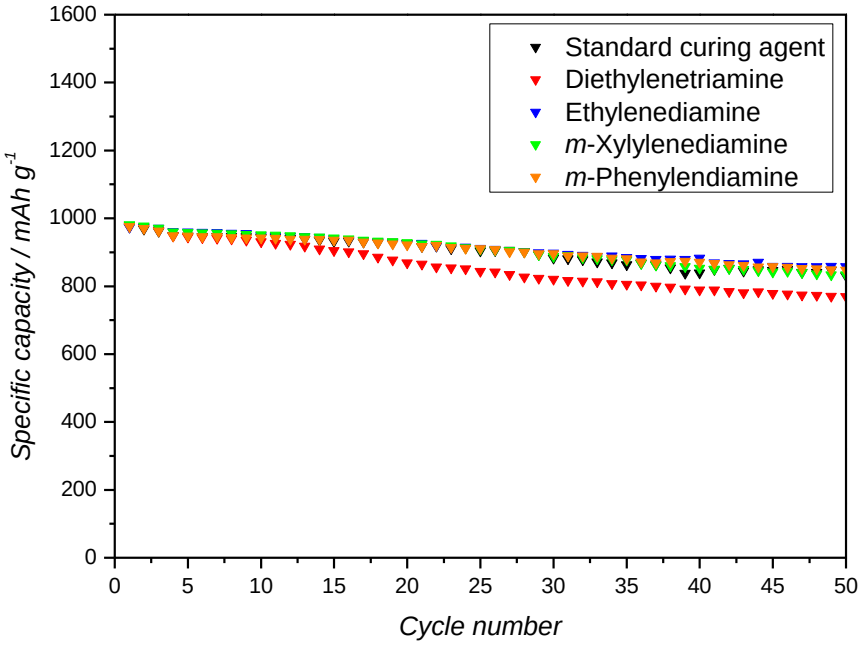

Figure 90. Delithiation capacities of core-shell structured composites produced with different curing agents

However, the fact that the difunctional curing agents do not differ electrochemically from the standard curing agent, make them good candidates for its replacement. This is attributed to their faster curing and higher structural stability in the non-pyrolyzed state.

4.5.6 Influence of a 2-step Pyrolysis

According to the previous chapter a 2-step pyrolysis is conceived and compared to the standard pyrolysis (Table 28). The conditions for the 2-step pyrolysis are shown in Table 38.

Table 38. Oven parameters of the 2-step pyrolysis

	Heating rate	Target temperature	Dwell time
Step 1	10 °C/min	280 °C	1 h 30 min
Step 2	10 °C/min	800 °C	2 h

The target temperature of 280 °C is chosen as the decomposition of the curing agent parts and the former glycidyl moieties is in an advanced stage at this temperature. The dwell time

of 1 h 30 min is chosen, as it is the heating-up time of the standard pyrolysis and to provide enough time to get rid of the low weight decomposition products. After the first step the sample is not allowed to cool down but is heated-up to the second target temperature. The temperature of 800 °C is chosen as the transformation observed in the DSC measurements should be completed. The dwell time of 2 h is chosen in order to have the same time at high temperatures as the standard pyrolysis.

The weight loss gained slightly due to the 2-step pyrolysis and is typically around 14 %. A different behavior can not only be observed for the weight loss but also the electrochemical performance differs, as shown in Figure 91.

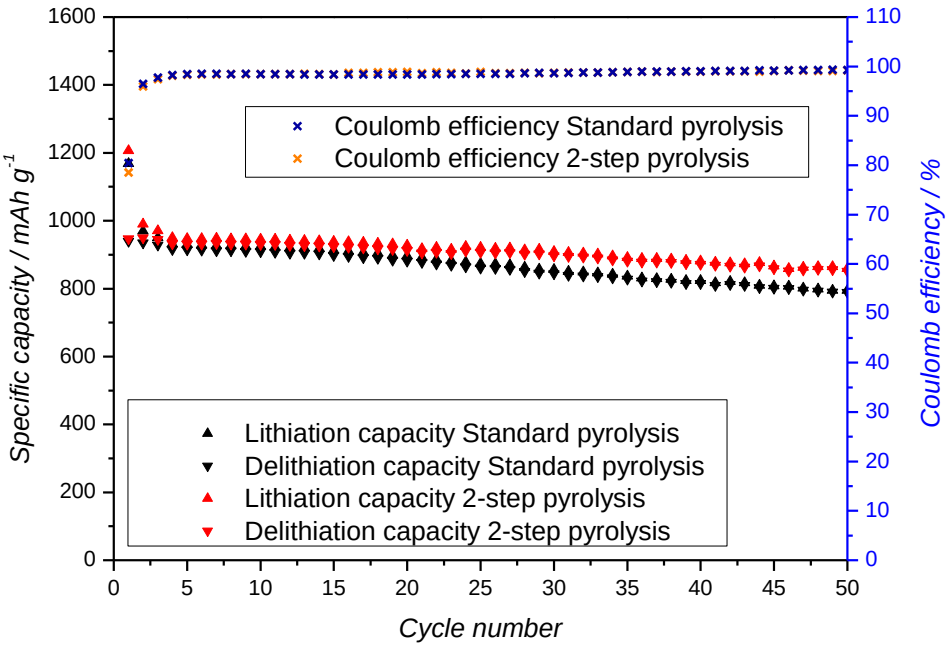

Figure 91. Comparison of the cyclizations of a standard core-shell structured composite pyrolyzed with standard parameters and a 2-step pyrolysis

The better electrochemical performance of the 2-step pyrolysis material is possibly caused by a better electrochemical conductivity and/or mechanical stability of the carbonaceous matrix. In addition, the lower CE in the first cycle indicates that this material has a higher porosity (larger surface) than the material obtained via standard pyrolysis. The higher porosity possibly leads to better soaking with the electrolyte and might offer more space for the volume expansion of the SiNPs during cycling. Hence, a 2-step pyrolysis is preferable compared to the standard pyrolysis.

4.5.7 Increase of the Epoxy Content

An increase of the epoxy content is contemplated, as the previous chapters revealed that the epoxy matrix and its pyrolysis have significant influence on the cycling performance. Furthermore, preliminary investigations with Si/C composites cured in a crystallizing dish showed improvement of the cycling performance correlating with an increase of the epoxy content (up to 40 %). For the synthesis the epoxy content is raised while the other component quantities are maintained (Figure 25). The synthesis proceeds according to the standard procedure.

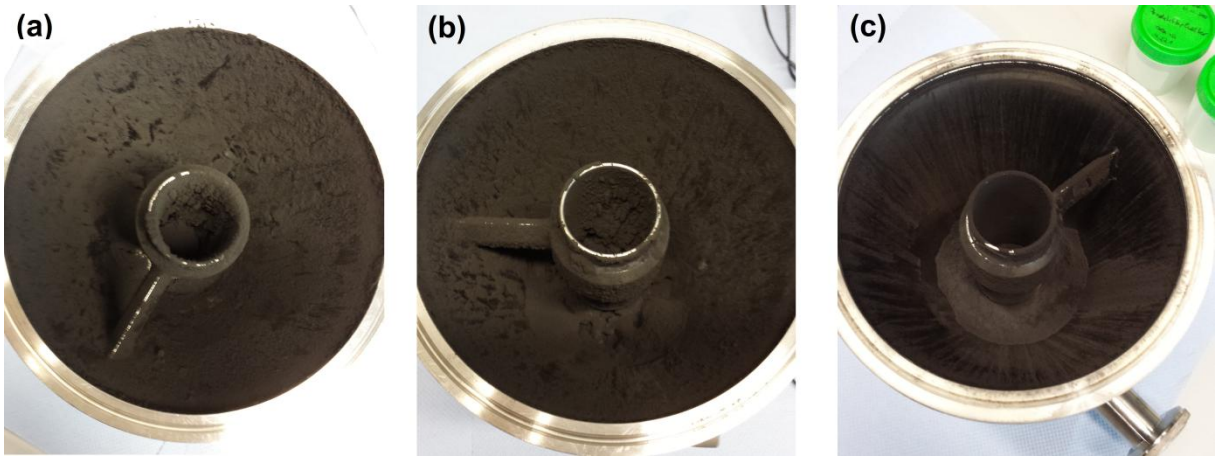

Figure 92. Wurster compartment after synthesis of composites with an epoxy content of 40 % (a), 30 % (b) and 20 % (c)

Figure 92 reveals the problems associated with an increase of the epoxy content. The epoxy resin cannot cure fast enough to warrant homogenous coating. Instead sticky lumps are formed in the case of 30 % and 40 % epoxy content, which are discarded as they are useless for electrode fabrication. Even an increase of the reactor temperature to 60 °C and use of diethylenetriamine leads to these lumps.

In order to obtain a powder after synthesis, the threshold value of the epoxy content turns out to be 25 %. However, this slight increase has a major impact on the particle size distribution, as shown in Figure 93. The material then consists almost exclusively of agglomerates and those are simply too big to be used for electrode fabrication. Thus, 20 % epoxy represents the ideal composition for the formation of uniformly composite particles with high epoxy content, as the number of agglomerates is negligible (see Figure 66).

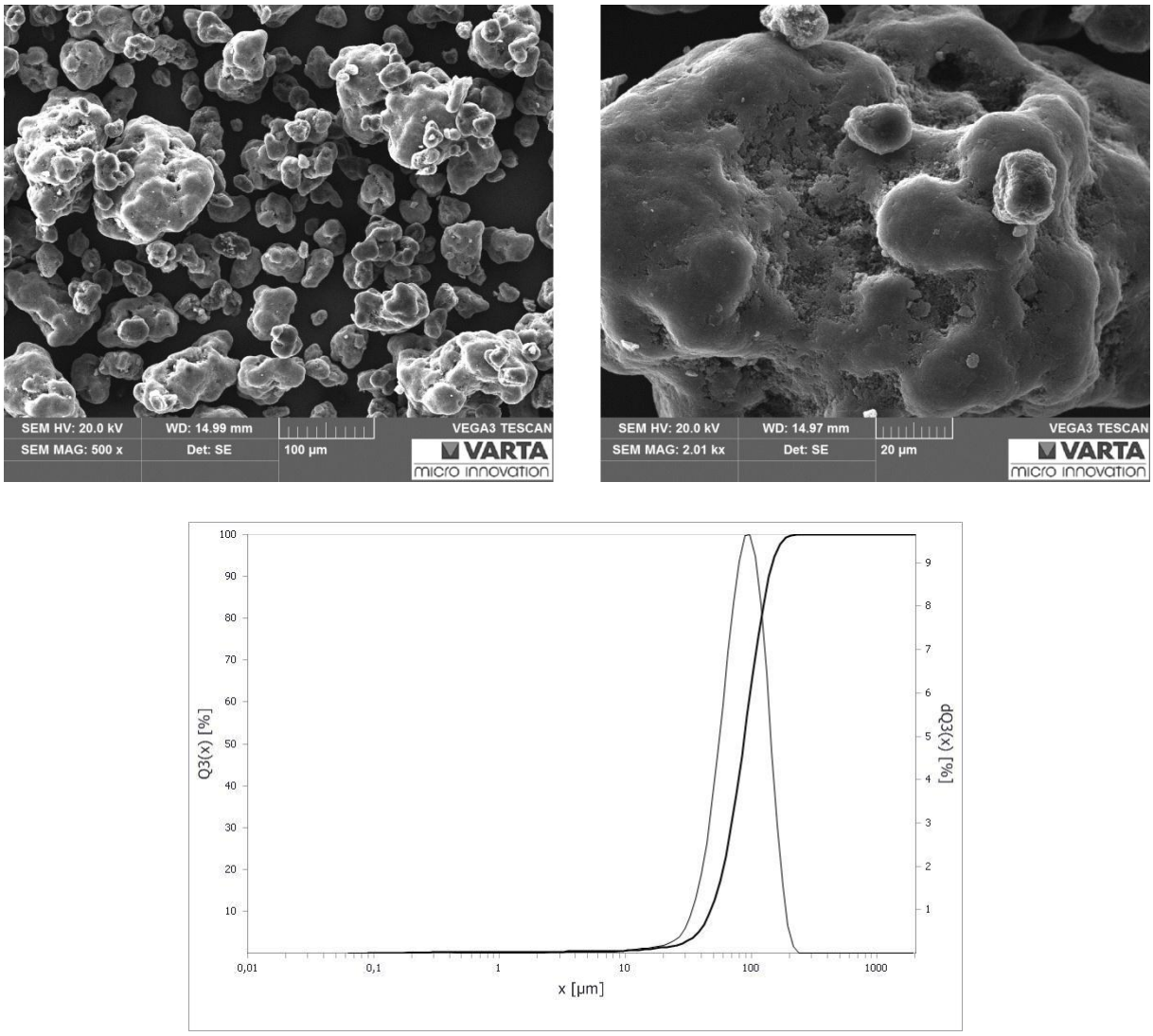

Figure 93. SEM micrographs of a core-shell structured composite with an epoxy content of 25 % at 500x (top left) 2,000x (top right) magnification and its particle size distribution (bottom)

Table 39. Particle size distribution values of the composite with 25 % epoxy content

Ø Particle size [µm]	D10 [µm]	D50 [µm]	D90 [µm]	$\frac{(D90 - D10)}{D50}$
90	47	87	138	1.05

Although it is nearly impossible to increase the epoxy content with this type of reactor and the standard quantities of Si, conductive additive and graphite, it can be performed by increasing the conductive additive content in the same manner as the epoxy. The conductive additive acts as filling material and reduces the “stickiness” of the epoxy resin during curing. Furthermore, diethylenetriamine is used as curing agent to guarantee fast curing. The used compositions are shown in Table 40.

Table 40. Used compositions for composites with increased epoxy and conductive additive content

Epoxy content [%]	Epoxy resin [g]	Curing agent [g]	Si [g]	Graphite [g]	Conductive additive [g]
22.3	12.8	1.43	9.6	33.6	6.4
26.2	16.46	1.84	9.6	33.6	8.23

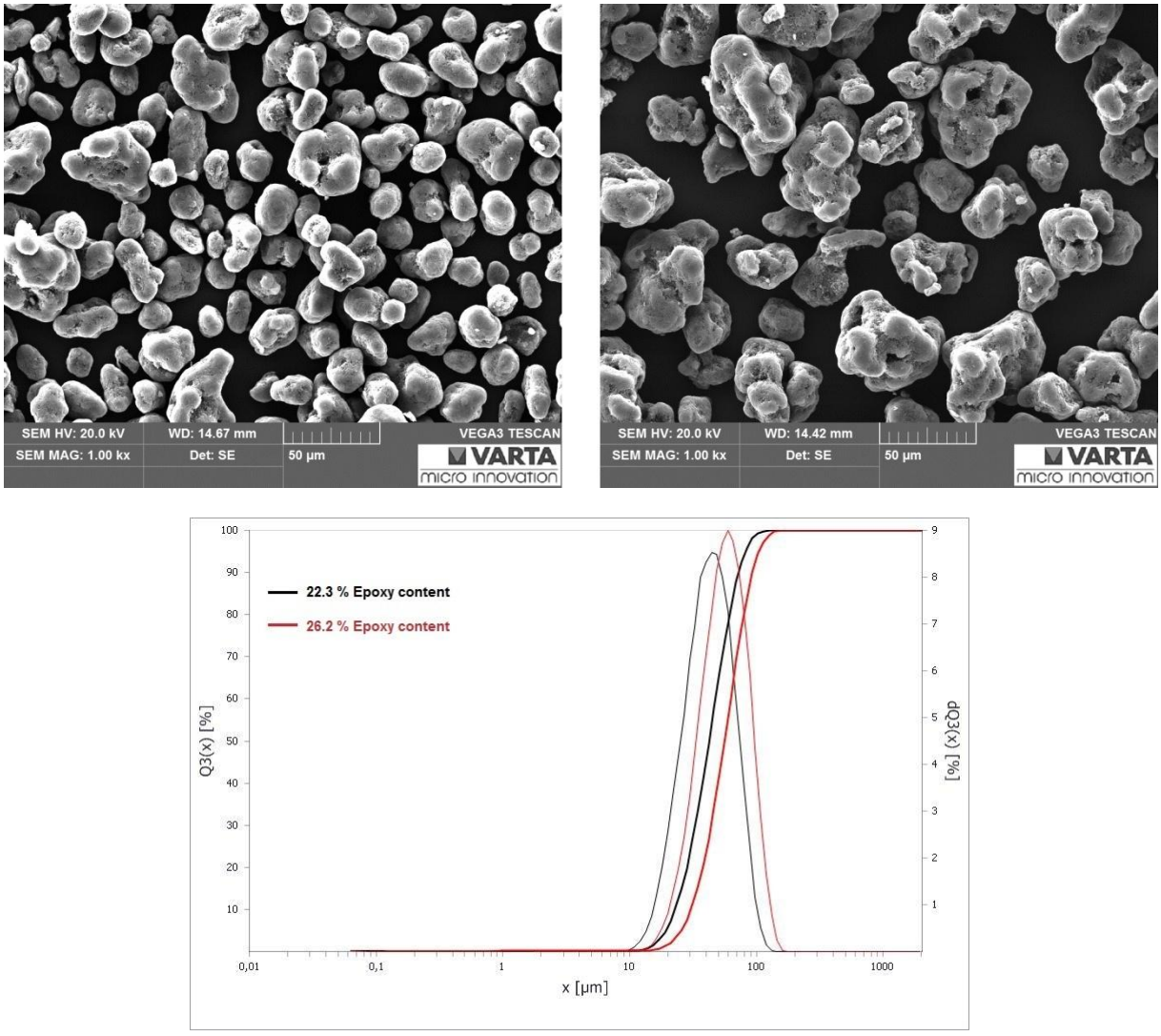

Figure 94. SEM micrographs of core-shell structured composites with epoxy contents (Diethylenetriamine) of 22.3 % (top left), 26.2 % (top right) and a comparison of their particle size distributions (bottom)

Table 41. Particle size distribution values of composites with 22.3 % and 26.2 % epoxy content

Epoxy content [%]	Ø Particle size [µm]	D10 [µm]	D50 [µm]	D90 [µm]	$\frac{(D90 - D10)}{D50}$
22.3	45	23	42	72	1.17
26.2	59	30	56	93	1.13

By a correlating increase of the conductive additive with the epoxy content it is possible to reduce agglomerate formation during synthesis, as shown in Figure 94 and Table 41. However, the tendency of a stronger agglomerate formation with increasing epoxy content is still visible. Therefore, more conductivity additive would be necessary to reduce this behavior. Unfortunately, more conductivity additive is coupled with the disadvantages of lower capacity and CEs.

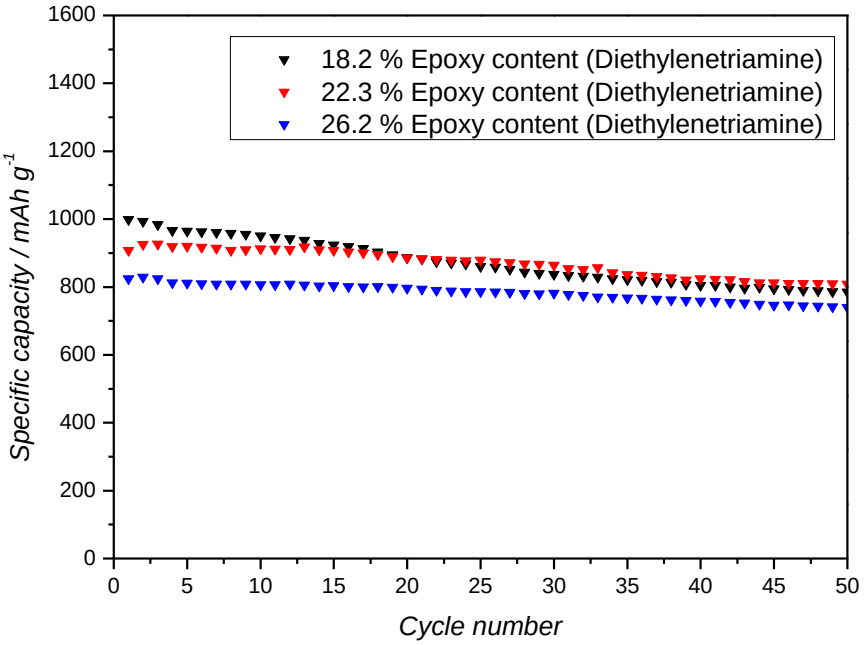

Figure 95. Delithiation capacities of core-shell structured composites with increased epoxy and conductive additive content

Table 42. CE comparison of composites with increased epoxy and conductive additive content

Cycle	CE for 18.2 % epoxy [%]	CE for 22.3 % epoxy [%]	CE for 26.2 % epoxy [%]
1.	81.93	77.57	74.12
2.	96.82	94.81	92.84
3.	97.99	97.05	95.80

Figure 95 shows the benefit of the higher epoxy and conductivity additive content in regard to the cycle stability. However, it is impossible to distinguish whether the improvement comes from the increase of the epoxy content, of the conductivity additive or if it is an effect of both.

In addition, it should be considered that the overall active material content decreases due to larger amounts of epoxy matrix and conductive additive, which decreases the capacity. Furthermore, the higher content also leads to a drastic decrease of the CEs, which causes detrimental capacity fade in full cells. Hence, an increase of the epoxy matrix does not contribute to the improvement of the active material particles.

4.5.8 Influence of the Binder on the Electrochemical Performance

Supplemental to the improvements of the composite material it is also necessary to clarify if the electrode composition can be improved too. Here the binder especially plays an extraordinary role as it ensures the integrity of the electrode. Changing the binder is therefore a simple and cost-effective method to improve cycle stability. Hence, different binders are investigated according to their electrochemical performance using core-shell structured composites. The binders used for this purpose are shown in Figure 96.

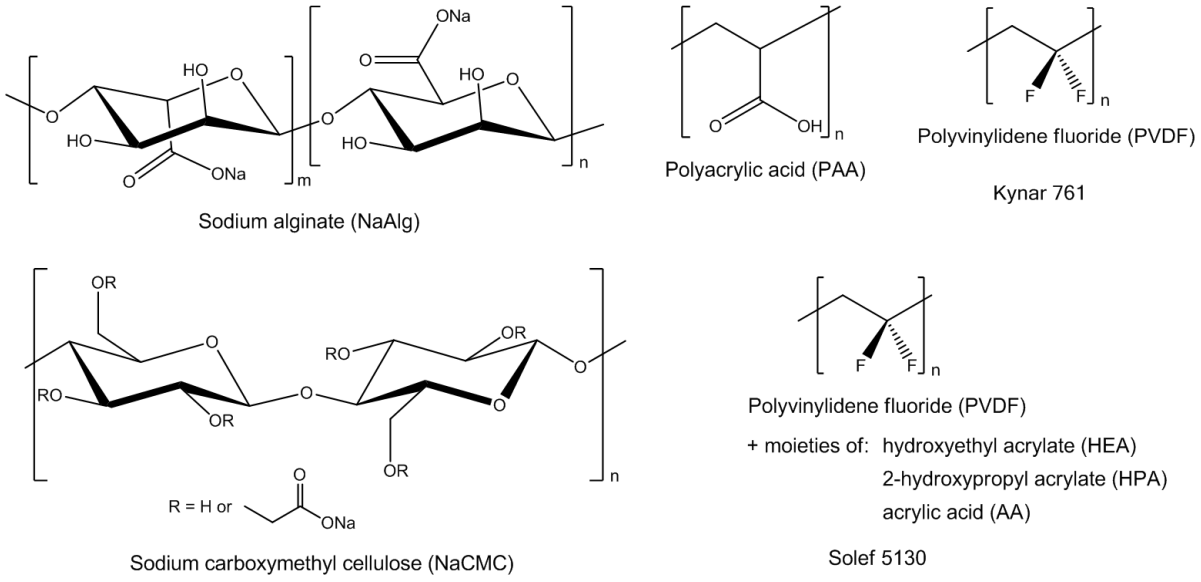

Figure 96. Binders investigated for core-shell structured composite material

As already mentioned, NaCMC is chosen as the standard binder according to its superior cycling performance of Si based electrodes. This behavior is attributed to hydrogen bonding and covalent bond formation between the polar carboxylic group of the binder and silanol groups present on the Si surface (*281*). However, in the composite material only a small amount of the Si is present at the surface and is possibly C-coated due to the pyrolyzed

epoxy matrix. Thus, the composite might act different than pristine SiNPs. It should be noted that NMP is used as solvent instead of deionized water for Kynar 761 and Solef 5130.

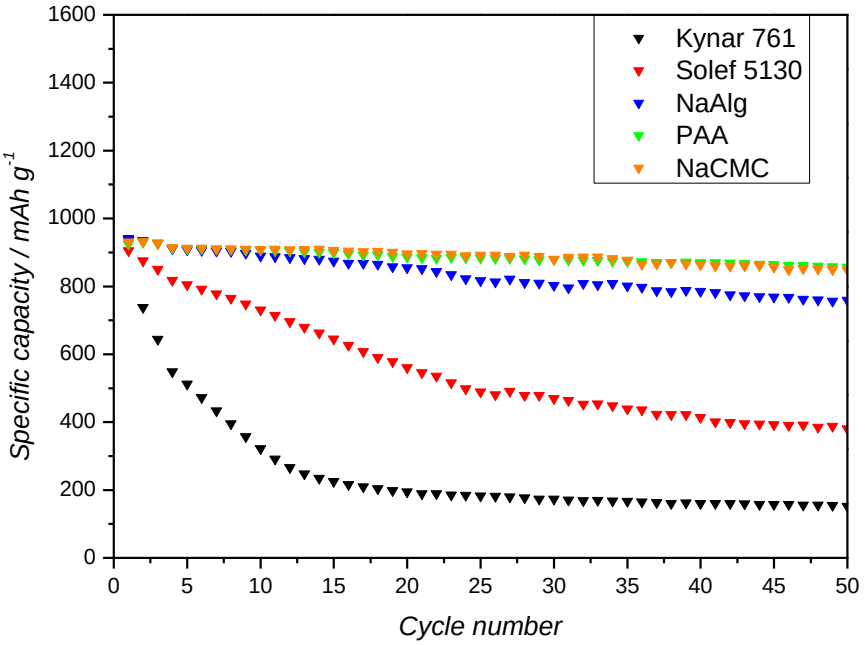

Figure 97. Delithiation capacities of core-shell composite electrodes produced with different binders

The comparison of the delithiation capacities shown in Figure 97 reveals an interesting trend. The more carboxy groups are present in the binder, the better the cycle stability is. This indicates that there are many polar groups present at the surface of the composite material. Hence, there are pristine SiNPs present at the composite surface or the pyrolyzed epoxy exhibits a considerable amount of oxidized moieties such as carboxy, hydroxy or carbonyl groups. The poor cycling behavior of PDVF (Kynar 761) is attributed to the low strength of the Van der Waals interactions compared to hydrogen bonding or covalent bonds. This can be especially seen in the remarkable cycling improvement if there are some carboxy groups present in the PDVF (Solef 5130) (*325*). The almost equal cycling performance of PAA and NaCMC (DS 1.2) reveals that the cycling performance is limited to the active material itself if a certain amount of carboxy groups are present. However, these binders will show differences concerning long term cyclizations, higher C-rates or higher mass loadings as then factors like tensile strength and elasticity will become more important. All in all, it can be said that NaCMC is a perfect choice not only for electrodes containing Si but also for the

fabrication of electrodes with this core-shell structured composite and PAA is an equal replacement.

Improvements of the cycle stability for these binders can probably be achieved by varying the pH value. This is because the carboxyl groups are electrostatically associated/dissociated depending on the neutralization degree and thus the polymer configuration can be modulated by the pH (*326*). The polymer configuration itself influences the distribution of the active materials and the conductive additive, as well as the adhesion strength (*327*).

4.5.9 Influence of the Cut-Off Voltages on the Electrochemical Performance

In addition to using different binders it is further investigated if the cut-off voltage of the lithiation or delithiation has a significant influence on the cycling performance. Regarding the lithiation it is examined whether the suppression of the c-$Li_{15}Si_4$ coupled with a limited lithiathion has a beneficial influence or not. In this context a cut-off voltage of 100 mV vs. Li/Li^+ is chosen, as the solid-state amorphization already takes place and the lithiation is limited approximately to 2/3 of the overall Si capacity (see Figure 98).

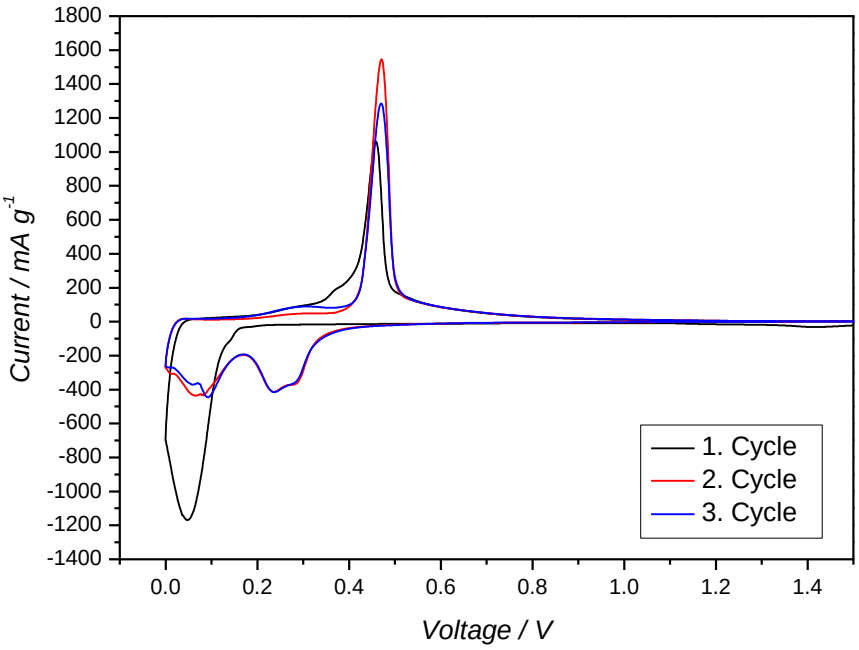

Figure 98. CV of a Si electrode with 10 µV/s scanning speed

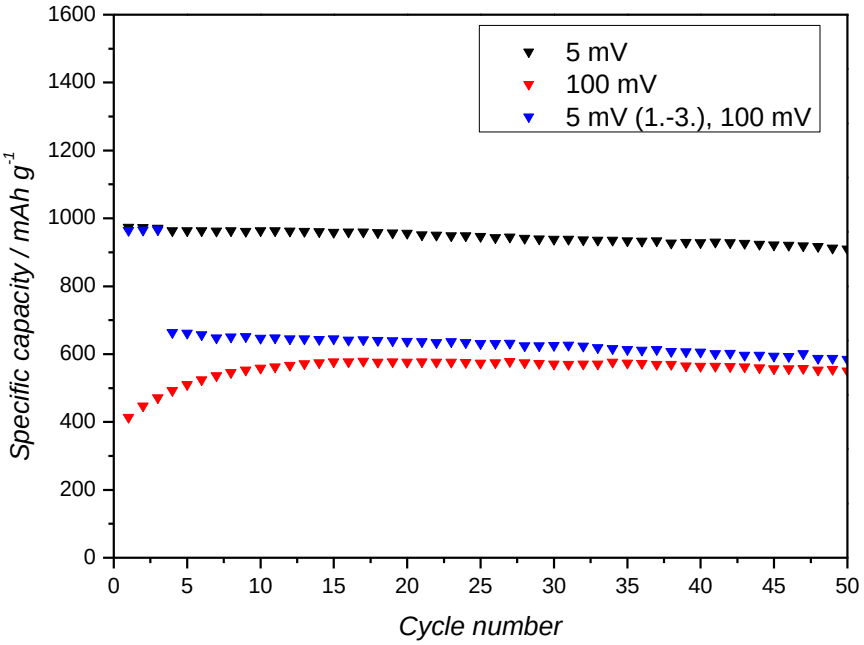

Figure 99. Delithiation capacities of a standard core-shell structured composite cycled with different lithiation cut-off voltages

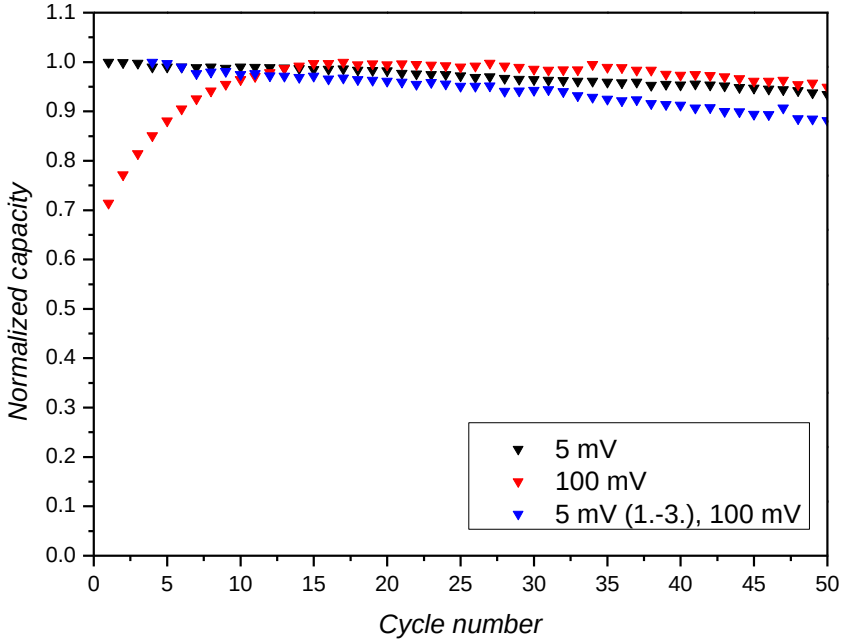

Figure 100. Normalized delithiation capacities of a standard core-shell structured composite cycled with different lithiation cut-off voltages

The previous figures reveal that using a higher cut-off voltage for the lithiation has no beneficial influence on the cycling performance. Instead the overall specific capacity is decreased enormously. The increase of the capacity during the first cycles, if a cut-off voltage of 100 mV vs. Li/Li^+ is used for all cycles, is very interesting. This behavior can be attributed to a gradually amorphization of the Si, which is then lithiated at higher potentials, and can be seen by the increase of the lithiation/delithiation signals for a-Si in Figure 101.

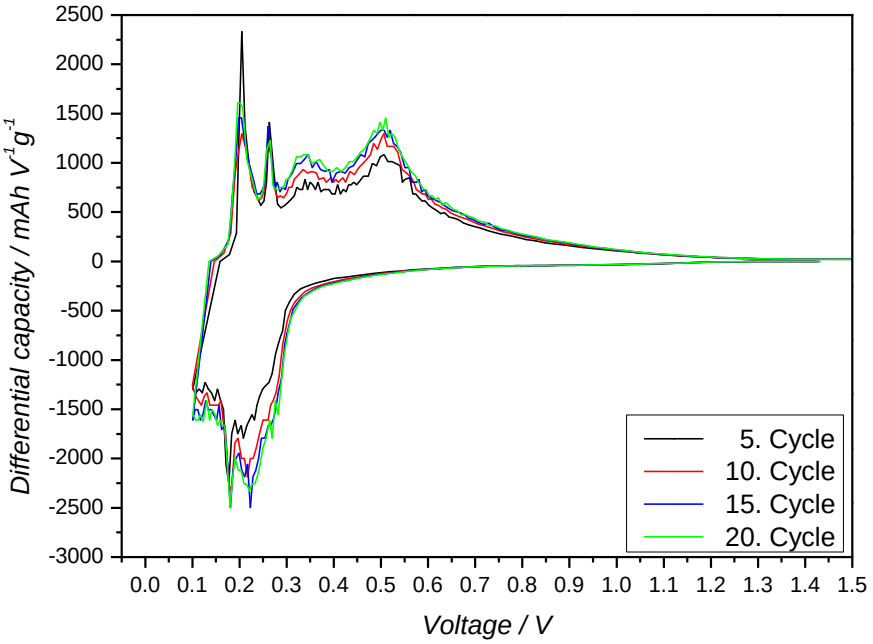

Figure 101. DCP comparison of different cycles using a lithiation cut-off voltage of 100 mV for all cycles

If the film forming cycles (cycle 1.-3.) have the standard lithiation cut-off voltage of 5 mV vs. Li/Li^+, the Si is already completely amorphous before applying 100 mV in the further cycles. This can be seen by the higher capacity in the 4. cycle and the gradually decreasing capacity upon cycling. However, the cycle stability does not improve and even deteriorates in regard to the normalized capacity. A possible explanation is the observed dynamic growth and dissolution of the SEI upon cycling (*328*,*329*). In the film forming cycles large amounts of passivating SEI are formed and they partially dissolve during delithiation. Due to the switch of the cut-off voltage to 100 mV vs. Li/Li^+ the balance between growth and dissolution seems to be disturbed, as usually a deep lithiation (< 20 mV) is necessary for a beneficial SEI formation (*330*,*331*). Hence, it seems that for the core-shell structured composite the SEI

plays the major role for the cycle stability compared to the mechanical stress induced to the volume changes and the c-$Li_{15}Si_4$ formation.

As a change of the lithiation cut-off voltage does not improve the cycling performance, it is investigated if a decrease of the delithiation cut-off voltage can do so. The benefit of this approach is a complete lithiation and consequently solid-state amorphization during the first cycle. Furthermore, the deep lithiation in the first and further cycles guarantees a beneficial SEI formation. By limiting the delithation cut-off voltage some Li remains (see Figure 102) in the SiNPs and increases their intrinsic electrical conductivity. Due to the limitation of the delithiation the overall cyclable capacity of the Si is reduced, as well as volume changes.

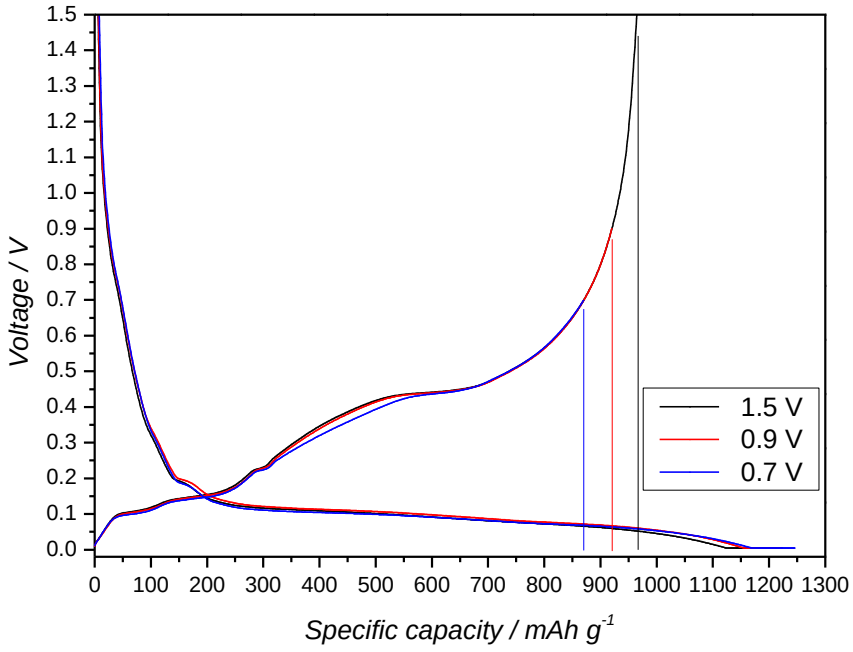

Figure 102. Voltage profiles of the first cycle of a standard core-shell structured composite cycled with different delithiation cut-off voltages

The cyclizations are performed with the standard delithiation cut-off voltage of 1.5 V, as well as 0.9 V and 0.7 V, and are compared with each other as shown in the following figures. If one takes a look at the delithiation capacities and the normalized capacities one can see an improvement of the cycle stability by using a cut-off voltage below 1.5 V. However, the capacity decreases too and hence a cut-off voltage of 0.9 V displays a good compromise between better cycle stability and only small loss of reversible capacity.

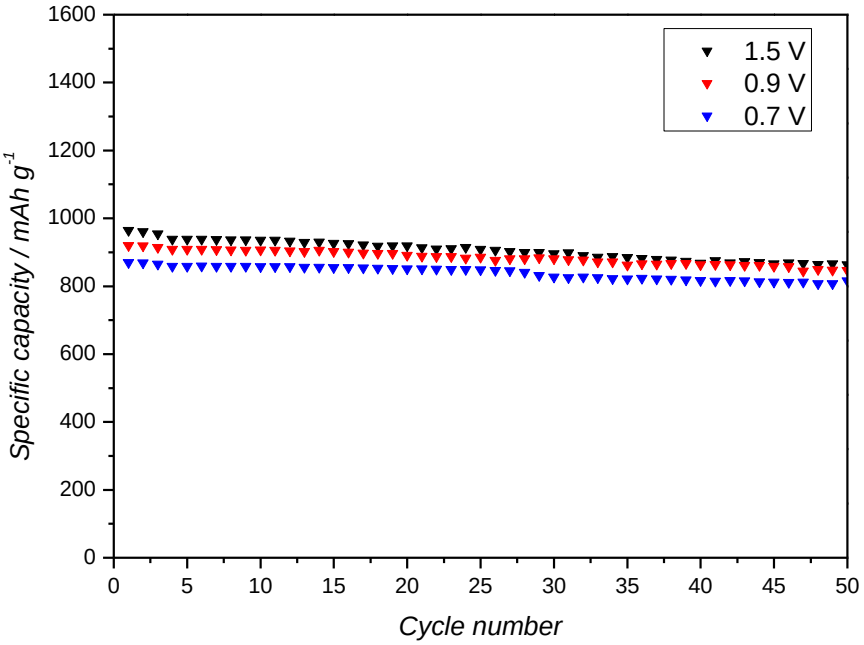

Figure 103. Delithiation capacities of a standard core-shell structured composite cycled with different delithiation cut-off voltages

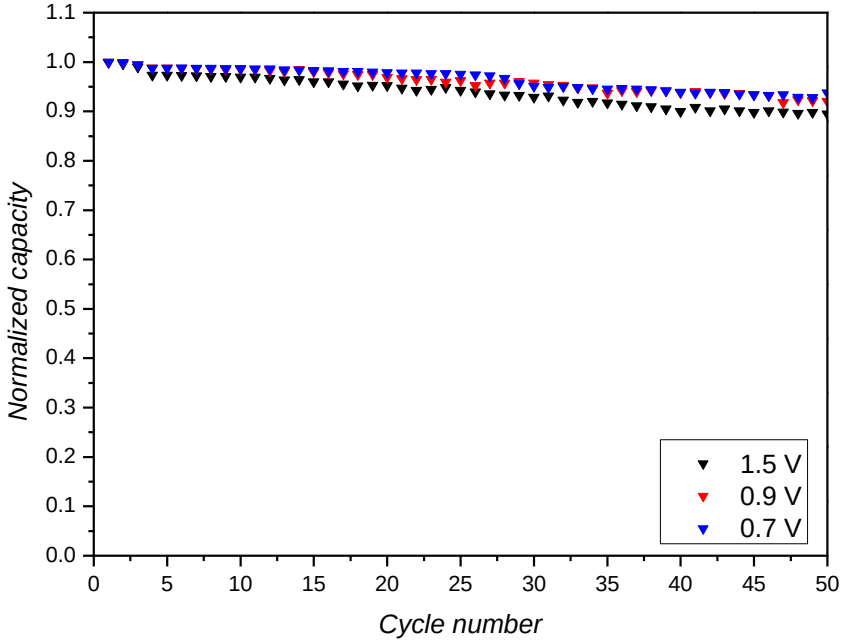

Figure 104. Normalized delithiation capacities of a core-shell structured composite cycled with different delithiation cut-off voltages

As the improvements of the cycle stability are generally low by limiting the cut-off voltages and thus the volume changes, one can say that the core-shell structured composite material is structurally very stable and the Si is well-embedded and electrochemically connected.

5 Conclusion

Within this doctoral thesis, the successful application of high energy planetary ball milling for the synthesis of nanosized Si as source for LIBs was demonstrated. In this context, the influence of various milling parameters on the particle size distribution was intensively studied in order to obtain a better understanding of the milling process for economical large scale production. Furthermore, the utilization of different milling solvents was studied and showed that the milling produces a highly reactive surface which leads to the functionalization of the Si. The radicals and dangling bonds on the surface are so reactive that they even react with C-H bonds of aliphatic or aromatic hydrocarbons. In addition, it could be shown that the milling process itself is strongly affected by the type of solvent used too. Alcohols typically accelerate the milling process and hence smaller particle sizes can be obtained economically. In contrast to alcohols, the use of alkanes, alkenes and benzene requires much longer milling durations, which is attributed to their lack of oxygen atoms, as an oxidized surface facilitates the particle cracking.

However, milled Si has the drawback that its particle size distribution leads to close packing densities of the particles if the solvent is removed. In combination with present silanol functionalities it facilitates the formation of aggregates whereat the particles are connected via Si-O-Si bonds and hence complete deagglomeration is impossible by applying ultrasonic. The negative effects of the agglomeration of these SiNPs on the electrochemical performance were studied and lead to the conclusion that the aggregates behave electrochemically like µm sized Si particles.

To cope with this problem, a method was developed at which the milling suspension itself can be used for the fabrication of a core-shell structured composite in a fluidized bed reactor and hence the formation of agglomerates can be suppressed. The SiNPs are embedded in a pyrolyzed epoxy matrix containing conductive additive, covering a graphite particle. As the matrix offers good electrochemical connectivity, mechanical stability and voids for volume expansion, it is an ideal method to make milled Si accessible for battery application. Investigations of these materials revealed the beneficial effect of planetary ball milling on the electrochemical performance, as milled Si with an average particle size of 130 nm shows an excellent cycling performance and further reduction of the particle size could not improve the cycling performance for the composite. This behavior is attributed to the special structure of milled Si at which a primary particle consists of small crystallites with amorphous crystallite boundaries. Furthermore it could be shown that the formation of c-$Li_{15}Si_4$ during complete lithiation is strongly dependend on the crystallite size and is keenly suppressed in milled Si

as a result of the small crystallite sizes obtained through the high energy ball impacts during milling. The suppression of this phase should be preferred as the delithiation of amorphous lithiated Si results in less mechanical stress, but more important is that the lower voltage hysteresis leads to higher energy efficiency. Very interestingly it was found that the amorphous and crystalline parts behave electrochemically different in milled Si, as due to the solid state amorphization all crystalline parts get amorphous during first lithiation and hence the particle is completely amorphous. If the electrochemically and mechanically induced amorphous parts act equally than the formation of the c-$Li_{15}Si_4$ would be more distinct for milled Si compared to the commercial pyrolysis-route Si with particle sizes of 30-50 nm. In this case, the c-$Li_{15}Si_4$ formation would be dependent on the primary Si particle size instead on the crystallite size.

Optimizations of the core-shell structured composite material showed that a large variety of curing agents can be used, which are usually cheaper and produce more stable shell due to the crosslinking of the epoxy. Too much crosslinking, however, is disadvantageous for the electrochemical performance as shown in the case of diethylenetriamine.

Furthermore, different pyrolysis conditions were investigated. The measurements revealed that a two-step pyrolysis showed better cycle stability compared to a single-step pyrolysis. This effect is attributed to the removal of decompositions products with low boiling point and high O- and N-content.

An increase of the epoxy content showed better cycle stability, but at the expense of lower CEs. This behavior is caused by the higher amount of conductive additive “filling material” needed to reduce the stickiness. The lower CE would then lead to rapid capacity fade in full cells and hence an increase of the epoxy should be avoided. Probably, the use of a different type of fluidized bed reactor enables an increase of the epoxy content without the addition of filling material.

Different binders were used for the fabrication of electrodes comprising the standard core-shell structured composite material. It could be shown that the electrochemical performance strongly depends on the amount of carboxy groups present in the binder. Hence, NaCMC and PAA showed the best performance as they have the largest number of the functionality. However, further studies are needed be carried out to investigate the long-term cycling performance and the dependency of the pH on the polymer configuration and thus in turn the electrode stability.

Furthermore, it is shown that the cycle stability can be improved if the cut-off voltage of the delithiation step is lower than 1.5 V.

6 Register

6.1 List of Chemicals

- Silicon powder, -325 mesh, 99 % trace metals basis, SIGMA-ALDRICH®, Stock # 215619
- Silicon Nanopowder, 50 g, 30-50 nm APS, 98 % purity, Nanostructured & Amorphous Materials Inc., Stock # 0141JS
- 1-Methoxy-2-propanol, ≥ 99 %, CARL ROTH®, Stock # 3123.2
- Ethanol, ≥ 99.8 %, CARL ROTH®, Stock # K928.4
- 1-Octene, ≥ 97 %, Merck Schuchardt, Stock # 8.20928.1000
- *n*-Heptane, 99 %, SIGMA-ALDRICH®, Stock # 246654
- Benzene, ≥ 99 %, SIGMA-ALDRICH®, Stock # 319953
- Qingdao, Qingdao Haida Graphite Co. Ltd.
- CNERGY™ Super C65, TIMCAL, Stock # 613 2707
- SOPROPHOR® FLK (Potassium polyarylphenyl ether phosphate), Rhodia, Stock # E90005300
- Sodium carboxymethyl cellulose, average M_w ~250,000; degree of substitution 1.2, SIGMA-ALDRICH®, Stock # 419281
- Electrolyte: 1.0 M $LiPF_6$ in EC/DEC (3:7), NOVOLYTE Technologies, Stock # 70001084
- Vinylene carbonate, 99 %, SIGMA-ALDRICH®, Stock # 757144
- Araldit® 506 epoxy resin, SIGMA-ALDRICH®, Stock # A3183
- 3-(Dimethylamino)-1-propylamine, 99 %, SIGMA-ALDRICH®, Stock # D145009
- Diethylenetriamine, 99 %, SIGMA-ALDRICH®, Stock # D93856
- Ethylenediamine, ≥ 99 %, SIGMA-ALDRICH®, Stock # E26266
- *m*-Xylylenediamine, 99 %, SIGMA-ALDRICH®, Stock # X1202
- *m*-Phenylenediamine, ≥ 99 %, SIGMA-ALDRICH®, Stock # P23954
- Poly(acrylic acid), average M_w ~450,000; SIGMA-ALDRICH®, Stock # 181285
- Alginic acid sodium salt, medium viscosity, SIGMA-ALDRICH®, Stock # A2033
- KYNAR® 761 PVDF, ARKEMA
- Solef 5130/1001, Solvay Speciality Polymers France

6.2 List of Figures

6.3 List of Tables

7 References

1. Wang, W.; Kumta, P. N. Reversible high capacity nanocomposite anodes of Si/C/SWNTs for rechargeable Li-ion batteries. *J. Power Sources* **2007,** *172,* 650-658.

2. Tarascon, J.-M.; Armand, M. Issues and challenges facing rechargeable lithium batteries. *Nature* **2001,** *414,* 359-367.

3. Pillot, C. The Rechargeable Battery Market and Main Trends 2014-2015. *32nd International Battery Seminar*, Fort Lauderale, USA, 2015; pp 1-69.

4. Scrosati, B.; Hassoun, J.; Sun, Y.-K. Lithium-ion batteries. A look into the future. *Energy Environ. Sci.* **2011,** *4,* 3287-3295.

5. Nitta, N.; Yushin, G. High-Capacity Anode Materials for Lithium-Ion Batteries: Choice of Elements and Structures for Active Particles. *Part. Part. Syst. Charact.* **2014,** *31,* 317-336.

6. Haas, M.; Korntner, R. Vorwort der Österreichischen NANO Inniative. In *Nano;* Gazso, A., Greßler, S., Schiemer, F., Eds.; Springer-Verlag: Wien, 2007; pp XI,XII.

7. Hornbogen, E.; Eggeler, G.; Werner, E. *Werkstoffe,* 10th ed.; Springer-Verlag: Berlin Heidelberg, 2012; pp 3-31.

8. Lechner, M. D.; Gehrke, K.; Nordmeier, E. H. Struktur der Makromoleküle. In *Makromolekulare Chemie,* 5th ed.; Lechner, M. D., Gehrke, K., Eds.; Springer-Verlag: Berlin Heidelberg, 2014; pp 3-60.

9. Schaefer, H.-E. *Nanoscience;* Springer-Verlag: Berlin Heidelberg, 2010; pp 1-7.

10. Sing, K. S.; Everett, D. H.; Haul, R. A.; Moscou, L.; Pierotti, R. A.; Rouquerol, J.; Siemieniewska, T. REPORTING PHYSISORPTION DATA FOR GAS/SOLID SYSTEMS with Special Reference to the Determination of Surface Area and Porosity. *Pure & Appl. Chem.* **1985,** *57* (4), 603-619.

11. Bargel, H.-J.; Schulze, G. *Werkstoffkunde,* 11th ed.; Springer-Verlag: Berlin Heidelberg, 2012; pp 392,393.

12. Benedix, R. *Bauchemie,* 4th ed.; Vieweg + Teubner: Wiesbaden, 2008; pp 493-506.

13. Hadley, P. http://lamp.tu-graz.ac.at//~hadley/nanoscience/week2/Nano-CdSe.png (accessed June 18, 2015).

14. Müller, U. *Anorganische Strukturchemie,* 6th ed.; Vieweg + Teubner: Wiesbaden, 2008; pp 349-355.

15. Daniel, M.-C.; Astruc, D. Gold Nanoparticles: Assembly, Supramolecular Chemistry,

Quantum-Size-Related Properties, and Applications toward Biology, Catalysis, and Nanotechnology. *Chem. Rev.* **2004,** *104,* 293-346.

16. Brust, M.; Kiely, C. J. Some recent advances in nanostructure preparation from gold and silver particles: a short topical review. *Colloids and Surfaces A: Physicochem. Eng. Aspects* **2002,** *175,* 175-186.

17. http://www.bbisolutions.com/media/cache/product_zoom/uploads/images/gold.jpg (accessed June 18, 2015).

18. Faraday, M. The Bakerian Lecture: Experimental Relations of Gold (and Other Metals) to Light. *Philos. Trans. R. Soc.* **1857,** *147,* 145-181.

19. Ostwald, W. F. Über die vermeintliche Isomerie des roten und gelben Quecksilberoxyds und die Oberflächenspannung fester Körper. *Z. Phys. Chem.* **1900,** *34,* 495-503.

20. Mie, G. Beiträge zur Optik trüber Medien, speziell kolloidaler Metallösungen. *Ann. Physik IV* **1908,** *25* (3), 377-445.

21. Rossetti, R.; Brus, L. Electron-hole recombination emission as a probe of surface chemistry in aqueous cadmium sulfide colloids. *J. Phys. Chem.* **1982,** *86* (23), 4470–4472.

22. Habenicht, G. *Kleben,* 6th ed.; Springer-Verlag: Berlin Heidelberg, 2009; pp 235-238.

23. Rähse, W. *Produktdesign in der chemischen Industrie;* Springer-Verlag: Berlin Heidelberg, 2007; pp 3-7.

24. Von Gleich, A.; Petschow, U.; Steinfeldt, M. Nachhaltigkeitspotenziale und Risiken von Nanotechnologien - Erkenntnisse aus der prospektiven Technikbewertung und Ansätze zur Gestaltung. In *Nano;* Gazso, A., Greßler, S., Schiemer, F., Eds.; Springer Verlag: Wien, 2007; pp 61-82.

25. Heath, J. R. A Liquid-Solution-Phase Synthesis of Crystalline Silicon. *Science* **1992,** *258* (5085), 1131-1133.

26. Baldwin, R. K.; Pettigrew, K. A.; Garno, J. C.; Power, P. P.; Liu, G.-y.; Kauzlarich, S. M. Room Temperature Solution Synthesis of Alkyl-Capped Tetrahedral Shaped Silicon Nanocrystals. *J. Am. Chem. Soc.* **2002,** *124* (7), 1150-1151.

27. Tilley, R. D.; Warner, J. H.; Yamamoto, K.; Matsui, I.; Fujimori, H. Micro-emulsion synthesis of monodisperse surface stabilized silicon nanocrystals. *Chem. Commun.* **2005,** 1833-1835.

28. Prabakar, S.; Shiohara, A.; Hanada, S.; Fujioka, K.; Yamamoto, K.; Tilley, R. D. Size Controlled Synthesis of Germanium Nanocrystals by Hydride Reducing Agents and Their Biological Applications. *Chem. Mater* **2010,** *22* (2), 482-486.

29. Wilcoxon, J. P.; Samara, G. A.; Provencio, P. N. Optical and electronic properties of Si

nanoclusters synthesized in inverse micelles. *Phys. Rev. B* **1999,** *60* (4), 2704-2714.

30. Wang, J.; Sun, S.; Cao, L.; Sun, L. Efficient one-pot synthesis of highly photoluminescent alkyl-functionalised silicon nanocrystals. *Chem. Commun.* **2011,** *47* (17), 4941-4943.

31. Rosso-Vasic, M.; Spruijt, E.; Popovic, Z.; Overgaag, K.; van Lagen, B.; Grandidier, B.; Vanmaekelbergh, D.; Dominguez-Gutierrez, D.; De Cola, L.; Zuilhof, H. Amine-terminated silicon nanoparticles: synthesis, optical properties and their use in bioimaging. *J. Mater. Chem.* **2009,** *19* (33), 5926-5933.

32. Wilcoxon, J. P.; Samara, G. A. Tailorable, visible light emission from silicon nanocrystals. *Appl. Phys. Lett.* **1999,** *74* (21), 3164-3166.

33. Shirahata, N.; Nakanishi, T.; Furumi, S.; Sakka, Y. One-Dimensional Self-Assembly of Alkoxy-Capped Silicon Nanoparticles. *J. Nanosci. Nanotechnol.* **2006,** *6* (6), 1823-1825.

34. Cheng, X.; Lowe, S. B.; Reece, P. J.; Justin Gooding, J. Colloidal silicon quantum dots: from preparation to the modification of self-assembled monolayers (SAMs) for bio-applications. *Chem. Soc. Rev.* **2014,** *43* (8), 2680-2700.

35. Tilley, R. D.; Yamamoto, K. The Microemulsion Synthesis of Hydrophobic and Hydrophilic Silicon Nanocrystals. *Adv. Mater* **2006,** *18* (15), 2053-2056.

36. Pan, X.-W.; Shi, M.-M.; Zheng, D.-X.; Liu, N.; Wu, G.; Wang, M.; Chen, H.-Z. Room-temperature solution route to free-standing SiO2-capped Si nanocrystals with green luminescence. *Mater. Chem. Phys.* **2009,** *117* (2-3), 517-521.

37. Gupta, A.; Swihart, M. T.; Wiggers, H. Luminescent Colloidal Dispersion of Silicon Quantum Dots from Microwave Plasma Synthesis: Exploring the Photoluminescence Behavior Across the Visible Spectrum. *Adv. Funct. Mater* **2009,** *19* (5), 696-703.

38. Ghosh, B.; Shirahata, N. Colloidal silicon quantum dots: synthesis and luminescence tuning from the near-UV to the near-IR range. *Sci. Technol. Adv. Mater* **2014,** *15,* 014207 (14pp).

39. Wiberg, N. *Lehrbuch der Anorganischen Chemie,* 102nd ed.; Walter de Gruyter & Co.: Berlin, 2007; pp 925-927.

40. Neiner, D.; Kauzlarich, S. M. Hydrogen-Capped Silicon Nanoparticles as a Potential Hydrogen Storage Material: Synthesis, Characterization, and Hydrogen Release. *Chem. Mater.* **2010,** *22* (2), 487-493.

41. Bley, R. A.; Kauzlarich, S. M. A Low-Temperature Solution Phase Route for the Synthesis of Silicon Nanoclusters. *J. Am. Chem. Soc.* **1996,** *118* (49), 12461-12462.

42. Bux, S. K.; Rodriguez, M.; Yeung, M. T.; Yang, C.; Makhluf, A.; Blair, R. G.; Fleurial, J.-P.; Kaner, R. B. Rapid Solid-State Synthesis of Nanostructured Silicon. *Chem. Mater* **2010,** *22* (8), 2534-2540.

43. Neiner, D.; Chiu, H. W.; Kauzlarich, S. M. Low-Temperature Solution Route to Macroscopic Amounts of Hydrogen Terminated Silicon Nanoparticles. *J. Am. Chem. Soc.* **2006,** *128* (34), 11016–11017.

44. Yang, C.-S.; Bley, R. A.; Kauzlarich, S. M.; Lee, H. W. H.; Delgado, G. R. Synthesis of Alkyl-Terminated Silicon Nanoclusters by a Solution Route. *J. Am. Chem. Soc.* **1999,** *121* (22), 5191-5195.

45. Shao, M.; Ma, D. D. D.; Lee, S.-T. Silicon Nanowires - Synthesis, Properties, and Applications. *Eur. J. Inorg. Chem.* **2010,** *2010* (27), 4264-4278.

46. Mangolini, L. Synthesis, properties and applications of silicon nanocrystals. *J. Vac. Sci. Technol. B* **2013,** *31* (2), 020801.

47. Calder, S.; Boies, A.; Lei, P.; Girshick, S.; Roberts, J. Photo-Assisted Hydrosilylation of Silicon Nanoparticles: Dependence of Particle Size on Grafting Chemistry. *Chem. Mater.* **2011,** *23* (11), 2917-2921.

48. Ostraat, M. L.; De Blauwe, J. W.; Green, M. L.; Bell, L. D.; Atwater, H. A.; Flagan, R. C. Ultraclean Two-Stage Aerosol Reactor for Production of Oxide-Passivated Silicon Nanoparticles for Novel Memory Devices. *J. Electrochem. Soc.* **2001,** *148* (5), G265-G270.

49. Lehtinen, K. E. J.; Zacharia, M. R. Energy accumulation in nanoparticle collision and coalescence processes. *Aerosol Sci.* **2002,** *33* (2), 357-368.

50. Mangolini, L.; Thimsen, E.; Kortshagen, U. High-Yield Plasma Synthesis of Luminescent Silicon Nanocrystals. *Nano Lett.* **2005,** *5* (4), 655-659.

51. Anthony, R. J.; Rowe, D. J.; Stein, M.; Yang, J.; Kortshagen, U. Routes to Achieving High Quantum Yield Luminescence. *Adv. Funct. Mater.* **2011,** *21* (21), 4042-4046.

52. Holmes, J. D.; Ziegler, K. J.; Doty, C. R.; Pell, L. E.; Johnston, K. P.; Korgel, B. A. Highly Luminescent Silicon Nanocrystals with Discrete Optical Transitions. *J. Am. Chem. Soc.* **2001,** *123* (16), 3743-3748.

53. Liu, S.-m.; Sato, S.; Kimura, K. Synthesis of Luminescent Silicon Nanopowders Redispersible to Various Solvents. *Langmuir* **2005,** *21* (14), 6324-6329.

54. Nesheva, D.; Raptis, C.; Perakis, A.; Bineva, I.; Aneva, Z.; Levi, Z.; Alexandranova, S.; Hofmeister, H. Raman scattering and photoluminescence from Si nanoparticles in annealed SiOx thin films. *J. Appl. Phys.* **2002,** *92* (8), 4678-4683.

55. Liu, S.-M.; Yang, Y.; Sato, S.; Kimura, K. Enhanced Photoluminescence from Si Nano-organosols by Functionalization with Alkenes and Their Size Evolution. *Chem. Mater.* **2006,** *18* (3), 637-642.

56. Hessel, C. M.; Reid, D.; Panthani, M. G.; Rasch, M. R.; Goodfellow, B. W.; Wei, J.; Fujii, H.; Akhavan, V.; Korgel, B. A. Synthesis of Ligand-Stabilized Silicon Nanocrystals with

Size-Dependent Photoluminescence Spanning Visible to Near-Infrared Wavelengths. *Chem. Mater.* **2012,** *24* (2), 393-401.

57. Kelly, J. A.; Henderson, E. J.; Veinot, J. G. C. Sol–gel precursors for group 14 nanocrystals. *Chem. Commun.* **2010,** *46,* 8704-8718.

58. Henderson, E. J.; Kelly, J. A.; Veinot, J. G. C. Influence of HSiO1.5 Sol-Gel Polymer Structure and Composition on the Size and Luminescent Properties of Silicon Nanocrystals. *Chem. Mater.* **2009,** *21* (22), 5426-5434.

59. Li, X.; He, Y.; Talukdar, S. S.; Swihart, M. T. Process for Preparing Macroscopic Quantities of Brightly Photoluminescent Silicon Nanoparticles with Emission Spanning the Visible Spectrum. *Langmuir* **2003,** *19* (20), 8490-8496.

60. Kang, Z.; Liu, Y.; Tsang, C. H. A.; Ma, D. D. D.; Fan, X.; Wong, N.-B.; Lee, S.-T. Water-Soluble Silicon Quantum Dots with Wavelength-Tunable Photoluminescence. *Adv. Mater.* **2009,** *21* (6), 661-664.

61. Bagabas, A. A.; Gondal, M. A.; Dastageer, M. A.; Al-Muhanna, A. A.; Alanazi, T. H.; Ababtain, M. A. A study of laser-induced blue emission with nanosecond decay of silicon nanoparticles synthesized by a chemical etching method. *Nanotechnology* **2009,** *20* (35), 355703.

62. Huang, Z.; Geyer, N.; Werner, P.; de Boor, J.; Gösele, U. Metal-Assisted Chemical Etching of Silicon: A Review. *Adv. Mater.* **2011,** *23* (2), 285-308.

63. Han, H.; Huang, Z.; Lee, W. Metal-assisted chemical etching of silicon and nanotechnology applications. *Nano Today* **2014,** *9* (3), 271-307.

64. Zhang, M.-L.; Peng, K.-Q.; Fan, X.; Jie, J.-S.; Zhang, R.-Q.; Lee, S.-T.; Wong, N.-B. Preparation of Large-Area Uniform Silicon Nanowires Arrays through Metal-Assisted Chemical Etching. *J. Phys. Chem. C* **2008,** *112* (12), 4444-4450.

65. Peng, K.-Q.; Hu, J.; Wu, Y.; Fang, H.; Xu, Y.; Lee, S.-T.; Zhu, J. Fabrication of Single-Crystalline Silicon Nanowires by Scratching a Silicon Surface with Catalytic Metal Particles. *Adv. Funct. Mater.* **2006,** *16* (3), 387-394.

66. Peng, K.-Q.; Wang, X.; Wu, X.-L.; Lee, S.-T. Platinum Nanoparticle Decorated Silicon Nanowires for Efficient Solar Energy Conversion. *Nano Lett.* **2009,** *9* (11), 3704-3709.

67. Weisse, J. M.; Kim, D. R.; Lee, C. H.; Zheng, X. Vertical Transfer of Uniform Silicon Nanowire Arrays via Crack Formation. *Nano Lett.* **2011,** *11* (3), 1300-1305.

68. Uhlir, A. Electrolytic shaping of germanium and silicon. *Bell Syst. Tech. J.* **1956,** *35* (2), 333-347.

69. Watanabe, Y.; Arita, Y.; Yokoyama, T.; Igarashi, Y. Formation and Properties of Porous Silicon and Its Application. *J. Electrochem. Soc.* **1975,** *122* (10), 1351-1355.

70. Cullis, A. G.; Canham, L. T. Visible light emission due to quantum size effects in highly porous crystalline silicon. *Nature* **1991,** *353* (6342), 335-338.

71. Cullis, A. G.; Canham, L. T.; Calcott, P. D. J. The structural and luminescence properties of porous silicon. *J. Appl. Phys.* **1997,** *82* (3), 909-965.

72. Bley, R. A.; Kauzlarich, S. M.; Davis, J. E.; Lee, H. W. H. Characterization of Silicon Nanoparticles Prepared from Porous Silicon. *Chem. Mater.* **1996,** *8* (8), 1881-1888.

73. Kang, Z.; Tsang, C. H.; Zhang, Z.; Zhang, M.; Wong, N.-B.; Zapien, J. A.; Shan, Y.; Lee, S.-T. A Polyoxometalate-Assisted Electrochemical Method for Silicon Nanostructures Preparation: From Quantum Dots to Nanowires. *J. Am. Chem. Soc.* **2007,** *129* (17), 5326-5327.

74. He, Y.; Su, Y.; Yang, X.; Kang, Z.; Xu, T.; Zhang, R.; Fan, C.; Lee, S.-T. Photo and pH Stable, Highly-Luminescent Silicon Nanospheres and Their Bioconjugates for Immunofluorescent Cell Imaging. *J. Am. Chem. Soc.* **2009,** *131* (12), 4434-4438.

75. Svrcek, V.; Mariotti, D.; Kondo, M. Ambient-stable blue luminescent silicon nanocrystals prepared by nanosecond-pulsed laser ablation in water. *Optics Express* **2009,** *17* (2), 520-527.

76. Zhang, Y. F.; Tang, Y. H.; Wang, N.; Yu, D. P.; Lee, C. S.; Bello, I.; Lee, S. T. Silicon nanowires prepared by laser ablation at high temperature. *Appl. Phys. Lett.* **1998,** *72* (15), 1835-1837.

77. Makino, T.; Inada, M.; Umezu, I.; Sugimura, A. Structural and optical properties of surface-hydrogenated silicon nanocrystallites prepared by reactive pulsed laser ablation. *J. Phys. D: Appl. Phys.* **2005,** *38* (18), 3507-3511.

78. Okada, R.; Iijima, S. Oxidation property of silicon small particles. *Appl. Phys. Lett.* **1991,** *58* (15), 1662-1663.

79. Torricelli, G.; Akraiam, A.; von Haeften, K. Size-selecting effect of water on fluorescent silicon clusters. *Nanotechnology* **2011,** *22* (31), 315711.

80. Svrcek, V.; Sasaki, T.; Shimizu, Y.; Koshizaki, N. Blue luminescent silicon nanocrystals prepared by ns pulsed laser ablation in water. *Appl. Phys. Lett.* **2006,** *89* (21), 213113.

81. Werwa, E.; Seraphin, A. A.; Chiu, L. A.; Zhou, C.; Kolenbrander, K. D. Synthesis and processing of silicon nanocrystallites using a pulsed laser ablation supersonic expansion method. *Appl. Phys. Lett.* **1994,** *64* (14), 1821-1823.

82. Yang, S.; Cai, W.; Zeng, H.; Li, Z. Polycrystalline Si nanoparticles and their strong aging enhancement of blue photoluminescence. *J. Appl. Phys.* **2008,** *104* (2), 023516.

83. Shirahata, N.; Linford, M. R.; Furumi, S.; Pei, L.; Sakka, Y.; Gates, R. J.; Asplund, M. C. Laser-derived one-pot synthesis of silicon nanocrystals terminated with organic monolayers. *Chem. Commun.* **2009,** No. 31, 4684–4686.

84. Tan, D.; Xu, B.; Chen, P.; Dai, Y.; Zhou, S.; Ma, G.; Qiu, J. One-pot synthesis of luminescent hydrophilic silicon nanocrystals. *RSC Adv.* **2012,** *2* (22), 8254–8257.

85. Pabi, S. K.; Joardar, J.; Murty, B. S. Mechanism and Kinetics of Alloying and Nanostructure Formation by Mechanical Methods. *PINSA* **2001,** *67 A* (1), 1-30.

86. Russo, L.; Colangelo, F.; Cioffi, R.; Rea, I.; De Stefano, L. A Mechanochemical Approach to Porous Silicon Nanoparticles Fabrication. *Materials* **2011,** *4* (6), 1023-1033.

87. Gaffet, E.; Bernard, F.; Niepce, J.-C.; Charlot, F.; Gras, C.; Le Caer, G.; Guichard, J.-L.; Delcroix, P.; Mocellin, A.; Tillement, O. Some recent developements in mechanical activation and mechanosynthesis. *J. Mater. Chem.* **1999,** *9* (1), 305-314.

88. Gaffet, E.; Le Caer, G. Mechanical Processing for Nanomaterials. In *Encyclopedia of Nanoscience and Nanotechnology;* Nalwa, H. S., Ed.; American Scientific Publisher, 2004; Vol. X, pp 1-39.

89. Suryanarayana, C. Mechanical alloying and milling. *Prog. Mater. Sci.* **2001,** *46* (1-2), 1-184.

90. Yadav, T. P.; Yadav, R. M.; Singh, D. P. Mechanical Milling: a Top Down Approach for the Synthesis of Nanomaterials and Nanocomposites. *Nanoscience and Nanotechnology* **2012,** *2* (3), 22-48.

91. Hallmann, S.; Fink, M. J.; Mitchell, B. S. The Mechanochemical Formation of Functionalized Semiconductor Nanoparticles for Biological, Electronic and Superhydrophobic Surface Applications. In *Advances in Nanomaterials and Nanostructures;* Lu, K., Manjooran, N., Radovic, M., Medvedovsk, E., Olevsky, E. A., Li, C., Singh, G., Chopra, N., Pickrell, G., Eds.; The American Ceramic Society, 2011; pp 129-142.

92. Heintz, A. S.; Fink, M. J.; Mitchell, B. S. Silicon nanoparticles with chemically tailored surfaces. *Appl. Organometal. Chem.* **2010,** *24* (3), 236-240.

93. Heintz, A. S.; Fink, M. J.; Mitchell, B. S. Mechanochemical Synthesis of Blue Luminescent Alkyl/Alkenyl-Passivated Silicon Nanoparticles. *Adv. Mater.* **2007,** *19* (22), 3984-3988.

94. Hallmann, S.; Fink, M. J.; Mitchell, B. S. Wetting properties of silicon films from alkyl-passivated particles produced by mechanochemical synthesis. *J. Colloid Interface Sci.* **2010,** *348* (2), 634-641.

95. Verdoni, L. P.; Fink, M. J.; Mitchell, B. S. A fractionation process of mechanochemically synthesized blue-green luminescent alkyl-passivated silicon nanoparticles. *Chem. Eng. J.* **2011,** *172* (1), 591-600.

96. Araujo-Andrade, C.; Espinoza-Beltran, F. J.; Jimenez-Sandoval, S.; Gonzalez-Hernandez, J. Synthesis of nanocrystalline Si particles from a solid-state reaction during

a ball-milling process. *Scr. Mater.* **2003,** *49* (8), 773-778.

97. Feng, X.; Yang, J.; Lu, Q.; Wang, J.; Nuli, Y. Facile approach to SiOx/Si/C composite anode material from bulk SiO for lithium ion batteries. *Phys. Chem. Chem. Phys.* **2013,** *15* (34), 14420-14426.

98. Chaudhary, A.-L.; Sheppard, D. A.; Paskevicius, M.; Saunders, M.; Buckley, C. E. Mechanochemical synthesis of amorphous silicon nanoparticles. *RSC Adv.* **2014,** *4* (42), 21979–21983.

99. Benyoucef, M.; Usman, M.; Alzoubi, T.; Reithmaier, J. P. Pre-patterned silicon substrates for the growth of III–V nanostructures. *Phys. Status Solidi A* **2012,** *209* (12), 2402–2410.

100. Tennant, D. M. Progress and issues in e-beam and other top down nanolithography. *J. Vac. Sci. Technol. A* **2013,** *31* (5), 050813.

101. Baumann, P. *Darstellung von oberflächenfunktionalisierten Silicium-Nanopartikeln als Hochleistungsanodenmaterial für Lithium-Ionen-Batterien;* Master Thesis; Technische Universität Graz, 2012.

102. Linden, D.; Reddy, T. B. Basic Concepts. In *Linden's Handbook of Batteries,* 4th ed.; Reddy, T. B., Linden, D., Eds.; Mc-Graw-Hill Companies: New York, 2011; pp 1.3-1.17.

103. Winter, M.; Brodd, R. J. What are Batteries, Fuel Cells, and Supercapacitors? *Chem. Rev.* **2004,** *104* (10), 4245-4269.

104. Hamann, C. H.; Vielstich, W. Galvanische Elemente. In *Elektrochemie,* 4th ed.; Hamann, C. H., Vielstich, W., Eds.; Wiley-VCH Verlag GmbH&Co: Weinheim, 2005; pp 481-558.

105. Yoshino, A. The Birth of the Lithium-Ion Battery. *Angew. Chem. Int. Ed.* **2012,** *51* (24), 5798-5800.

106. Long, J. W.; Dunn, B.; Rolison, D. R.; White, H. S. Three-Dimensional Battery Architectures. *Chem. Rev.* **2004,** *104* (10), 4463-4492.

107. Scrosati, B. History of lithium batteries. *J. Solid State Electrochem.* **2011,** *15* (7-8), 1623–1630.

108. Whittingham, M. S. Chemistry of intercalation compounds: Metal guests in chalcogenide hosts. *Prog. Solid State Chem.* **1978,** *12* (1), 41-99.

109. Winter, M.; Besenhard, J. O.; Spahr, M. E.; Novak, P. Insertion Electrode Materials for Rechargeable Lithium Batteries. *Adv. Mater.* **1998,** *10* (10), 725-763.

110. Broussely, M.; Biensan, P.; Simon, B. Lithium insertion into host materials: the key to success for Li ion batteries. *Electrochim. Acta* **1999,** *45* (1-2), 3-22.

111. Nishi, Y. Lithium ion secondary batteries; past 10 years and the future. *J. Power Sources* **2001,** *100* (1-2), 101–106.

112. Murphy, D. W.; Di Salvo, F. J.; Carides, J. N.; Waszczak, J. V. Topochemical reactions of rutile related structures with lithium. *Mater. Res. Bull.* **1978,** *13* (12), 1395-1402.

113. Di Pietro, B.; Patriarca, M.; Scrosati, B. On the use of rocking chair configurations for cyclable lithium organic electrolyte batteries. *J. Power Sources* **1982,** *8* (2), 289-299.

114. Yoshino, A.; Sanechika, K.; Nakajima, T. Secondary battery. USP4,668,595, May 10, 1985.

115. Mizushima, K.; Jones, P. C.; Wiseman, P. J.; Goodenough, J. B. LixCoO2: A new cathode material for batteries of high energy density. *Solid State Ionics* **1981,** *3-4,* 171–174.

116. Nagaura, T.; Tozawa, K. Lithium ion rechargeable battery. *Prog. Batteries Solar Cells* **1990,** *9,* 209-217.

117. Wang, Y.; Liu, B.; Cartmell, S.; Ferrara, S.; Deng, Z. D.; Xiao, J. Lithium and lithium ion batteries for applications in microelectronic devices: A review. *J. Power Sources* **2015,** *286,* 330-345.

118. Varta Storage GmbH. Engion Broschüre. http://varta-storage.de/fileadmin/media/files/downloads/2015-06-09-210x297_VARTA_Storage_Broschuere_VARTA_Storage.pdf (accessed Juli 6, 2015).

119. Goodenough, J. B.; Park, K.-S. The Li-Ion Rechargeable Battery: A Perspective. *J. Am. Chem. Soc.* **2013,** *135* (4), 1167−1176.

120. Xu, B.; Qian, D.; Wang, Z.; Meng, Y. S. Recent progress in cathode materials research for advanced lithium ion batteries. *Mater. Sci. Eng. R* **2012,** *73* (5-6), 51-65.

121. Fergus, J. W. Recent developments in cathode materials for lithium ion batteries. *J. Power Sources* **2010,** *195* (4), 939-954.

122. Whittingham, M. S. Lithium Batteries and Cathode Materials. *Chem. Rev.* **2004,** *104* (10), 4271-4301.

123. He, P.; Yu, H.; Li, D.; Zhou, H. Layered lithium transition metal oxide cathodes towards high energy lithium-ion batteries. *J. Mater. Chem.* **2012,** *22* (9), 3680–3695.

124. Kraytsberg, A.; Ein-Eli, Y. Higher, Stronger, Better… A Review of 5 Volt Cathode Materials for Advanced Lithium-Ion Batteries. *Adv. Energy Mater.* **2012,** *2* (8), 922-939.

125. Bazito, F. F. C.; Torresi, R. M. Cathodes for Lithium Ion Batteries: The Benefits of Using Nanostructured Materials. *J. Braz. Chem. Soc.* **2006,** *17* (4), 627-642.

126. Pitchai, R.; Thavasi, V.; Mhaisalkar, S. G.; Ramakrishna, S. Nanostructured cathode materials: a key for better performance in Li-ion batteries. *J. Mater. Chem.* **2011,** *21*

(30), 11040-11051.

127. Goodenough, J. B. Cathode materials: A personal perspective. *J. Power Sources* **2007,** *174* (2), 996–1000.

128. Xu, X.; Lee, S.; Jeong, S.; Kim, Y.; Cho, J. Recent progress on nanostructured 4 V cathode materials for Li-ion batteries for mobile electronics. *Mater. Today* **2013,** *16* (12), 487–495.

129. Koksbang, R.; Barker, J.; Shi, H.; Saidi, M. Y. Cathode materials for lithium rocking chair batteries. *Solid State Ionics* **1996,** *84* (1-2), 1–21.

130. Ohzuku, T.; Brodd, R. J. An overview of positive-electrode materials for advanced lithium-ion batteries. *J. Power Sources* **2007,** *174* (2), 449–456.

131. Guilmard, M.; Croguennec, L.; Denux, D.; Delmas, C. Thermal Stability of Lithium Nickel Oxide Derivatives. Part I: LixNi1.02O2 and LixNi0.89Al0.16O2 (x = 0.50 and 0.30). *Chem. Mater.* **2003,** *15* (23), 4476–4483.

132. Bruce, P. G.; Armstrong, A. R.; Gitzendanner, R. L. New intercalation compounds for lithium batteries: layered LiMnO2. *J. Mater. Chem.* **1999,** *9* (1), 193-198.

133. Whittingham, M. S. Ultimate Limits to Intercalation Reactions for Lithium Batteries. *Chem. Rev.* **2014,** *114* (23), 11414−11443.

134. Lee, K.-S.; Myung, S.-T.; Amine, K.; Yashiro, H.; Sun, Y.-K. Structural and Electrochemical Properties of Layered $Li[Ni_{1-2x}Co_xMn_x]O_2$ $(x = 0.1 - 0.3)$ Positive Electrode Materials for Li-Ion Batteries. *J. Electrochem. Soc.* **2007,** *154* (10), A971-A977.

135. Yu, H.; Zhou, H. High-Energy Cathode Materials (Li_2MnO_3−$LiMO_2$) for Lithium-Ion Batteries. *J. Phys. Chem. Lett.* **2013,** *4* (8), 1268−1280.

136. Yan, J.; Liu, X.; Li, B. Recent progress in Li-rich layered oxides as cathode materials for Li-ion batteries. *RSC Adv.* **2014,** *4* (108), 63268-63284.

137. Yu, L.; Qiu, W.; Lian, F.; Huang, J.; Kang, X. Understanding the phenomenon of increasing capacity of layered $0.65Li[Li_{1/3}Mn_{2/3}]O_2 \cdot 0.35Li(Ni_{1/3}Co_{1/3}Mn_{1/3})O_2$. *J. Alloys Compd.* **2009,** *471* (1-2), 317-321.

138. Song, B.; Liu, Z.; Lai, M. O.; Lu, L. Structural evolution and the capacity fade mechanism upon long-term cycling in Li-rich cathode material. *Phys. Chem. Chem. Phys.* **2012,** *14* (37), 12875-12883.

139. Wang, Y.; Cao, G. Developments in Nanostructured Cathode Materials for High-Performance Lithium-Ion Batteries. *Adv. Mater.* **2008,** *20* (12), 2251–2269.

140. Aravindan, V.; Gnanaraj, J.; Lee, Y.-S.; Madhavi, S. $LiMnPO_4$ – A next generation cathode material for lithium-ion batteries. *J. Mater. Chem. A* **2013,** *1* (11), 3518-3539.

141. Zhang, Y.; Huo, Q.-y.; Du, P.-p.; Wang, L.-z.; Zhang, A.-q.; Song, Y.-h.; Lv, Y.; Li, G.-y. Advances in new cathode material LiFePO4 for lithium-ion batteries. *Synth. Met.* **2012,** *162* (13-14), 1315– 1326.

142. Chang, Z.-R.; Lv, H.-J.; Tang, H.-W.; Li, H.-J.; Yuan, X.-Z.; Wang, H. Synthesis and characterization of high-density LiFePO4/C composites as cathode materials for lithium-ion batteries. *Electrochim. Acta* **2009,** *54* (20), 4595-4599.

143. Wu, S.-h.; Chen, M.-S.; Chien, C.-J.; Fu, Y.-P. Preparation and characterization of Ti4+-doped LiFePO4 cathode materials for lithium-ion batteries. *J. Power Sources* **2009,** *189* (1), 440–444.

144. Hu, M.; Pang, X.; Zhou, Z. Recent progress in high-voltage lithium ion batteries. *J. Power Sources* **2013,** *237* (1), 229–242.

145. Liu, D.; Trottier, J.; Gagnon, C.; Barray, F.; Guerfi, A.; Mauger, A.; Groult, H.; Julien, C. M.; Goodenough, J. B.; Zaghib, K. Spinel materials for high-voltage cathodes in Li-ion batteries. *RSC Adv.* **2014,** *4* (1), 154-167.

146. Liu, Q.; Wang, S.; Tan, H.; Yang, Z.; Zeng, J. Preparation and Doping Mode of Doped LiMn2O4 for Li-Ion Batteries. *Energies* **2013,** *6* (3), 1718-1730.

147. Kim, J.-H.; Pieczonka, N. P. W.; Yang, L. Challenges and Approaches for High-Voltage Spinel Lithium-Ion Batteries. *ChemPhysChem* **2014,** *15* (10), 1940-1954.

148. Manthiram, A.; Chemelewski, K.; Lee, E.-S. A perspective on the high-voltage LiMn1.5Ni0.5O4 spinel cathode for lithium-ion batteries. *Energy Environ. Sci.* **2014,** *7* (4), 1339-1350.

149. Masquelier, C.; Croguennec, L. Polyanionic (Phosphates, Silicates, Sulfates) Frameworks as Electrode Materials for Rechargeable Li (or Na) Batteries. *Chem. Rev.* **2013,** *113* (8), 6552–6591.

150. Scrosati, B.; Garche, J. Lithium batteries: Status, prospects and future. *J. Power Sources* **2010,** *195* (9), 2419–2430.

151. Manthiram, A. Materials Challenges and Opportunities of Lithium Ion Batteries. *J. Phys. Chem. Lett.* **2011,** *2* (3), 176–184.

152. Manthiram, A.; Fu, Y.; Su, Y.-S. Challenges and Prospects of Lithium-Sulfur Batteries. *Acc. Chem. Res.* **2013,** *46* (5), 1125–1134.

153. Girishkumar, G.; McCloskey, B.; Luntz, A. C.; Swanson, S.; Wilcke, W. Lithium-Air Battery: Promise and Challenges. *J. Phys. Chem. Lett.* **2010,** *1* (14), 2193–2203.

154. Xu, J.; Dou, S.; Liu, H.; Dai, L. Cathode materials for next generation lithium ion batteries. *Nano Energy* **2013,** *2* (4), 439–442.

155. Liang, C.; Gao, M.; Pan, H.; Liu, Y.; Yan, M. Lithium alloys and metal oxides as high-

capacity anode materials for lithium-ion batteries. *J. Alloys Compd.* **2013,** *575,* 246–256.

156. Choi, N.-S.; Chen, Z.; Freunberger, S. A.; Ji, X.; Sun, Y.-K.; Amine, K.; Yushin, G.; Nazar, L. F.; Cho, J.; Bruce, P. G. Challenges Facing Lithium Batteries and Electrical Double-Layer Capacitors. *Angew. Chem. Int. Ed.* **2012,** *51* (40), 9994 – 10024.

157. Monroe, C.; Newman, J. The Impact of Elastic Deformation on Deposition Kinetics at Lithium/Polymer Interfaces. *J. Electrochem. Soc.* **2005,** *152* (2), A396–A404.

158. Zheng, G.; Lee, S. W.; Liang, Z.; Lee, H.-W.; Yan, K.; Yao, H.; Wang, H.; Li, W.; Chu, S.; Cui, Y. Interconnected hollow carbon nanospheres for stable lithium metal anodes. *Nat. Nanotechnol.* **2014,** *9* (8), 618–623.

159. Xu, W.; Wang, J.; Ding, F.; Chen, X.; Nasybulin, E.; Zhang, Y.; Zhang, J.-G. Lithium metal anodes for rechargeable batteries. *Energy Environ. Sci.* **2014,** *7* (2), 513-537.

160. Goriparti, S.; Miele, E.; De Angelis, F.; Di Fabrizio, E.; Zaccaria, R. P.; Capiglia, C. Review on recent progress of nanostructured anode materials for Li-ion batteries. *J. Power Sources* **2014,** *257* (1), 421–443.

161. Endo, M.; Kim, C.; Nishimura, K.; Fujino, T.; Miyashita, K. Recent development of carbon materials for Li ion batteries. *Carbon* **2000,** *38* (2), 183–197.

162. Roy, P.; Srivastava, S. K. Nanostructured anode materials for lithium ion batteries. *J. Mater. Chem. A* **2015,** *3* (6), 2454-2484.

163. Noel, M.; Suryanarayanan, V. Role of carbon host lattices in Li-ion intercalation/de-intercalation processes. *J. Power Sources* **2002,** *111* (2), 193–209.

164. Wakihara, M. Recent developments in lithium ion batteries. *Mater. Sci. Eng. R* **2001,** *33* (4), 109-134.

165. He, H.; Huang, C.; Luo, C.-W.; Liu, J.-J.; Chao, Z.-S. Dynamic study of Li intercalation into graphite by in situ high energy synchrotron XRD. *Electrochim. Acta* **2013,** *92,* 148–152.

166. Ohzuku, T.; Iwakoshi, Y.; Sawai, K. Formation of Lithium-Graphite Intercalation Compounds in Nonaqueous Electrolytes and Their Application as a Negative Electrode for a Lithium Ion (Shuttlecock) Cell. *J. Electrochem. Soc.* **1993,** *140* (9), 2490-2498.

167. Wang, S.; Matsumura, Y.; Maeda, T. A model of the interactions between disordered carbon and lithium. *Synth. Met.* **1995,** *71* (1-3), 1759-1760.

168. Schauerman, C. M.; Ganter, M. J.; Gaustad, G.; Babbitt, C. W.; Raffaelle, R. P.; Landi, B. J. Recycling single-wall carbon nanotube anodes from lithium ion batteries. *J. Mater. Chem.* **2012,** *22* (24), 12008-12015.

169. Ji, L.; Lin, Z.; Alcoutlabi, M.; Zhang, X. Recent developments in nanostructured anode materials for rechargeable lithium-ion batteries. *Energy Environ. Sci.* **2011,** *4* (8), 2682-

2699.

170. Wagemaker, M.; Mulder, F. M. Properties and Promises of Nanosized Insertion Materials for Li-Ion Batteries. *Acc. Chem. Res.* **2013,** *46* (5), 1206–1215.

171. Chen, Z.; Belharouak, I.; Sun, Y.-K.; Amine, K. Titanium-Based Anode Materials for Safe Lithium-Ion Batteries. *Adv. Funct. Mater.* **2013,** *23* (8), 959–969.

172. Fröschl, T.; Hörmann, U.; Kubiak, P.; Kucerova, G.; Pfanzelt, M.; Weiss, C. K.; Behm, R. J.; Hüsing, N.; Kaiser, U.; Landfester, K.; Wohlfahrt-Mehrens, M. High surface area crystalline titanium dioxide: potential and limits in electrochemical energy storage and catalysis. *Chem. Soc. Rev.* **2012,** *41* (15), 5313–5360.

173. Jiang, C.; Honma, I.; Kudo, T.; Zhou, H. Nanocrystalline Rutile TiO2 Electrode for High-Capacity and High-Rate Lithium Storage. *Electrochem. Solid-State Lett.* **2007,** *10* (5), A127-A129.

174. Bruce, P. G.; Scrosati, B.; Tarascon, J.-M. Nanomaterials for Rechargeable Lithium Batteries. *Angew. Chem. Int. Ed.* **2008,** *47* (16), 2930 – 2946.

175. Dey, A. N. Electrochemical Alloying of Lithium in Organic Electrolytes. *J. Electrochem. Soc.* **1971,** *118* (10), 1547-1549.

176. Park, C.-M.; Kim, J.-H.; Kim, H.; Sohn, H.-J. Li-alloy based anode materials for Li secondary batteries. *Chem. Soc. Rev.* **2010,** *39* (8), 3115-3141.

177. Zhang, W.-J. Lithium insertion/extraction mechanism in alloy anodes for lithium-ion batteries. *J. Power Sources* **2011,** *196* (3), 877-885.

178. Obrovac, M. N.; Chevrier, V. L. Alloy Negative Electrodes for Li-Ion Batteries. *Chem. Rev.* **2014,** *114* (23), 11444–11502.

179. Beaulieu, L. Y.; Hatchard, T. D.; Bonakdarpour, A.; Fleischauer, M. D.; Dahn, J. R. Reaction of Li with Alloy Thin Films Studied by In Situ AFM. *J. Electrochem. Soc.* **2003,** *150* (11), A1457-A1464.

180. Zhang, W.-J. A review of the electrochemical performance of alloy anodes for lithium-ion batteries. *J. Power Sources* **2011,** *196* (1), 13–24.

181. Larcher, D.; Beattie, S.; Morcrette, M.; Edström, K.; Jumas, J.-C.; Tarascon, J.-M. Recent findings and prospects in the field of pure metals as negative electrodes for Li-ion batteries. *J. Mater. Chem.* **2007,** *17* (36), 3759-3772.

182. Poizot, P.; Laruelle, S.; Grugeon, S.; Dupont, L.; Tarascon, J.-M. Nano-sized transition-metal oxides as negative-electrode materials for lithium-ion batteries. *Nature* **2000,** *407* (6803), 496-499.

183. Cabana, J.; Monconduit, L.; Larcher, D.; Palacin, M. R. Beyond Intercalation-Based Li-Ion Batteries: The State of the Art and Challenges of Electrode Materials Reacting

Through Conversion Reactions. *Adv. Mater.* **2010,** *22* (35), E170–E192.

184. Yamakawa, N.; Jiang, M.; Grey, C. P. Investigation of the Conversion Reaction Mechanisms for Binary Copper(II) Compounds by Solid-State NMR Spectroscopy and X-ray Diffraction. *Chem. Mater.* **2009,** *21* (14), 3162–3176.

185. Zu, C.-X.; Li, H. Thermodynamic analysis on energy densities of batteries. *Energy Environ. Sci.* **2011,** *4* (8), 2614-2624.

186. Lee, W. W.; Lee, J.-M. Novel synthesis of high performance anode materials for lithium-ion batteries (LIBs). *J. Mater. Chem. A* **2014,** *2* (6), 1589-1626.

187. Valvo, M.; Rehnlund, D.; Lafont, U.; Hahlin, M.; Edström, K.; Nyholm, L. The impact of size effects on the electrochemical behaviour of Cu2O-coated Cu nanopillars for advanced Li-ion microbatteries. *J. Mater. Chem. A* **2014,** *2* (25), 9574-9586.

188. Reddy, M. V.; Subba Rao, G. V.; Chowdari, B. V. R. Metal Oxides and Oxysalts as Anode Materials for Li Ion Batteries. *Chem. Rev.* **2013,** *113* (7), 5364–5457.

189. Zhang, S. S. A review on the separators of liquid electrolyte Li-ion batteries. *J. Power Sources* **2007,** *164* (1), 351–364.

190. Lee, H.; Yanilmaz, M.; Toprakci, O.; Fu, K.; Zhang, X. A review of recent developments in membrane separators for rechargeable lithium-ion batteries. *Energy Environ. Sci.* **2014,** *7* (12), 3857-3886.

191. Orendorff, C. J. The Role of Separators in Lithium-Ion Cell Safety. *Electrochem. Soc. Interface* **2012,** *21* (2), 61-65.

192. Yang, M.; Hou, J. Membranes in Lithium Ion Batteries. *Membranes* **2012,** *2* (3), 367-383.

193. Arora, P.; Zhang, Z. J. Battery Separators. *Chem. Rev.* **2004,** *104* (10), 4419-4462.

194. Xu, K. Nonaqueous Liquid Electrolytes for Lithium-Based Rechargeable Batteries. *Chem. Rev.* **2004,** *104* (10), 4303–4418.

195. Schaefer, J. L.; Lu, Y.; Moganty, S. S.; Agarwal, P.; Jayaprakash, N.; Archer, L. A. Electrolytes for high-energy lithium batteries. *Appl. Nanosci.* **2012,** *2* (2), 91-109.

196. Aravindan, V.; Gnanaraj, J.; Madhavi, S.; Liu, H.-K. Lithium-Ion Conducting Electrolyte Salts for Lithium Batteries. *Chem. Eur. J.* **2011,** *17* (51), 14326–14346.

197. Koch, V. R. Reactions of Tetrahydrofuran and Lithium Hexafluoroarsenate with Lithium. *J. Electrochem. Soc.* **1979,** *126* (2), 181-187.

198. Aurbach, D.; Markovsky, B.; Salitra, G.; Markevich, E.; Yossi, T.; Koltypin, M.; Nazar, L.; Ellis, B.; Kovacheva, D. Review on electrode–electrolyte solution interactions, related to cathode materials for Li-ion batteries. *J. Power Sources* **2007,** *165* (2), 491–499.

199. Etacheri, V.; Marom, R.; Elazari, R.; Salitra, G.; Aurbach, D. Challenges in the development of advanced Li-ion batteries: a review. *Energy Environ. Sci.* **2011,** *4* (9), 3243-3262.

200. Xu, K. Electrolytes and Interphasial Chemistry in Li Ion Devices. *Energies* **2010,** *3* (1), 135-154.

201. Zhang, S. S. A review on electrolyte additives for lithium-ion batteries. *J. Power Sources* **2006,** *162* (2), 1379–1394.

202. Goodenough, J. B.; Kim, Y. Challenges for Rechargeable Li Batteries. *Chem. Mater.* **2010,** *22* (3), 587–603.

203. Verma, P.; Maire, P.; Novak, P. A review of the features and analyses of the solid electrolyte interphase in Li-ion batteries. *Electrochim. Acta* **2010,** *55* (22), 6332–6341.

204. Okamoto, H. Li-Si (Lithium-Silicon). *J. Phase Equilib. Diffus.* **2009,** *30* (1), 118-119.

205. Wen, C. J.; Huggins, R. A. Chemical Diffusion in Intermediate Phases in the Lithium-Silicon System. *J. Solid State Chem.* **1981,** *37* (3), 271-278.

206. Ng, S.-H.; Wang, J.; Wexler, D.; Konstantinov, K.; Guo, Z.-P.; Liu, H.-K. Highly Reversible Lithium Storage in Spheroidal Carbon-Coated Silicon Nanocomposites as Anodes for Lithium-Ion Batteries. *Angew. Chem. Int. Ed.* **2006,** *45* (41), 6896-6899.

207. Nesper, R.; Von Schnering, H. G. Li21Si5, a Zintl Phase as Well as a Hume-Rothery Phase. *J. Solid State Chem.* **1987,** *70* (1), 48-57.

208. Obrovac, M. N.; Christensen, L. Structural Changes in Silicon Anodes during Lithium Insertion/Extraction. *Electrochem. Solid-State Lett.* **2004,** *7* (5), A93-A96.

209. Braga, M. H.; Debski, A.; Gasior, W. Li–Si phase diagram: Enthalpy of mixing, thermodynamic stability, and coherent assessment. *J. Alloys Compd.* **2014,** *616,* 581–593.

210. Thomas, D.; Abdel-Hafiez, M.; Gruber, T.; Hüttl, R.; Seidel, J.; Wolter, A. U. B.; Büchner, B.; Kortus, J.; Mertens, F. The heat capacity and entropy of lithium silicides over the temperature range from (2 to 873) K. *J. Chem. Thermodynamics* **2013,** *64,* 205-225.

211. Zamfir, M. R.; Nguyen, H. T.; Moyen, E.; Lee, Y. H.; Pribat, D. Silicon nanowires for Li-based battery anodes: a review. *J. Mater. Chem. A* **2013,** *1* (34), 9566-9586.

212. Liu, X. H.; Wang, J. W.; Huang, S.; Fan, F.; Huang, X.; Liu, Y.; Krylyuk, S.; Yoo, J.; Dayeh, S. A.; Davydov, A. V.; Mao, S. X.; Picraux, S. T.; Zhang, S.; Li, J.; Zhu, T.; Huang, J. Y. In situ atomic-scale imaging of electrochemical lithiation in silicon. *Nat. Nanotechnol.* **2012,** *7* (11), 749-756.

213. Limthongkul, P.; Jang, Y.-I.; Dudney, N. J.; Chiang, Y.-M. Electrochemically-driven

solid-state amorphization in lithium-silicon alloys and implications for lithium storage. *Acta Mater.* **2003,** *51* (4), 1103–1113.

214. Limthongkul, P.; Jang, Y.-I.; Dudney, N. J.; Chiang, Y.-M. Electrochemically-driven solid-state amorphization in lithium–metal anodes. *J. Power Sources* **2003,** *119-121,* 604–609.

215. Li, J.; Dahn, J. R. An In Situ X-Ray Diffraction Study of the Reaction of Li with Crystalline Si. *J. Electrochem. Soc.* **2007,** *154* (3), A156-A161.

216. McDowell, M. T.; Lee, S. W.; Nix, W. D.; Cui, Y. 25th Anniversary Article: Understanding the Lithiation of Silicon and Other Alloying Anodes for Lithium-Ion Batteries. *Adv. Mater.* **2013,** *25* (36), 4966–4985.

217. Wang, J. W.; He, Y.; Fan, F.; Liu, X. H.; Xia, S.; Liu, Y.; Harris, C. T.; Li, H.; Huang, J. Y.; Mao, S. X.; Zhu, T. Two-Phase Electrochemical Lithiation in Amorphous Silicon. *Nano Lett.* **2013,** *13* (2), 709–715.

218. Ma, D.; Cao, Z.; Hu, A. Si-Based Anode Materials for Li-Ion Batteries: A Mini Review. *Nano-Micro Lett.* **2014,** *6* (4), 347-358.

219. Kang, Y.-M.; Lee, S.-M.; Kim, S.-J.; Jeong, G.-J.; Sung, M.-S.; Choi, W.-U.; Kim, S.-S. Phase transitions explanatory of the electrochemical degradation mechanism of Si based materials. *Electrochem. Commun.* **2007,** *9* (5), 959–964.

220. Xiao, Y.; Hao, D.; Chen, H.; Gong, Z.; Yang, Y. Economical Synthesis and Promotion of the Electrochemical Performance of Silicon Nanowires as Anode Material in Li-Ion Batteries. *ACS Appl. Mater. Interfaces* **2013,** *5* (5), 1681–1687.

221. Obrovac, M. N.; Krause, L. J. Reversible Cycling of Crystalline Silicon Powder. *J. Electrochem. Soc.* **2007,** *154* (2), A103-A108.

222. Chan, C. K.; Ruffo, R.; Hong, S. S.; Huggins, R. A.; Cui, Y. Structural and electrochemical study of the reaction of lithium with silicon nanowires. *J. Power Sources* **2009,** *189* (1), 34–39.

223. McDowell, M. T.; Lee, S. W.; Harris, J. T.; Brian, A. K.; Wang, C.; Nix, W. D.; Cui, Y. In Situ TEM of Two-Phase Lithiation of Amorphous Silicon Nanospheres. *Nano Lett.* **2013,** *13* (2), 758–764.

224. Baggetto, L.; Niessen, R. A. H.; Roozeboom, F.; Notten, P. H. L. High Energy Density All-Solid-State Batteries: A Challenging Concept Towards 3D Integration. *Adv. Funct. Mater.* **2008,** *18* (7), 1057–1066.

225. Pollak, E.; Salitra, G.; Baranchugov, V.; Aurbach, D. In Situ Conductivity, Impedance Spectroscopy, and Ex Situ Raman Spectra of Amorphous Silicon during the Insertion/Extraction of Lithium. *J. Phys. Chem. C* **2007,** *111* (30), 11437–11444.

226. Li, J.; Xiao, X.; Yang, F.; Verbrugge, M. W.; Cheng, Y.-T. Potentiostatic Intermittent

Titration Technique for Electrodes Governed by Diffusion and Interfacial Reaction. *J. Phys. Chem. C* **2012,** *116* (1), 1472–1478.

227. Su, X.; Wu, Q.; Li, J.; Xiao, X.; Lott, A.; Lu, W.; Sheldon, B. W.; Wu, J. Silicon-Based Nanomaterials for Lithium-Ion Batteries: A Review. *Adv. Energy Mater.* **2014,** *4* (1), 1300882.

228. Li, X.; Zhi, L. Managing voids of Si anodes in lithium ion batteries. *Nanoscale* **2013,** *5* (19), 8864-8873.

229. Rhodes, K.; Dudney, N.; Edgar, L.-C.; Daniel, C. Understanding the Degradation of Silicon Electrodes for Lithium-Ion Batteries Using Acoustic Emission. *J. Electrochem. Soc.* **2010,** *157* (12), A1354-A1360.

230. Wu, H.; Cui, Y. Designing nanostructured Si anodes for high energy lithium ion batteries. *Nano Today* **2012,** *7* (5), 414–429.

231. Terranova, M. L.; Orlanducci, S.; Tamburri, E.; Guglielmotti, V.; Rossi, M. Si/C hybrid nanostructures for Li-ion anodes: An overview. *J. Power Sources* **2014,** *246,* 167–177.

232. Chan, C. K.; Peng, H.; Liu, G.; McIlwrath, K.; Zhang, X. F.; Huggins, R. A.; Cui, Y. High-performance lithium battery anodes using silicon nanowires. *Nat. Nanotechnol.* **2008,** *3* (1), 31 - 35.

233. Radvanyi, E.; Porcher, W.; De Vito, E.; Montani, A.; Franger, S.; Si Larbi, S. J. Failure mechanisms of nano-silicon anodes upon cycling: an electrode porosity evolution model. *Phys. Chem. Chem. Phys.* **2014,** *16* (32), 17142-17153.

234. Wu, H.; Chan, G.; Choi, J. W.; Ryu, I.; Yao, Y.; McDowell, M. T.; Lee, S. W.; Jackson, A.; Yang, Y.; Hu, L.; Cui, Y. Stable cycling of double-walled silicon nanotube battery anodes through solid–electrolyte interphase control. *Nat. Nanotechnol.* **2012,** *7* (5), 310–315.

235. Szczech, J. R.; Jin, S. Nanostructured silicon for high capacity lithium battery anodes. *Energy Environ. Sci.* **2011,** *4* (1), 56-72.

236. Liu, X. H.; Zhong, L.; Huang, S.; Mao, S. X.; Zhu, T.; Huang, J. Y. Size-Dependent Fracture of Silicon Nanoparticles During Lithiation. *ACS Nano* **2012,** *6* (2), 1522–1531.

237. Ruy, I.; Choi, J. W.; Cui, Y.; Nix, W. D. Size-dependent fracture of Si nanowire battery anodes. *J. Mech. Phys. Solids* **2011,** *59* (9), 1717-1730.

238. Li, J.; Dozier, A. K.; Li, Y.; Yang, F.; Cheng, Y.-T. Crack Pattern Formation in Thin Film Lithium-Ion Battery Electrodes. *J. Electrochem. Soc.* **2011,** *158* (6), A689-A694.

239. Liu, N.; Lu, Z.; Zhao, J.; McDowell, M. T.; Lee, H.-W.; Zhao, W.; Cui, Y. A pomegranate-inspired nanoscale design for large-volume-change lithium battery anodes. *Nat. Nanotechnol.* **2014,** *9* (3), 187–192.

240. Yin, Y. X.; Wan, L. J.; Guo, Y. G. Silicon-based nanomaterials for lithium-ion batteries. *Chin. Sci. Bull.* **2012,** *57* (32), 4104-4110.

241. Chen, L.; Wang, K.; Xie, X.; Xie, J. Effect of vinylene carbonate (VC) as electrolyte additive on electrochemical performance of Si film anode for lithium ion batteries. *J. Power Sources* **2007,** *174* (2), 538–543.

242. Choi, N.-S.; Yew, K. H.; Lee, K. Y.; Sung, M.; Kim, H.; Kim, S.-S. Effect of fluoroethylene carbonate additive on interfacial properties of silicon thin-film electrode. *J. Power Sources* **2006,** *161* (2), 1254–1259.

243. Profatilova, I. A.; Stock, C.; Schmitz, A.; Passerini, S.; Winter, M. Enhanced thermal stability of a lithiated nano-silicon electrode by fluoroethylene carbonate and vinylene carbonate. *J. Power Sources* **2013,** *222,* 140–149.

244. Zhang, X.; Kostecki, R.; Richardson, T. J.; Pugh, J. K.; Ross, P. N. Electrochemical and Infrared Studies of the Reduction of Organic Carbonates. *J. Electrochem. Soc.* **2001,** *148* (12), A1341-A1345.

245. Xu, C.; Lindgren, F.; Philippe, B.; Gorgoi, M.; Björefors, F.; Edström, K.; Gustafsson, T. Improved Performance of the Silicon Anode for Li-Ion Batteries: Understanding the Surface Modification Mechanism of Fluoroethylene Carbonate as an Effective Electrolyte Additive. *Chem. Mater.* **2015,** *27* (7), 2591–2599.

246. Xu, K. Electrolytes and Interphases in Li-Ion Batteries and Beyond. *Chem. Rev.* **2014,** *114* (23), 11503–11618.

247. Nakai, H.; Kubota, T.; Kita, A.; Kawashima, A. Investigation of the Solid Electrolyte Interphase Formed by Fluoroethylene Carbonate on Si Electrodes. *J. Electrochem. Soc.* **2011,** *158* (7), A798-A801.

248. Etacheri, V.; Haik, O.; Goffer, Y.; Roberts, G. A.; Stefan, I. C.; Fasching, R.; Aurbach, D. Effect of Fluoroethylene Carbonate (FEC) on the Performance and Surface Chemistry of Si-Nanowire Li-Ion Battery Anodes. *Langmuir* **2012,** *28* (1), 965–976.

249. Kasavajjula, U.; Wang, C.; Appleby, A. J. Nano- and bulk-silicon-based insertion anodes for lithium-ion secondary cells. *J. Power Sources* **2007,** *163* (2), 1003–1039.

250. Wolfenstine, J. CaSi2 as an anode for lithium-ion batteries. *J. Power Sources* **2003,** *124* (1), 241-245.

251. Roberts, G. A.; Cairns, E. J.; Reimer, J. A. Magnesium silicide as a negative electrode material for lithium-ion batteries. *J. Power Sources* **2002,** *110* (2), 424-429.

252. Kim, H.; Choi, J.; Sohn, H.-J.; Kang, T. The Insertion Mechanism of Lithium into Mg2Si Anode Material for Li-Ion Batteries. *J. Electrochem. Soc.* **1999,** *146* (12), 4401-4405.

253. Olesinski, R. W.; Gokhale, A. B.; Abbaschian, G. J. The Ag-Si (Silver-Silicon) System. *Bull. Alloy Phase Diagr.* **1989,** *10* (6), 635-636.

254. Hwang, S.-M.; Lee, H.-Y.; Jang, S.-W.; Lee, S.-M.; Lee, S.-J.; Baik, H.-K.; Lee, J.-Y. Lithium Insertion in SiAg Powders Produced by Mechanical Alloying. *Electrochem. Solid-State Lett.* **2001,** *4* (7), A97-A100.

255. Yu, Y.; Gu, L.; Zhu, C.; Tsukimoto, S.; van Aken, P. A.; Maier, J. Reversible Storage of Lithium in Silver-Coated Three-Dimensional Macroporous Silicon. *Adv. Mater.* **2010,** *22* (20), 2247–2250.

256. Farooq, U.; Yaqub, A.; Choi, J.-H.; Pervez, S. A.; Kim, D.-H.; Lee, Y.-J.; Doh, C.-H. Metal-assisted silicon based negative electrode for Li-ion batteries. *Mater. Lett.* **2014,** *126,* 291–294.

257. Kang, H.-K.; Lee, S.-R.; Cho, W. I.; Cho, B. W. Effect of multilayer structure on cyclic performance of Si/Fe anode electrode in Lithium-ion secondary batteries. *Phys. Chem. Chem. Phys.* **2013,** *15* (5), 1569-1577.

258. Cetinkaya, T.; Uysal, M.; Akbulut, H. Electrochemical performance of electroless nickel plated silicon electrodes for Li-ion batteries. *Appl. Surf. Sci.* **2015,** *334,* 94–101.

259. Li, T.; Cao, Y. L.; Ai, X. P.; Yang, H. X. Cycleable graphite/FeSi6 alloy composite as a high capacity anode material for Li-ion batteries. *J. Power Sources* **2008,** *184* (2), 473-476.

260. Lee, K. J.; Yu, S.-H.; Kim, J.-J.; Lee, D.-H.; Park, J.; Suh, S. S.; Cho, J. S.; Sung, Y.-E. Si7Ti4Ni4 as a buffer material for Si and its electrochemical study for lithium ion batteries. *J. Power Sources* **2014,** *246,* 729–735.

261. Yu, B.-C.; Hwa, Y.; Kim, J.-H.; Sohn, H.-J. A New Approach to Synthesis of Porous SiOxAnode for Li-ion Batteries via Chemical Etching of Si Crystallites. *Electrochim. Acta* **2014,** *117,* 426–430.

262. Liu, H. K.; Guo, Z. P.; Wang, J. Z.; Konstantinov, K. Si-based anode materials for lithium rechargeable batteries. *J. Mater. Chem.* **2010,** *20* (45), 10055-10057.

263. Guo, C.; Wang, D.; Wang, Q.; Wang, B.; Liu, T. A SiO/graphene Nanocomposite as a High Stability Anode Material for Lithium-Ion Batteries. *Int. J. Electrochem. Sci.* **2012,** *7* (9), 8745 - 8752.

264. Lee, J. K.; Yoon, W. Y.; Kim, B. K. Electrochemical Behavior of Si Nanoparticle Anode Coated with Diamond-Like Carbon for Lithium-Ion Battery. *J. Electrochem. Soc.* **2012,** *159* (11), A1844-A1848.

265. Martin, C.; Alias, M.; Christien, F.; Crosnier, O.; Belanger, D.; Brousse, T. Graphite-Grafted Silicon Nanocomposite as a Negative Electrode for Lithium-Ion Batteries. *Adv. Mater.* **2009,** *21* (46), 4735–4741.

266. Wang, Y.-X.; Chou, S.-L.; Kim, J. H.; Liu, H.-K.; Dou, S.-X. Nanocomposites of silicon and carbon derived from coal tar pitch: Cheap anode materials for lithium-ion batteries with long cycle life and enhanced capacity. *Electrochim. Acta* **2013,** *93,* 213–221.

267. Magasinski, A.; Dixon, P.; Hertzberg, B.; Kvit, A.; Ayala, J.; Yushin, G. High-performance lithium-ion anodes using a hierarchical bottom-up approach. *Nat. Mater.* **2010,** *9* (4), 353–358.

268. Fan, Y.; Zhang, Q.; Lu, C.; Xiao, Q.; Wang, X.; Tay, B. k. High performance carbon nanotube–Si core–shell wires with a rationally structured core for lithium ion battery anodes. *Nanoscale* **2013,** *5* (4), 1503-1506.

269. Xu, Z.-L.; Zhang, B.; Zhou, Z.-Q.; Abouali, S.; Garakani, M. A.; Huang, J.; Huang, J.-Q.; Kim, J.-K. Carbon nanofibers containing Si nanoparticles and graphene-covered Ni for high performance anodes in Li ion batteries. *RSC Adv.* **2014,** *4* (43), 22359-22366.

270. Wu, H.; Zheng, G.; Liu, N.; Carney, T. G.; Yang, Y.; Cui, Y. Engineering Empty Space between Si Nanoparticles for Lithium-Ion Battery Anodes. *Nano Lett.* **2012,** *12* (2), 904–909.

271. Hertzberg, B.; Alexeev, A.; Yushin, G. Deformations in Si-Li Anodes Upon Electrochemical Alloying in Nano-Confined Space. *J. Am. Chem. Soc.* **2010,** *132* (25), 8548–8549.

272. Tong, Y.; Xu, Z.; Liu, C.; Zhang, G.; Wang, J.; Wu, Z. G. Magnetic sputtered amorphous Si/C multilayer thin films as anode materials for lithium ion batteries. *J. Power Sources* **2014,** *247,* 78–83.

273. Luo, J.; Zhao, X.; Wu, J.; Jang, H. D.; Kung, H. H.; Huang, J. Crumpled Graphene-Encapsulated Si Nanoparticles for Lithium Ion Battery Anodes. *J. Phys. Chem. Lett.* **2012,** *3* (13), 1824–1829.

274. Li, H.; Lu, C.; Zhang, B. A straightforward approach towards Si@C/graphene nanocomposite and its superior lithium storage performance. *Electrochim. Acta* **2014,** *120,* 96–101.

275. Zhu, S.; Zhu, C.; Ma, J.; Meng, Q.; Guo, Z.; Yu, Z.; Lu, T.; Zhang, D.; Lau, W. M. Controlled fabrication of Si nanoparticles on graphene sheets for Li-ion batteries. *RSC Adv.* **2013,** *3* (17), 6141-6146.

276. Yin, Y.-X.; Xin, S.; Wan, L.-J.; Li, C.-J.; Guo, Y.-G. Electrospray Synthesis of Silicon/Carbon Nanoporous Microspheres as Improved Anode Materials for Lithium-Ion Batteries. *J. Phys. Chem. C* **2011,** *115* (29), 14148–14154.

277. Liu, N.; Wu, H.; McDowell, M. T.; Yao, Y.; Wang, C.; Cui, Y. A Yolk-Shell Design for Stabilized and Scalable Li-Ion Battery Alloy Anodes. *Nano Lett.* **2012,** *12* (6), 3315–3321.

278. Niu, J.; Lee, J. Y. Improvement of Usable Capacity and Cyclability of Silicon-Based Anode Materials for Lithium Batteries by Sol-Gel Graphite Matrix. *Electrochem. Solid-State Lett.* **2002,** *5* (6), A107-A110.

279. Gauthier, M.; Reyter, D.; Mazouzi, D.; Moreau, P.; Guyomard, D.; Lestriez, B.; Roue, L.

From Si wafers to cheap and efficient Si electrodes for Li-ion batteries. *J. Power Sources* **2014,** *256,* 32–36.

280. Yim, C.-H.; Courtel, F. M.; Abu-Lebdeh, Y. A high capacity silicon–graphite composite as anode for lithium-ion batteries using low content amorphous silicon and compatible binders. *J. Mater. Chem. A* **2013,** *1* (28), 8234-8243.

281. Hochgatterer, N. S.; Schweiger, M. R.; Koller, S.; Raimann, P. R.; Wöhrle, T.; Wurm, C.; Winter, M. Silicon/Graphite Composite Electrodes for High-Capacity Anodes: Influence of Binder Chemistry on Cycling Stability. *Electrochem. Solid-State Lett.* **2008,** *11* (5), A76-A80.

282. Koller, S. *About the Nature of the Electrochemical Formation of Binary Lithium-Silicon Intermetallic Phases from Nonaqueous Electrolytes;* Doctoral Thesis; Technische Universität Graz, 2009.

283. Ulldemolins, M.; Le Cras, F.; Pecquenard, B.; Phan, V. P.; Martin, L.; Martinez, H. Investigation on the part played by the solid electrolyte interphase on the electrochemical performances of the silicon electrode for lithium-ion batteries. *J. Power Sources* **2012,** *206,* 245–252.

284. *Operating instructions PULVERISETTE 7 premium line;* Manual; Fritsch GmbH: Idar-Oberstein, 2013.

285. http://www.cmcmilling.com/milling-vs-grinding.html (accessed September 02, 2015).

286. *Planetary Mills premium line;* Product brochure; Fritsch GmbH: Idar-Oberstein, 2013.

287. Wiberg, N. Tafeln. In *Lehrbuch der Anorganischen Chemie,* 102nd ed.; Walter de Gruyter & Co: Berlin, 2007; pp 2143-2149.

288. Weast, R. C. Hardness of Materials. In *Handbook of Chemistry and Physics,* 55th ed.; CRC Press: Cleveland, 1974-1975; p F22.

289. Foster, L. S. Comparison of hardness values of various materials on Mohs and Knoop scales. In *Handbook of Chemistry and Physics,* 55th ed.; Weast, R. C., Ed.; CRC Press: Cleveland, 1974-1975; p F22.

290. Galasso, F.; Kuntz, U.; Croft, W. J. Pyrolytic Si3N4. *J. Am. Ceram. Soc.* **1972,** *55* (8), 431.

291. http://www.sigmaaldrich.com/chemistry/stockroom-reagents/learning-center/technical-library/particle-size-conversion.html (accessed September 03, 2015).

292. *Operating instructions ANALYSETTE 22 NanoTec plus;* Manual; Fritsch GmbH: Idar-Oberstein, 2009.

293. Dufficy, M. K.; Khan, S. A.; Fedkiw, P. S. Galactomannan binding agents for silicon anodes in Li-ion batteries. *J. Mater. Chem. A* **2015,** *3* (22), 12023-12030.

294. Agarwala, A.; Subramani, T.; Goldbourt, A.; Danovich, D.; Yerushalmi, R. Facile Monolayer Formation on SiO2 Surfaces via Organoboron Functionalities. *Angew. Chem. Int. Ed.* **2013,** *52* (29), 7415 –77418.

295. Wang, H.; Wu, P.; Shi, H.; Tang, W.; Tang, Y.; Zhou, Y.; She, P.; Lu, T. Hollow porous silicon oxide nanobelts for high-performance lithium storage. *J. Power Sources* **2015,** *274,* 951-956.

296. Cui, L.; Xia, W. W.; Wang, F.; Yang, L. J.; Hu, Y. J. Investigations on the Si/SiO2 interface defects of silicon nanowires. *Physica B* **2013,** *409,* 47-50.

297. Ding, Y.; Chu, X.; Hong, X.; Zou, P.; Liu, Y. The infrared fingerprint signals of silica nanoparticles and its application in immunoassay. *Appl. Phys. Lett.* **2012,** *100* (1), 013701.

298. Pan, G.-H.; Barras, A.; Boussekey, L.; Addad, A.; Boukherroub, R. Alkyl passivation and SiO2 encapsulation of silicon nanoparticles: preparation, surface modification and luminescence properties. *J. Mater. Chem. C* **2013,** *1* (34), 5261-5271.

299. Effati, E.; Pourabbas, B. One-pot synthesis of sub-50 nm vinyl- and acrylate-modified silica nanoparticles. *Powder Technol.* **2012,** *219,* 276–283.

300. Lee, J.; Bae, J.; Heo, J.; Han, I. T.; Cha, S. N.; Kim, D. K.; Yang, M.; Han, H. S.; Jeon, W. S.; Chung, J. Effect of Randomly Networked Carbon Nanotubes in Silicon-Based Anodes for Lithium-Ion Batteries. *J. Electrochem. Soc.* **2009,** *156* (11), A905-A910.

301. Dai, F.; Yi, R.; Gordin, M. L.; Chen, S.; Wang, D. Amorphous Si/SiOx/SiO2 nanocomposites via facile scalable synthesis as anode materials for Li-ion batteries with long cycling life. *RSC Adv.* **2012,** *2* (33), 12710-12713.

302. Kummer, M.; Badillo, J. P.; Schmitz, A.; Bremes, H.-G.; Winter, M.; Schulz, C.; Wiggers, H. Silicon/Polyaniline Nanocomposites as Anode Material for Lithium Ion Batteries. *J. Electrochem. Soc.* **2014,** *161* (1), A40-A45.

303. Smith, B. C. *Infrared Spectral Interpretation: A Systematic Approach;* CRC Press LLC: Boca Raton, 1999; pp 70-75.

304. Mizuhata, M.; Katayama, A.; Maki, H. On-site fabrication and charge–discharge property of TiO2 coated porous silicon electrode by the liquid phase deposition with anodic oxidation. *J. Fluorine Chem.* **2015,** *174,* 62–69.

305. Lee, J.-K.; Kung, M. C.; Trahey, L.; Missaghi, M. N.; Kung, H. H. Nanocomposites Derived from Phenol-Functionalized Si Nanoparticles for High Performance Lithium Ion Battery Anodes. *Chem. Mater.* **2009,** *21* (1), 6–8.

306. Launer, P. J. Infrared Analysis of Organosilicon Compounds: Spectra-Structure Relations. In *Silicon Compounds: Silanes & Silicones;* Gelest, Inc.: Morrisville, 2013; pp 175-178.

307. Kaspar, J.; Terzioglu, C.; Ionescu, E.; Graczyk-Zajac, M.; Hapis, S.; Kleebe, H.-J.; Riedel, R. Stable SiOC/Sn Nanocomposite Anodes for Lithium-Ion Batteries with Outstanding Cycling Stability. *Adv. Funct. Mater.* **2014,** *24* (26), 4097–4104.

308. Sun, C.-F.; Zhu, H.; Okada, M.; Gaskell, K.; Inoue, Y.; Hu, L.; Wang, Y.-H. Interfacial Oxygen Stabilizes Composite Silicon Anodes. *Nano Lett.* **2015,** *15* (1), 703−708.

309. Xu, W.; Vegunta, S. S. S.; Flake, J. C. Surface-modified silicon nanowire anodes for lithium-ion batteries. *J. Power Sources* **2011,** *196* (20), 8583–8589.

310. Maroni, F.; Raccichini, R.; Birrozzi, A.; Carbonari, G.; Tossici, R.; Croce, F.; Marassi, R.; Nobili, F. Graphene/silicon nanocomposite anode with enhanced electrochemical stability for lithium-ion battery applications. *J. Power Sources* **2014,** *269,* 873–882.

311. Seo, H.; Kim, K.; Yi, C.-W. Physico-Chemical and Electrochemical Properties of Si-Ti-Ni Alloy Modified with poly(3,4-ethylenedioxythiophene). *Electrochim. Acta* **2015,** *165,* 247–254.

312. Smith, B. C. *Infrared Spectral Interpretation: A Systematic Approach;* CRC Press LLC: Boca Raton, 1999; pp 43-47.

313. John, P.; Odeh, I. M.; Thomas, M. J. K. A Reassessment of the Vibrational Spectrum of Hydrogenated Amorphous Silicon. *Solid State Commun.* **1982,** *41* (4), 341-344.

314. Baretzky, B.; Baro, M. D.; Grabovetskaya, G. P.; Gubicza, J.; Ivanov, M. B.; Kolobov, Y. R.; Langdon, T. G.; Lendvai, J.; Lipnitskii, A. G.; Mazilkin, A. A.; Nazarov, A. A.; Nogues, J.; Ovidko, I. A.; Protasova, S. G.; Raab, G. I.; Revesz, A.; Skiba, N. V.; Sort, J.; Starink, M. J.; Straumal, B. B.; Surinach, S.; Ungar, T.; Zhilyaev, A. P. Fundamentals of Interface Phenomena in Advanced Bulk Nanoscale Materials. *Rev. Adv. Mater. Sci.* **2005,** *9* (1), 45-108.

315. Weidlein, J.; Müller, U.; Dehnicke, K. *Schwingungsspektroskopie: Eine Einführung;* Georg Thieme Verlag: Stuttgart, New York, 1982; pp 152-156.

316. Kalsi, P. S. *Spectroscopy of Organic Compounds,* 6th ed.; New Age International (P) Ltd.: New Delhi, 2004; pp 95-103.

317. Scharfegger, M.; Kren, H.; Koller, S. Structurally stable active material for battery electrodes. WO2013045327, April 13, 2013.

318. http://www.glatt.com/fr/verfahren/coating/wirbelschicht-coating/bottom-spray/ (accessed October 1, 2015).

319. *Innovative Technologies for Granules and Pellets;* Product Folder; Glatt GmbH: Binzen, 2015.

320. Charlton, J. R. Cured epoxy resin compositions useful in the protection of electrical cables. US3878146, April 15, 1975.

321. http://www.sigmaaldrich.com/catalog/product/sial/a3183?lang=de&region=AT (accessed October 13, 2015).

322. Wiberg, N. In *Lehrbuch der Anorganischen Chemie,* 102nd ed.; Walter de Gruyter & Co: Berlin, 2007; p 143.

323. Dominghaus, H. *Die Kunstoffe und ihre Eigenschaften,* 6th ed.; Springer-Verlag: Berlin Heidelberg, 2005.

324. Scharfegger, M. *Highly Structured Silicon-Graphite Composite Materials for Lithium-Ion Batteries;* Doctoral Thesis; Technische Univeristät Graz, 2013.

325. Fouda, O. F.; Pieri, R.; Apostolo, M.; Miltner, H. E.; Goffin, A.-L.; Chen, S. Electrode-forming composition. WO2013092446, June 27, 2013.

326. Han, Z.-J.; Yamagiwa, K.; Yabuuchi, N.; Son, J.-Y.; Cui, Y.-T.; Oji, H.; Kogure, A.; Harada, T.; Ishikawa, S.; Aoki, Y.; Komaba, S. Electrochemical lithiation performance and characterization of silicon–graphite composites with lithium, sodium, potassium, and ammonium polyacrylate binders. *Phys. Chem. Chem. Phys.* **2015,** *17* (5), 3783-3795.

327. Han, Z.-J.; Yabuuchi, N.; Hashimoto, S.; Sasaki, T.; Komaba, S. Cross-Linked Poly(acrylic acid) with Polycarbodiimide as Advanced Binder for Si/Graphite Composite Negative Electrodes in Li-Ion Batteries. *ECS Electrochem. Lett.* **2013,** *2* (2), A17-A20.

328. Zheng, J.; Zheng, H.; Wang, R.; Ben, L.; Lu, W.; Chen, L.; Chen, L.; Li, H. 3D visualization of inhomogeneous multi-layered structure and Young's modulus of the solid electrolyte interphase (SEI) on silicon anodes for lithium ion batteries. *Phys. Chem. Chem. Phys.* **2014,** *16* (26), 13229-13238.

329. Pereira-Nabais, C.; Swiatowska, J.; Rosso, M.; Ozanam, F.; Seyeux, A.; Gohier, A.; Tran-Van, P.; Cassir, M.; Marcus, P. Effect of Lithiation Potential and Cycling on Chemical and Morphological Evolution of Si Thin Film Electrode Studied by ToF-SIMS. *ACS Appl. Mater. Interfaces* **2014,** *6* (15), 13023−13033.

330. Markevich, E.; Fridman, K.; Sharabi, R.; Elazari, R.; Salitra, G.; Gottlieb, H. E.; Gershinsky, G.; Garsuch, A.; Semrau, G.; Schmidt, M. A.; Aurbach, D. Amorphous Columnar Silicon Anodes for Advanced High Voltage Lithium Ion Full Cells: Dominant Factors Governing Cycling Performance. *J. Electrochem. Soc.* **2013,** *160* (10), A1824-A1833.

331. Yuge, R.; Toda, A.; Fukatsu, K.; Tamura, N.; Manako, T.; Nakahara, K.; Nakano, K. Effect of Volume Expansion on SEI Covering Carbon-Coated Nano-Si/SiO Composite. *J. Electrochem. Soc.* **2013,** *160* (10), A1789-A1793.